Ultrasound-instantiated statistical shape models for image-guided hip replacement surgery

Chan, See Kay Carolyn

Ultrasound-Instantiated Statistical Shape Models for Image-Guided Hip Replacement Surgery

See Kay Carolyn Chan

A thesis submitted in partial fulfillment of the requirements for the degree of Doctor of Philosophy of the University of London

October 2005

Division of Imaging Sciences,

Guy's, King's and St. Thomas' School of Medicine,

King's College London

Abstract

This thesis contributes to knowledge by describing a method that uses tracked ultrasound as a non-invasive localiser to simultaneously instantiate and register 3D statistical shape models (SSMs) for image-guided hip replacement surgery. A novel approach is proposed by using bone surface points derived from a set of tracked B-mode ultrasound images acquired on humans to instantiate a patient-specific 3D model of the relevant anatomy.

Two methods were used to produce the SSMs. For both methods, a database of computed tomography (CT) scans were registered to a segmented template using an intensity-based non-rigid registration algorithm which generated deformation fields. The first method involves using these deformation fields to propagate the template bone surface to each of the other datasets, to produce an SSM on these surface points. The second method involves generating the SSMs directly from the deformation fields that are capable of providing a much more densely sampled bone surface for higher accuracy instantiations.

The thesis started with proof of principle through a study using a femur in a water bath. Later the method was validated with a carefully designed cadaver study to better test the validity and robustness of the method, using 3 complete cadavers where high-resolution CT scans and accurate image-physical registration transformations were available to provide gold standard measurements of shape and registration.

In the cadaver study, the femur and pelvis SSMs were built using 16 and 10 CT images respectively. The root mean square (RMS) distance between the model surface and ultrasound-derived bone surface points were iteratively minimised, the results ranged between 1.1 and 2.0mm for the femurs and 2.3 and 4.2mm for the pelves. RMS distance between instantiated model and gold standard surface ranged from 1.8 to 3.7mm in the region of the femoral head when ultrasound images were sufficiently sampled, and 2.1 to 3.5mm in the region of the acetabulum.

Acknowledgements

Firstly, I would like to give thanks to the Lord of heaven and earth.

Special thanks to Dad and Mum - without you I would not be doing this PhD at all. Also my sister Evelyn - thanks - without you I would not be surviving in London, and how could I have gone through the past few years without you!

Thank you to all those involved and helped me throughout the project. Dave, my supervisor - thanks so much for your support and encouragement despite your busy schedule. I really appreciate your spending much time discussing and giving comments on my work. Eddie, thanks for being my supervisor too, you have supported me wherever you are. Graeme, my unofficial 3rd supervisor, thanks for understanding my work, your help, comments and suggestions were a lot of inspiration, really appreciate it. Dean, your expertise in ultrasound has made this project possible! Thanks! Mike, your enthusiasm as a surgeon gave me good encouragement. Thanks to all other folks at CISG, some at CMIC now. Phillipp, thanks for helping me with compiling stuff and thanks for suggesting the use of the Opt++ library. Also thanks to Thomas, Jane, Julia, Tim and Nick.

This project is funded by the Engineering and Physical Sciences Research Council (EPSRC)(GR/R03525/01) without which this thesis would not exist; I would also like to thank the following: DePuy International for providing the femur and pelvis images that were used to build the shape models; Professor Dr. med. R. Putz, Institute of Anatomy, Ludwig-Maximilians University (LMU), for the cadavers and facilities for the cadaver experiments. Also thanks to the staff of the Radiology Department at LMU for their assistance with CT scanning; and Philips Medical Systems for advice on ultrasound.

I would like to give my final thanks to brothers and sisters and friends at Chinese Church in London who prayed and supported me throughout the past few years. Thank you all!

"Except the LORD build the house, they labour in vain that build it; except the LORD keep the city, the watchman waketh but in vain." (Psalm 127:1 KJV)

Contents

List of Tables

List of Figures

List of Abbreviations

2D	Two-Dimensional
3D	Three-Dimensional
CT	Computed Tomography
DOF	Degrees of Freedom
FFD	Free-Form Deformation
FLE	Fiducial Localisation Error
FRE	Fiducial Registration Error
ICA	Independent Component Analysis
ICP	Iterative Closest Point
IGS	Image-Guided Surgery
MDL	Minimum Description Length
MRI	Magnetic Resonance Imaging
NMI	Normalised Mutual Information
PCA	Principal Component Analysis
RMS	Root Mean Square
SDM	Statistical Deformation Model
SSM	Statistical Shape Model
SVD	Singular Value Decomposition
TRE	Target Registration Error
US	Ultrasound
VTK	Visualization Toolkit

Chapter 1

Introduction

This thesis proposes a new method in which ultrasound imaging might be used intraoperatively in hip replacement surgery, in order to avoid the traditional procedure of doing expensive computed tomography (CT) scans, reduce the invasiveness of surgical procedure, reduce radiation dose to both staff and patient, and reduce surgery times. Ultimately, ultrasound and/or X-ray would be used to reconstruct or instantiate 3D models of the femur and pelvis, and ultrasound would also be used for registration. My approach uses a statistical shape model (SSM) of the 3D shape of these bones.

Hip replacement surgery involves an extensive surgical exposure and use of prostheses that can be quite significant in size. On average, the patient stays in the hospital for 11 days following the surgery, with limited weight bearing and further rehabilitation taking up to 3 months. The demand for total hip replacement is growing steadily with the ageing population. The American hip replacement market alone is estimated to exceed $2 billion by the year 2007 (Datamonitor, 2004).

Recently, minimally invasive techniques were introduced into the market. In these techniques the implants were inserted with minimal disruption to the joint capsule and the procedure was able to significantly reduce hospital stays by up to 10 days. Together with image guidance technology the procedure has the potential to become much less invasive, faster and easier to perform, and might improve the accuracy with which the prosthesis was implanted.

A number of groups have developed shape models for orthopaedic surgery. Yao and Taylor (2002) have demonstrated 2D/3D non-rigid registration between a statistical bone density atlas of the hip and a set of X-ray images, and instantiated a deformable hemi-pelvis model with anatomical structures visible in a CT image (Yao and Taylor, 2003). Fleute et al. (2002) instantiated 3D anatomical surfaces of the spine from a point distribution model with a few X-rays using a

contour-based registration method. To the best of my knowledge no other groups have attempted instantiation of a 3D model using tracked ultrasound on real human. This will be reviewed in Chapter 2.

This thesis describes details of a method that uses tracked ultrasound derived data to instantiate a 3D model, including generation and instantiation of the shape model. The potential of the new method was demonstrated on a dry bone immersed in water, where ultrasound scans were acquired in regions that would be accessible *in vivo* (Chan et al., 2003, 2004b). This is followed by validation using cadaveric data where an accurate gold standard image-to-physical registration transformation, based on bone-implanted fiducial markers, to a high-resolution CT scan was also provided, preliminary results of which were presented in Chan et al. (2004a). The cadaver study shows the combined instantiation and registration of femur and pelvis SSMs using ultrasound data collected on 3 cadavers, with corresponding CT volumes providing the ground-truth shape. Cadavers are used rather than a dry bone in a water bath to better test the validity and robustness of the method to soft tissue structure, image distortions and other typical artefacts expected in ultrasound scanning *in vivo*. This work represents part of a larger programme to incorporate active computational models, with knowledge of shape, motion and biomechanics, into image-guided procedures (Hawkes et al., 2005).

1.1 Motivation

Traditional hip replacement surgery requires X-rays to be taken preoperatively. Conventional image-guided hip replacement surgery, meanwhile, requires expensive CT scans before the surgery for planning purposes, which delivers high radiation dose to the patient but increases accuracy of prosthesis placement and reduces failure rate. CT-free methods were recently introduced to the industry and these involve palpating optically tracked probes on the surgically exposed bone surface of the patient.

In conventional image-guided total hip replacement a 3D plan of the procedure is generated using a volume CT scan of the femur and pelvis. A 3D model is generated from these scans and this is used to determine the location of the hip centre and plan the appropriate implant size. Image-guided total hip replacement has the potential to provide more accurate surgical placement of prostheses with the aid of a surgical plan derived from a 3D model of the femur and pelvis and their relationship via the hip joint. It also provides the opportunity to develop less invasive procedures that reduce surgical exposure of bone and results in less disruption of the joint cap-

sule. A good guidance system coupled with minimally invasive methods could make the patient's recovery quicker and less painful.

The proposed method will allow exploitation of these advantages without the need for a patient specific preoperative CT scan, and its associated radiation dose, inconvenience and expense. In this method bone surface points are derived from a set of tracked B-mode ultrasound images. Only a proportion of the bone surface is accessible to ultrasound, so an SSM is used to generate an anatomically realistic model of bony anatomy.

Ultrasound provides a safe, non-invasive and relatively inexpensive method for locating bone surfaces intraoperatively. The use of ultrasound to instantiate and register bone also results in a reduction in invasiveness of the procedure compared to some standard image-guided procedures where a significant area of bone surface is surgically exposed in order to palpate sufficient bone surface to achieve an accurate surface registration with the CT-derived model.

1.2 Aims of the Thesis

The aim of this work is to determine the location of bone surface intraoperatively using percutaneous ultrasound and, with the help of a SSM, reconstruct a complete three-dimensional model of relevant anatomy. It was hoped that this could provide accurate guidance without having to acquire a CT scan.

These are the research questions to be addressed in this thesis:

- Can a SSM be used to instantiate 3D models from ultrasound? This thesis will introduce two methods to produce SSMs and these will be tested.

- Can ultrasound be used to reconstruct a complete 3D representation of the bony anatomy for image-guided surgery? Ultrasound data will be obtained from a dry bone immersed in a water bath and 3 cadavers, and their corresponding complete 3D surfaces reconstructed.

- How accurate is this reconstructed surface by comparison with the ground truth? The algorithm is validated using independent gold standards.

- Can the centre of the femoral head be incorporated in the instantiation algorithm to further improve the method?

- Where can ultrasound images be obtained around the hip joint and the femur? Regions accessible to percutaneous ultrasound are investigated through the cadaver experiments.

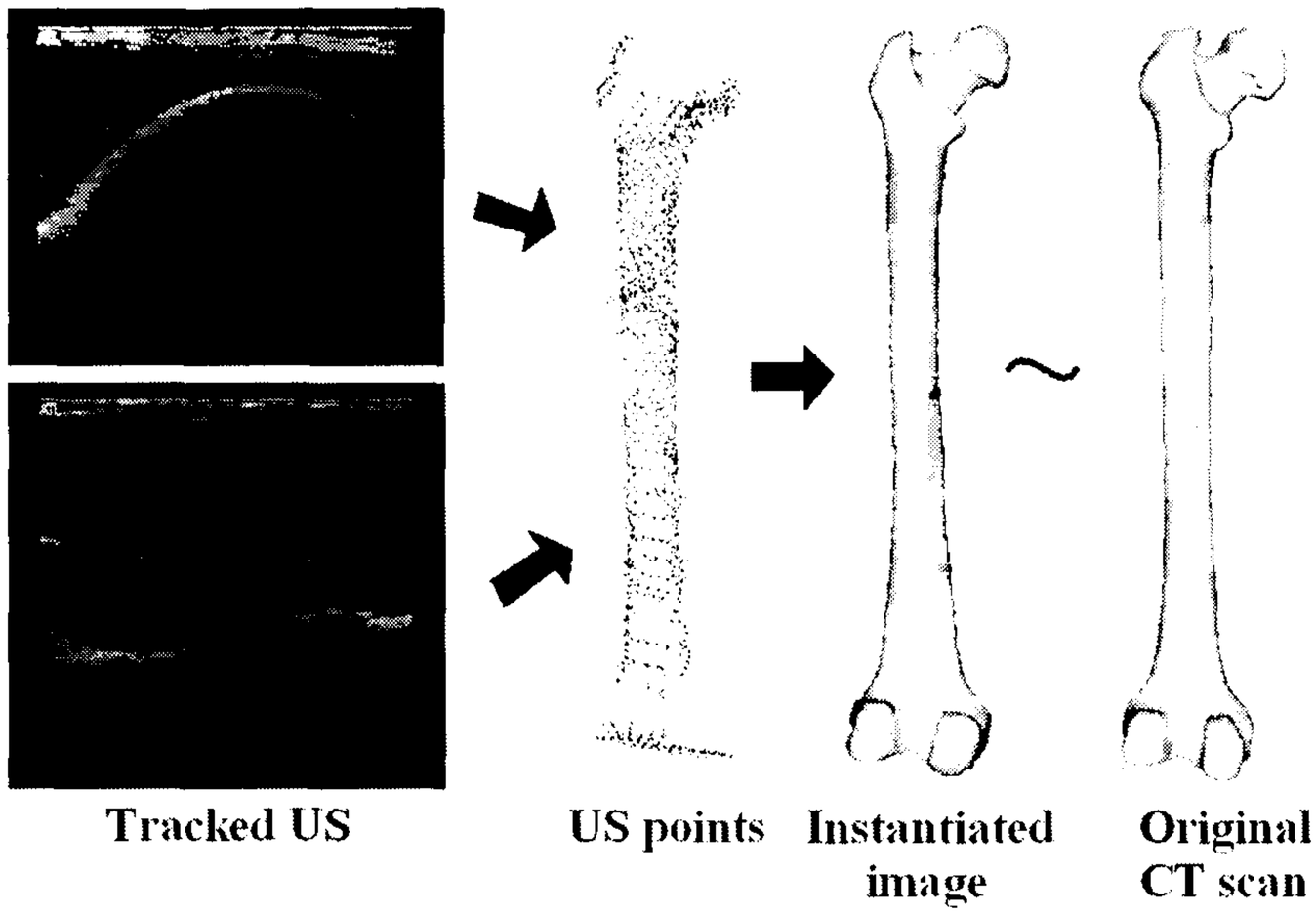

Figure 1.1: Using ultrasound of bone to generate the original surface

The application takes the ultrasound images of bone. From these images the method generates the surface of this bone which will closely approximate to the original shape. This idea is illustrated in Figure 1.1.

The method starts with producing a SSM of bone. This should be able to model how an individual's bone, might it be femur or pelvis, vary in shape across a population. One of the ways to produce the model is to gather information about bones with respect to a reference, which is referred to as the "template" throughout this thesis. This template is segmented and then non-rigidly registered to other bones in the database. The non-rigid registration algorithm is based on deforming a regular grid of B-spline node points. All the registrations are performed on voxel images, the output of the algorithm is therefore a set of B-spline node points that describe the mapping from the template to the other images in the database.

After the registration process, principal component analysis (PCA) is used to find the principal components of shape variation by computing the main modes of variation. PCA allows the population variation of complicated shapes to be captured with a very small number of parameters.

The method described in this thesis models these modes of variation in two ways - based on the deformation of the surface points (Chapter 3 - Surface Statistical Shape Model for the Femur) and based on the deformation of the B-spline node points (Chapter 4 - Volume Statistical Shape Model for the Femur).

Once the model has been produced, a patient specific 3D representation of the femur or pelvis

(Chapter 5 - Volume Statistical Shape Model for the Pelvis) is generated as follows. Ultrasound images of the patient are acquired that include the bone surface. Then from the model, the weights of each mode of shape variation of the bone shape that contributes to the instantiated model is changed, so as to find the closest instance that matches the ultrasound-derived surface points of the femur or pelvis. From that a 3D surface of the bone will be obtained, so that the surgeon can use it for planning.

1.3 Contribution

The main contribution of this thesis is the method which uses ultrasound to instantiate and register a SSM of bone with validation on 3 cadavers. For the study on femurs, the centre of the femoral head was also incorporated in the shape model to better constrain the reconstruction of shape. In practice, this point can be obtained intraoperatively by pivoting the tracked femur around the hip joint.

Two methods were used to produce the SSMs. For both methods, a database of CT scans were registered to a segmented template using an intensity-based non-rigid registration algorithm which generated deformation fields. The first method involves using these deformation fields to propagate the template bone surface to each of the other datasets, to produce an SSM on these surface points that provides a low-resolution representation of the bone surface. The second method involves generating the SSMs directly from the deformation fields that are capable of providing a much more densely sampled bone surface for higher accuracy instantiations. The 3D shape of the model was described by 5 parameters (the first 5 modes of shape variation with weights corresponding to up to ± 3 standard deviations).

The instantiation algorithm is implemented. Surface points extracted from freehand 3D ultrasound images were used as input data for instantiating a 3D surface of bones, represented by a densely triangulated mesh. During each iteration of the instantiation algorithm, bone surface points from the ultrasound scans were aligned with the instantiated surface using the iterative closest point (ICP) algorithm. The resulting root mean square point-to-surface distance was minimised over the modes of variation of the model. Two different optimisation strategies for achieving this were investigated.

The cadaver experiments were carefully designed by incorporating CT visible bone implanted markers, such that the CT scans of the cadavers were available to act as the gold standard.

1.4 Structure of the Thesis

The structure of this thesis is as follows:

Chapter 2 is a literature review of the techniques involved in this thesis including statistical shape models, ultrasound, registration techniques, various imaging modalities, optimisation methods and other relevant background information.

Chapter 3 describes the production of surface statistical shape model for the femur, where the models were produced based on bone surface points. Results for instantiating from a phantom femur in a water bath were given, it also introduces the addition of the centre of the femoral head as a pivoting point in the algorithm.

Chapter 4 describes the production of volume statistical shape models for the femur, where the models were produced using the B-spline node points obtained from the results of non-rigid registration. Results were given for instantiating from a phantom femur in a water bath. A new optimisation method is also adopted for the instantiation-registration algorithm.

Chapter 5 introduces the volume statistical shape model for the pelvis and paves the way for the cadaver study in the following chapter.

Chapter 6 presents a carefully designed cadaver study, utilising the volume statistical shape models, with 3 preserved female cadavers. The ground truth is available and the method is tested on 6 femurs and 3 pelves with robustness results presented. The use of the centre of the femoral head as the pivoting point in the algorithm is also reviewed.

Chapter 7 concludes this thesis with a discussion on the experiments conducted and describing future work directions.

Chapter 2

Literature Review

2.1 Introduction

The aim of this thesis is to provide the statistical shape model of the femur and pelvis and use them to instantiate from tracked ultrasound. A non-rigid registration algorithm is used to propagate the surface points of the bone, and then build the model on these propagated surfaces or the B-spline node points of the registration deformation fields. Ultrasound was used to register and instantiate.

In this chapter, I will explore the following areas which are important to this thesis, reviewing the relevant research. The chapter starts with a brief summary of the anatomy around the hip, associated diseases and an overview of hip replacement surgery and image-guided surgery. To set the scene for the technology related to this thesis, the subsequent sections describe the relevant imaging technology (namely ultrasound, X-rays and CT), registration methods, statistical shape models, other work in using shape models in orthopaedic surgery and finally optimisation methods.

2.2 Hip Anatomy, Pathology and Treatment

The hip joint, made up of the pelvis and the femur, is one of the major weight-bearing joints in the body and is normally very stable, allowing a wide range of motion. Its anatomy is described briefly in this section. This section also introduces some disorders associated with this joint and one of the treatments, hip replacement surgery, to reduce the effects of these disorders.

2.2.1 Anatomy of the Hip

The pelvis consists of two coxal bones sometimes referred to as the hemi-pelvis, each is made up of three bones, the ilium, ischium and pubis, fusing at a deep fossa called the acetabulum on the

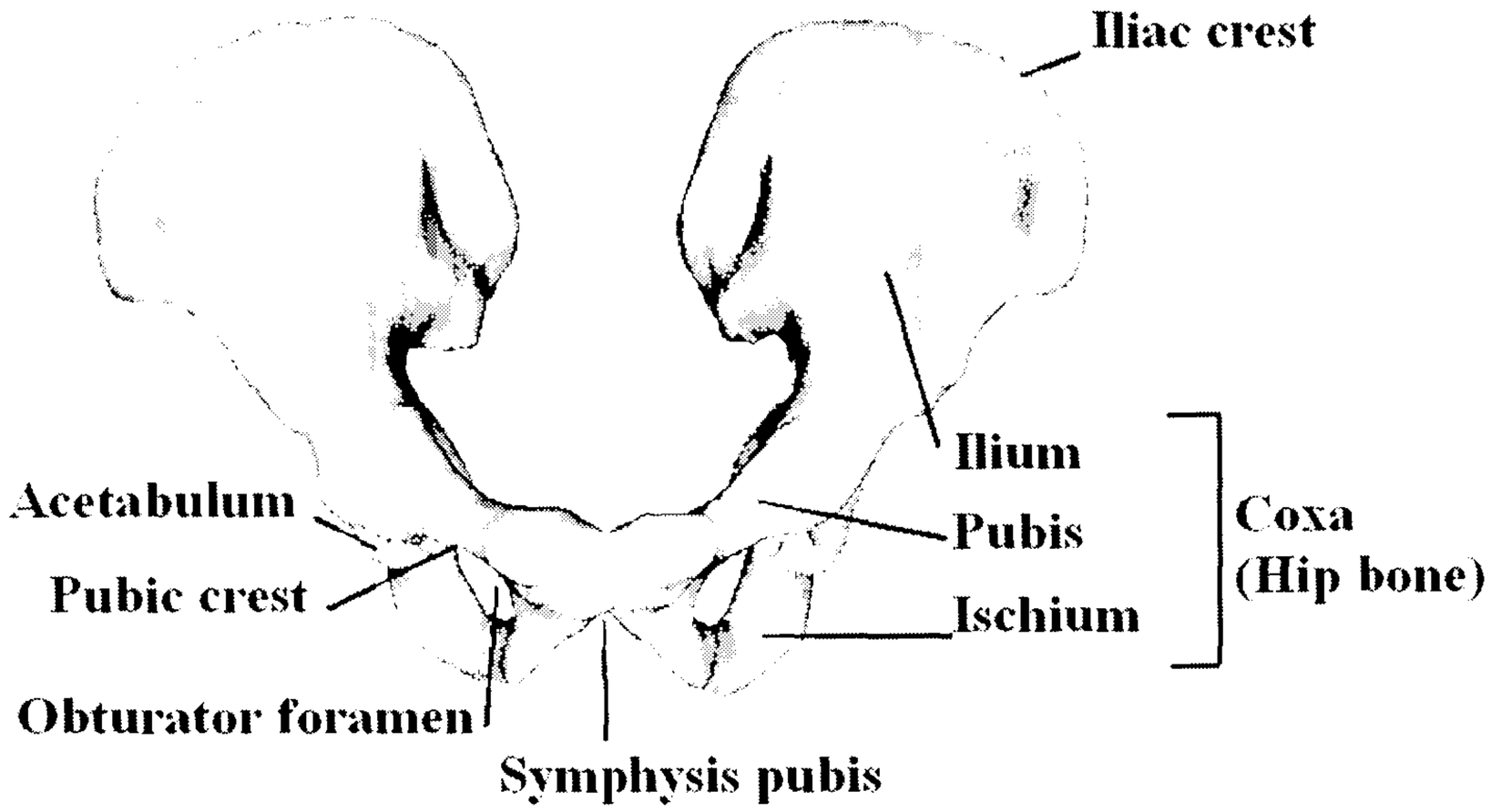

Figure 2.1: Anatomy of the pelvis (front view).

lateral side of each coxal bone (Gray, 1918; Martini and Timmons, 1997).

The ilium is the superior portion of the coxal bone, mainly a big broad curved surface offering a large area for attachment of muscles, ligaments and tendons. The ischium forms the inferior and posterior part of the coxal bone. It mainly bears most of the body weight when the person is seated, via the ischial tuberosities. The pubis from the left and right coxal bones joins both sides at the symphysis pubis, to complete the shape of the hip. See Figures 2.1 and 2.2.

The female pelvis has a different shape to the male mainly because of childbearing. It is usually smoother and with less prominent markings. In Gray (1918), the main different features include the female pelvis being more shallow but having larger apertures and stronger muscles; the ischial tuberosities are farther apart with wider, or more rounded, pubic arch with a slightly shallower pubic symphysis.

The femur, the upper part of the leg bone, is the longest and largest bone in the body. The proximal end is made of a rounded epiphysis or head (the femoral head) which articulates with the coxal bone within the acetabulum to form the hip joint, a synovial, ball-and-socket joint. This joint is very stable; this is achieved by holding the femoral head firmly inside the acetabulum through strong ligaments attached to the acetabulum and the trochanters on the femurs. These ligaments, with muscles and tendons, provide strength, stability and flexibility to the joint. See Figure 2.3.

Movement is allowed in all three planes including flexion and extension, abduction (movement of leg away from the midline) and adduction (movement of the leg towards the midline), medial to lateral rotation. The greater trochanter restricts abduction due to contact with the outer

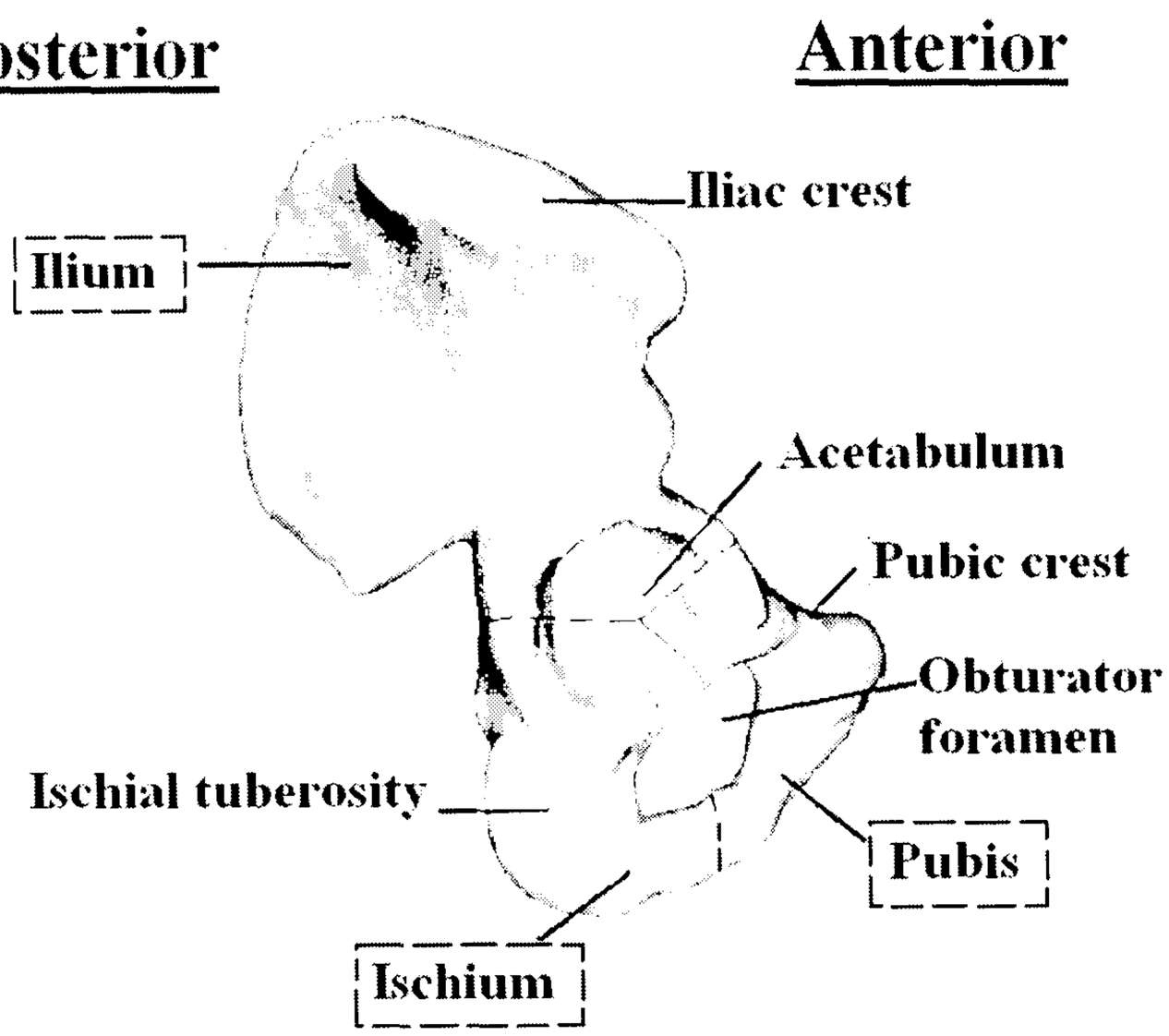

Figure 2.2: Anatomy of the pelvis (lateral view). This figure shows the right coxal bone. The dotted lines show roughly where the ilium, pubis and ischium fuse.

ridge of the acetabulum.

The main body of the femur, or shaft, has a prominent elevation on the posterior surface, the linea aspera, for the attachment of muscles. It extends down to the distal third of the shaft and diverges into a plateau. On the distal and posterior ends of the epicondyles are the smoothly rounded lateral and medial condyles, these articulate with the corresponding condyles of the tibia, the anterior ends merge to form the patellar surface.

2.2.2 Diseases of the Hip

The common causes for the degeneration of the hip joint resulting in the need for total hip replacement surgery include osteoarthritis, aseptic necrosis, fracture and other abnormalities (such as presence of a tumour) of the hip joint.

Osteoarthritis is a disease of the joint articular cartilage, where the cartilage progressively disintegrates. This is coupled by new growth of osteophytes and irregularity at the joint. In the early stages of this disease, the articular cartilage surface progressively softens and fibrillation (the formation of minute fibrous tissue) occurs. In the advanced stages the fibrillated cartilage

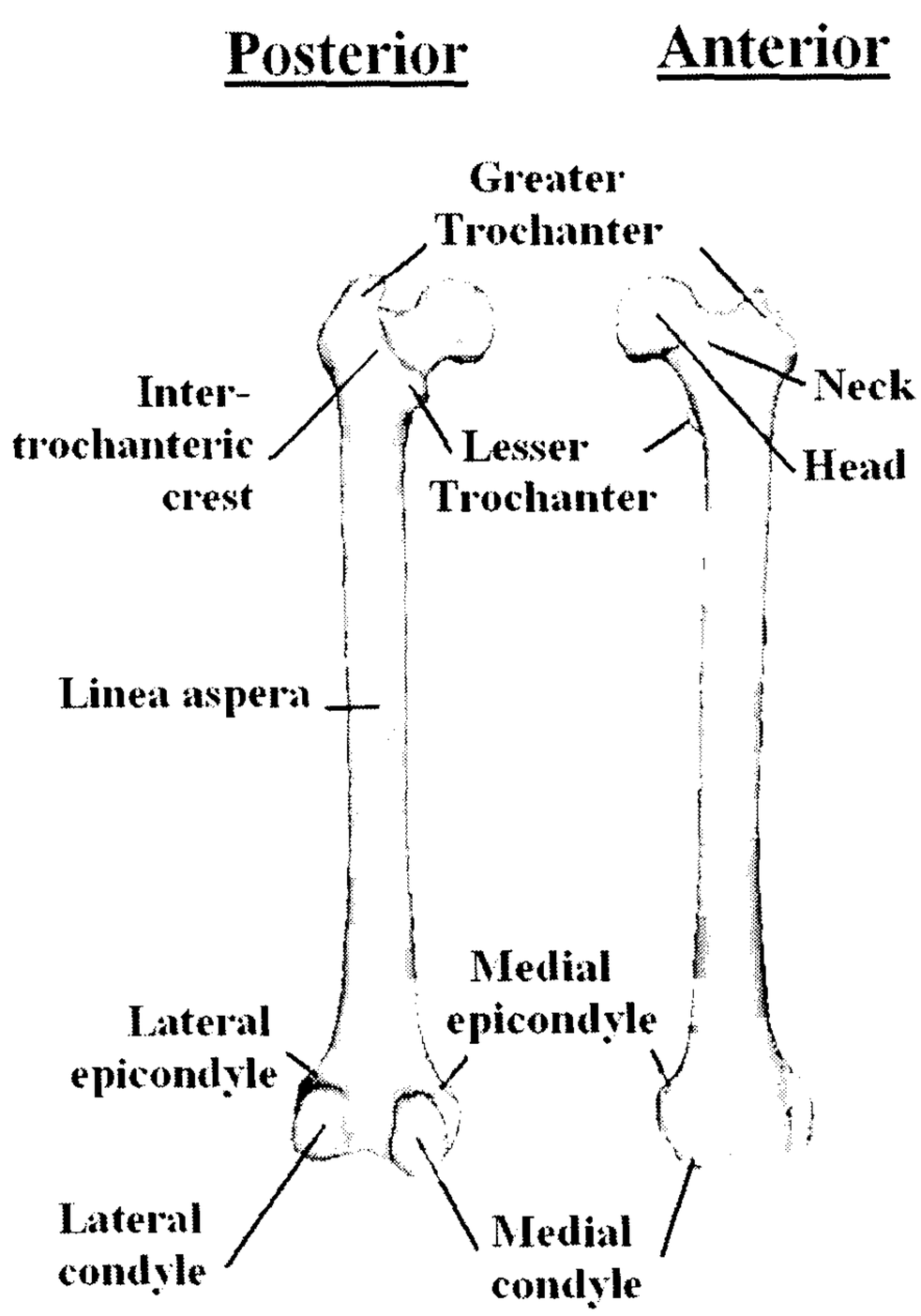

Figure 2.3: Anatomy of the femur.

are released into the narrowing joint space and the underlying bone is exposed. The joint might become a bone-on-bone articulating surface and the bone shows signs of remodelling. It affects mostly the weight-bearing joints in the body like the hip and the knee, sometimes the spine. The main symptoms are pain, stiffness, intermittent swelling, deformity due to joint instability, and loss of function.

Aseptic necrosis refers to the femoral head losing part of the blood supply and the tissue of the bone dying, leading to collapse of this part. The blood supply could be interrupted due to fracture or vascular damage. The main symptoms are pain and stiffness of the joint. Hip replacement surgery is normally recommended for patients in the advanced stage of this disease who would be affected by severe joint dysfunction.

2.2.3 Total Hip Replacement

Total hip replacement (THR) surgery, sometimes referred to as total hip arthroplasty (THA), is a branch of orthopaedic surgery and was first performed in the 1960s. THR is a procedure where

the diseased joint is replaced with an artificial one. There are two components to the artificial hip prosthesis: the femoral component (stem) and the acetabular component (cup). The prosthesis could be inserted into the patient using either the cemented or cementless method. These two methods will be introduced shortly. The surgeon will decide which prosthesis and method to use based on the patient's age, degree of the disease, lifestyle, the surgeon's experience and other factors.

Before the surgery there must be careful planning. An anteroposterior (AP) X-ray of the hip is commonly taken to determine the degree of the disease, and a template of the prosthesis is drawn on a translucent sheet. Occasionally a lateral radiograph of the patient's hip may also be taken for acetabular implants. There are several things to consider during the planning stage, including the position of the hip centre, the most favourable size and design of the prosthesis to be used and the location of the femoral neck osteotomy (Sugano et al., 1998).

The surgery starts by making an incision on the hip joint. Ligaments and muscles are separated carefully to allow access to the femoral head area. The femoral head is detached from the acetabulum and removed. Excess cartilage is then removed from the acetabulum to form a hemispheric space for the new acetabular cup which is either hammered into place (cementless) or attached using cement.

The femur is then prepared by reaming it hollow. The femoral stem prosthesis is inserted into the cement-filled femoral canal (cemented) or just hammered into place (cementless). The femoral head ball is then attached to the stem and the joint is put together to test the degree of movement.

2.2.3.1 Hip Resurfacing

Unlike THR, hip resurfacing involves reshaping and resurfacing the femoral head with a metallic femoral cap, whereas the acetabulum is replaced by a metallic cup. Less bone has to be removed for this procedure, thereby preserving most of the femoral head and all of the femoral neck. This promotes joint stability and lowers the chance of dislocation compared to THR.

2.2.3.2 The Demand of Total Hip Replacement procedures

Improvements in the surgical techniques, materials and technology have increased the effectiveness of the procedure. Similar surgical procedures are performed on other joints like the knee and shoulder. In the full first annual report of The National Joint Registry (NJR) Centre (2004) for England and Wales, between 1 April and 31 December 2003, the number of total hip replacement procedures carried out in England and Wales entered into the NJR are 24997 of which over 90%

were primary procedures. The number of surgeries performed was provided by orthopaedic units in England and Wales, these include 84.5% of NHS Trusts, 91.6% of all independent hospitals and 75% of all treatment centres. The mean age of patients that underwent primary hip replacement surgery was between 61.1 and 76.1 years old.

According to the report, amongst all primary hip replacement procedures, 0.9% were performed using image-guided systems. This proportion is set to rise as the cost of image-guided procedures falls and becomes more popular. As the population ages, the demand for hip replacement surgery grows every year.

2.3 Image-Guided Surgery

As discussed in the previous section, planning of THR surgery has commonly been done using an AP X-ray of the hip, with a template of the prosthesis and the surgeon's knowledge of human anatomy used to prepare for the surgery. The template on a translucent sheet shows the outlines of the profile of each of the implant components (Eggli et al., 1998). This method has lots of potential sources of error, mainly because it is often difficult to acquire the true AP view of the proximal femur (Sugano et al., 1998) and the template cannot provide accurate estimates of the prosthesis size and position. Standard radiographs are 2-dimensional (2D) projections through the patient's body and the 3-dimensional (3D) information is lost. Since X-rays from a point source diverge, a differential magnification factor distorts the perceived sizes of imaged structures making it difficult to determine the structure's actual size or measure effective distances (Seeram, 1994).

Computed tomography (CT) scans are capable of providing the surgeon with useful information regarding the patient's anatomy, but if used without guidance, the surgeon would have to mentally correlate the 3D CT images with the 2D intraoperative images which would be highly inconvenient and inaccurate. The CT images, therefore, cannot be taken intraoperatively and could only be used as part of preoperative planning. Intraoperatively 2D radiographs can be used to update the prosthesis or surgical tool positions but this would also increase radiation exposure and increase operating time (Mehlman and DiPasquale, 1997).

Image-guided surgery (IGS) makes use of medical imaging and spatial tracking technology to provide preoperative planning and guidance during the procedure. In IGS for hip replacement, a preoperative CT scan is taken to produce a 3D model of the patient's femur and pelvis. This 3D model is used to determine the location of the hip centre and plan the appropriate implant size, as well as providing accurate guidance for the surgeon. Image-guided total hip replacement has the

potential to provide more accurate surgical placement of prostheses with the aid of a surgical plan derived from a 3D model of the pelvis and femur and their relationship via the hip joint (Stulberg and Kienzle III, 1995; DiGioia et al., 1998a; Noble et al., 2003). It also provides the opportunity to develop less invasive procedures that reduce surgical exposure of bone and disruption of the joint capsule. The technology could be very precise and surgeons can have better access to areas otherwise inaccessible.

IGS combines the use of tracking devices, often using light-emitting diodes (LEDs) and cameras, to help the surgeons navigate through the body, with the help of 3D images. During the surgery, the patient is fitted with markers which are visible to the optical tracking device. Other instruments used in the surgery are also tracked so that the surgeon can get live feedback from the IGS system which advises on the best positions to place an incision or the extent of reaming. This arrangement makes it possible for the surgeon to couple the preoperative plan with the current position and orientation of the patient's hip and the implant.

IGS is generally suitable for orthopaedics mainly because bone is more rigid than most organs in the body and it can withstand reaming, drilling and sawing without deforming significantly, and hence can work more consistently with a computer-generated model and results from the surgery are beneficial to the patient. Although surgical navigation has a high price tag and also the risk of user and system error, the IGS technology is able to assist the surgeon to accomplish tasks that were otherwise impossible for each to achieve on its own (DiGioia et al., 1998b).

2.3.1 CT-Free Image Guidance

There are generally two kinds of surgical navigation systems: image-based and image-free. Image-based systems requires preoperative CT or intraoperative fluoroscopic images which produces patient-specific models that is an exact match of the anatomy. It is the relatively high cost and radiation dose associated with CT scans that have proven unpopular with many orthopaedic surgeons and image guidance has yet to be widely accepted for THR. The surgery itself is also expensive and invasive.

Image-free systems use patient-specific data obtained intraoperatively or kinematic calculations by registering limb motion to create virtual reality images by changing bone models in the atlas. The models produced by these systems are then displayed for surgical planning and navigation. Although no preoperative image is taken before the surgery, these systems are still categorised as IGS systems. The Echomorphing system introduced in Section 2.5.5.6 is an example of a CT-free system for the knee.

The work described in this thesis aims at providing accurate image-guided total hip replacement without the need for a preoperative CT scan. Although CT-free systems are already available, these commonly require acquiring radiographs incurring radiation exposure or palpating points directly on bone surfaces which makes the operation invasive. One way of doing so is through the use of statistical shape model (SSM) and ultrasound.

2.4 Relevant Imaging Techniques

2.4.1 Ultrasound

Ultrasound (US) has become a very widespread medical imaging technique. It is safe, non-invasive and inexpensive compared with other modalities, with typical diagnostic frequencies between 2.0MHz to 20MHz. The basic principle is based on a simple relationship, that the time for a short burst of sound to be reflected from a stationary object (echo) at a distance is proportional to the distance, that is, assuming that the velocity of sound in tissue is constant. Ultrasound is transmitted into the body through a transducer placed on the surface of the skin. The US reflects off structures in the body, returns to the receiving transducer, and causes the transducer to vibrate, resulting in a voltage being generated across the piezoelectric element. This is the idea of the traditional pulse-echo systems. The voltage signal provides an image of the structures, where, for each pixel, depth is determined by echo arrival time and brightness is determined by echo intensity. Modern US systems use the same transducer to transmit and receive.

Reflection of the propagating US waves occurs whenever there is a change in acoustic impedance, defined as the product of density and speed of sound. Such changes occur at tissue interfaces, but also on a much smaller scale within tissues. In the classical simplified model of US imaging, the proportion of US energy reflected at a boundary is equal to the ratio of the acoustic impedances on each side of the boundary. Since the acoustic impedance of bone is high compared to soft tissue, bones are strongly reflecting to US. The US signal hits a bone/tissue interface, the signal produced is strongly reflecting, leading to shadowing and reduced echoes from deeper structures.

A-mode (Amplitude-mode) is the simplest Ultrasound mode. In a typical A-mode scan, the horizontal axis represents the time after transmission of the pulse, whereas the vertical axis represents the amplitude of the instantaneous echo signal. Each of these amplitude peaks corresponds to a tissue interface. Figure 2.4 shows an A-mode US image taken from the skull, where US signals were reflected from various structures. B-mode (Brightness mode) Ultrasound, on the other hand, uses brightness to represent the amplitude of the echo. Figure 2.5 shows a B-mode image

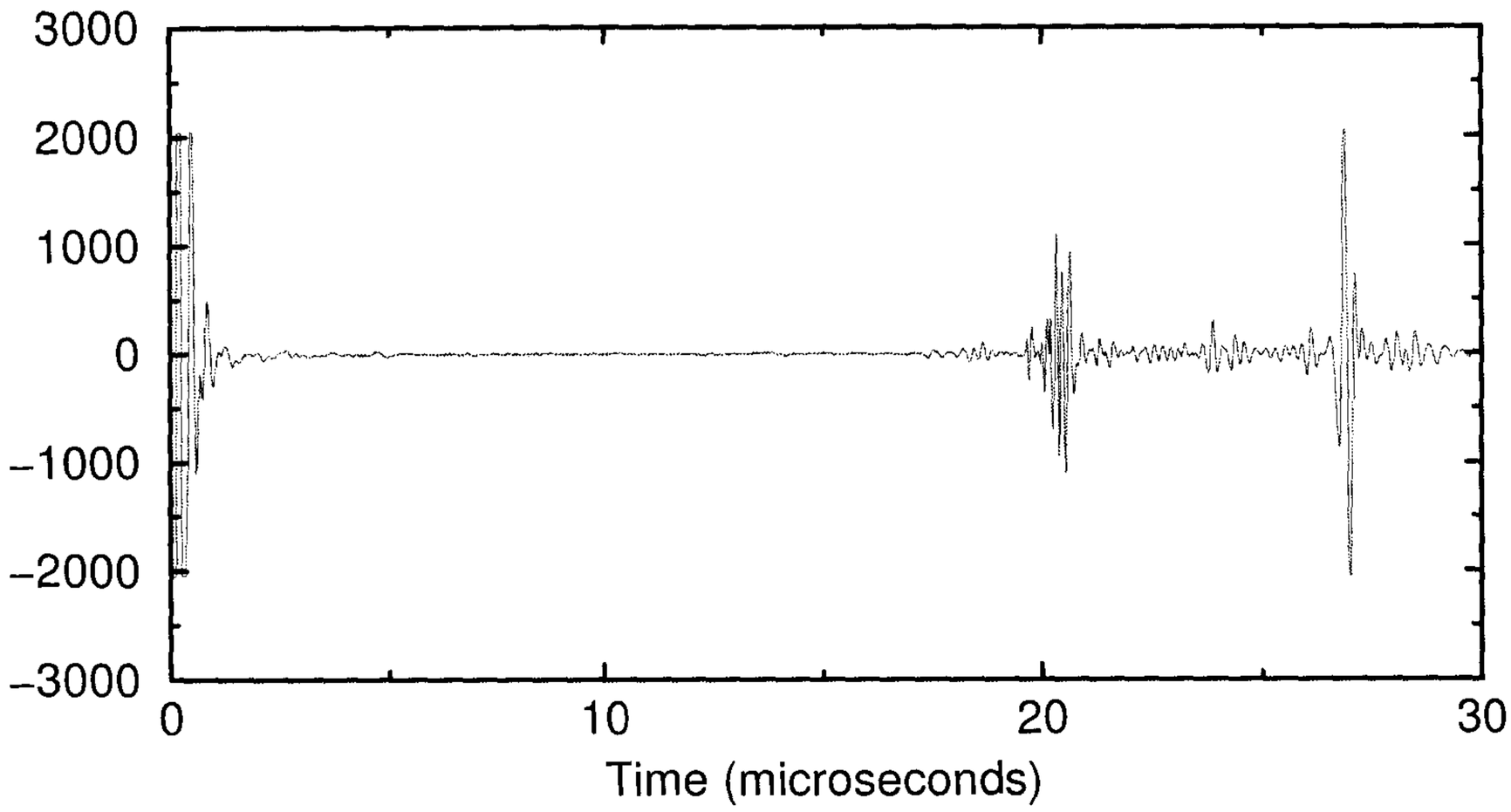

Figure 2.4: Example A-mode US image of the skull. The signal on the very left at time = 0 is the "main bang". The spikes that occurred around time = 21μs and 27μs are reflections from skin and bone respectively. The corresponding distances from the probe are 1.6cm and 2.1cm respectively.

taken from the pelvis, this image was formed by transmitting a series of pulses along a transducer array.

Ultrasound probes are small in size, easy to manipulate, compact and portable. The main perceived drawbacks with US are the poor quality due to artefacts and relatively poor soft tissue contrast, which can give rise to low resolution images although in many modern scanning systems the spatial resolution can be better than 1mm. Being a uniquely interactive modality the image quality and accuracy are highly operator-dependent (Hedrick et al., 1995; Wells, 1999).

2.4.1.1 3D Ultrasound

Traditional 2D US, described above, allows the user to move the transducer freely to view the desired anatomy across accessible surfaces. Recently, 3D US has advanced sufficiently to be useful for routine diagnostic and interventional applications (Nelson and Pretorius, 1998; Downey et al., 2000). Development in technology and visualisation techniques mean real-time reconstruction and manipulation of 3D images is now available on commercial US scanners.

Conventional 2D US images are planar. The user has to manipulate the orientation and the quality of a region of interest is dependent on the user's skill. 3D US addresses this problem by allowing the user to acquire images in many arbitrary orientations, thus allowing more complete

Figure 2.5: Example B-mode US image of the pelvis, taken along the iliac crest. The picture shows some soft tissue and then a strongly reflecting bone surface. The region deeper than the bone surface created a shadow and very little signal was received.

imaging for surgery and therapy planning.

There are several ways of acquiring a 3D US volume. The one adopted in this thesis is called freehand 3D US and involves tracking a 2D probe using a position sensing device. This provides its relative position and orientation in one space. A 3D volume can then be reconstructed using this information (Prager et al., 1998). The advantage of this method is that the movement of the probe is unconstrained, therefore, much larger volumes can be imaged than is possible using 2D matrix array or mechanically swept 3D US systems. Some authors refer to this technique as 2.5D US because the 2D probe has a rigid body attached to it (Barbe et al., 1993). This provides unconstrained movement of the probe. Nelson and Pretorius (1998) produced a rather extensive list of applications for 3D US.

Ultrasound provides a safe, non-invasive and relatively inexpensive method for locating bone surfaces intraoperatively. Recent registration applications include the femur (Ault and Siegel, 1995; Penney et al., 2001; Jaramaz et al., 2003) and pelvis (Tonetti et al., 2001a,b; Amin et al., 2001b, 2003; Heger et al., 2003; Hufner et al., 2003) as well as the tibia (Jaramaz et al., 2003), spine (Lavallée et al., 1995; Tonetti et al., 1997, 1998; Ionescu et al., 1999; Brendel et al., 2002; Muratore et al., 2002; Kowal et al., 2003) and skull (Schreiner et al., 1998; Maurer et al., 1999; Amstutz et al., 2003).

This thesis uses 3D US to determine the location of US bone surfaces which are used to produce an instantiated bone surface from an SSM, and register a CT scan to the physical space

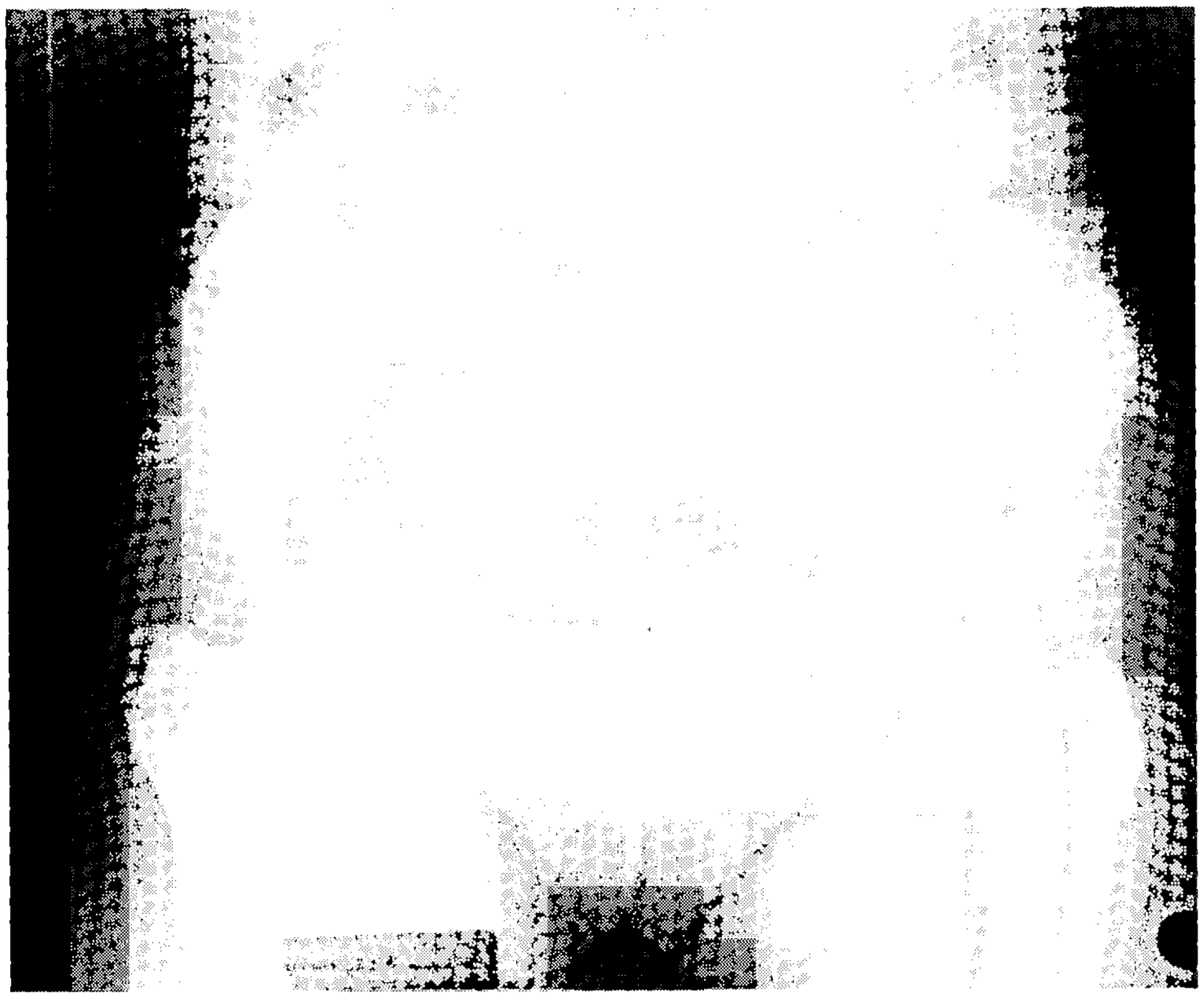

Figure 2.6: Example X-ray image showing the distal spine, pelvis and proximal femur. The left femur has an implant with the femoral stem and acetabular cup, shown on the right of the picture.

of the patient. While US has been known to suffer from drawbacks when imaging soft tissues, the strongly reflecting nature of bones in US images are useful for this thesis.

2.4.2 X-rays

X-rays were first discovered by Röntgen in 1895. X-rays are part of the electromagnetic spectrum and utilises ionising radiation. It passes through the body and provides information on how these X-rays interact with different tissue types and the associated attenuating properties along the path. X-ray radiographic images are a 2D projection of the attenuating properties of tissues and structures in the body along the path of the X-rays (Dance, 1988). The higher the atomic weight of a structure, the clearer it will appear on the photographic film. For example, bone (consisting mainly of calcium) shows brighter and clearer on X-rays films because calcium atoms are heavier than soft tissue (which might compose of carbon, oxygen and hydrogen) and hence more attenuating. Figure 2.6 shows an X-ray image around the area of the distal spine, pelvis and proximal femur with an implant to one side. The implant components are showing as very bright features because they are made of high atomic weight materials.

2.4.3 Computed Tomography

Computed tomography (CT) is one of the main imaging modalities for surgical planning and diagnosis and has been available for more than 25 years. CT is a fast and patient-friendly imaging technique. It combines the use of computer reconstruction with the X-ray source mounted on a rotating gantry, to give the capability of imaging two-dimensional slices of the patient's internal structures. These can be combined to give 3D volumes. It is also able to resolve soft tissues, bones and blood vessels inside the patient. The invention of CT enabled clinicians to better diagnose a wide range of diseases and injury, including cancer and tumours. Nowadays, CT can be used for viewing various body parts or organs, such as kidneys, brain, spine, blood vessels and as with X-rays, bones and lungs (Seeram, 1994). CT progressed from a slow single-slice head scan to fast 3D scans. It has also improved in terms of speed, image quality and patient comfort. Researchers are now working on even faster scans to reduce patient dose and motion artefacts due to bodily movements.

CT scanners evolved from different geometries of detectors and scanning motion, overall scanning times and shapes of the X-ray beam to the recent introduction of spiral scanners which dramatically reduced the scanning time. The very first type of scanners adopted a translation/rotation scanning motion with an X-ray pencil beam, soon to be replaced by a narrow fan beam, but these scanners offered a very limited field of measurement for head examinations only and are not in use today. Then came a rotation/rotation scanning motion with a wider fan beam or a stationary ring beam, these are being used commercially with the wider fan beam scanners incurring a lower cost. The current generation of CT scanners, sometimes called spiral or helical CT, employs a volume scanning mode and uses an alternative scanning motion which has a non-planar geometry. The X-ray tube and detector move continuously on a helical trajectory around the patient ("spiralling"), while the patient table remains on linear motion, that is, the patient is being scanned along the z-axis in time, making acquisition of data even faster (Kalender, 2000). The main disadvantages of CT are the high cost involved, the ionising radiation dose and that the image could be affected by metallic implants already inside the patient. The recent generation of detectors are thought to be geometrically accurate devices (Peters, 2000) and are therefore employed in image-guided surgery.

2.5 Registration Techniques

Registration is an important issue in medical imaging and indeed computer-assisted surgery. It is the process which aligns images by establishing spatial correspondence between one image and another, or between an image and physical space. The images could be from the same or different modalities, and by determining the transformation, or mapping, from coordinates in one space to another, features in the aligned images should correspond to the same anatomy.

Depending on the application, the transformation could be simple or complex. The most basic type of transformation is the rigid registration. In 3D, rigid registration deals specifically with 6 degrees of freedom (DOF), 3 translations and 3 rotations, where the objects in question do not deform in any way.

To deal with images from different modalities, rigid registration is often extended to include affine transformation which includes scaling and shearing, this adds a further 6 degrees of freedom; this type of transformation preserves parallelism but does not include non-linear motion. It is sometimes used in correcting calibration differences.

The human body is made up of different structures that do not necessarily conform to a rigid approximation. Organs of soft tissue, for example liver and breast, may deform due to external conditions. When there are visible shape changes, rigid and affine registrations might not be sufficient. Therefore more degrees of freedom are required to model such transformation. This is referred to as non-rigid registration. The larger the number of degrees of freedom allowed for the transformation, the more complex the computation and the longer the time required to register. Therefore there needs to be a compromise between the accuracy and speed of the registration. Non-rigid registration can be used to align inter-subject where there is clearly non-linear shape difference. An application of this is atlas-based segmentation, where labelling is done on a template image which is then registered to an individual. Non-rigid registration can also be used for intra-subject alignment where soft tissue has deformed or growth (e.g. tumour) has occurred.

There are many ways to classify registration, some of which can be found in Maurer and Fitzpatrick (1993), Maintz and Viergever (1998) and Fitzpatrick et al. (2000). This section will focus on some registration techniques relevant to this thesis, looking at 2 main methods of registration: feature-based and intensity-based, introducing some methods of rigid registration. Several similarity measures and non-linear transformation models will also be reviewed and finally the application of some of these to ultrasound localisation.

2.5.1 Transformation

To achieve registration, a measure of correspondence between the two images is needed. This could be the squared distance between identified landmarks or surfaces, a measure of correlation between the grey levels in the images. Define a transformation **T**, from image 1 to image 2, which is optimised for the given correspondence measure. **T** can be rigid, affine or non-rigid. Let **T** be a transformation that maps a point (x, y, z) in one image onto the corresponding target image coordinates, (x', y', z')

$$\mathbf{T} : (x, y, z) \mapsto (x', y', z')$$

2.5.2 Feature-Based Correspondence

The feature-based method relates corresponding features in one image with another. These features could be point landmarks, anatomical landmarks, markers (fiducials) attached to structures on the body which would be made visible in the imaging modalities, and surfaces.

2.5.2.1 Point-Based Registration

One of the methods used is the point-based registration (PBR) described below. The landmark points need to be identified by hand. If these points were to be identified anatomically they need to be reliably and accurately identified. Rigid transformations need to be determined between two sets of points to establish spatial correspondence between them. The point-based registration algorithm can be generalised as follows by minimising the distance between the points under the transformation. This is sometimes called the orthogonal Procrustes problem (Fitzpatrick et al., 2000), where the minimisation problem is:

Find R and $\mathbf{t}$ to minimise

$$\sum_{i}^{N} |R\mathbf{x}_i + \mathbf{t} - \mathbf{y}_i|^2$$

where

R the rotation is a 3×3 orthogonal matrix, that is $R^tR = RR^t = I$ and $R^{-1} = R^t$

$\mathbf{t}$ the translation is a 3D vector that may be specified by giving the three coordinates t_x, t_y, t_z relative to a set of *x*, *y*, *z* Cartesian axes

$\mathbf{x}$ and $\mathbf{y}$ are both column vectors each representing a point. The algorithm continues as follows:

1. Compute the centroid of the points in each space

$$\bar{\mathbf{x}} = \frac{\sum_i^N \mathbf{x}_i}{N} \qquad \bar{\mathbf{y}} = \frac{\sum_i^N \mathbf{y}_i}{N}$$

2. Compute the displacement from the centroid to each of the points in each space

$$\tilde{\mathbf{x}}_i = \mathbf{x}_i - \bar{\mathbf{x}} \qquad \tilde{\mathbf{y}}_i = \mathbf{y}_i - \bar{\mathbf{y}}$$

3. Compute the covariance matrix, H

$$H = \sum_i^N \tilde{\mathbf{x}}_i \tilde{\mathbf{y}}_i^t$$

4. Perform SVD of H

$$H = U\Lambda V^t$$

Where $U^tU = V^tV = I$, $\Lambda = \text{diag}(\lambda_1, \lambda_2, \lambda_3)$ and $\lambda_1 \geq \lambda_2 \geq \lambda_3 \geq 0$

5. Calculate R - rotation

$$R = V\,\text{diag}(1, 1, det(VU))U^t$$

6. Calculate $\mathbf{t}$ - transformation

$$\mathbf{t} = \bar{\mathbf{y}} - R\bar{\mathbf{x}}$$

Singular value decomposition (SVD) is a very powerful technique to provide a numerically robust solution to least squares problems (Schönemann, 1966; Arun et al., 1987). The SVD of a matrix H, is a factorization process $H = U\Lambda V^t$ as described in step 4 in the above algorithm. The column values of U are left singular vectors, Λ has the singular values and is diagonal whereas the row values of V^t are the right singular vectors. Both U and V are orthogonal matrices. The SVD is a representation of the original data expanded in a coordinate system where the covariance matrix is diagonal (Press et al., 1992; Golub and van Loan, 1996).

The PBR method is a good method for registering two images if the transformation is constrained to be rigid. PBR is used to find the translation vector and rotation matrix that produces the least-squares fit of the corresponding points. This method is particularly useful in image-guided surgery for fiducial registration and calibration, by computing the rigid transformation (translation and rotation) that minimises the fiducial registration error (FRE) (Fitzpatrick et al., 1998). The FRE is a measure of how well the centroid of an anatomical landmark or fiducial marker localised in 3D (e.g. CT of the patient), registered with the corresponding centroid in another image (e.g. magnetic resonance (MR) image) or centroid that was measured physically in the operating room. This will be discussed more in Chapter 6.

2.5.2.2 Surface-Based Registration

Instead of using distinct points, the surface of corresponding anatomical structures can be used to register two images. The iterative closest point (ICP) algorithm is a surface-based registration method, which can be used to register 3D shapes. It has been applied to medical images with some success and is probably one of the most widely used surface matching algorithm for medical imaging.

The algorithm always converges monotonically to a close minimum of a mean-square distance metric at a rapid rate during the first few iterations. Experiments were performed to show the capabilities of the registration algorithm on point sets, curves and surfaces (Besl and McKay, 1992).

If the surface of one image could be represented by a set of points, then these points are registered to the other surface by going through the following steps iteratively:

1. For each source point, compute the closest points on the target surface.

2. For all these corresponding points, compute a rigid transformation from source to target using PBR.

3. Apply the transformation and repeat until the change in root mean square (RMS) distance meets a certain stopping criterion.

The ICP is simple and relatively easy to implement, and with a reasonably good starting estimate, the algorithm converges quickly. However, it is prone to finding a local minimum if the starting estimate is not good enough.

Since the introduction of the ICP algorithm, there were different modifications to the algorithm. One of them was proposed by Penney et al. (2001) called stochastICP, to improve robustness and precision. This modified version adds random Gaussian noise to perturb the source point positions, allowing the algorithm to move the result out of some local minima. The noise is reduced until it is set to zero when the algorithm runs as normal ICP. The method was tested using freehand 3D US data from a phantom femur, a volunteer's skull and liver, matching onto either CT or MR of these structures. The results have shown that when local minima are present, stochastICP is more robust and precise than standard ICP.

2.5.2.3 Application

A group from Vanderbilt university described a technique for surface registration to map physical space into CT image space, which is used in image-guided liver surgery (Herline et al., 2000). A liver phantom is produced with a phantom tumour derived from pieces of cork and fiducial

markers attached. A liver CT scan is produced and segmented, and the surface is represented using a triangle set. The surface of the liver phantom is digitised using approximately 900 points. PBR is performed as the gold standard.

The registration process is performed using an implementation of the ICP algorithm. Results for surfaces (8 segments of the liver and one complete surface) and 8 segment boundaries gave an average of 2.99±0.006mm for three different trials. Another set of registration was performed for six tumours distributed in clinically relevant positions. The RMS errors were calculated for 306 trials and the range in error was 2.45-3.35mm. Sources of error included the ballpoint tip of the optically tracked position sensor being displaced from the actual surface by the radius of the tip, which is about 1.5mm. Also, the presumed physical space locations of the tumours were obtained by PBR and the FRE was 0.95mm.

Surface-based registration uses more of the available information from the two sources than point-based methods, hence making them more robust and accurate. One of the drawbacks is that their performance can be affected by the accuracy of the delineation of the corresponding surfaces, which often rely on human intervention. The next section discusses the use of intensity-based techniques which eliminates the need for prior segmentation or delineation of corresponding structures.

2.5.3 Intensity-Based Correspondence

This method uses intensities and is sometimes referred to as voxel similarity-based registration. The method is applied to all the overlapping voxels in the image instead of particular points. To obtain the best transformation, intensity values in each of the images are matched using a statistical or mathematical criteria. This will determine how similar the images are. This also utilises most of the information available and hence reduces the effect of noise.

2.5.3.1 Similarity Measures

There are several measures of similarity, the simplest one being sum of squared differences (SSD) which the sum of the squared intensities of all corresponding voxels is minimised when the two images were registered (Fitzpatrick et al., 2000; Hill and Batchelor, 2001). So, for images A and B with voxels i, find the transformation to minimise

$$\text{SSD} = \frac{1}{N}\sum_{i}^{N} |A(i) - B'(i)|^2$$

where $\forall i \in A \cap B'$ and B' is the transformed image B.

Correlation coefficient (CC) is another simple measure which assumes the intensities between corresponding voxels in two images have a linear relationship, such that CC is maximised when the images are registered (Fitzpatrick et al., 2000; Hill and Batchelor, 2001). For images A and B with voxels i, find the transformation to minimise

$$\text{CC} = \frac{\sum_i (A(i) - \bar{A}) \cdot (B'(i) - \bar{B'})}{\{\sum_i (A(i) - \bar{A})^2 \cdot \sum_i (B'(i) - \bar{B'})^2\}^{\frac{1}{2}}}$$

where $\forall i \in A \cap B'$ and $\bar{A}$ and $\bar{B'}$ are the mean values of the voxels in image A and transformed image B respectively.

Both of the above measures are suitable for mono-modal image registration, because the images' intensity characteristics would be similar. There is another class of measure that is suitable for multi-modal image registration, utilising entropy. The Shannon entropy, H, was developed originally as part of information theory and is used as a measure of information (Hill and Batchelor, 2001; Fitzpatrick et al., 2000). H can be seen as the average information supplied by a set of symbols s, with probabilities given by $p_1, p_2, ..., p_s$,

$$H = -\sum_i p_s \log p_s$$

Joint entropy is a measure of the amount of information in two combined images. For the joint probability density function (PDF) of images A and B, find the transformation to minimise the joint entropy $H(A, B')$

$$H(A, B') = -\sum_a \sum_b \text{PDF(a, b) log PDF (a, b)}$$

The images should be registered when the joint entropy is minimised. Joint entropy includes calculating the entropies of overlapping parts of the images, it could therefore be quite sensitive to these overlaps. Mutual information (MI) (Viola and Wells III, 1997), on the other hand, calculates the mutual information and joint entropy of the overlapping part of the two images, this helps with making the measure less sensitive to overlap. MI is defined as

$$MI(A, B') = H(A) + H(B') - H(A, B')$$

MI tends to be sensitive to changes in overlap, especially regions with very low intensity. Therefore Studholme et al. (1999) introduced a normalised form of MI, called normalised mutual information (NMI), aimed at minimising this problem. NMI is defined as

$$NMI(A, B') = \frac{H(A) + H(B')}{H(A, B')}$$

2.5.4 Non-Linear Transformation Models

Linear transformation models are used widely for registering images with limited variability. They are ones which involve rigid and affine transformations with a maximum of 12 DOFs. As described earlier at the beginning of the section, structures or tissues in the human body may deform and therefore the registration may involve more than the 12 DOFs provided by rigid and affine registrations. Non-linear transformation models are used to define how one image deforms to match another. A non-rigid registration algorithm may be needed to handle this increased number of DOFs.

Even though bone itself is a rigid body, a rigid or even affine approximation is not enough to model inter-subject differences. Non-rigid registration is required to model global as well as some localised differences between subjects. In later sections of this chapter it will be shown how non-rigid registration is used in this thesis for inter-subject registration.

The family of splines is a commonly used transformation model in non-rigid registration of medical images. Transformation based on splines use a 3D lattice of node points, sometimes called control points, to define the transformation.

2.5.4.1 Thin-Plate Splines

The thin-plate spline (TPS) was introduced by Bookstein (1989). A TPS is fixed at positions defined by control points. Each of these control points has a global influence on the transformation. This is a major disadvantage when modelling inter-subject bone shapes where the bones could have complex or localised deformations. Because of the interpolation involved, the computations can be very time consuming even if only a single point is moved.

2.5.4.2 B-Splines

B-splines, in contrast, are only defined in the vicinity of each control point. Displacement at one control point would only change the transformation in the neighbourhood of that point, this is a property sometimes referred to as having "local support". Because B-splines are locally controlled, B-spline based methods are computationally more efficient than TPS even if there is a large number of control points (Rueckert, 2001).

One B-spline based non-rigid registration method is an automated algorithm proposed by Rueckert et al. (1999). Global motion is modelled by rigid transformation with 6 DOFs (rotations and translations) or affine transformation which has another 6 DOF (scaling and shearing). Local motion is modelled by free-form deformation (FFD) based on approximating B-splines defined by

a 3D lattice of node points. The flexibility of the B-splines and the number of DOFs are defined by the resolution of the B-splines. The FFD has a potentially large number of degrees of freedom, and is defined by the deformed positions of a regular grid of B-spline node points. The global transformation describes the overall motion of the bone, while the local transformation is used to describe shape deformation. So if $\mathbf{T}$ is the combined transformation and $\mathbf{x}$ denotes any point, $\mathbf{x} = (x, y, z)$, in the target CT image:

$$\mathbf{T}(\mathbf{x}) = \mathbf{T_{global}}(\mathbf{x}) + \mathbf{T_{local}}(\mathbf{x})$$

To define the FFD, assuming the domain of the image volume is denoted as

$$\Omega = \{(x, y, z) | \, 0 \leq x < X, 0 \leq y < Y, 0 \leq z < Z\}$$

Let $\mathbf{c}$ denote a $n_x \times n_y \times n_z$ mesh of control points $c_{i,j,k}$, which has uniform spacing δ.

The FFD can be written as the 3D tensor product of the 1D cubic B-splines:

$$\mathbf{T_{local}}(\mathbf{x}) = \sum_{l=0}^{3} \sum_{m=0}^{3} \sum_{n=0}^{3} B_l(u) B_m(v) B_n(w) \mathbf{c}_{i+l,j+m,k+n}$$

where $i = \lfloor \frac{x}{n_x} \rfloor - 1, j = \lfloor \frac{y}{n_y} \rfloor - 1, k = \lfloor \frac{z}{n_z} \rfloor - 1,$

$u = \frac{x}{n_x} - \lfloor \frac{x}{n_x} \rfloor, v = \frac{y}{n_y} - \lfloor \frac{y}{n_y} \rfloor, w = \frac{z}{n_z} - \lfloor \frac{z}{n_z} \rfloor$

and where B_l represents the l^{th} basis function of the B-spline (Lee et al., 1997).

This algorithm makes no assumption about underlying tissue or material properties. With the ability of having locally controlled functions, computational efficiency and general applicability, it makes a powerful tool for modelling deformable objects such as patients' bone shapes. One of the applications of this algorithm was used to compensate for motion in 3D MR mammography and the study used NMI as a measure of image alignment.

2.5.4.3 Elastic and Fluid Registrations

These are other non-linear models based on physical models.

In elastic registration (Bajcsy and Kovačič, 1989), the images are modelled as elastic materials like rubber, where external forces stretch the image and internal forces including stress counteract opposing forces until an equilibrium is reached. The main disadvantage is that registration based on this transformation cannot model highly localised deformations.

Fluid registration (Christensen et al., 1996), however, uses a model of viscous fluid, in contrast can model large and highly localised deformation, but blurring is introduced during the registration because of its higher flexibility.

2.5.5 Ultrasound Registration and Localisation

While ultrasound reflects very strongly from bone surfaces, the resulting images tend to be of low quality compared to CT due to noise from speckle and the presence of significant artefacts. The position of the surface as seen in the images may be distorted by a variety of effects related to image formation. As a result the accurate and robust registration of bone surfaces visible in US images to CT images remains a challenge. This section reviews the relatively small number of reported work in the literature, to extract bone information from US images or to register US to CT images.

2.5.5.1 Bone Localisation

Ultrasound can be a useful tool in establishing bone surface locations. One of its applications is in image-guided surgery. This technology is highlighted in a publication on the AcouStick, a location device based on a tracked A-mode ultrasound system for image-to-physical registration in image-guided neurosurgery. It is able to non-invasively determine cranial surface points using an optically tracked A-mode ultrasound transducer. Calibration is based on a variation of the invariant point method. Registrations were validated using eight markers implanted into the skull as the gold standard and the target registration error (TRE) over the head volume was calculated to be between 1.03mm and 1.73mm (Maurer et al., 1999).

2.5.5.2 Bone Extraction from Ultrasound

Ionescu et al. (1999) reported extraction of the bone surface from US images, by registering between a 3D CT model and a set of freehand 3D US images. US segmentation was performed using the watershed segmentation. To extract relevant contours from these segmented US images, an elastic registration was carried out between simulated US and real US data optimised based on gradient calculation. Finally, the relevant contours were rigidly registered to the preoperative model. The method was applied to the vertebra, sacro-iliac and prostate regions. The results were compared with either manual segmentation or manual digitisation of the bone surface, and the maximum errors were 2.58mm translation and 1.90° rotation. The optimisation procedure generally depends on the precision of the initial positions of the US probe and affects the global computing time. There needs to be a procedure that estimates an initial position as close as possible to the final position for each application.

Another method has been proposed for automatically segmenting ultrasound images to measure foetal femur length using morphological operators. This approach makes use of a priori

knowledge of the general size and shape of the foetal femur. The resulting image is thought to approximate closely the size and shape of the femur. This algorithm is not ideal for non-foetal images and also, the ratio of pixels to millimetres will be different in adult ultrasound data, so the algorithm would need to be adapted for use in adult patients (Thomas et al., 1991).

2.5.5.3 Registration to CT

Freehand 3D US images could be quantitatively registered to corresponding CT images for image-guided spinal surgery. In Muratore et al. (2002), US images were collected from a tracked phantom spine and the laminae and spinous process were segmented through the use of a morphological open operator, linear threshold of intensity and ray-tracing. ICP was used to match these segmented surface points to the corresponding CT images. Generally the registration quality improved as CT resolution increased. Further tests were performed to test the robustness of the algorithm, and the conclusion from the paper indicates that the results are sufficiently accurate for clinical purposes. Earlier studies quantitatively assessed vertebral registration accuracy where the results were generally below 1mm. Evaluation of registration accuracy reveals that a very small portion of the vertebral surface is sufficient to accurately register physical space to image space (Herring et al., 1998). The algorithm would be more susceptible to error due to much manual intervention involved.

Intraoperative US can also be registered to preoperative CT data, and used to non-invasively locate the pelvis and allow for computer-assisted surgical navigation. Anatomical landmark points were collected with a 3D position sensing probe to give an initial registration estimate. Bone contours were registered with the ICP algorithm. The method works with 20 images over the iliac wing which was sufficient to obtain clinically acceptable accuracy (Amin et al., 2001a).

A further refinement was given in Amin et al. (2003) which detailed an automatic registration of US images to surface models generated from preoperative CT scans. The method combines 3 sources of information: spatial prior based on a set of anatomic landmarks, bone surface reflection, and a bone shadow region indicated by a directional edge detector. These three information are weighted in the ICP algorithm for US to surface model registration. Experiments were performed on a plastic phantom pelvis with 4 fiducials to obtain the gold standard. The maximum registration error compared with the gold standard were less than 1mm and 2° in each axis. On another experiment intraoperative US were collected from a patient. Since no gold standard was available, the results were compared with the results using PBR, and the maximum difference between the method and those obtained using PBR were 2.1mm and 1.6°. This method is suitable

for procedures with limited or difficult access to the bone surface, and minimally invasive surgery.

Thresholding is also suggested as a method to register preoperative CT with intraoperative US. The method first extracts the bone surface from CT by simple thresholding, and then performs surface-volume registration by searching for a position of the estimated surface that maximises the average grey value of the voxels in the US (Winter et al., 2002). The full method was tested *in vitro* on the lumbar spine and it was discovered that it has a large radius of convergence and is considered robust (Brendel et al., 2002). A preprocessing step was added after surface extraction to emphasise the bone shape and to suppress overlaying tissues using adaptive depth gain compensation. The algorithm was implemented and validated using a cadevaric lumbar spine with surrounding muscle tissues (Brendel et al., 2003). The improved algorithm seems feasible and robust with respect to the rigid registration parameters. The algorithm has not yet been tailored in the clinical environment.

There was also a technique that increases the accuracy of iliosacral screw insertion for pelvis ring fractures (Tonetti et al., 1997). The technique is based on preoperative CT images registered with US acquisition of the anatomy of the subject during surgery. The experiments showed that differences were at most 2mm in translation and 2° rotation with clinical results available in Tonetti et al. (2001a). Later, Carrat et al. (1998, 2000) presented a percutaneous fixation method for pelvic ring fractures using ultrasound-based registration. A preoperative 3D model of the pelvis constructed from CT (using semi-automatic segmentation) scans were registered with curves segmented from the ultrasound scans, using a surface-based algorithm, where the surgeons defined the optimal placement of the screws. The system was validated on four cadaver pelves, with up to 3 bone screws inserted into each. All the bone screws were placed within acceptable positions and would not cause neurological lesion. The US registration was compared to a gold standard and the RMS errors were 2.6mm translation and 1.5° rotation. The algorithm took some time (nearly 20 minutes for 40 images) in particularly for US acquisition, segmentation and registration, and required extensive experience from the surgeon.

2.5.5.4 Fiducial Localisation

Lewis et al. (1998) and Schreiner et al. (1998) presented a new approach for marker-localisation in image-guided neurosurgery. The technique proposed is for transcutaneously detecting the location of permanent fiducial markers implanted into the surface of the skull to be used for the registration of image space and physical space. An algorithm was incorporated based on detection of characteristic properties of the reflected A-mode ultrasonic waveform, and is able to determine the 3D

location of small implanted cylindrical markers. Results have shown that the system is easy to use and finds each implanted marker in about 20 seconds.

2.5.5.5 Patents

There are three patents related to using ultrasound for detecting bone in surgery.

The first is a general patent filed by Cinquin et al. (1995), describing a method for determining the position of a particular patient's organ. The patent describes a system which provides the use of a device, in particular "echography probes" (ultrasound), which provides a 3D morphologic image of the surface points of organs, to be combined with the preoperative 3D image for localisation of the points. The patent also proposes aligning the coordinates of the tool with the coordinate system used.

The second patent describes a method for surface-based registration of bone with tomographic images and for guidance of instruments. It is a system which could be used to guide the position and orientation of instruments during surgery. The US probe used is an A-mode transducer, tracked in 3D by an optical position tracking system. The tracking signals and the US signals are used to produce a 3D physical space model of the bone surface. This model is registered with an image space model derived from the tomographic image with which the computer aligns (Bass et al., 2000).

The third patent is for a system and method for detecting surface points on bone. An US image is obtained and by applying a series of image processing filters (median, normalisation, edge detection and erosion), the US image could be refined. Outliers are removed by connecting between the points to obtain smooth lines. The points are then graded to obtain the "best" graded points. This system can also be used on other structures on a body (Yagel et al., 2002).

2.5.5.6 Echomorphing

A recent paper introduces a technique called echomorphing (Lavallée et al., 2004) which utilises freehand 3D US acquisition principles to collect US images. The bone surface is reconstructed using a bone morphing algorithm. The bone morphing algorithm (Stindel et al., 2002) uses palpated points on the patient's bone surface. To obtain the 3D shape of the structure, this cloud of bone surface points is fitted to an SSM of the femur or tibia using the algorithm of Fleute et al. (1999) that will be reviewed in Section 2.7.1. The computer automatically detects and segments the bone surface from images obtained from freehand 3D US. At least 6 images were collected and the morphing method was applied on the interface points. It has been tested on plastic bones,

moulded as condyles. This method was also tested on volunteers to test for flexibility and collected 3D data, however these data were not checked against a gold standard for verification. This is also an example of a CT-free system for the knee.

2.6 Statistical Shape Models

The use of SSM (Dryden and Mardia, 1998) to model human organs or bones has been a technique used by many. These models can be used to build an atlas of the average anatomy and its variability across the population.

An example is the point distribution model (PDM) proposed by Cootes et al. (1992). It is a SSM based on corresponding point positions. There is a wide variation of shape of the human femur and pelvis. It is hoped that this shape variation can be modelled with a SSM which can capture the variation of the shape of bones across a population using just a few modes of variation.

If a shape can be described using n points in d dimensions, it could be represented by a nd element vector. For example, a femur or pelvis surface can be represented as a $3n$-element vector, $\mathbf{x}$, where

$$\mathbf{x} = (\mathbf{x}_1, ..., \mathbf{x}_n, \mathbf{y}_1, ..., \mathbf{y}_n, \mathbf{z}_1, ..., \mathbf{z}_n)^T$$

The aim in building this model is to use a number of training datasets to calculate the principal components of shape variation.

2.6.1 Principal Component Analysis

Principal component analysis (PCA) is used to describe the different modes of variation with a small number of parameters (Cootes and Taylor, 2001). The data gets compressed by reducing the number of dimensions without losing the majority of the information. PCA breaks down the data into components, $\mathbf{c} = (c_1, c_2, ...c_n)$, so that they explain the highest amount of variance possible by n linearly transformed components.

The approach of the analysis is firstly to calculate the mean shape $\bar{\mathbf{x}}$ and covariance matrix $\mathbf{S}$ for the total number of datasets, s:

$$\bar{\mathbf{x}} = \frac{1}{s}\sum_{i=1}^{s}\mathbf{x}_i$$

$$\mathbf{S} = \frac{1}{s-1}\sum_{i=1}^{s}(\mathbf{x}_i - \bar{\mathbf{x}})(\mathbf{x}_i - \bar{\mathbf{x}})^T$$

Next, compute the eigenvectors ϕ_i and the corresponding eigenvalues λ_i of the covariance $\mathbf{S}$. The eigenvectors and the corresponding eigenvalues are the solutions of the equation:

$$\mathbf{S}\phi_i = \lambda_i \phi_i$$

λ_i is the i^{th} eigenvalue of $\mathbf{S}$ and $\lambda_i \geq \lambda_{i+1}$. Eigenvectors corresponding to the largest eigenvalues describe the most significant modes of variation in the datasets used to calculate the covariance matrix.

2.6.2 Approximating the Model

Following PCA, a specific instance of the model can then be approximated

$$\mathbf{x} = \bar{\mathbf{x}} + \sum_{i=1}^{m} \mu_i \phi_i \tag{2.1}$$

where $\mathbf{x}$ is the approximated instance and μ_i are the weights for the first m eigenvectors to be used in this approximation.

The calculated eigenvalues will show how much variation is covered by each mode, while the corresponding eigenvector (or eigenmode) is a vector of shape parameters. The higher the eigenvalue the greater the shape of change associated with a mode of variation. Often the first few eigenmodes are enough to cover most of the shape variation. Linear combination of these first few modes can then provide an approximation to an individual's anatomy. Three standard deviations of the mean should be enough to cover most of the population (Cootes et al., 1995).

The method relies on the assumption that the shape variation across the population has a normal distribution, and that one model fits all the people using it. It may be better split by factors such as sex, ethnic origin and pathology.

There is a huge variety in the population, it is hoped to describe the variations in the most compact way. As with the PDM, the method described in this thesis performs eigenvector analysis but the points being modelled do not necessarily have anatomical meaning since they are not anatomical landmarks.

By varying the contribution from each of the eigenmodes, new examples can be created. The active shape model (ASM) represents shape, using an iterative method to match a set of points from a shape model to a new image, constrained by a statistical model of shape, around each of these points local searches are performed (Cootes et al., 1995). The active appearance model (AAM) , on the other hand, represents both shape variation and the texture of the model region. An AAM contains grey-level information available across the object of interest. It uses all the information in

the target object region, not just those near the modelled edges, to minimise the difference between the new image and the synthesised version. However, this method could potentially involve a vast number of parameters, and creates a difficult optimisation problem (Cootes et al., 1998). In a comparison of the two methods (Cootes et al., 1999) using datasets of face images and MR brain slices, ASM was found to be faster and was able to obtain more accurate feature points while AAM provides a better match to the texture.

2.6.3 Applications

Frangi et al. (2001) introduced a method for obtaining 3D landmarks and the construction of the corresponding 3D ASM. They use a free-form elastic registration technique based on maximisation of volume-based normalised mutual information. This technique can be applied on any elastic registration algorithm. Tests were carried out on the left and right ventricles of the heart from 3D magnetic resonance imaging (MRI) images, the resulting accuracy in landmark propagation was under 2.2mm (Frangi et al., 2002). Wrong correspondences were not observed which proved to be an important improvement.

Meller and Kalender (2004) also produced SSMs of the pelvis and approximated a surface. The steps involved were manual landmarking including the centre of the acetabulum, then correcting any incorrectly propagated landmark on each segmented surface; the template is warped using thin plate splines and then put through a surface morphing process to minimise the shape difference between the template and propagated surfaces. Pelvic surfaces not used in the model were then approximated with an average of 2mm distance in the acetabular region.

Rajamani et al. (2004c,a) produced a SSM of the femur. Later, the method was enhanced to identify stable predictions and exclude outliers (Rajamani et al., 2004b). Using a few digitized landmarks and surface points, the patient-specific 3D shape was produced by minimising an objective function. The method was tested on a plastic femur. The method is quite fast and rejecting outliers seem to be robust, but creating the model required segmentation of each training dataset and instantiations done in a realistic way (where point correspondence is not available) appears to incur rather big errors. In other applications, ASM has also been used in assessing the shape of the proximal femur to predict hip fracture (Gregory et al., 2004).

It is difficult to quantify the accuracy necessary for the application in this thesis, and the user requirements are often application-specific (Simon et al., 1995). Computer-assisted orthopaedic surgery, coupled with SSMs, have the potential of increasing the accuracy of these applications, this will be illustrated further in later chapters. In this thesis, only a very general measure of

accuracy has been used, namely the mean TRE value. Examples of accuracy in various pieces of work in relation to computer-assisted orthopaedic surgery includes applications in the pelvis with surface matching results of TRE 3.8mm (van Hellemondt et al., 2002) and 1.6mm (Bachler et al., 2001).

2.6.4 Optimising Point Correspondence

Minimum description length (MDL) is an approach to the point correspondence problem in producing SSMs. Davies et al. (2001b,a, 2002b) defined a new method to produce SSMs automatically from a set of boundaries or surfaces. The new objective function has an information theory grounding independent of quantisation error and does not involve arbitrary parameters, using MDL as the basis. The MDL is based on computing the cost of transmitting the model and the data as a coded-message. The "best" model is one which describes the entire training set as efficiently as possible, thus adopting a MDL criterion. The paper also introduced a new method of representing parameterisation of curves in two dimensions that could be extended to 3D and results in improved convergence. When using a stochastic optimisation method it took several hours to complete a large number of function evaluations and is impractical for this application. The method has been implemented in 3D using hand-segmented MRI images of rat kidneys and brain ventricles (Davies et al., 2002a). The function can also be used to calculate the number of modes to be used for a certain model. It is still required to verify whether the optimal landmarks in the model are also optimal in terms of anatomical correspondence.

2.6.5 Independent Component Analysis

Independent component analysis (ICA) (Hyvärinen et al., 2001) is a statistical technique that could be used to filter out independent sources of information from linearly mixed variables. One of the definitions of ICA uses latent variables, which means these variables cannot be directly observed. Let $\mathbf{x}$ be the random vector of m dimensions, then the ICA of $\mathbf{x}$ is the estimation of this generative model of the data:

$$\mathbf{x} - \bar{\mathbf{x}} = \mathbf{A}\mathbf{s}$$

where $\bar{\mathbf{x}}$ is the mean of $\mathbf{x}$,

$\mathbf{s}$ is the random vector made up of n independent components, $\mathbf{s} = (s_1, s_2, ..., s_n)^T$; these are sometimes referred to as "sources", assumed to be statistically independent and have non-Gaussian distributions.

A is a constant $m \times n$ matrix of mixing parameters and is unknown. The matrix **A** needs to be estimated and its inverse, **U**, computed. To solve for the independent component, calculate

$$\mathbf{s} = \mathbf{U}(\mathbf{x} - \bar{\mathbf{x}}) \tag{2.2}$$

U is sometimes called the filter or projection matrix, and may also be called the "pseudoinverse" of **A**. It is worth noting that from Equation 2.2 the independent components have zero mean and it can also be assumed that they also have unit variance, without loss of generality.

Methods of computing ICA can be found in Hyvärinen (1999) with a survey of ICA. The more popular applications of ICA include blind source separation (BSS) and feature extraction. ICA was used to extract local shape deformation in cardiac contraction (Suinesiaputra et al., 2004), image feature extraction (Hurri et al., 1996) and also as an alternative to PCA (Bell and Sejnowski, 1997).

It may be possible to use ICA as an alternative to PCA for computing the SSM (Üzümcü et al., 2003). ICA could potentially be a good method for detecting local features and could also be a good choice for a linear model if there are plausible bases to assume that the modes are independent of each other, which is not the case in relation to this thesis when applied to shapes of femurs and pelves. A recent study by Bressan and Vitrià (2001) concluded that if shape deformations were not related, then ICA could be a good choice.

There are two main ambiguities of ICA which makes it unsuitable for this application. The first is that it is not possible to determine the variances of the independent components; the second is that the independent components are not ordered or ranked in anyway, such that an accurate and credible approximation of shape variations using a small number of parameters could not be obtained (Hyvärinen and Oja, 2000). This topic is the subject of on-going research, however.

2.6.6 Building SSM based on Node Points

It was introduced earlier that the ASM captures statistical information on shapes across a population. Since this thesis incorporates non-rigid registration to register training data sets to the target image, a model could also be built on the resulting B-spline node points (the FFDs). A method was first proposed by Rueckert et al. (2001) who introduced the idea of the statistical deformation model (SDM), applied to MR images of the brain. One of these 25 MR images was randomly chosen as the reference. In Rueckert et al. (2001), this reference image was not segmented. In Rueckert et al. (2003), the reference image was segmented to remove the effects of extracranial structures. The reference was then registered to other unsegmented images using a non-rigid registration algorithm (Rueckert et al., 1999). A SDM was constructed by performing PCA on the

deformation fields from the non-rigid registration algorithm, the outcome contains the mean deformation field for all the images and the principal modes of variation of the deformation fields. Unlike the AAM, the SDM does not include statistical information about intensities.

2.7 Previous Work in SSMs and Orthopaedics

2.7.1 Use of Shape Models to match Anatomical Structures

Fleute and Lavallée were one of the first groups to use SSMs to obtain a complete surface model of a bone by manually digitizing a few points on the femoral surface. This is a multi-resolution elastic registration technique based on octree-splines. The application is to improve visualisation systems developed for computer-assisted anterior cruciate ligament (ACL) reconstruction. 10 dry femurs were firstly registered to 1 template femur and then registered to the mean shape. PCA was then applied to the dataset to produce the SSM. ICP was used to fit the palpated points acquired on the tibial and femoral joint surfaces. The template femur was used as a test, it was shown that the RMS between the test data and the shape model was about 0.4mm using 5 modes. Using the template as a test could bias the experiment because the model would contain the information from that template femur. Another experiment was performed with real intraoperative data, where the surgeon acquired 100 points on the femoral notch surface. The resulting RMS for two clinical cases gave RMS values of between 1.6mm and 1.9mm with six modes of variation (Fleute and Lavallée, 1998; Fleute et al., 1999). This application to the knee is quite encouraging, but the invasiveness of the method is yet to be addressed.

Yao and Taylor (2003) presented a method for non-rigid registration of a deformable hemi-pelvis model with anatomical structures from a CT image. The model was represented as a hierarchical tetrahedral mesh and incorporates both shape and density properties. The non-rigid registration process consists of three steps: affine transformation (to set the size and pose of the model), global deformation (optimising statistical deformation parameters) and local deformation (driven by a multiple-layer flexible mesh template matching method associated with each model vertex). Allowing local deformation can lead to more accurate matching rather than simply adding more global modes. It is thought that this technique can be used to perform 3D patient specific modelling and analysis without the patient specific CT image. A leave-one-out validation showed the method could achieve about 94% volume overlap and 5.5% density error between the registered model and the ground truth model. This is based on selecting one pelvis in the training data set and using the other seven to build the atlas, which is a very small number for a credible

atlas. This method suffers from limited variability of the statistical atlas, so there would still be differences between the two images.

2.7.2 Statistical Shape Model and X-rays

The use of X-rays with shape models to produce surfaces of bone has been investigated. An algorithm was suggested by Fleute and Lavallée (1999) to reconstruct bones by registering a PDM to a few X-ray views, utilising contour-based registration. The contours were fitted to a bone model using ICP. The 3D shape of the patient bones or organs is built intraoperatively by deforming a statistical 3D model to the contours segmented on the X-ray views. Simulated data for the distal femur was used, up to 200 X-ray projections were used to match with the deformed model and the RMS distance was 0.77mm. When the deformed model was matched with the reference shape, the RMS distance was 0.99mm.

Another approach was suggested by Fleute et al. (2002) for intraoperative reconstruction of 3D anatomical surfaces. The method combines methods from Fleute and Lavallée (1998) and Fleute and Lavallée (1999) to match 2D or 3D image data to an SSM to provide the surgeon with a complete surface representation of the object of interest. In the 3D/3D matching, 450 surface points of a lumar vertebra model were collected. These were matched to the SSM with a mean RMS distance of 1.2mm. In 2D/3D matching using 2 orthogonal simulated X-rays, the contour points were registered with the SSM using all deformation modes and the average RMS distance between the deformed model and the reference was 0.62mm. A cadaver lumbar spine was also matched with the final RMS distance between the deformed model and the CT model was 1.27mm. Finally, an integrated method was proposed which uses both X-ray and approximately 70 data points acquired on a CT based spine model. The final average RMS between the deformed shape model and reference was 0.68mm. This method can be applied to healthy organs and pathological shapes which can be captured by statistical analysis, and it does not take into account any gender, ethical or other related anatomical differences .

Yao and Taylor (2001) demonstrated 2D/3D non-rigid registration between a statistical bone density atlas and a set of X-ray images. Bone density atlases were produced for the proximal femur and hemi-pelvis, represented as a tetrahedral mesh structure and characterising statistical variations in both the shape and density where typically two to three fluoroscopic X-ray images are acquired (See Section 2.7.1). Preliminary validation using simulated X-rays achieved about 88% volume overlap between the model and ground truth model of hemi-pelves. A "virtual CT" is obtained by registering the atlas to a set of X-ray images, which could be used for surgical pre-

treatment planning and intraoperative guidance. The registration method used has the advantage of not being affected by the view angle relative to the anatomical structure if using two orthogonal X-rays, but is sensitive to image distortion and image co-registration errors (Yao and Taylor, 2002).

In another work, a 3D volumetric model of the human tibia is constructed based on two conventional orthogonal two-dimensional radiographic images. The method makes use of a database of 80 2D and 3D cadaveric tibiae, which contains the CT data of each tibia and digitized 2D orthogonal radiographic images of left and right tibiae from adult patients both male and female. The computer finds the most similar tibia to the patient's tibia among the 2D radiographic images in the database, using Fourier descriptors for shape similarity detection, retrieve the corresponding CT, then 3D reconstruction is performed. The 3D model is derived from the CT data using linear warping to the 2D slices of the CT data, guided by the difference of contours. The method is quite adequate for visualisation, but is subject to noise, especially in the 2D X-Ray images during the digitisation process (Messmer et al., 2001).

2.8 Optimisation

Optimisation could be described as locating the best solution to a cost function within a set of feasible values of the parameter. This best solution could be a maxima or minima of the function, for simplicity this section will consider minimisation problems. For a solution sought over the entire region of the parameter space a global minimiser is required. Local minimisers are used for locating the lowest value within the valley of a small neighbourhood.

There are a few things to consider when choosing a suitable optimiser, including the number of dimensions (normally either 1-D or multi-dimensional), whether the function in question can be differentiated and how noisy the function is.

There are many optimisation methods and this section reviews a few of the more common techniques that are relevant to this application. This will not be a complete survey nor a definitive guide to all optimisation techniques. For a more comprehensive survey and details for some of the algorithms introduced here, see Press et al. (1992).

This section starts by describing a one-dimensional optimiser, the golden section search, while the rest of the review focuses on multi-dimensional problems.

2.8.1 Golden Section Search in One Dimension

The golden section search deals with a function of a single variable. The golden section is a line segment divided into two parts. Between two points A and B, point C is positioned such that the ratio of the short half to the long half is equal to the ratio of the long half to the whole, this is illustrated symbolically:

A _____C _____B

$$\text{where } \frac{\text{CB}}{\text{AC}} = \frac{\text{AC}}{\text{AB}}, \qquad \text{or} \qquad \text{AC}^2 = \text{BC} \times \text{AB}$$

If AB is unit length, let ϕ be the length BC. Then the above relationship becomes

$$(1-\phi)^2 = \phi \qquad \text{yielding} \qquad \phi^2 - 3\phi + 1 = 0$$

giving

$$\phi = \frac{3-\sqrt{5}}{2} \approx 0.38197$$

It could be said that C is at a fractional distance of 0.38197 from one end B or (1 - ϕ) $\approx$ 0.61803 from the other end, A. These fractions are called the golden section or "golden mean".

The golden section search (Press et al., 1992; Thacker and Cootes, 1996) in one dimension is a modification of the bisection method which provides a neat and robust way to locate the minimum in a bracketed interval. The size of the interval is then systematically reduced and new points introduced to achieve the best minimum.

When there is a triplet of points, a $<$ b $<$ c, if f(b) is less than or equal to both f(a) and f(c), a minimum is known to be bracketed in the interval (a, c).

If a new point x is chosen within this interval, for example between b and c, f(x) needs to be evaluated.

If f(b) $<$ f(x), the new interval becomes a $<$ b $<$ x.

If f(b) $>$ f(x), the new interval becomes b $<$ x $<$ c.

This process of bracketing is repeated until the interval attains an arbitrary tolerance. To obtain the optimal subinterval, x should be chosen to be a fraction $\frac{3-\sqrt{5}}{2}$ from the larger subinterval.

The golden section search does not require calculating the derivative of the function, and does not assume the function to be nicely parabolic. It is designed to handle the worst possible case of function minimisation.

Sometimes optimisation in many dimensional space can be broken down into many 1-D line minimisations and golden section search could be used for this local optimisation purpose.

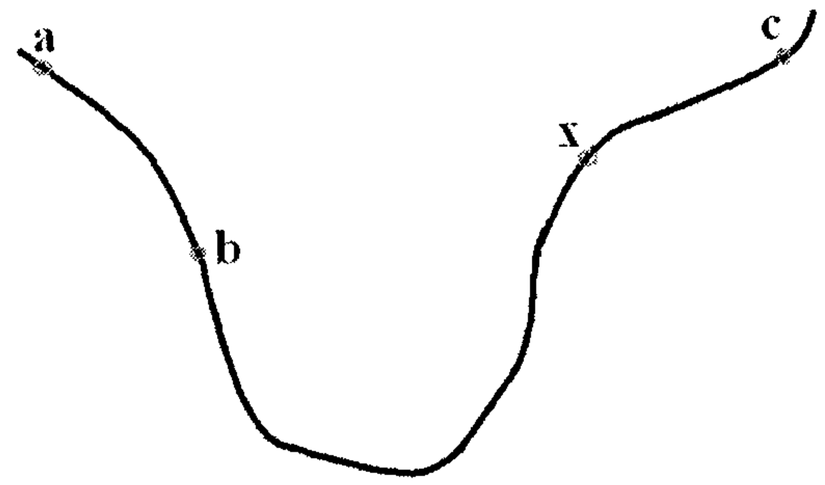

Figure 2.7: The golden section search bracketing. The minimum is originally bracketed by points a, b and c, the function is then evaluated at x.

2.8.2 Downhill Simplex Method

The downhill simplex method (Press et al., 1992) makes no assumptions about the function and proceeds downhill in a straightforward way. It does not require derivatives, and is able to break out of a local minima. The method can be very slow but is very robust, which makes it ideal for noisy functions.

A simplex is a geometrical shape that consists of $N + 1$ points or vertices in N dimensions. In 2D a simplex is a triangle, in 3D a tetrahedron, and so on. The simplex formed should be non-degenerate, meaning one that encloses a finite (non-zero) inner N-dimensional volume.

The method must be started with a simplex, one of $N + 1$ points. If the starting point is $\mathbf{a}_0$, then the other N points can be taken to be $\mathbf{a}_i = \mathbf{a}_0 + \lambda \mathbf{e}_i$, where $\mathbf{e}_i$ are unit vectors, $i = 1, 2, ..., N$.

The method takes a series of steps, namely:

- *Reflect*: these are the most steps taken, to move the point with the highest function evaluation (called the "highest point") through the plane of the simplex to a lower point. This step is taken to conserve the volume of the simplex.

- *Expand*: take larger steps by taking the simplex in one or another direction.

- *Contract*: to shrink the simplex in the transverse direction when it reaches a "valley floor".

The main aim of this method by taking these steps, are for the simplex to crawl around the parameter space, through reflecting, expanding and contracting, go down valleys and eventually to the very bottom where the minimum lies.

2.8.3 Conjugate Directions and Powell's Method

Take a point **a** which is the origin of a coordinate system with coordinates **x**. Using a Taylor series expansion, the function f can be approximated as:

$$f(\mathbf{a}+\mathbf{x}) = f(\mathbf{a}) + \sum_i \frac{\partial f}{\partial a_i} x_i + \frac{1}{2}\sum_{i,j} \frac{\partial^2 f}{\partial a_i \partial a_j} x_i x_j + \ldots$$

$$\approx c - \mathbf{b}.\mathbf{x} + \frac{1}{2}\mathbf{x}^T \mathbf{A}\mathbf{x}$$

$$\text{where } c = f(\mathbf{a}), \mathbf{b} = -\nabla f, [\mathbf{A}]_{ij} = \frac{\partial^2 f}{\partial a_i \partial a_j}$$

The matrix **A** is called the Hessian matrix of the function at point **a**.

When a function is minimum at a certain point, the gradient of the function must be perpendicular to the direction of the minimum and hence **b** = 0. Therefore, at the minimum point $\mathbf{a}_{min}$,

$$f(\mathbf{a}_{min} + x) \approx c + \frac{1}{2}\mathbf{x}^T \mathbf{A}\mathbf{x}$$

So assume **a** is an estimate of the minimum of the function f(a), this can be refined by defining some direction vector **u** and a line minimisation search performed along the line **a** + λ**u**. A simple method would be to move along the first unit direction vector to its minimum, and then from there search along the second direction to its minimum, and then onto the third and so on, cycling through all the unit direction vectors in the parameter space until the function decreases no more. This method can be very inefficient, taking lots of unnecessary small steps, unless the valley is optimally oriented.

2.8.3.1 Conjugate Directions

From the above equations, the gradient of f near point **a** is

$$\nabla f(\mathbf{a}+\mathbf{x}) = \mathbf{A}\mathbf{x} - \mathbf{b} \tag{2.3}$$

After minimising along direction **u**, $\nabla f.\mathbf{u} = 0$

Moving along another direction, the gradient changes by: $\partial(\nabla f) = \mathbf{A}.(\partial\ \mathbf{x})$

To avoid the inefficiency of taking too many small steps, one of the ways is to choose another direction **v** after finding the first line minimum (from **u**), on condition that moving along **v** would not degrade the minimisation already achieved by the previous moving along **u**, that is, such that the change in gradient of **v** stays perpendicular to **u**. This is illustrated as

$$\mathbf{u}\ .\ \partial(\nabla f) = \mathbf{u}.\mathbf{A}.\mathbf{v} = 0 \tag{2.4}$$

When Equation 2.4 holds, the vectors **u** and **v** are said to be conjugate. When this holds for all the pairs of vectors in a set of vectors, they are said to be conjugate sets.

If line minimisation is performed along a conjugate set of directions, the function will get closer to the minimum efficiently. One pass of all line minimisations will put the function at the minimum if the function has an exact quadratic form, but if this is not the case, repeated cycles of the line minimisations will be necessary.

2.8.3.2 Powell's Method

When derivatives are not available or easily calculated, Powell's method can be used to produce the mutually conjugate directions. The starting point is the description of the planes and the initial directions, let $\mathbf{e}_i$ be the unit basis directions where $i = 1, 2, ...,n$. The method repeats the following steps until the function reaches a minimum:

- Save the starting position as $\mathbf{P}_0$.
- For $i = 1, 2, ...,n$, minimise the function starting from $\mathbf{P}_{i-1}$ along the direction $\mathbf{e}_i$ and store the minimum as the next position $\mathbf{P}_i$. All $\mathbf{P}_i$ will be computed after the loop.
- Set $\mathbf{e}_n$ to be the direction given by ($\mathbf{P}_n$ - $\mathbf{P}_0$).
- Move $\mathbf{P}_n$ along direction $\mathbf{e}_n$ to the minimum and set $\mathbf{P}_0 = \mathbf{P}_n$. The iteration process continues until the minimum is reached.

Powell's method works well if there is a reasonable starting approximation to the function and if the function is not too noisy.

2.8.4 Variable Metric (Quasi-Newton)

The variable metric methods (Press et al., 1992) require that the gradient of the function be available. The method attempts to generate a good approximation to the inverse of the Hessian matrix $\mathbf{A}^{-1}, \mathbf{H} \approx \mathbf{A}^{-1}$, such that a sequence of matrices $\mathbf{H}_i$ with the property:

$$\lim_{x \to \infty} \mathbf{H}_i = \mathbf{A}^{-1}$$

From Equation 2.3 above, the gradient of f near point **a** is

$$\nabla f(\mathbf{a} + \mathbf{x}) = \mathbf{A}\mathbf{x} - \mathbf{b}$$

At the minima, the gradient is 0, so $\mathbf{A}\mathbf{x} - \mathbf{b} = 0$

Therefore, the next best direction step would be

$$\mathbf{x} = \mathbf{A}^{-1}\mathbf{b} \qquad \text{which becomes} \qquad \mathbf{x} \approx \mathbf{H}\mathbf{b}$$

Having obtained the estimate of the inverse of the Hessian, this is used to determine the next iteration point.

One of the main advantages of the variable metric methods is that it avoids the calculation of the Hessian which may take considerable computational time, while still maintaining a fast local convergence.

2.8.5 Parallel Direct Search

Parallel direction search (PDS) (Torczon, 1992) is a derivative-free algorithm, extended from the downhill simplex method introduced earlier and uses the concept of searching in several different directions simultaneously. It performs unconstrained and bound constrained minimisation without using gradient (derivative) information. For each iteration, the objective function is evaluated around the current set of input points. The lowest function value evaluated will be chosen as the new input. If none of the points returns a lower value, the spacing between the points around the current set will be reduced. The evaluation terminates when the spacing is smaller than a specified convergence tolerance. The number of points and the spacing between them controls how sensitive PDS is to local minima. PDS is fairly easy to implement on parallel machines and can be applied to most nonlinear optimisation problems.

2.8.6 Simulated Annealing

All of the above methods are optimisers that deal with local minima. However, if the function contains a lot of local minima, this will make it hard to localise the global minimum. Simulated annealing (SA) applies stochastic components to explore the search space for the global minimum.

SA is an analogy with thermodynamics, in which a liquid cools, freezes and turns crystalline (the process of annealing), in search for a minimum energy state (Press et al., 1992; Thacker and Cootes, 1996). This method is often used for non-linear functions when finding the global minimum and is thought to be well suited for problems with a lot of local extrema.

In an annealing process, a liquid at a high temperature would have its molecules disordered; as it is slowly cooled to being approximately in thermodynamic equilibrium, the system becomes more ordered and approaches a crystalline state at temperature T = 0. If the initial temperature is too low or if the cooling is done too quickly, the system may create defects, analogous to

being trapped in a local minimum energy state. To proceed with the algorithm, the means of evaluating the function and the "annealing schedule" (initial temperature and rules for lowering it) are required.

One main advantage of SA is its ability to avoid being trapped in local minima. However, generating new random points can be inefficient, making the algorithm slow compared to gradient-based methods. Determining the parameters for the annealing schedule is also quite challenging and could be time consuming.

2.9 Chapter Summary

This literature review has shown that SSMs have recently generated considerable interest for use in orthopaedic surgery, both for image segmentation and for navigation. It has been shown that a 3D surface model can be instantiated using an SSM from X-ray images and from physically digitised landmark or surface points. Some of these methods were suggested as alternatives to CT-based methods. These 3D surface models were applied to IGS. CT-free systems exist but require either radiographs or palpating points; this means radiation or invasive procedures are still an issue.

Ultrasound is therefore suggested as an alternative. Ultrasound is a safe, relatively inexpensive and non-invasive imaging modality. Although there are some perceived drawbacks of US relating to artefacts and relatively poor tissue contrast, the strongly reflecting nature of bones in US images are useful for locating bone surfaces and registering various parts of the body including the hip.

A novel method is therefore proposed in this thesis. US images obtained on the patient could be used to simultaneously instantiate and register the SSM to produce a bone surface that will closely approximate the patient's anatomy. This will allow surgical navigation without the need for a preoperative CT scan and its associated radiation dose, inconvenience and expense. It also provides the opportunity to develop less invasive procedures that reduce surgical exposure of bone and disruption of the joint capsule.

The next chapter starts by formulating this method and it is then tested on a phantom femur in a water bath.

Chapter 3

Surface Statistical Shape Model for the Femur

3.1 Introduction

This chapter describes the production of a statistical shape model (SSM) based on a set of points on the surface of a femur. This SSM is instantiated using points acquired from 3D ultrasound (US) of a phantom femur. The proposed method produces a 3D model of the phantom femur from US images, by instantiating from a SSM of the femur created using a database of computed tomography (CT) scans. The segmented bone surface from one CT image is propagated to the other images using a non-rigid registration algorithm. This provides a database of corresponding surface points and a left femur model was generated from 10 clinical CT datasets, showing the first five modes of shape variations.

Also in this chapter to demonstrate proof of principle, a cadaveric femur, immersed in a water bath, which was not used in the shape model construction was scanned using freehand 3D US. The iterative closest point (ICP) algorithm (Besl and McKay, 1992) was used to match points corresponding to the bone surface derived from US with the statistical bone surface model. The resulting root mean square (RMS) point-to-surface distance from ICP was minimised to provide the best fit of the model to the US data. The gold standard CT-derived surface of the cadaveric femur, and the gold standard registration was available for validation of the method's accuracy.

In an exploration of the cost function shape space, a modification of the ICP algorithm was utilised. This chapter also investigates methods to optimise the procedure, including the suggestion of adding an extra point in the centre of the femoral head to be used as the centre of rotation in the ICP algorithm.

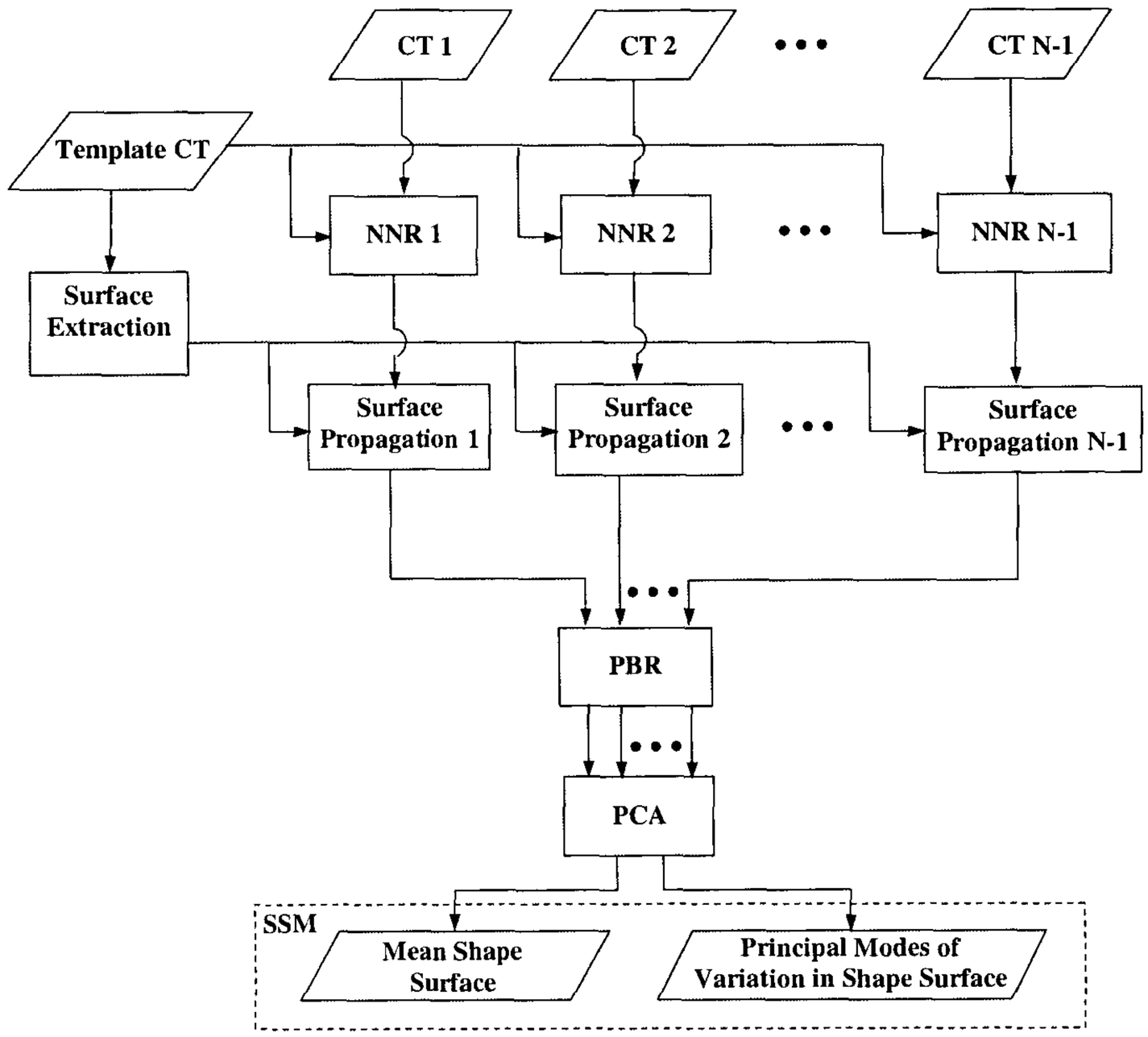

Figure 3.1: Constructing the surface SSM. "NNR1"... "NNR N-1" stands for the non-rigid registrations between each individual and the template CT; The mean shape surface and principal modes of variation in shape surface make up the SSM.

3.2 Construction of the Surface Statistical Shape Model

In order to obtain point correspondence, the SSM was generated from datasets that were non-rigidly registered. The database of CT scans was collected as part of the Depuy implant development programme. The method starts with extraction of the surface from one of the CT datasets. This will be called the template bone. This template was then non-rigidly registered to the other CT scans in the database. Using these non-rigid transformations, the template surface was propagated to each individual in the dataset to produce surfaces. The SSM was then built on these surface points. A flow diagram of this method is shown in Figure 3.1.

3.2.1 Template Segmentation

The template image ("Template CT") was selected from the CT database as being of average shape and size by visual inspection.

The non-rigid registration algorithm to be used is voxel-based and is able to register high

variability structures such as soft tissues, but in this application the region of interest is the femur bone. In theory, for voxel-based registration algorithms, the more voxels included, the more information available and hence the better the algorithm can perform. Because of high variability of soft tissue around bones, the template bone had to be segmented so that the effects and possible errors from registering with the soft tissue registration could be minimised. A reasonable overlap between the template image and other bones in the dataset is needed for registration. A thin rim of soft tissue, obtained by dilation of the segmented bone CT image, provides adequate soft tissue around the bone to ensure the whole bone was sampled, including the effect of partial volume. This has the effect of improving the registration to the bone boundary, as more information could be used by the registration algorithm to obtain a transformation as accurate as possible on the femur bone surface. Other voxels outside of the region of interest are labelled as missing data and do not contribute to the registration.

The segmentation was done using ANALYZE 6.0 (Robb et al., 1989, Mayo Foundation, Rochester, MN, USA). Initially an intensity threshold was performed but a few problems occurred.

Bone has a much higher CT number (a measure of how much the incident X-rays are absorbed as they go through a structure) than soft tissue, it appears brightly on a CT scan while other structures with smaller CT numbers are less bright. In the human body, however, bone lies side-by-side with soft tissue in a typical transverse view of the CT slice, this can cause part of the bone to be "missing" caused by partial volume effects. Take a voxel as an example, if the voxel contains both bone (high CT number) and soft tissue (low CT number), the resulting CT number for that voxel is an average of these numbers. A voxel with this averaged and reduced CT number may not necessarily be classified by the thresholding method. If the threshold is set too high, where bone is quite thin (e.g. on the iliac crest of the pelvis), the voxel may be wrongly classified as not bone. If the threshold is set too low, soft tissues and other structures apart from bone could be wrongly classified as bone. It is difficult to set a mutually acceptable threshold.

Therefore the CT images had to be segmented manually by hand to obtain the highest possible accuracy. This is done by delineating the boundary of the bone surface on each transverse slice, and then removing the region exterior to the bone by setting the intensity to zero, leaving non-zero voxels to define the region of the image corresponding to bone.

The segmentation was then dilated by 5-8mm to include a thin rim of soft tissue. An example of this process is shown in Figure 3.2. Note that only one femur, the template, was segmented for matching. All other femurs in the CT database were non-rigidly registered to this template femur. This non-rigid registration process is described in the next section.

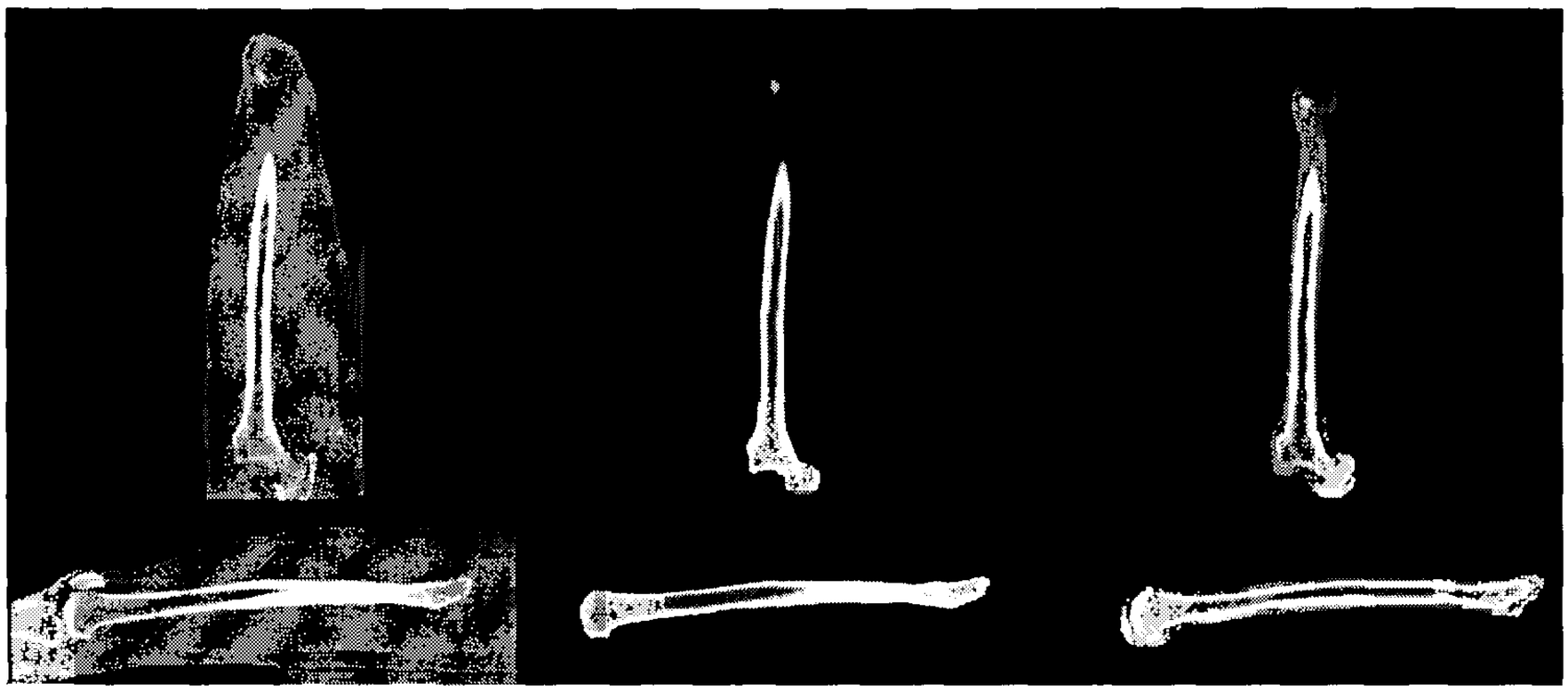

Figure 3.2: Examples of the left femur in coronal (*top*) and sagittal (*bottom*) views. From left to right: the original femur, the segmented femur, the femur dilated by 5mm.

3.2.2 Non-Rigid Registration

The template image is aligned to the other images in the database using a non-rigid registration algorithm (Rueckert et al., 1999) described in Section 2.5.4. This is illustrated by the "NRR 1" to "NRR N-1" in the flow diagram. This algorithm matches on image intensity, meaning that it does not match on bone boundary alone or a segmented surface.

The flexibility of the deformation is determined primarily by the spacing of the B-spline node points. The shape of the femur is challenging for non-rigid registration algorithms because it is long, narrow and much of the length is near a cylindrical symmetry. Another region that could confuse the registration algorithm was around the femoral head. This area articulates with the acetabulum of the pelvis and the boundary between the femoral head and the acetabulum is sometimes unclear due to diseases like arthritis.

Most non-rigid registration algorithms will require a starting estimate. To overcome some of the problems outlined above, an initial alignment was defined manually as the starting estimate, and also to incorporate rigid movement and scaling (a total of nine degrees of freedom) to reduce the likelihood of obviously incorrect correspondences. The local transformation was then modelled by the free-form deformation (FFD).

Normalised mutual information (NMI), described in Section 2.5.3.1, was employed as a voxel-based similarity measure (Studholme et al., 1999). In principle, as all scans were from the same modality, sum of squared intensity difference (SSD) (Section 2.5.3.1) could have been used, but in practice NMI was found to be more robust, probably due to small variations in inten-

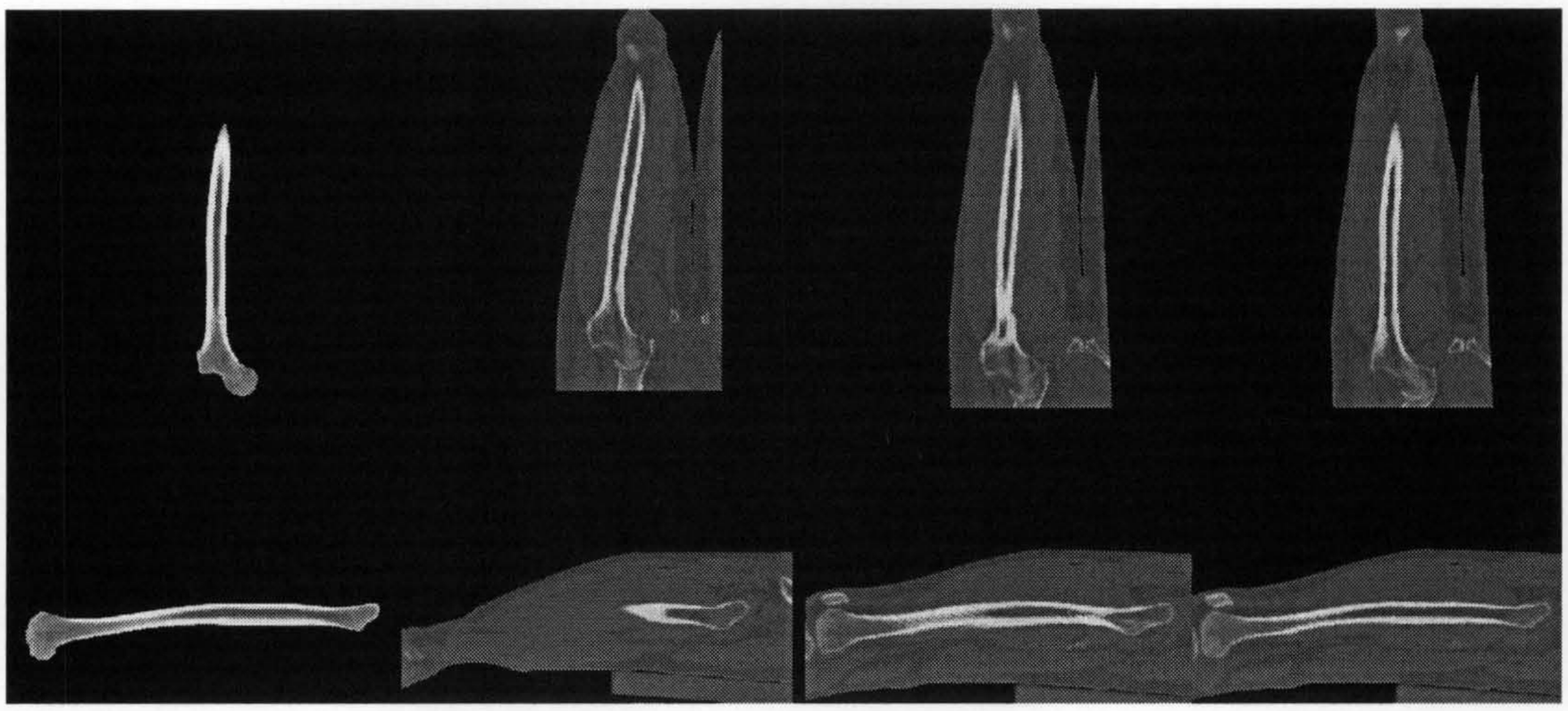

Figure 3.3: Example registration for the left femur in coronal (*top*) and sagittal (*bottom*) views. From left to right: the target femur, the source femur, after rigid registration, after non-rigid registration.

sity and bone mineralisation across the database. Each registration took between 2 and 7 hours on one processor of the Condor Cluster, with processor speeds of 1.4MHz to 1.8MHz and 1Gb memory. An example of the resulting alignment can be seen in Figure 3.3 showing coronal and sagittal slices of the non-rigid registration results.

A node point spacing of 20mm was used. Experiments were undertaken using finer node spacings but the deformation became unstable and often produced visually implausible deformation fields, mainly over-matching and visually large errors. It also took much longer to compute. For example, when the control spacing of 20mm was doubled to a finer spacing of 10mm, the computational time increased by more than double but the registration results only improved by very little. Greater than 20mm node spacing resulted in too few node points to define the necessary transformation with sufficient accuracy. Therefore, the finest node spacing was selected that consistently produced plausible good quality images with no visually observed folding.

3.2.3 Surface Extraction and Propagation

The femur template was segmented in a previous step, a bone surface is also necessary for matching with US-derived points. A triangulated surface was produced using an implementation of marching cubes (Lorensen and Cline, 1987) from the VTK libraries (Schroeder et al., 1997; Hartkens et al., 2002). This triangulated surface is further smoothed and subsampled to reduce the number of polygons at the cost of some accuracy, to provide a simplified surface with just 832

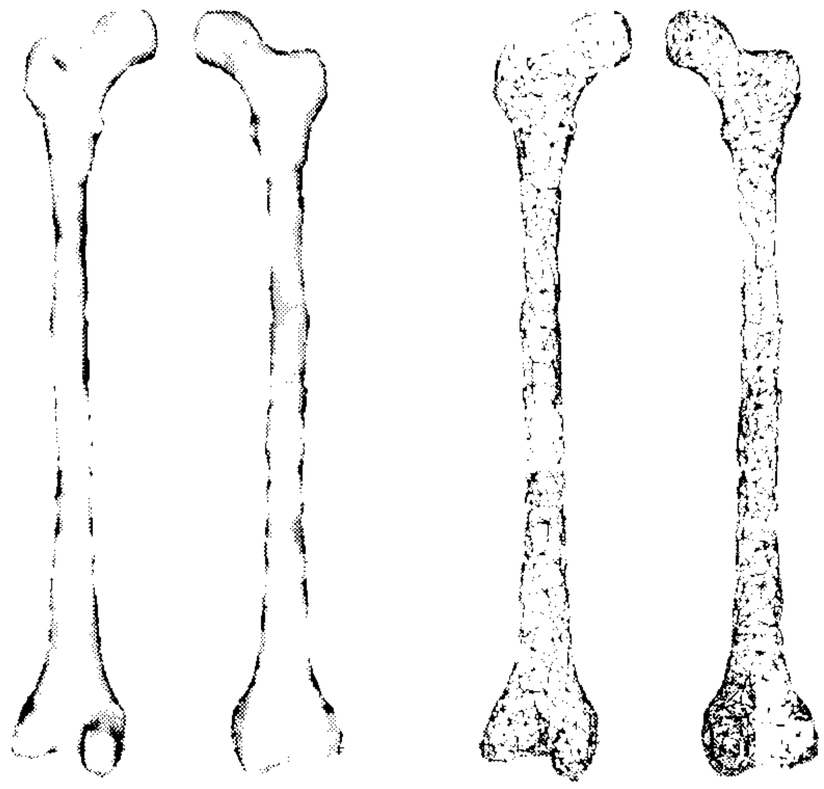

Figure 3.4: Femur template surface produced using 832 points, shown on the left with anterior and posterior views; and the template mesh, shown on the right with anterior and posterior views.

points for the femur. This surface was visually checked against the original CT scan to see that the bone contours coincided with that on the original image. Using a simplified surface will enable an SSM to be generated faster; this is a compromise between computational time and quality of the surface images and accounts for the blocky appearance. The template surface of the femur and mesh (with vertices) is shown in Figure 3.4.

Though the non-rigid registrations were performed on voxel images, the result of the algorithm is a set of B-spline node points that describe the mapping from the template to the other images in the database. These mappings can be used to propagate the triangulated surface from the template to each individual in the CT dataset. This is shown in the flow diagram as "Surface Propagation 1" to "Surface Propagation N-1". The result is a set of corresponding surface points for all examples in the training set. In general when generating a SSM from 3D surface data finding point correspondences can be a difficult problem. This method provides such correspondence automatically.

3.2.4 Building the Model

Before building the SSM, any motion between the different surfaces that is not associated with shape change needs to be taken out. The process starts by performing point-based rigid registration with 6 DOFs, from each propagated individual surface to the template. This is illustrated by the step "PBR" in the flow diagram. These registered surfaces are then used to build the SSM. This removes rigid motion but any changes in size, shape or skew are left to be modelled by the SSM.

One could argue that technically speaking scaling does not really represent a change of shape. However, in this application, these should be incorporated into the model, since there may be general changes in shape that occur with size.

The output of the principal component analysis (PCA) (See Section 2.6.1 on Page 47) was the mean shape of the data population, with the eigenmodes representing the change in shape and eigenvalues representing the principal modes of shape variations. The number of surface points used for the models are the same as that of the template.

3.2.5 Results: The Femur Surface Models

This section presents the SSMs produced from femur CT scans by showing the first two modes of shape variations. Two SSMs were constructed using a CT database of 10 each of left and right femurs. The femurs were scanned with voxel dimensions $0.48\times0.48\times1.5\text{mm}^3$ through the femoral head and knee, and $0.48\times0.48\times4\text{mm}^3$ through the shaft of the femur, and then resampled to 2mm slice thickness.

Figure 3.5 shows two surface models: left femur and right femur. For each model the first two modes are shown, when applying plus or minus three standard deviations (SDs) to the mean shape. There are some significant changes in shape. For both models, the first two modes appear to correspond to a change in the femur size and length, and a change in the femoral head angle respectively; other modes of variation of these models include twisting of the bone, change of trochanter position, and change in femoral head or condyle sizes.

All the eigenvalues of the covariance matrix derived from the left femur surfaces and right femur surfaces are shown in Tables 3.1 and 3.2 respectively. This information is plotted in Figures 3.6 and 3.7 for the left femur and Figures 3.8 and 3.9 for the right femur. For each femur, the first graph shows all of the modes with the principal mode dominating the plot, the second graph shows more clearly the rest of the modes.

For the left femur, the first 5 modes of variation explain almost 99% of the variance. The principal mode describes the most significant modes of variation in the variables that were used to derive the covariance matrix. In this model, the principal mode is very large that it explains over 93% of the shape variance due to variation in overall length of the femur. For the right femur, on the other hand, the first 5 modes of variation explain almost 98% of the variance while the principal mode explains over 89% of the total variance, similarly, with the principal mode largely describing the length and size of the femur.

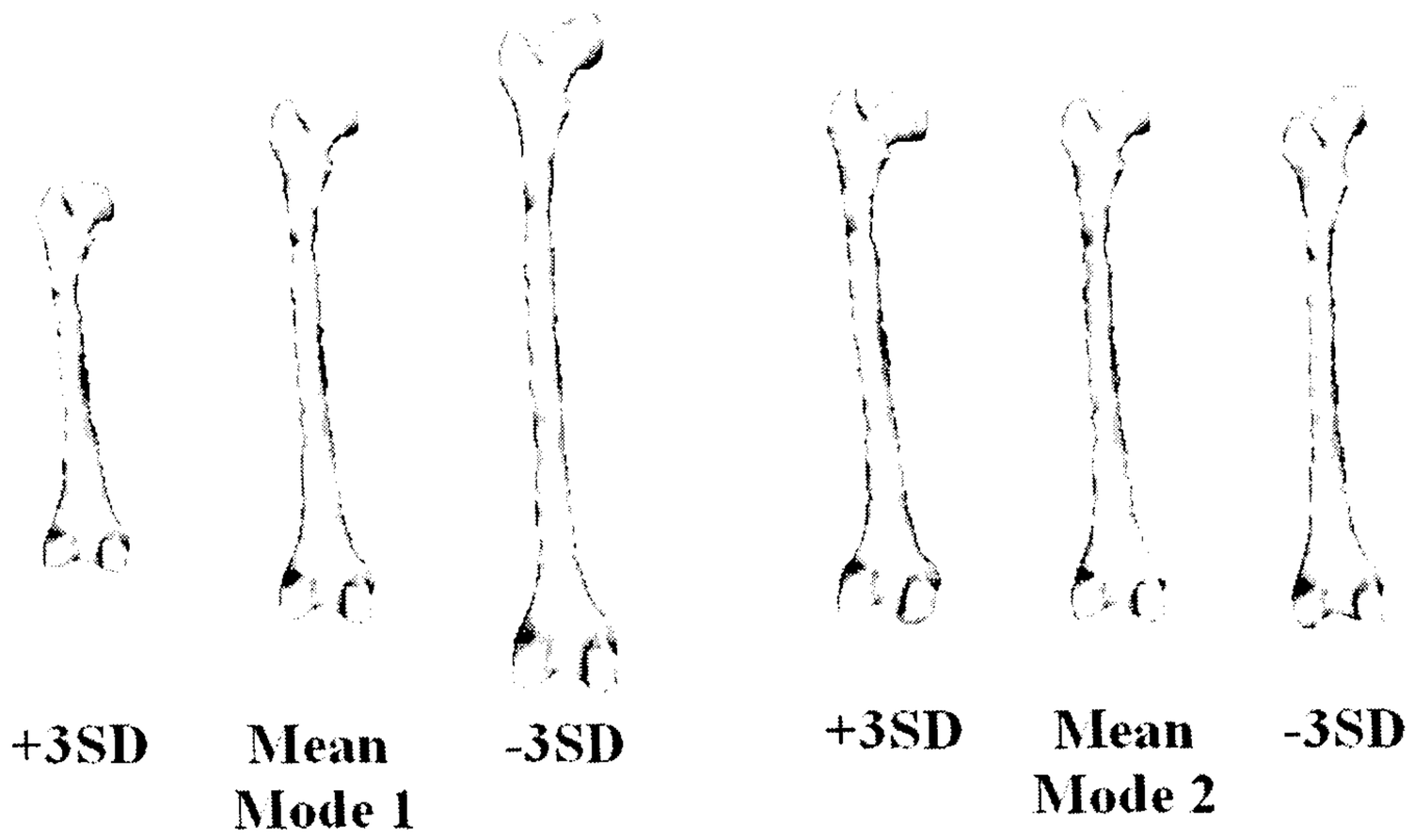

Figure 3.5: The left femur (*top*) and right femur (*bottom*) femur SSMs showing the first 2 modes of shape variations with three standard deviations.

Table 3.1: Eigenvalues λ_i of the covariance matrix derived from the left femur surfaces

Eigenvalue $i = 1..9$	λ_i (to 1d.p.)	$\frac{\lambda_i}{\lambda_{TOTAL}}$ (to 3d.p.)	Cumulative (to 3d.p.)
λ_1	192348.0	0.939	0.939
λ_2	3785.0	0.018	0.957
λ_3	3044.3	0.015	0.972
λ_4	1408.0	0.007	0.979
λ_5	1273.4	0.006	0.985
λ_6	1044.3	0.005	0.990
λ_7	916.1	0.004	0.995
λ_8	713.8	0.003	0.998
λ_9	352.8	0.002	1.000

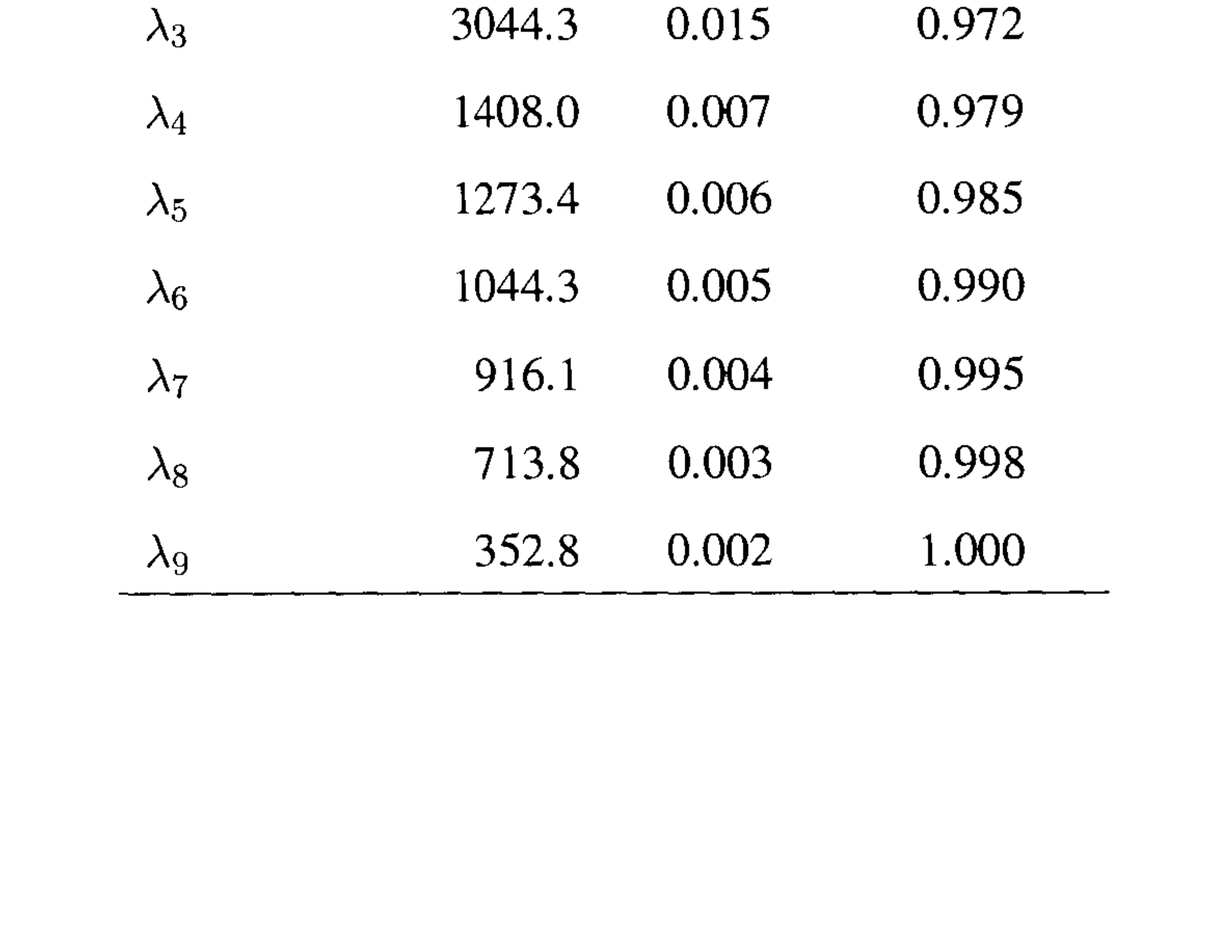

Figure 3.6: Eigenvalues λ_i of the covariance matrix derived from the left femur surfaces (i=1-9)

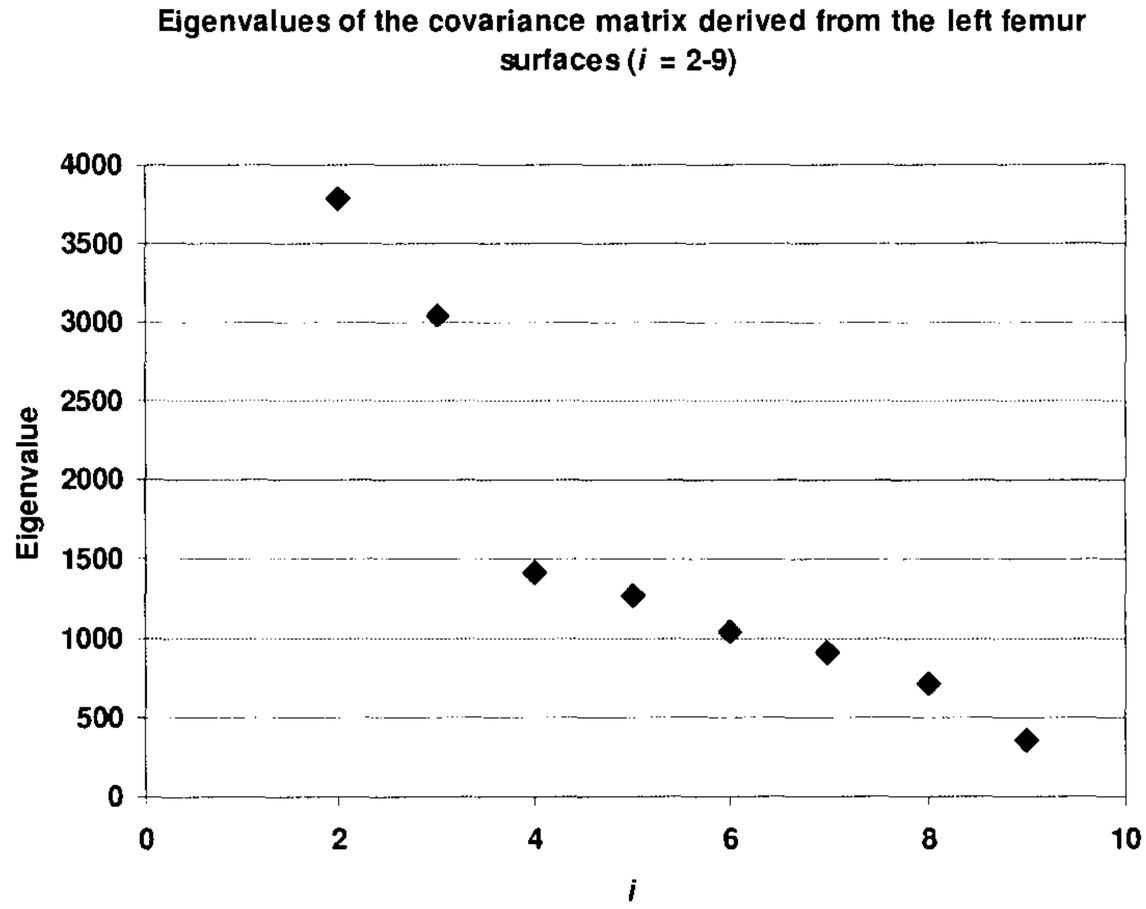

Figure 3.7: Eigenvalues λ_i of the covariance matrix derived from the left femur surfaces (i=2-9)

Table 3.2: Eigenvalues λ_i of the covariance matrix derived from the right femur surfaces

Eigenvalue $i = 1..9$	λ_i (to 1d.p.)	$\frac{\lambda_i}{\lambda_{TOTAL}}$ (to 3d.p.)	Cumulative (to 3d.p.)
λ_1	106036.0	0.891	0.891
λ_2	4409.6	0.037	0.928
λ_3	2858.0	0.024	0.952
λ_4	1782.9	0.015	0.967
λ_5	1072.1	0.009	0.976
λ_6	974.2	0.008	0.984
λ_7	844.9	0.007	0.991
λ_8	581.6	0.005	0.996
λ_9	433.9	0.004	1.000

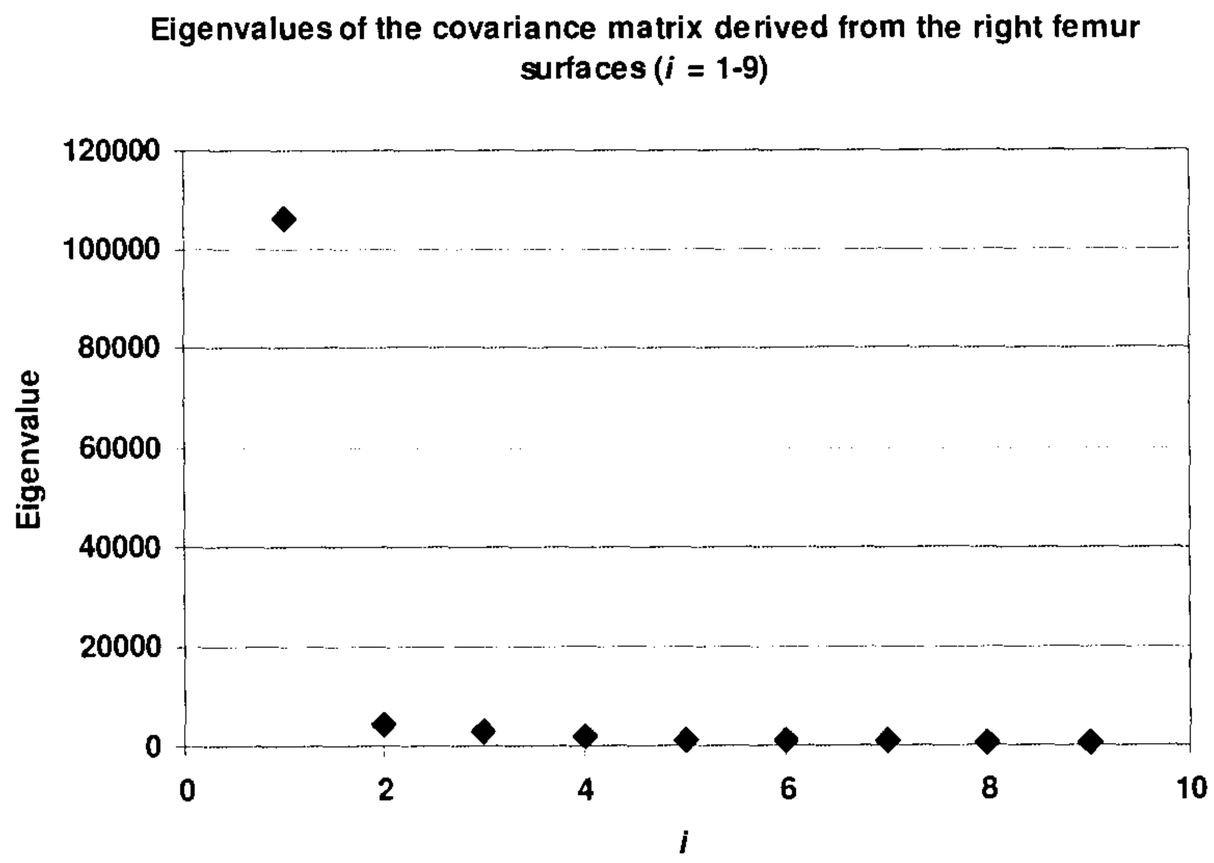

Figure 3.8: Eigenvalues λ_i of the covariance matrix derived from the right femur surfaces (i=1-9)

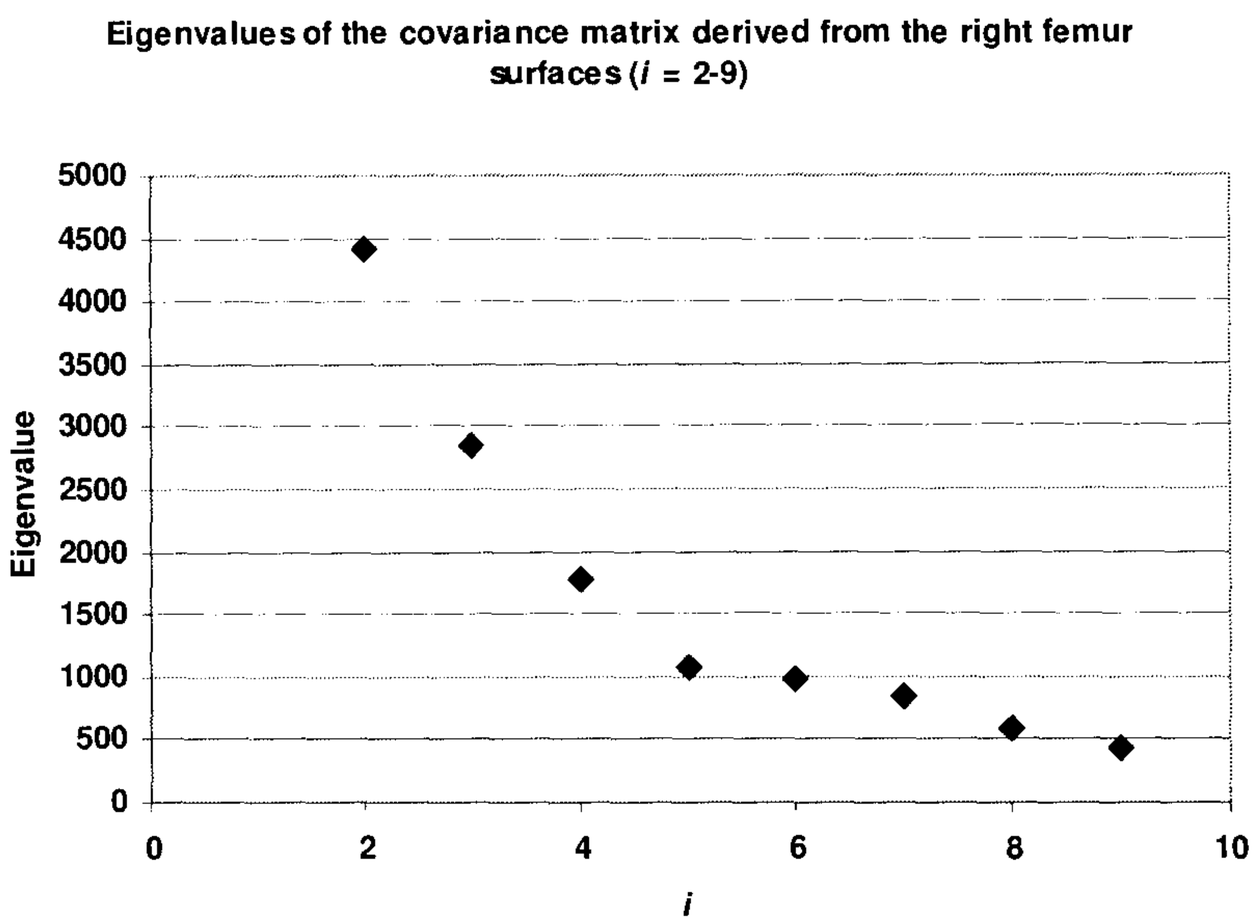

Figure 3.9: Eigenvalues λ_i of the covariance matrix derived from the right femur surfaces (i=2-9)

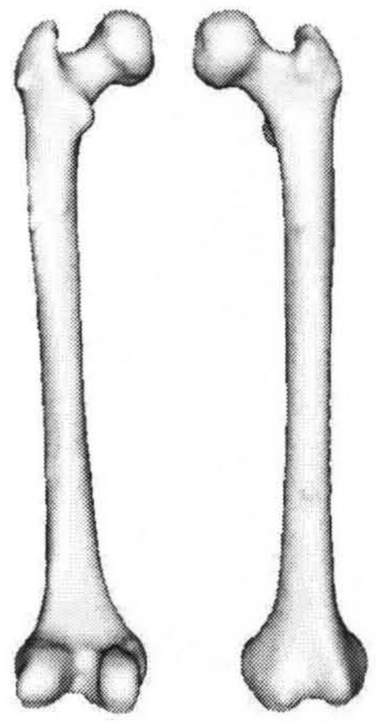

Figure 3.10: The phantom femur surface rendering from the CT scan.

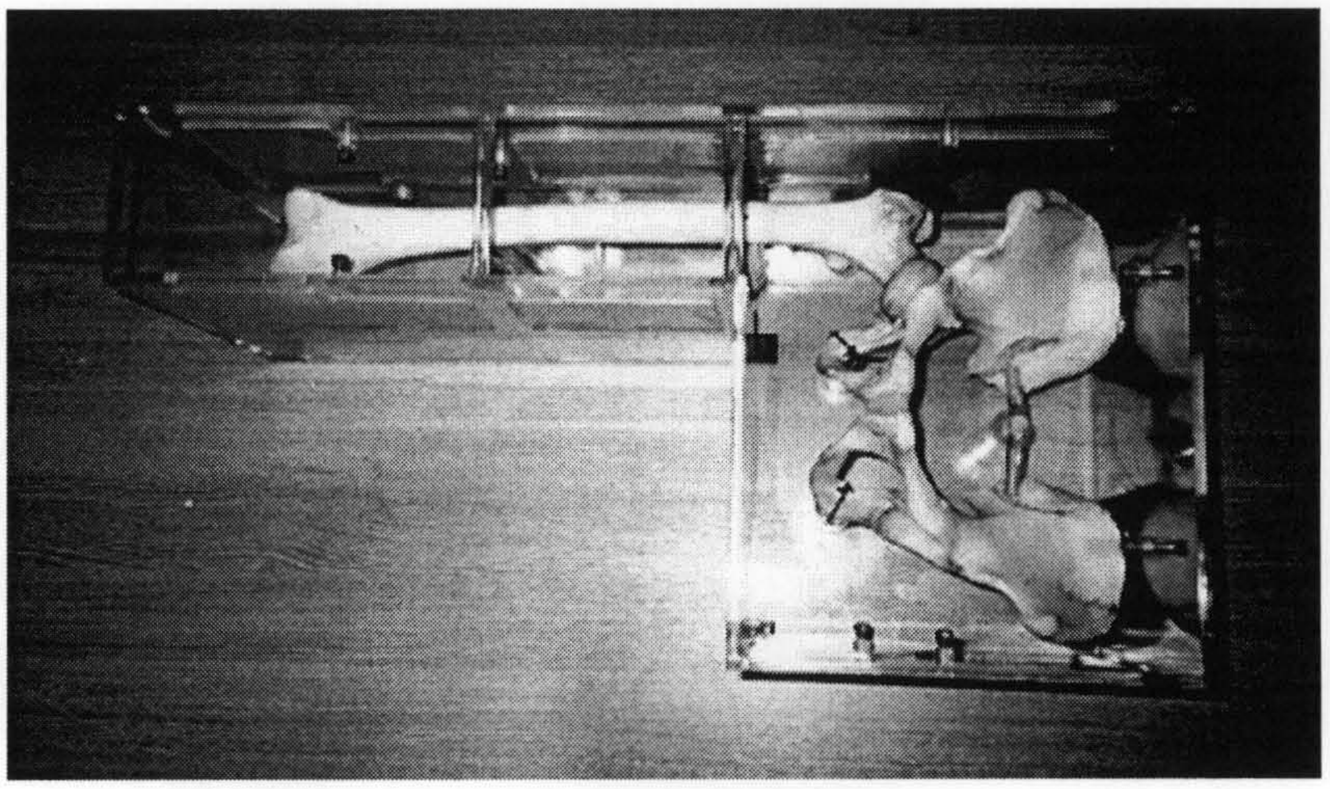

Figure 3.11: Dry femur and pelvis mounted rigidly in the perspex box.

3.3 Phantom Experimental Procedure

A dry femur phantom not included in the SSM, was scanned using a CT scanner (Philips Tomoscan SR7000) with a size of $320\times320\times177$ voxels and a spatial resolution of $1.094\times1.094\times3mm^3$. A rendering of the femur surface is shown in Figure 3.10.

A dry femur and a dry pelvis were rigidly mounted in a water-tight perspex box, shown in Figure 3.11. The box has acoustic windows on the side for collecting US data in all kinds of directions. The box was designed in such a way that fiducial markers could be attached to it for tracking by an optical localiser, Optotrak 3020 (Northern Digital, Toronto, Canada), for calculating the gold standard registration. The box is then filled with water.

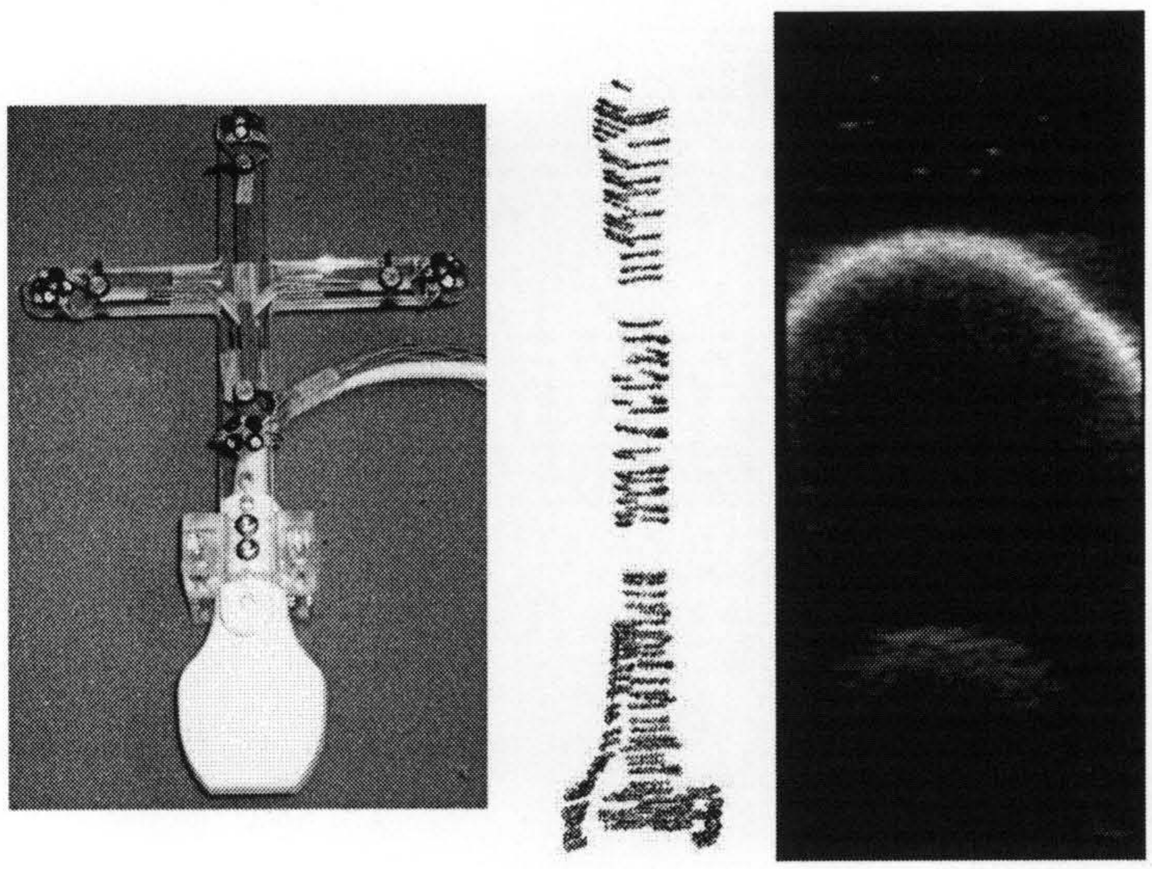

Figure 3.12: Tracked US probe (*left*), femur US surface points (*middle*) and femur example US sweep (*right*).

3.3.1 Ultrasound Data Collection

The aim of this experiment is to instantiate and register a SSM using information from 3DUS. In this study, a commercial US scanner (Siemens Sonoline Versa Pro) and a scan probe of 10.5MHz were used to acquire images. The US scan probe had a custom-built object with 20 infrared emitting diodes (IREDs) for tracking. This is shown in Figure 3.12. The RMS error in localising individual IREDs is of the order of 0.2mm (Edwards et al., 2000) hence this should enable accurate determination of the US probe's 3D position. The bone surface can be easily seen in the US images. Ultrasound images were acquired from most of the bone, from the distal femur around the condyles, along the femoral shaft, up to and around the lesser trochanter and some near the anterior surface of the greater trochanter. The US points were then extracted by manually picking points on each US image and a total of 1668 points were picked.

3.3.2 Ultrasound Instantiation and ICP

Recall from Equation 2.1 (Section 2.1, Page 48):

$$\mathbf{x} = \bar{\mathbf{x}} + \sum_{i=1}^{m} \mu_i \phi_i$$

where $\mathbf{x}$ is a shape to be approximated, $\bar{\mathbf{x}}$ is the mean shape, and μ_i is a vector of weights for the first m eigenvectors, ϕ_i, to be used in this approximation.

An instance of the model, described by a few parameters (μ_i in the above equation), provides a triangulated surface. The aim is to generate such a surface, which matches as closely as possible

to points picked from a number of freehand 3D US images. US-derived bone surface points were registered to the SSM surface using the ICP algorithm (Besl and McKay, 1992) described in Section 2.5.2.2 to find the parameters that define an instantiated surface from the SSM that will give the lowest RMS residual between them.

3.3.3 Matching Ultrasound Points with Instantiated Surface

As a preliminary study to investigate the shape of the cost function, an implementation of the StochastICP method (Penney et al., 2001) described in Section 2.5.2.2 (Page 38) was utilised. This implementation was found to be more robust in the presence of some local minima, and its performance is more precise than standard ICP. This is an advantage when doing manual optimisation in this study.

The mean of the search space was used as the starting shape, this is depicted by setting all weights on the modes to 0. This mean shape instance was generated and registered against the US surface points using StochastICP, the final RMS residual error was then noted down. The first (principal) mode weight was then changed manually while other modes' weights were kept constant, and another instance generated to match again. The whole process was repeated over the range where the weights of the first mode were varied between -0.46 and +1.71SD, and the RMS residual values are plotted in Figure 3.13.

There was 1 global minimum when the weight of the first mode was set to be +1.14SD with RMS residual = 2.00mm; there was also 1 local minimum at weight value 0.31SD with RMS residual = 2.03mm, the RMS residual values are quoted to 2 decimal places. Both the global minimum (RMS residual = 2.00mm) and local minimum (RMS residual = 2.03mm) were investigated further. The weight of the first mode was then set to be either one of the two corresponding weight values. Going down both paths, the weight of the second mode was varied while all other modes' weights were kept constant. This is repeated for the third, forth and fifth modes accordingly in a sequential way. The weight values are all plotted on graphs to show where the minima are for each mode being minimised. The plots for the weight of the second mode, for either of the first mode weight values, are shown in Figures 3.14 and 3.15. Unlike the first mode, just one minimum exists for the weights of each mode. The subsequent plots for other modes were similar to these plots with one minimum each, and will not be shown here.

After all the RMS residuals were minimised using the method described above, the final instantiated surfaces were produced using the weights for each mode. Here are the final results:

Global minimum: RMS residual = 1.81mm, weights for the first to fifth mode values were

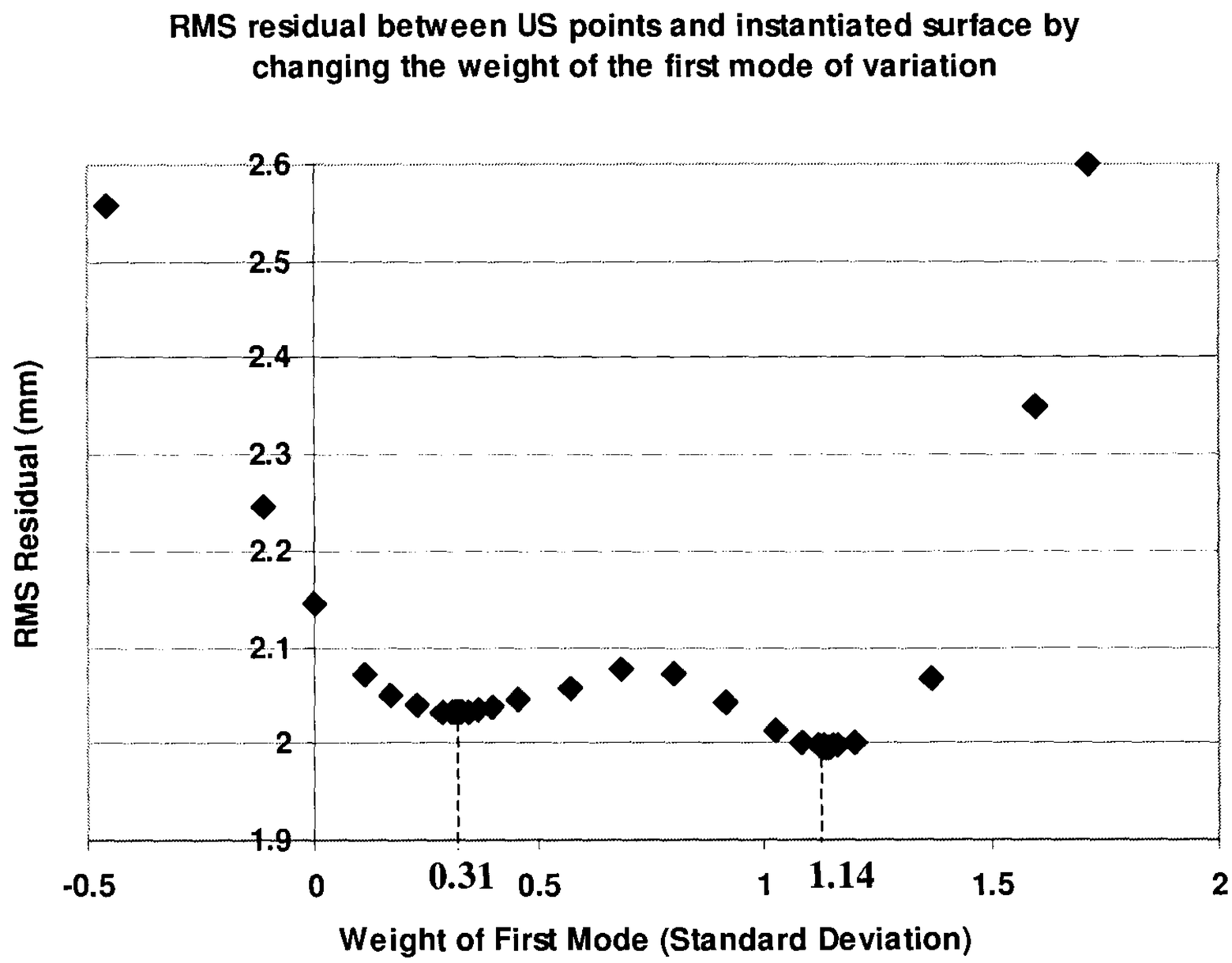

Figure 3.13: Matching the US surface points with instantiated surfaces by varying the weight of the first mode, using StochastICP

(in units of SD) 1.14, 0.55, -1.34, -0.16, -0.61.

Local minimum: RMS residual = 1.98mm, weights for the first to fifth mode values were (in units of SD) 0.31, 0.70, 0.15, -0.43, -0.68.

Figure 3.16 shows the two instantiated surfaces with the US-derived points overlaid. Both instances showed a good match against their corresponding US point sets. However, when these instantiated surfaces were registered with the gold standard CT-derived surface of the original phantom femur, there is a significant difference. See Figure 3.17 where it was shown that the instantiated surface resulting from the local minimum (using weight of first mode = 0.31SD) was obviously too long compared with the gold standard CT-derived surface.

On closer examination, the first mode of variation of the left femur surface SSM largely describes a change in the length of the femur. Therefore, when the weight of the first mode was changed, the US-derived points registered well onto the distal femur where the condyles provided some structure; meanwhile near the proximal femur, the US surface points should have been registered near the top of the femur and the anterior side of the greater trochanter, however, a local minimum was also found along this surface matching more to the lesser trochanter. For the rest of the modes, there was only one single minimum each for the cost function.

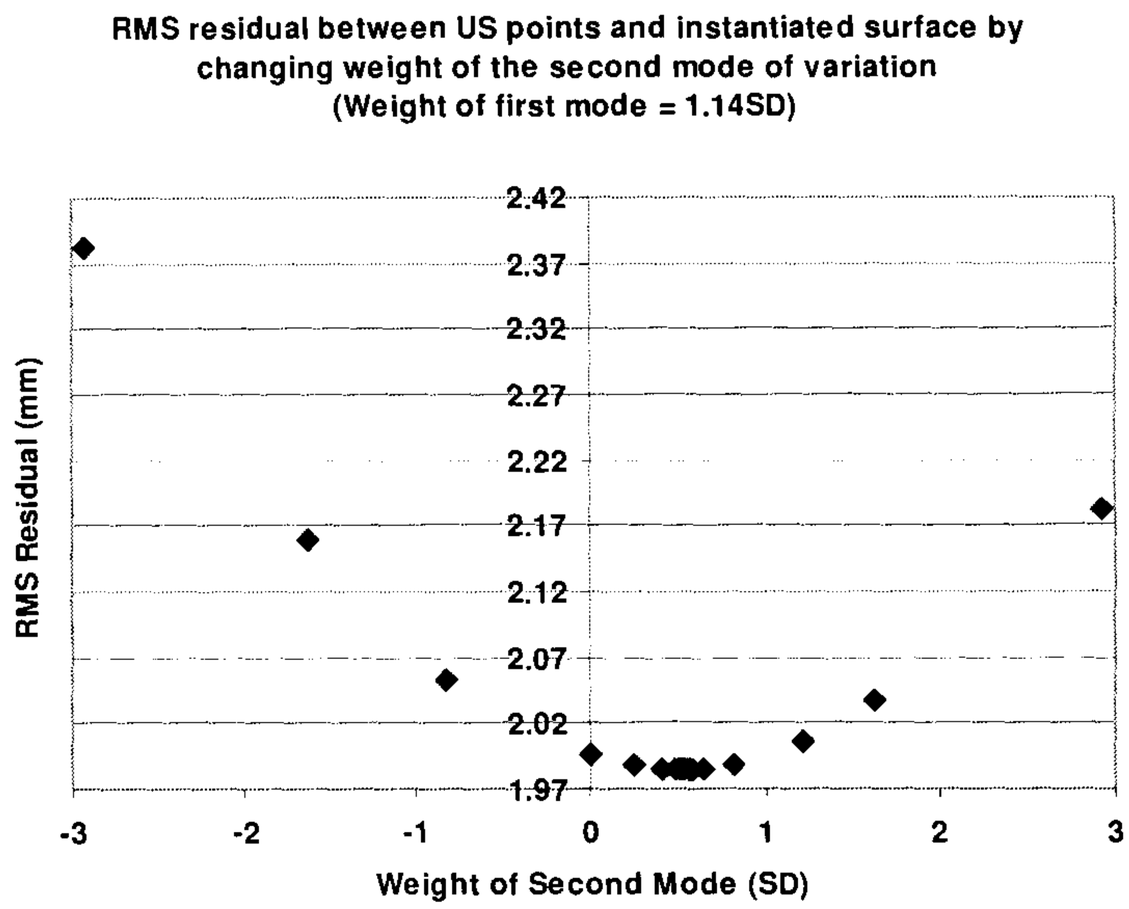

Figure 3.14: Matching the US surface points with instantiated surfaces by varying the weight of the second mode, using StochastICP, setting weight of first mode = +1.14SD and weights of other modes kept constant

This search is labour-intensive and very exhaustive. StochastICP normally requires more iterations to converge than standard ICP. The time taken for each StochastICP was between a few minutes to more than an hour. It adds up significantly when at least 15 searches were performed to find the minimum for each mode of variation and is very inefficient. This was a very simple and manual optimisation, aimed at exploring the optimisation space and getting an idea of how it looks like. This experiment has shown that shape and optimisation are very complex. It also showed that even though the RMS residual is low does not mean it was a good instantiation or registration.

There are some questions relating to choosing a suitable minimisation technique, these include whether the optimisation problem is multi-dimensional and whether the cost function can be differentiated efficiently. This is discussed in the next section.

3.3.4 Optimisation

The optimisation problem is as follows: the point-to-surface distance between the US-derived points and model-instantiated surface needs to be optimised over the significant modes of shape variation of the model. The RMS residual distance is measured and this needs to be minimised so as to provide the best fit. It is possible that the ICP algorithm can become trapped at a local minimum, an optimisation method is needed which is able to avoid or escape from each local

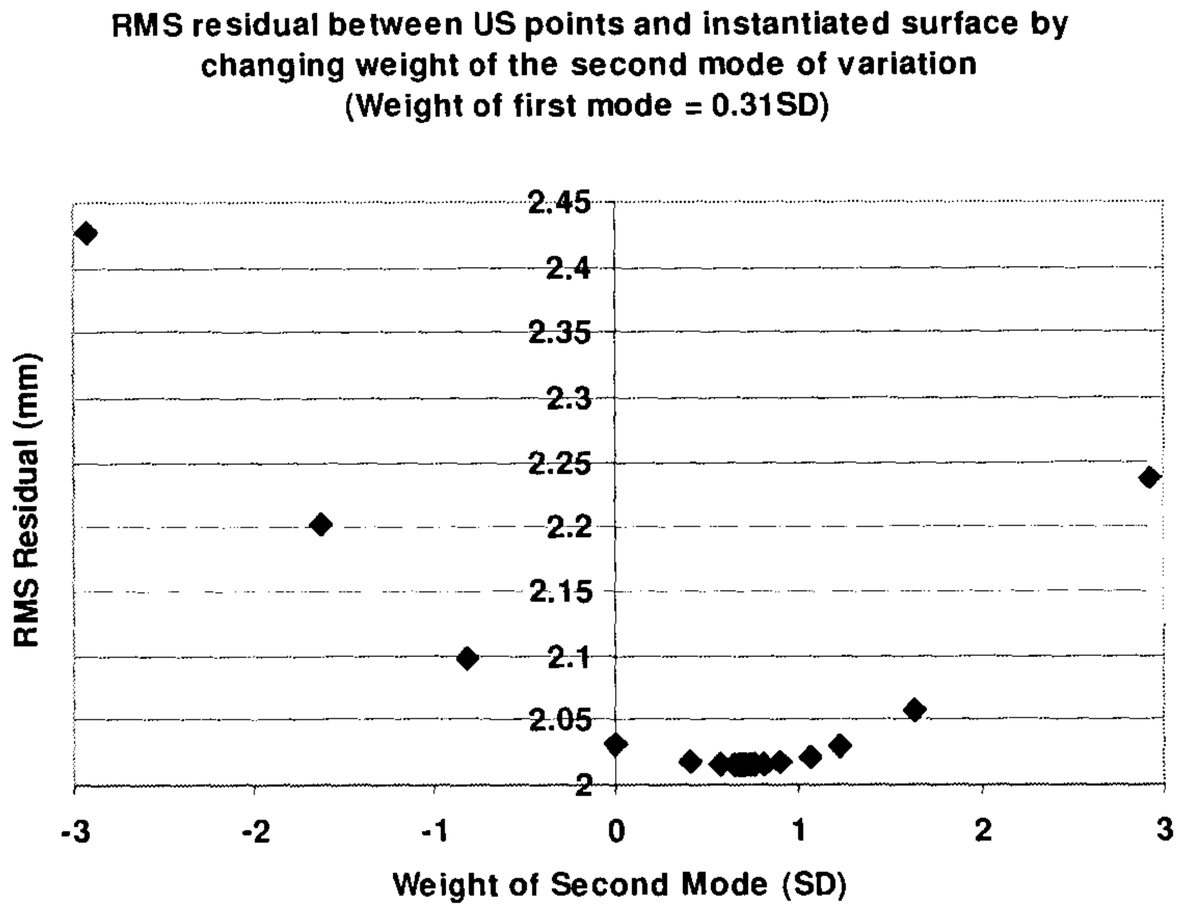

Figure 3.15: Matching the US surface points with instantiated surfaces by varying the weight of the second mode, using StochastICP, setting weight of first mode = +0.31SD and weights of other modes kept constant.

minimum. The parameters that require optimising are the first five modes of shape variation. A summary of this whole instantiation-registration process including the optimisation step is given in Figure 3.18.

I began by investigating an "off the shelf" optimisation package called the Opt++ library (Meza, 1994). The Opt++ library is a collection of nonlinear optimisation algorithms including parallel direct search (PDS), which was reviewed in the previous chapter (Dennis and Torczon, 1991, see Section 2.8.5 on Page 59). This method slowly converged to a minimum, and therefore was employed for rapid prototyping.

In subsequent experiments, the method StochastICP is no longer used and the standard ICP will be utilised as the algorithm for aligning the US-derived points with the instantiated image. This is mainly because the StochastICP method was very inefficient and time-consuming as mentioned earlier, and it was believed that an optimisation method "off the shelf" can run more efficiently while providing the same or higher level of accuracy and robustness.

3.3.4.1 Initial Parameters for Optimisation

The mean of the search space would make a logical starting shape. Taking a step further, for this application to the femur, it was shown earlier in Section 3.2.5 (Page 67) that the first mode of

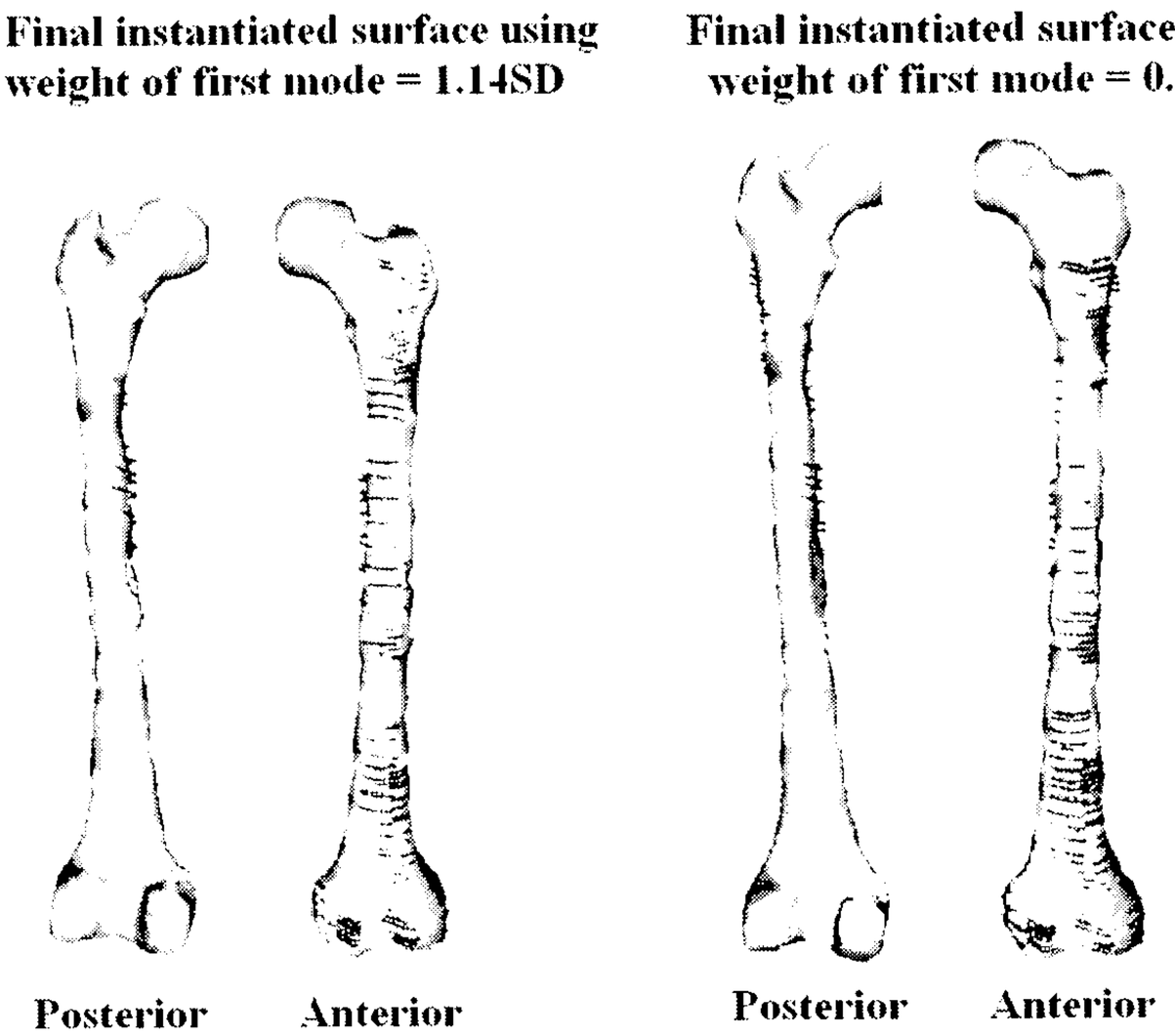

Figure 3.16: Final instantiated surfaces using StochastICP, (*white*) with US-derived points (*black*) overlaid using (*left*) weight of first mode = 1.14SD and (*right*) weight of first mode = 0.31SD,

while minimising the RMS residual distance by changing the weights of other modes one by one

shape variation of the femur surface SSM refers to largely the length of the femur. The experiments earlier using StochastICP have also shown that if the weight of this mode could be set to be near the correct value, it helps with the algorithm to locate the global minimum. The weight of this mode can therefore be set to roughly the length of the femur to be instantiated, this information can be collected during US image acquisition. The weights corresponding to the rest of the modes could be set to the mean (that is, the weights are set to 0) and the search space is restricted to $\pm$3SD [1] which accounts for most of the population included in the SSM.

3.3.5 Incorporating the Centre of Femoral Head

It must be noted that in this experiment, the US-derived points were not collected as far as the femoral neck or the hip joint itself. The addition of the centre of the femoral head provides some information in the region around the femoral head. Therefore, as a possible further constraint, the centre of the rotation of the femoral head was added as an extra point to the template by defining it from the CT image. To check whether this point has been defined properly, the template was propagated to each of the individuals using the surface transformations obtained earlier, this point

[1] A more appropriate way of determining how many SDs to use is provided in Section 6.5 on Page 142

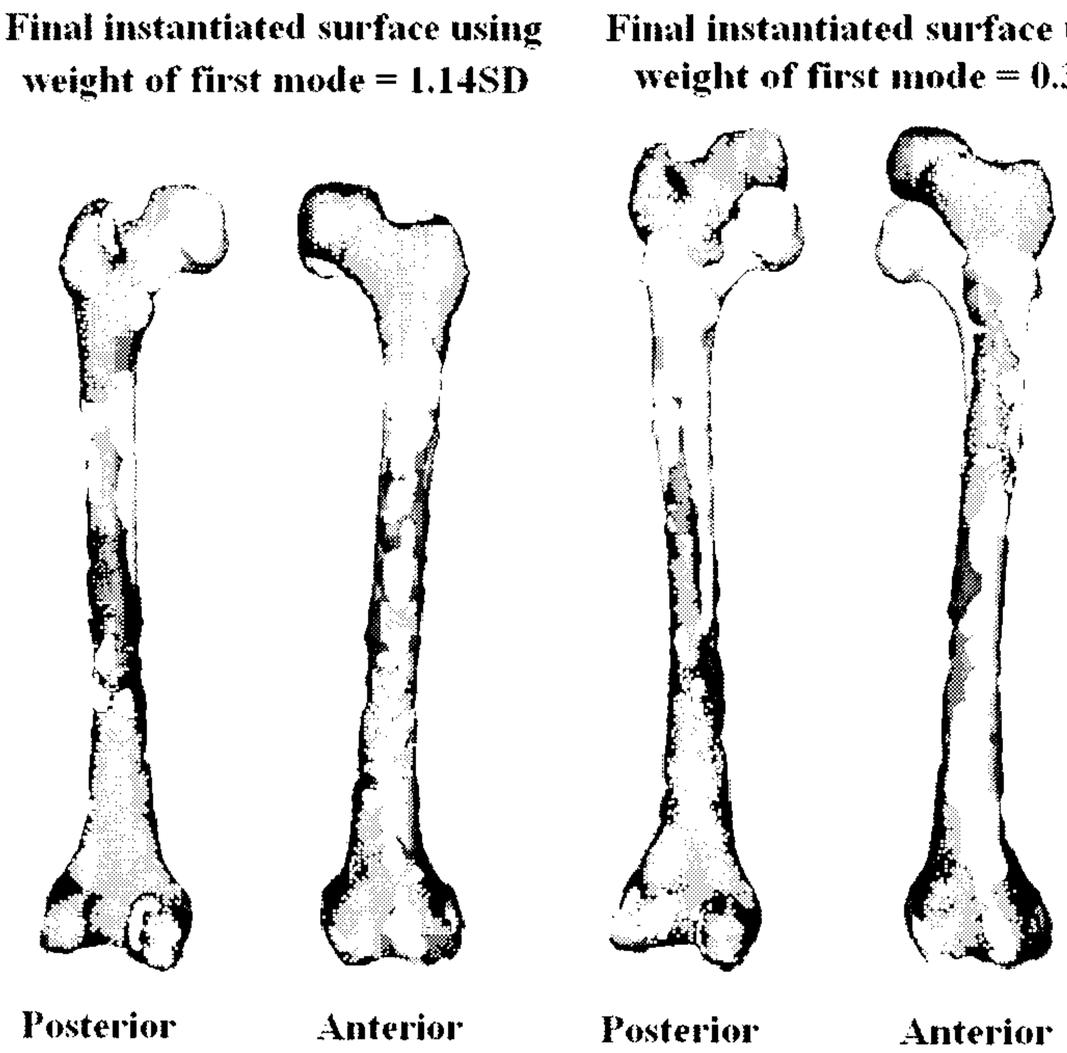

Figure 3.17: Final instantiated surfaces using StochastICP, (*grey*) with original CT-derived surface (*white*) overlaid using (*left*) weight of first mode = 1.14SD and (*right*) weight of first mode = 0.31SD, while minimising the RMS residual distance by changing the weights of other modes one by one

was checked visually that it has been well propagated in all datasets. Another model was produced on the left femur with this extra point at the centre of the femoral head as well as the surface points. The models look visually the same as the ones shown earlier. Later on, the ICP was run using this point as the centre of rotation. This means in the PBR step, replace the centroid of the points in each space by the centre of the femoral head, and the rigid registration problem has been reduced from 6DOFs to 3DOFs with only 3 rotations.

In this experiment, because there was no tracking device on the femur, this point was defined manually for 4 times and the average of these 4 points was taken. This was also visually checked that it has been well defined and then put to use in the instantiation. In practice, this point could be obtained intraoperatively by pivoting the femur around the hip joint, as is done in some commercial image-guided surgery systems on the market. The use of this point is discussed more in Sections 4.5.1 (Page 105) and 6.6.1.1 (Page 152).

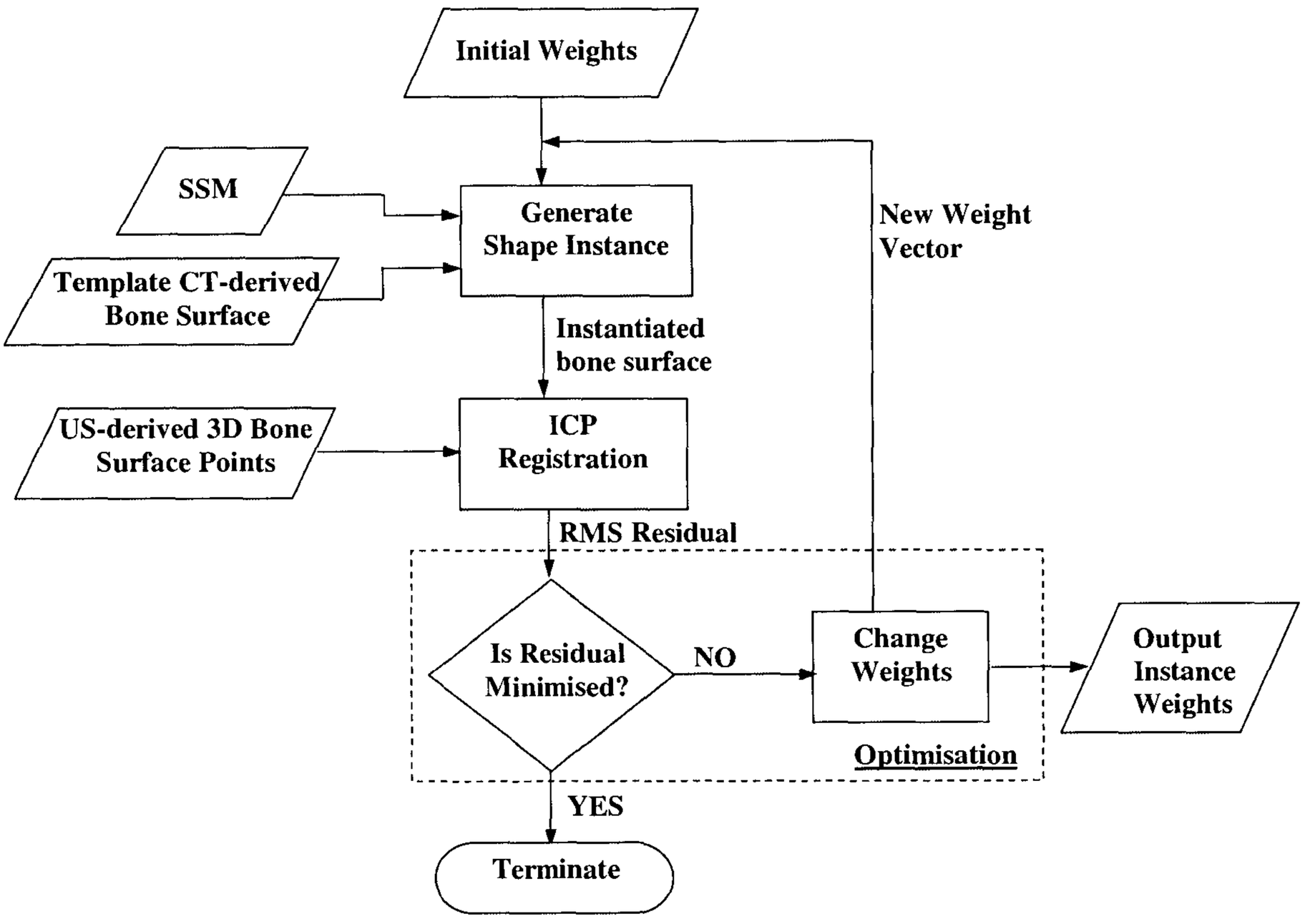

Figure 3.18: The instantiation-registration process.

3.3.6 Robustness Experiments

Multiple starting positions were used at the start of the whole matching process. An initial starting position was produced manually. Different starting positions were then created by adding random noise of a standard deviation of 10° and 10mm to the initial position. The starting shape, along with 3 examples of the US starting positions, are shown in Figure 3.19.

3.4 Instantiation Results

This section presents the results from instantiating the SSMs by the optimisation method PDS, using US only or US with the centre of the femoral head as the pivoting point, and the bone surface from the CT scan was used as the ground-truth shape model. The results are shown graphically as example contours of the overlaid surfaces in Figures 3.20 and 3.21. The numerical results for both methods are given side-by-side for comparison in Tables 3.3 and 3.4, with a brief discussion on a failed instantiation.

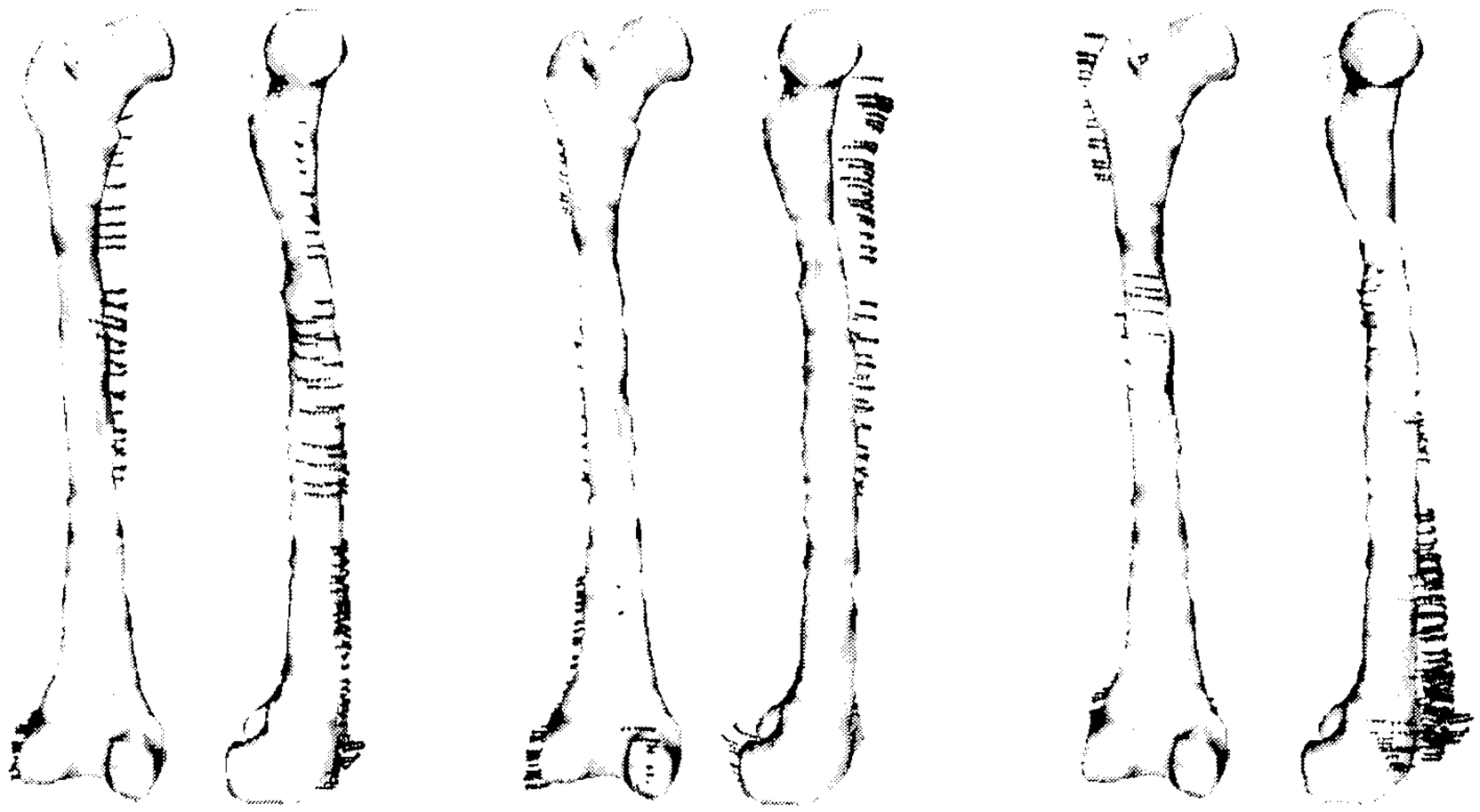

Figure 3.19: Example starting positions of the ICP process with the US-derived surface points (*black*) overlaid on the starting shape (*white*).

3.4.1 Error Measures

Numerical results are given in Tables 3.3 and 3.4 calculated in two main different ways. The table marked "ICP" measures how accurate are the shapes of the instantiated surfaces, while that of the tables marked "GS" measures how accurate are the shapes and positions of the instantiated surfaces. These are explained further below.

3.4.1.1 Global and Regional Measures

The column "US-Model" measures the RMS residual distance calculated between the instantiated SSM and the US-derived bone surface points. In the last two columns of each table, the column marked "CT-Model (global)" measures the RMS distance across the entire surface of the bone, while that marked "CT-Model (regional)" measures the RMS distance around the area of clinical relevance. For the purpose of hip replacement surgery, the area of interest would be around the femoral head, femoral neck, and the greater and lesser trochanters for the femur.

3.4.1.2 Residual Error

All measures in Table 3.3 are a result directly from ICP and no gold standard transformation was used in this measure. In the column "US-Model", the RMS residual was calculated between the instantiated SSM and the US-derived bone surface points registered using the ICP algorithm. This

is a measure of how consistent the bone shape was with the original US data. For other columns in this ICP table, the ICP algorithm was used to register the instantiated model and CT-derived surface to provide a measure of the geometric accuracy of the instantiated shape.

3.4.1.3 Gold Standard

In Table 3.4, the residual distance error was calculated between the instantiated SSM and the CT-derived surface, using the gold standard transformation. The gold standard transformation was calculated from point-based registration of the fiducial markers attached to the box which was used to mount the femur. This measure indicates the combined accuracy of the geometry of the instantiated model and its registration in physical space.

3.4.2 Results: Ultrasound Instantiation

The phantom femur and the left femur SSM were used in the matching process. The optimisation was run with 20 starting positions. 14 of these returned a RMS residual distance of 1.7mm between the US-derived points and the instantiated model surface. There were two very close local minima, with RMS residuals differing by no more than 0.002mm. When comparing the two sets of weights for the modes of variation to instantiate the two surfaces, the biggest difference were in the weights of the third mode, which differed by less than 0.17SD and the instantiated surfaces looked the same visually. Six starting positions arrived at a higher RMS residual of 1.9mm. Upon visual inspection, it could be seen that these final positions were registered incorrectly to the instantiated surface, and this will be discussed in Section 3.4.4. The distance between all points were then calculated on the instantiated surface and the phantom CT-derived surface, yielding an RMS distance of 4.5mm. Figure 3.20 shows the resulting instantiation with example contours. This shape is overlaid on the phantom CT-derived surface.

3.4.3 Results: Ultrasound with Centre of the Femoral Head

As mentioned earlier, another model was produced which included an extra point - the centre of the femoral head. It was noticed that two of the modes of variation in the SSM were the angle change of the femoral neck to shaft and a twist in the bone. The addition of the centre of the femoral head provides some information in this region and hence may help constrain these two modes.

The same phantom femur data was used, and the left femur SSM with the extra point was incorporated in the matching process. Again 14 out of 20 starting shapes gave a good RMS residual

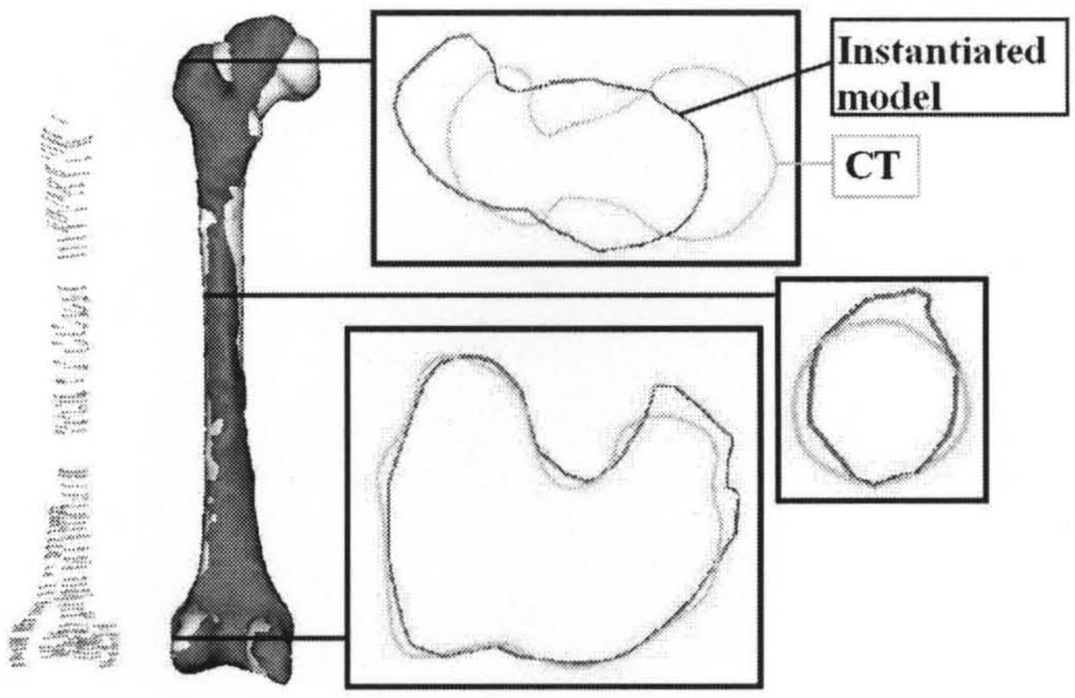

Figure 3.20: Visualisation of US only instantiation of the phantom femur produced using weights of mode values resulting from the optimised ICP process (RMS residual=1.7mm): Parts of the instantiation (*black*) matched to the phantom CT (*grey*), showing the contours in the femoral head, shaft and near the condyles. The part near the condyles and the femoral shaft were matched accurately while that in the femoral head showed large errors.

of 1.9mm with two very close local minima. The comparison of the instantiated surface and the phantom CT this time gave an RMS distance of 4.0mm. The results are shown in Figure 3.21. When looking at the contours of the bones, the area around the femoral head managed to register significantly better.

3.4.4 Failed Registrations

The final position for the failed registrations showed the instantiated image to be rotated too much from the phantom CT image. One result shows that the algorithm actually registered to the wrong side of the US-derived points of the femur. Figure 3.22 shows the final position for one of the failed registrations. This could be due to the random noise of 10° and 10mm SD being added to the initial position, which produced some starting positions which, when minimising the RMS residual error, were nearer to a local minima than the global minimum. In practice, the starting positions are not likely to be in the same order in all directions, as will be illustrated later. It will be shown in Section 6.3.4 (Page 129) that the rotation problem will be less prominent and affects the femur more or less in the z-direction.

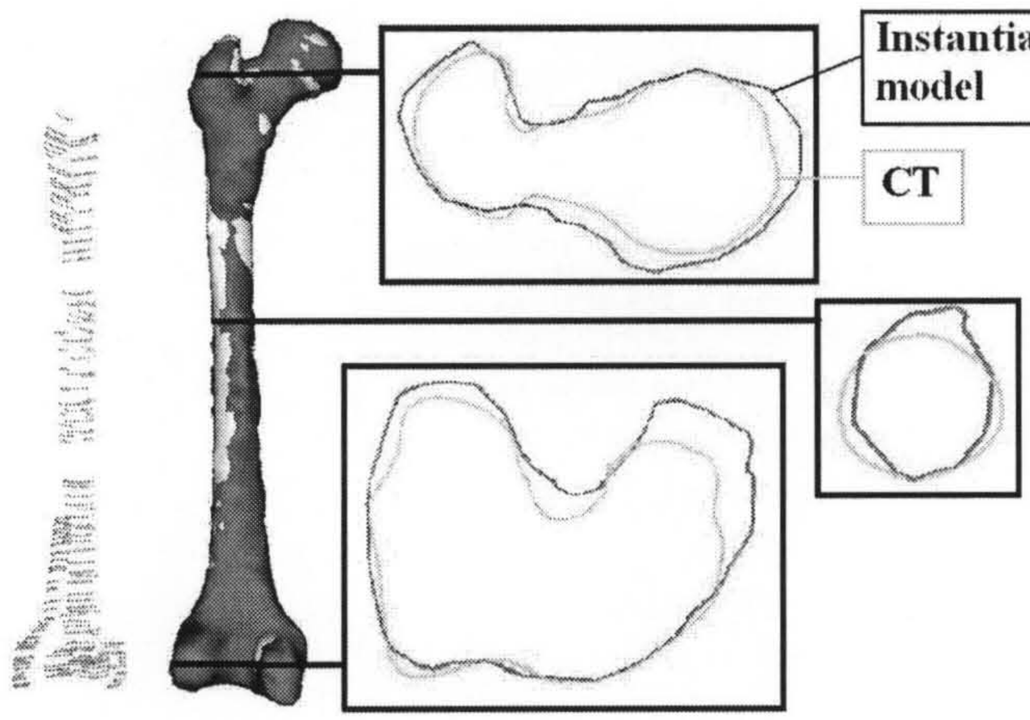

Figure 3.21: Visualisation of US with centre of femoral head instantiation of the phantom femur produced using weights of mode values resulting from the optimised ICP process (RMS residual=1.9mm): Parts of the instantiation (*black*) matched to the phantom CT (*grey*), showing the contours in the femoral head, shaft and near the condyles. Unlike that of the US only instantiations, the area around the condyles were not registered very accurately compared with the US only instantiation, but that the area around the femoral head registered better.

Table 3.3: Errors for instantiated phantom femur surface using surface SSM (shape) (mm) - ICP

Phantom	Error statistic	US-Model* residual	CT-Model (global)**	CT-Model (regional)***
Ultrasound Only	RMS	1.7	4.5	7.2
	Median	1.1	2.9	4.9
	95% CL	3.5	8.9	13.4
Ultrasound with centre of rotation	RMS	1.9	4.0	4.7
	Median	1.2	3.1	3.7
	95% CL	3.8	7.3	8.6

95% CL = 95% Confidence Level

*Distance between US-derived bone surface points and the instantiated SSM surface.

**Distance between the vertices of the surface mesh, which describes the instantiated SSM surface, and the CT-derived bone surface calculated by aligning the datasets using the ICP algorithm.

***As for that in **, but with the measure restricted to regions of clinical interest.

Table 3.4: Errors for instantiated phantom femur surface using surface SSM (shape and final position) (mm) - GS

Phantom	Error statistic	CT-Model (global)*	CT-Model(regional)**
Ultrasound Only	RMS	5.8	8.9
	Median	3.2	6.6
	95% CL	12.4	14.9
Ultrasound with centre of rotation	RMS	4.8	4.8
	Median	3.4	3.6
	95% CL	9.1	8.5

95% CL = 95% Confidence Level

*Distance between the vertices of the surface mesh, which describes the instantiated SSM surface, and the CT-derived bone surface calculated after transforming the CT-derived surface to physical space using the Gold Standard, fiducial-based registration transformation.

**As for that in *, but with the measure restricted to regions of clinical interest.

Figure 3.22: A failed registration: instantiation (*white*) overlaid with phantom's original CT scan (*grey*)

3.5 Discussion

The RMS distance is an average value of how close the points are to the surface. When only using US-derived points, the residual error between the US-derived points with the instantiated surface is lower than that of using the option with the centre of rotation of the femoral head. When the instantiated surface was registered to the gold standard phantom CT-derived surface, the RMS distance was 4.5mm and 4.0mm for US-only and US with the centre of the femoral head as pivoting point respectively. When only the area around the femoral head was registered, the RMS distance became 7.2mm and 4.7mm respectively. The RMS distance obtained using the gold standard registration, which shows how well the shape registered with the gold standard as well as the final position of the instantiation, it was interesting to see that results from using the centre of the femoral head as the pivoting point performed better both along the whole femur and around the femoral head area.

For the US-only instantiations, even though the final RMS residual was lower, the algorithm did not match the femoral head area well enough because there was not enough information there. The area around the condyles and shaft registered quite accurately. When using the centre of the femoral head as the pivoting point, the area around the femoral head was registered better, at the same time the area around the condyles registered slightly worse than the US only option, but the regional CT-Model was significantly better than that using US only.

It is evident that the method which incorporates the centre of the femoral head as the pivoting point performed significantly better. The original US-derived points concentrated around the shaft and condyles, therefore it is not surprising that the algorithm registered well in these areas. In contrast, the area around the femoral neck and head was not registered properly. Without more information in this region it would be difficult to produce a better result. In the time of this experiment, it was believed that US data could only be taken from regions up to and around the anterior surface of the greater trochanter, therefore US data was only collected up to this area (see Section 3.3.1). However, later in the cadaver experiments in Chapter 6, this will be investigated further and discovered that more data can actually be collected in the clinical setting.

3.6 Chapter summary

This chapter presented the left and right femur surface SSM and an initial study on the use of US to instantiate and register a SSM of a femur in a box filled with water.

An implementation of the StochastICP algorithm was used for exploring the shape space of

the cost function and returned some encouraging results; the parallel direct search was utilised to perform multidimensional optimisation of the instantiation parameters.

The left femur model instantiation results have shown an RMS distance of under 2mm between US-derived points and the instantiated surface, where the RMS distance error between the instantiated surface and the gold standard CT-derived surface are good in the region of accessible US scanning and the RMS distance error between the instantiated surface and the gold standard CT-derived surface occurred most in the femoral head area. There is not much information from US in this region and it is therefore not surprising that this led to an inaccurate instantiation result.

A proposed solution to this problem is to acquire an extra point at the centre of the femoral head. Another model was produced which included this point and the ICP algorithm used this as the centre of rotation. This improved the accuracy of the instantiation, especially in the region that is inaccessible to percutaneous US.

There are certain limitations on this study, including the low-resolution blocky appearance of the surfaces, and the use of a dry femur with soft tissue, instead of real human data for matching purposes. These limitations are addressed in the next chapter.

Chapter 4

Volume Statistical Shape Model for the Femur

4.1 Introduction

In chapter 3, a method was described showing how a 3D surface model of the left femur can be instantiated from tracked ultrasound (US). This chapter describes important modifications to the method for generating the shape model. Instead of building the statistical shape model (SSM) directly from the surface points of propagated femurs in the dataset, the SSM was built on the B-spline node points from non-rigid registration of CT images to a single target CT image. Only the target CT image, the template, was segmented in the whole process. This model was used to instantiate the model by iteratively minimising the root mean square (RMS) distance between the model surface and the ultrasound-derived bone surface points.

This method used 3D vector fields, calculated by non-rigid registration of each training CT image onto a template image, in order to estimate correspondence between all the images in the database. This approach has the advantage that a complete reconstruction of a synthetic 3D volume can be achieved, including estimates of density changes and the internal structure of bony anatomy that is represented in the CT scans of the training data, although the instantiation of a complete 3D volume in this way is not considered in this thesis. The chapter ends with an evaluation of the optimisation strategy used and a closer look at devising a new optimisation method which could improve the performance of the instantiation algorithm.

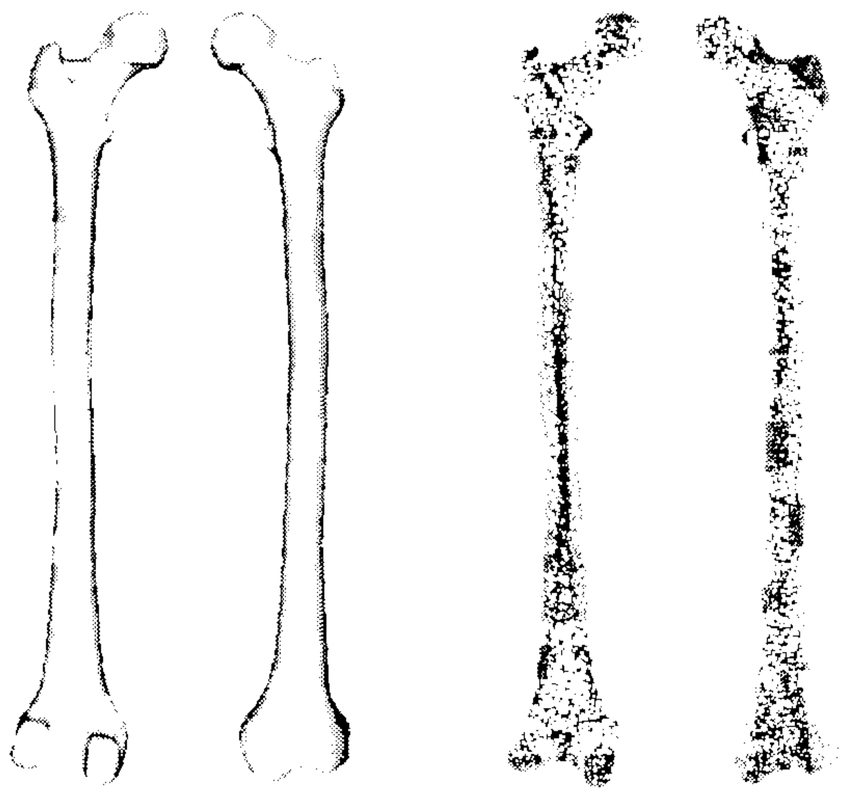

Figure 4.1: Femur template surface with 5977 points, shown on the left with anterior and posterior views; and the template with vertices, shown on the right with anterior and posterior views.

4.2 Construction of the Volume Statistical Shape Model

In this chapter, the SSM is being built on the B-spline node points from non-rigid registration. However, for the purpose of instantiating surfaces from the model, a template surface is required. The template surface was also produced for visualising the modes of variation of the model. The template femur was segmented as described in Section 3.2.1 (Page 62) and the non-rigid registration was carried out as in Section 3.2.2 (Page 64). The method for generating the surface of the template was the same as Section 3.2.3 (Page 65), except that the template surface was smoothed and subsampled to provide a femur surface with 5977 points. This template surface is of much higher resolution than the surface-based model of 832 points. The template surface and mesh (with vertices) are shown in Figure 4.1. Note that this template surface was not propagated to each individual in the database.

4.2.1 Building the Model

Figure 4.2 shows a summary of the method used to produce the model. Using the results from the non-rigid registrations described in Figure 4.2 ("NNR 1"... "NNR N-1"), which registered training CT datasets to one template image ("Template CT"). An SSM was built on the node points of the approximating B-splines used to define the free-form deformation (FFD). The method of producing this kind of SSM is very similar to the one which was first proposed by Rueckert et al. (2001) who introduced the idea of the statistical deformable model (SDM) applied to magnetic resonance (MR) images of the brain, described in Section 2.6.6 on page 51. However, unlike the

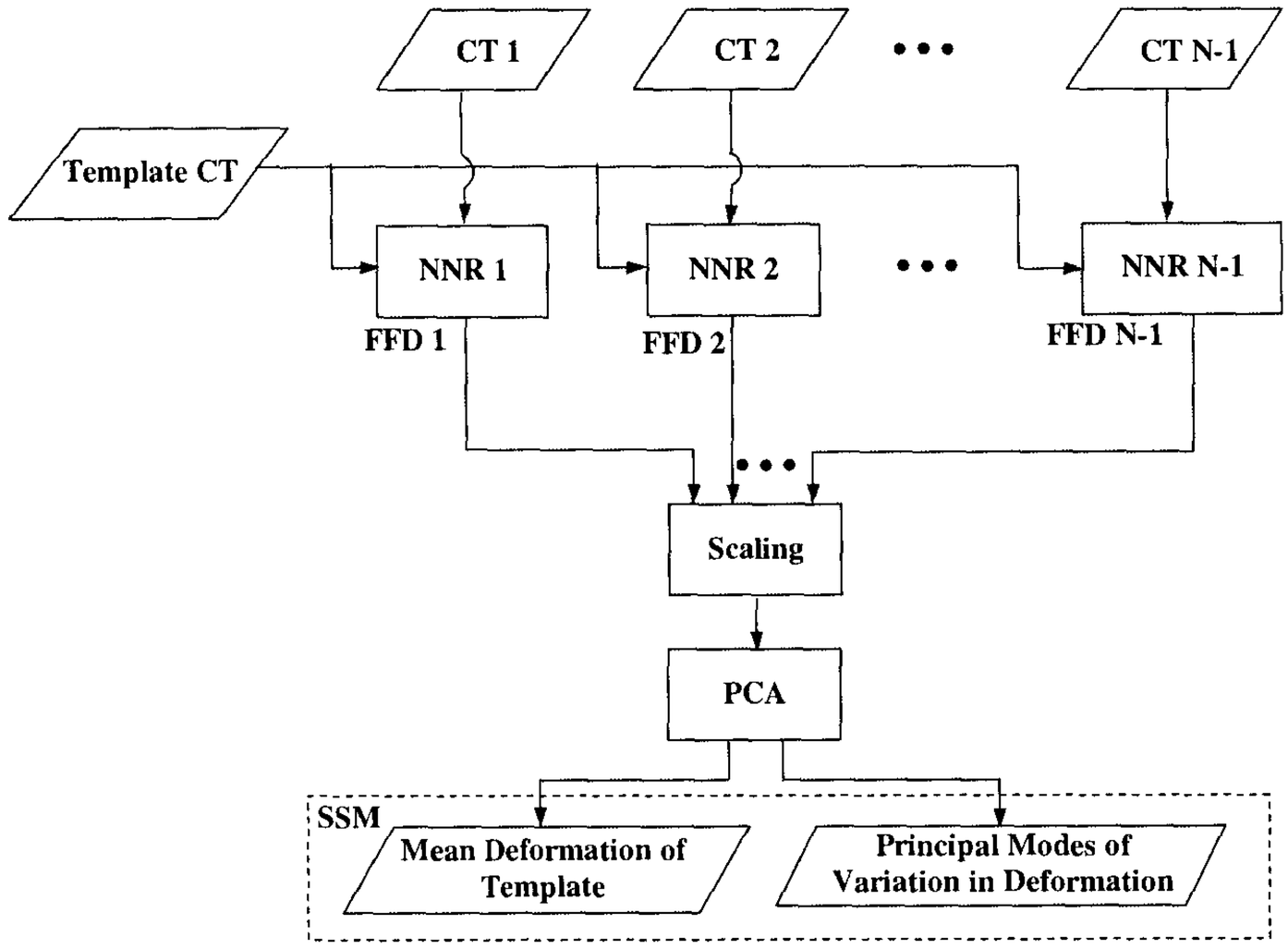

Figure 4.2: Constructing the volume SSM on the B-spline node points. "NNR1"... "NNR N-1" stands for the non-rigid registrations between each individual and the template CT; "FFD" stands free-form deformations. The mean deformation of the template and principal modes of variation in the deformation fields make up the SSM.

SDM which randomly chose a template image, the template chosen here was selected from the CT database as being of average shape and size by visual inspection.

In addition, the approach applied here is similar to the SDM, but to bones, which required more care in getting the scaling of the model correct. Unlike the brain which is enclosed by the skull, the bone shapes relevant to this thesis, namely femur and pelvis, can vary greatly across a population, especially in terms of size (scaling). Section 3.2.2 on Page 64 introduced a non-rigid registration algorithm proposed by Rueckert et al. (1999, see Section 2.5.4.2 on Page 41), where for any point $\mathbf{x} = (x, y, z)$ in the target CT image, the combined transformation $\mathbf{T}$

$$\mathbf{T}(\mathbf{x}) = \mathbf{T}_{\mathbf{global}}(\mathbf{x}) + \mathbf{T}_{\mathbf{local}}(\mathbf{x})$$

Global motion $\mathbf{T}_{\mathbf{global}}(\mathbf{x})$ is modelled by affine transformation which has 12 DOF. Local motion $\mathbf{T}_{\mathbf{local}}(\mathbf{x})$ is modelled by FFD based on approximating B-splines defined by a 3D lattice of node points. In the B-spline mesh of node points, the femur and pelvis surfaces occupy the middle of the image space and rarely come in contact with the boundaries of the mesh space. Four points are defined at the corners of the node points mesh. This is illustrated in Figure 4.3. The box can be thought of as the boundary of the mesh of B-spline node points.

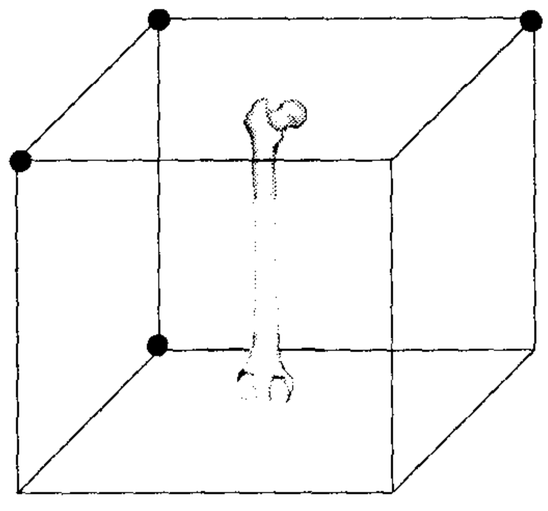

Figure 4.3: Figure illustrating the definition of 4 points *(black dots)* at the corners of the node points mesh (*the box*). Typically a femur or pelvis occupies the space in the middle and rarely near the boundaries.

One of these 4 points is defined as the origin. In the example shown in the figure, the top left hand corner point is defined as the origin. The other 3 points are used to define the scaling in the x, y and z directions. After an individual image is non-rigidly registered to the template image, these 3 points would not be deformed in the local deformation because they are non-moving during the FFD transformation. However, they could be transformed by the global transformation. Figure 4.4 shows how the position of these 3 points might have changed after applying scaling from the global transformation.

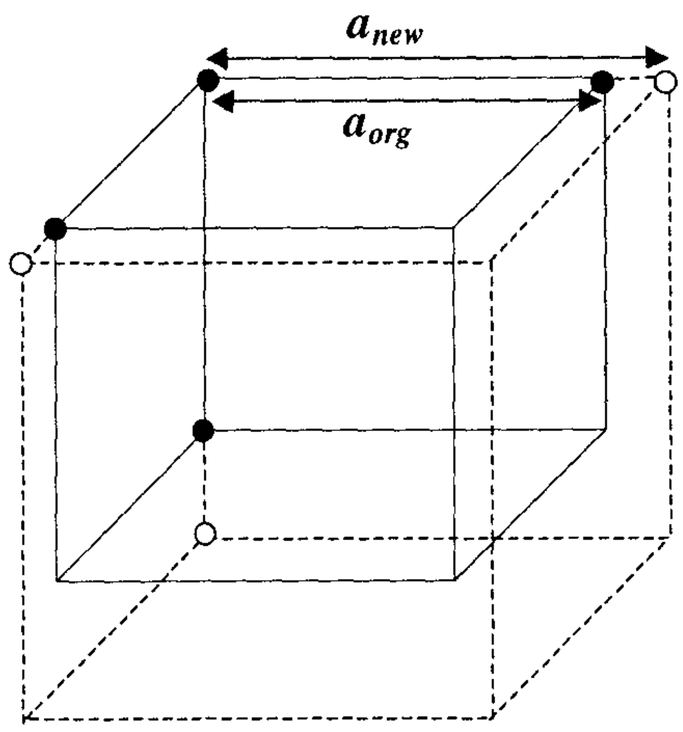

Figure 4.4: Figure illustrating positions of the 3 points at the corners of the node points mesh after applying scaling, the new positions are shown as white circles.

The scaling in one direction can be calculated as follows: Let a_{org} be the original distance of one of the corners to the origin and a_{new} be the distance between the new position and the origin. Scaling can be calculated by dividing the new distance with the original distance, that is, $\frac{a_{new}}{a_{org}}$. This calculation is performed for each of the x, y and z directions.

These 4 corner points were added as the last 4 points in the list of node points that were deformed for each transformation. Adding these 4 points is a way of describing the scaling for each individual's global transformation. The femur volume model was built on this list of B-spline node points used to define the FFD, including these 4 points. Following PCA, the first five modes of variation were used in the model (again as a compromise between computational time and population coverage), with individual variation within each mode allowed up to three standard deviations (SDs)[1].

When an instance is created, the instance contains the deformation of the template, which will give the x, y and z positions of all node points, as well as the positions of these 4 corner points. These 4 corner points can then be used in order to calculate the scaling in the global transformation.

The number of B-spline node points involved for this femur model was 180 with the addition of these 4 points. The total number of points used for the femur volume SSM was 184. This is a significantly smaller number than that of the femur surface SSM. Building this volume SSM has the added advantage that since fewer points are involved, the time to compute the model is greatly reduced because less time is required to invert the covariance matrix (See Section 2.5.2.1 on Page 36).

4.2.2 Results: The Femur Volume Model

The femur volume model was built on the B-spline node points used to define the FFD and 4 corner points to calculate scaling. The model consists of how these node points and the scaling deform the template. To represent the model visually, the template was transformed using the mean deformation and the principal modes of variation in the deformation fields. These are shown in Figure 4.5 with the first and second modes for the left femur volume model when applying plus or minus three standard deviations to the mean shape. This model includes 8 male and 8 female datasets (16 datasets in total). Figure 4.5 has shown representations of the volume model with significantly smoother surfaces than the surface SSMs because the template surface used here contains much more points than the template used in the surface SSM.

There are some significant shape features. As with the left femur surface model described in the previous chapter, the first mode can be seen to correspond to a change in the femur size and length. Other significant modes of variation include bending and twisting of the bone, change of the femoral head angle and change of trochanter and condyle sizes.

[1] A more appropriate way of determining how many SDs to use is provided in Section 6.5 on Page 142

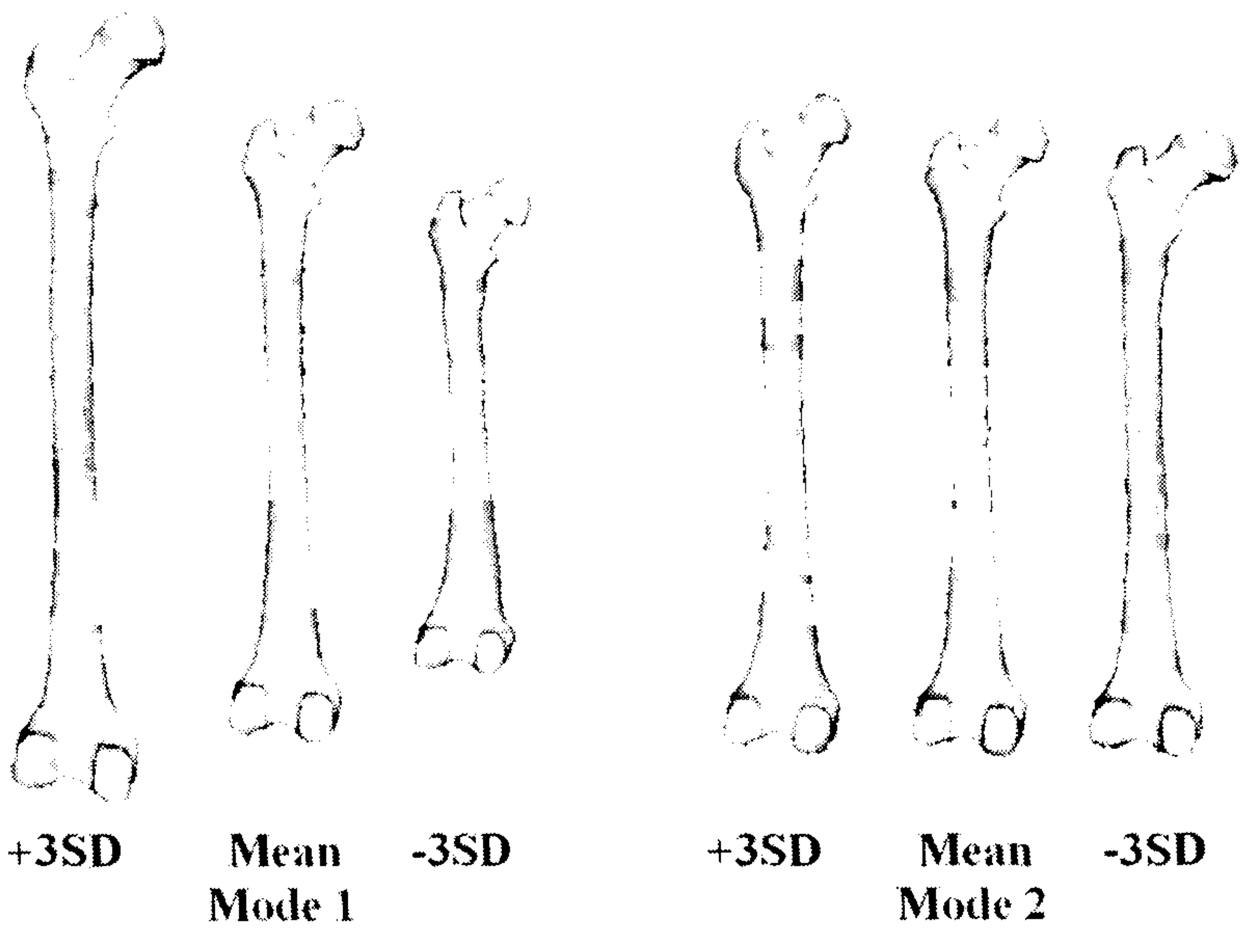

Figure 4.5: Representation of the left femur volume SSM. These were produced by deforming the template surface using the mean deformation and the principal and second modes of variation in the deformation fields, with three standard deviations.

It was decided that shape variations in the left and right femurs are very similar and therefore the current model combines the use of both left and right femurs by reflecting the CT scans of the right femur, to form an overall model of the left femur.

Using 16 femurs for the input to the SSM, all the modes of variation for the left femur volume SSM are shown in Table 4.1. This information is plotted in Figures 4.6 and 4.7. The first 5 modes of variation explain at least 92% of the variation. The principal mode explains over 80% of the total variance.

4.3 Instantiation Experiment using Volume SSM

The phantom used and the experimental procedure are the same as the those described in the previous chapter, Section 3.3 starting at Page 72. The following sections describe the instantiation results.

4.3.1 Method

The phantom femur immersed in a water bath was scanned using freehand 3DUS. US points were extracted from US images obtained from scanning the femur, these bone surface points and the left femur volume SSM were used in the matching process. ICP was used to minimise the resulting

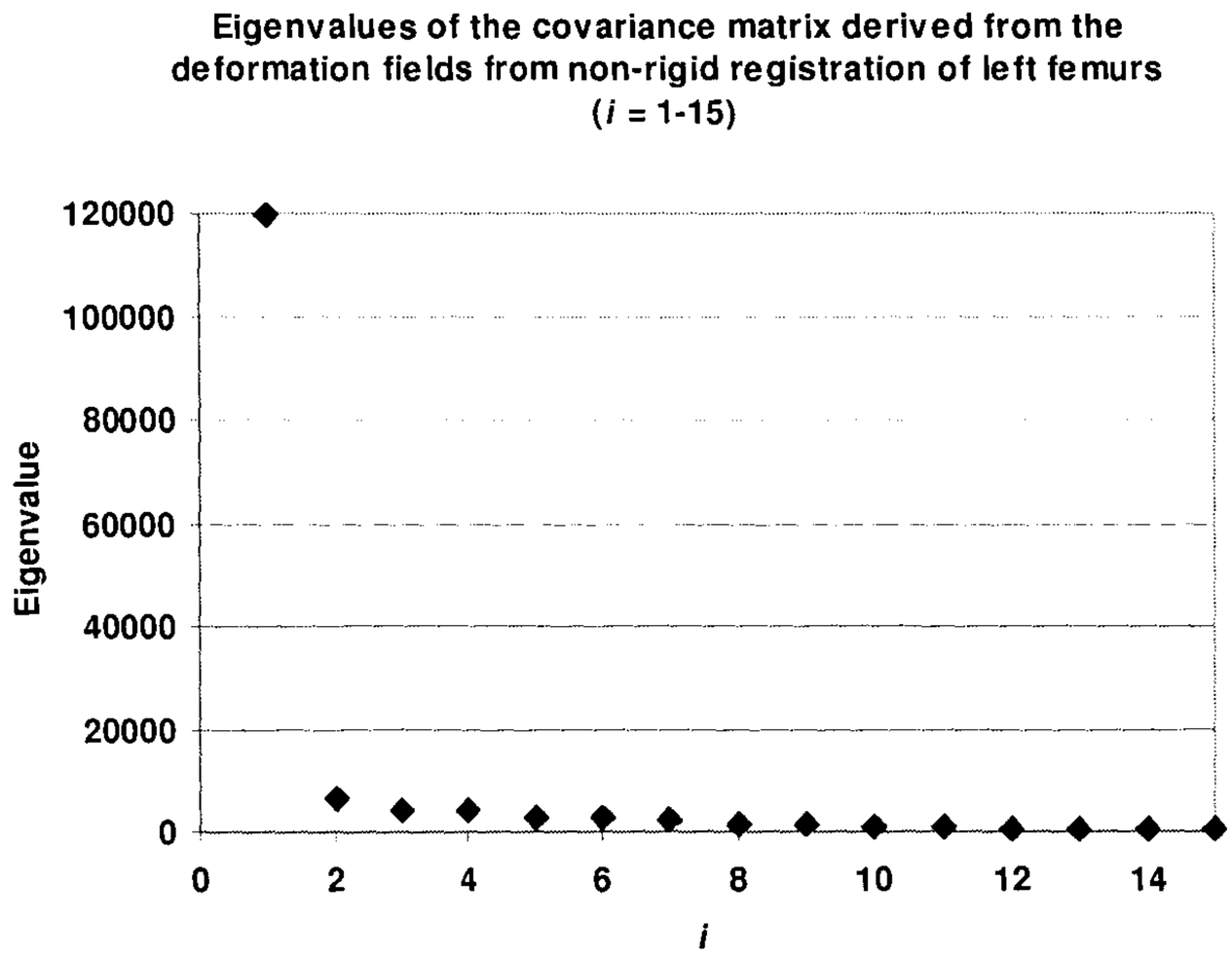

Figure 4.6: Eigenvalues λ_i of the covariance matrix derived from the deformation fields from non-rigid registration of left femurs (i=1-15)

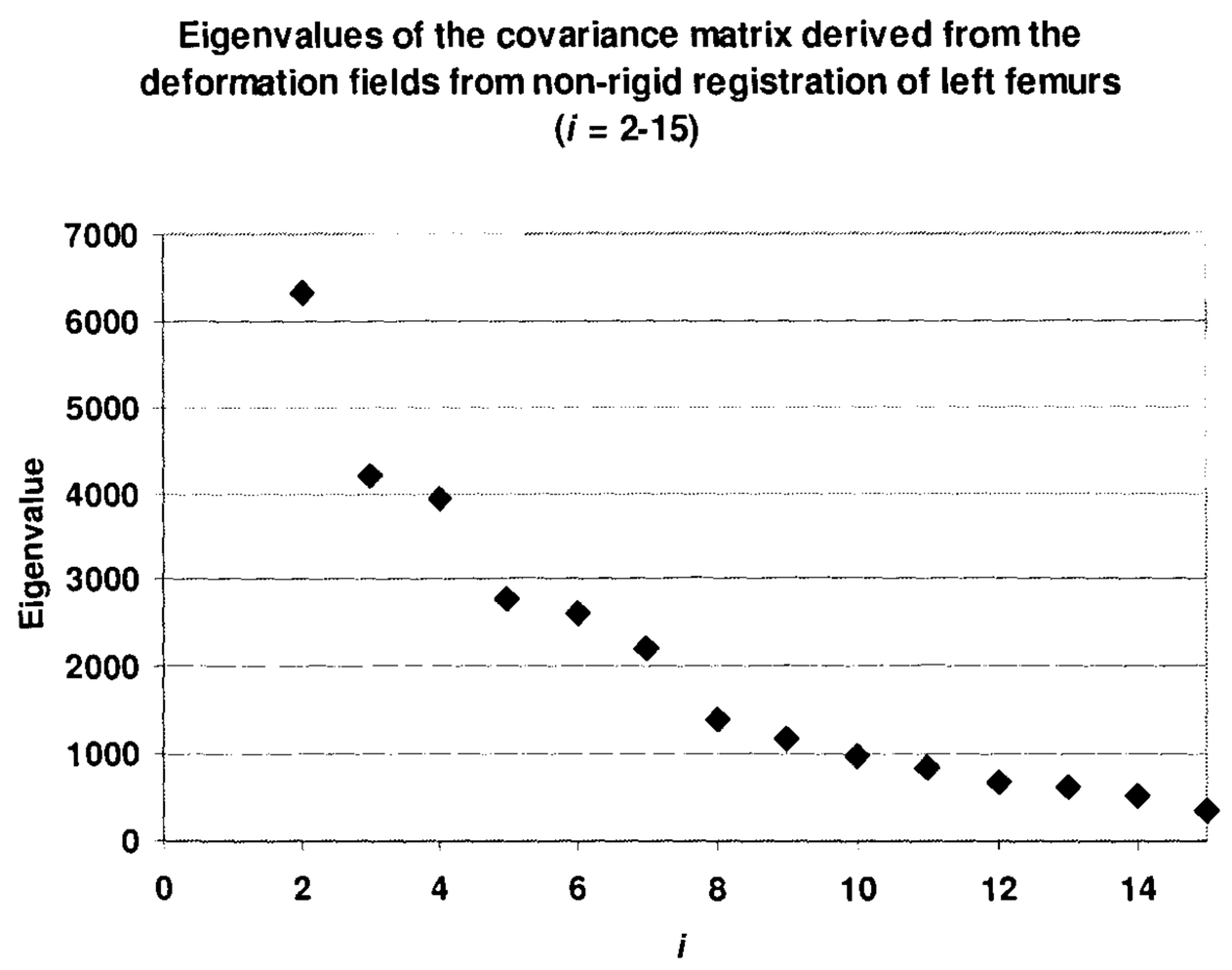

Figure 4.7: Eigenvalues λ_i of the covariance matrix derived from the deformation fields from non-rigid registration of left femurs (i=2-15)

Table 4.1: Eigenvalues λ_i of the covariance matrix derived from the deformation fields from non-rigid registration of left femurs

Eigenvalue $i = 1..15$	λ_i (to 1d.p.)	$\frac{\lambda_i}{\lambda_{TOTAL}}$ (to 3d.p.)	Cumulative (to 3d.p.)
λ_1	119487.0	0.807	0.807
λ_2	6308.4	0.043	0.850
λ_3	4197.2	0.028	0.878
λ_4	3936.9	0.027	0.905
λ_5	2780.9	0.019	0.924
λ_6	2605.1	0.018	0.941
λ_7	2197.4	0.015	0.956
λ_8	1388.0	0.009	0.965
λ_9	1155.7	0.008	0.973
λ_{10}	965.2	0.008	0.980
λ_{11}	829.0	0.006	0.985
λ_{12}	680.4	0.005	0.990
λ_{13}	617.5	0.004	0.994
λ_{14}	505.5	0.003	0.998
λ_{15}	362.1	0.002	1.000

RMS point-to-surface distance to provide the best fit of the model to the US data.

Tables 4.2 and 4.3 show the results when calculating various error measures using the method in Section 3.4.1 on page 81. Table 4.2 shows the RMS residual distance between the instantiated surface and the US-derived phantom surface points registered using ICP, and RMS distance calculated between the instantiated SSM and the CT surface registered using ICP. This table shows how consistent is the resulting bone shape with the original shape. Table 4.3 shows the RMS distance calculated between the instantiated SSM and the CT-derived gold standard surface. This measure indicates the combined accuracy of the geometry of the instantiated model and its registration in physical space.

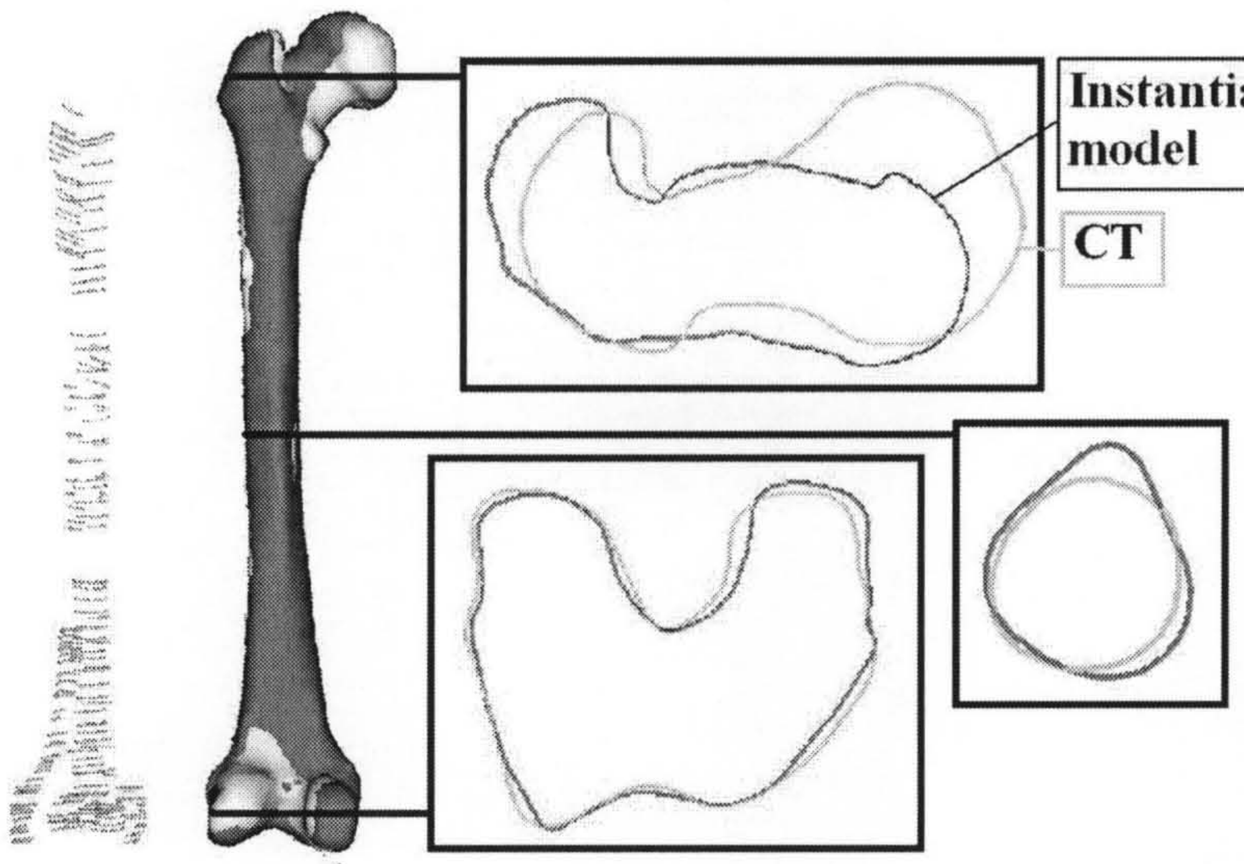

Figure 4.8: Visualisation of US only instantiation of the phantom femur using volume SSM (PDS optimisation): Parts of the US only instantiation (*black*) matched to the phantom CT (*grey*), showing the contours in the femoral head, shaft and near the condyles. The part near the condyles and shaft registered accurately while that near the femoral head showed errors.

4.3.2 Results: Ultrasound Instantiation

Instantiation results using ultrasound only are shown in Figure 4.8. The optimisation was run with 20 starting positions, same as those produced in Section 3.3.4.1 (Page 77), and the final RMS residual distance recorded. Fifteen out of these returned a RMS residual distance of 1.7mm between the US-derived points and the instantiated model surface converging to one minimum. The RMS distance between all points on the instantiated surface and the phantom CT surface was also calculated to be 2.7mm. When only the section near the femoral head is measured, the RMS distance was 3.3mm.

4.3.3 Results: Ultrasound with Centre of the Femoral Head

Experiments were also performed by using the centre of the femoral head as the rotation point in the ICP algorithm. Again, 15 out of 20 starting positions converged to one minimum of final RMS residual distance 1.8mm. The RMS distance between all points on the instantiated surface and the phantom CT surface was 2.7mm and when only the section near the femoral head is measured, the RMS distance was 3.3mm. The results are shown in Figure 4.9.

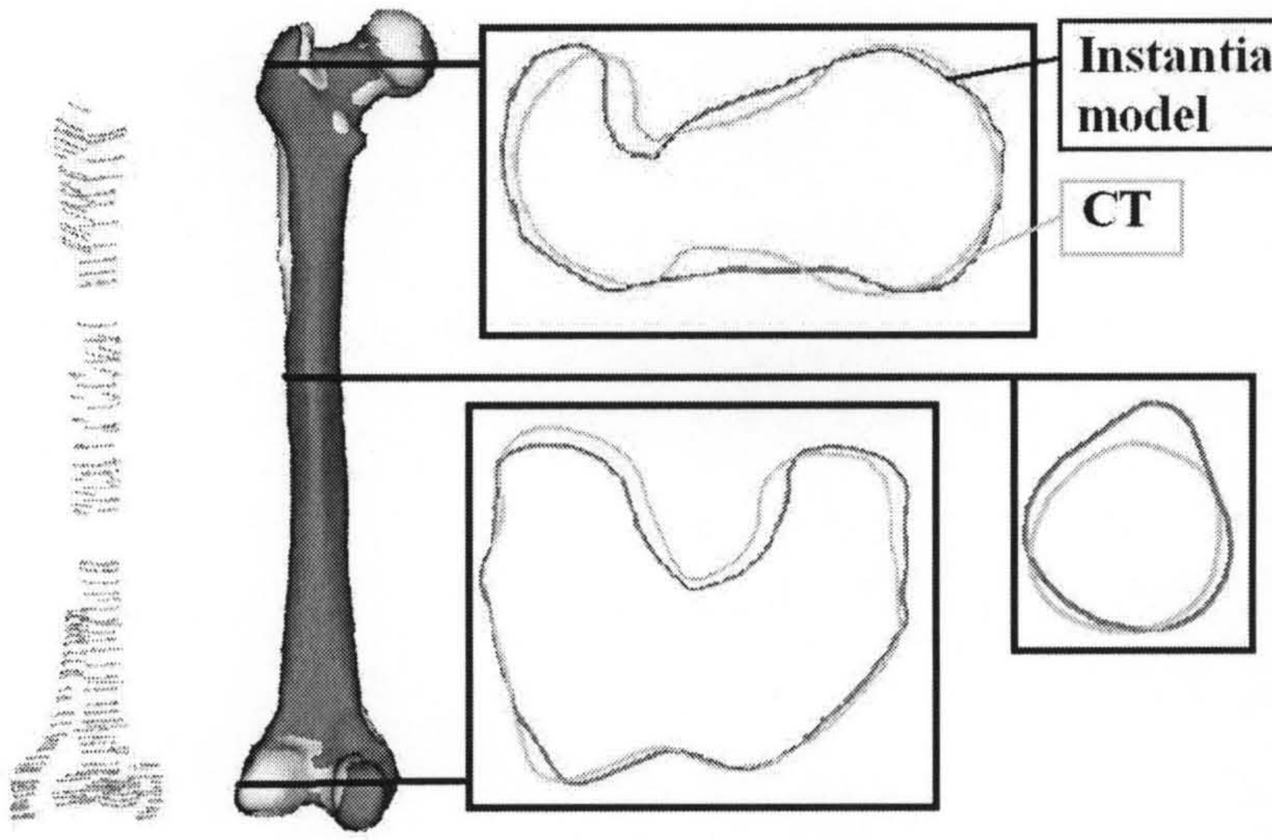

Figure 4.9: Visualisation of US with centre of rotation of femoral head instantiation of the phantom femur using volume SSM (PDS optimisation): Parts of the US with centre of rotation of femoral head instantiation (*black*) matched to the phantom CT (*grey*), showing the contours in the femoral head, shaft and near the condyles. The part near the condyles and shaft are also registered accurately while that near the femoral head also shows good alignment.

4.4 Optimisation Readdressed

Two different types of SSM were introduced in this and the previous chapters. The RMS point-to-surface distance between the US-derived points and the instantiated surface was optimised over the significant modes of variation of the model.

Using the volume SSM and surface SSM, both instantiation experiments used the same US data, same weights for the starting shape and positions. The experiments have also made use of the same optimisation method, an implementation of the parallel direct search (PDS) method, which was readily available "off the shelf" for optimising the instantiation algorithm. But the PDS implementation has its inadequacies. It was originally thought to be a robust and quick way to optimise the cost function. It was soon discovered that the optimisation method took a long time to converge to the final RMS distance. It was also overly complicated for the task in hand and did not provide enough level of user control. It would be very useful if there could be more control over how the optimisation worked, this would enable me to investigate more into how the optimisation algorithm was performing. It was therefore decided to readdress the issue of optimisation method.

For the application which this instantiation algorithm would be used for, it was decided that a simple optimisation method should be implemented such that it was tailor-made for this applica-

Table 4.2: Errors for instantiated phantom femur surface using volume SSM - PDS (shape) (mm) - ICP

Phantom	Error statistic	US-Model*	CT-Model (global)**	CT-Model (regional)***
Ultrasound Only	RMS	1.7	2.7	3.3
	Median	1.0	1.9	2.2
	95% CL	3.4	5.1	6.6
Ultrasound with centre of rotation	RMS	1.8	2.7	3.3
	Median	1.1	2.0	1.9
	95% CL	3.7	4.9	5.3

95% CL = 95% Confidence Level

*Distance between US-derived bone surface points and the instantiated SSM surface.

**Distance between the vertices of the surface mesh, which describes the instantiated SSM surface, and the CT-derived bone surface calculated by aligning the datasets using the ICP algorithm.

***As for **, but with the measure restricted to regions of clinical interest.

tion. This method will be designed based upon one of the most simple and effective optimisation methods. The rationale is described below.

4.4.1 Design Rationale

This optimisation problem is a multidimensional problem. The optimiser is required to optimise the weights that change the first 5 modes of variation of the SSM so as to find the lowest RMS residual between the US-derived points and model-instantiated surface. The weights are thought to be linearly independent but there could still be nonlinear dependencies (Cootes et al., 1992), hence changing one weight value could affect other weights. There needs to be an optimisation strategy that can look for the optimal of the weight of one mode, then going back to the weights on other modes to look for the best combination of weights.

The first mode of variation describes the most significant mode of variation and accounts for the most variance. The second mode of variation describes less modes of variation than the first mode, and so on for other modes of variation. Therefore, the optimiser is designed to use this

Table 4.3: Errors for instantiated phantom femur surface using volume SSM - PDS (shape and final position) (mm) - GS

Phantom	Error statistic	CT-Model (global)*	CT-Model(regional)**
Ultrasound	RMS	3.8	5.6
Only	Median	2.5	4.5
	95% CL	7.7	9.8
Ultrasound	RMS	3.3	3.8
with centre of	Median	2.1	2.4
rotation	95% CL	6.7	7.3

95% CL = 95% Confidence Level

*Distance between the vertices of the surface mesh, which describes the instantiated SSM surface, and the CT-derived bone surface calculated after transforming the CT surface to physical space using the gold standard, fiducial-based registration transformation.

**As for *, but with the measure restricted to regions of clinical interest.

information that different modes of variation account for different amounts of variance, embedded in the training datasets.

Multidimensional optimisation can be computationally costly. On the other hand, optimisation for one variable could be simple to implement and relatively computationally inexpensive. Press et al. (1992) state that the two major families of multidimensional optimisation algorithms with the calculation of first derivatives require a one-dimensional minimisation sub-algorithm. Therefore, this instantiation optimisation problem in multidimensional space has been broken down into a series of 1-D minimisations to simplify the problem.

The cost function of each mode cannot be assumed to be parabolic, this is why the golden section search is better geared than some other one-dimensional optimisation methods to search for the minimum. The golden section search is easy to implement, and is less complicated in itself than PDS and many other optimisers.

One of the advantages of this optimisation strategy, designed solely for this application, is that it gives more user-level control; it can be shown later on that it also ran faster than PDS without any loss of robustness, this could be very important in a real-time application. This strategy gives me a flexible environment which can experiment and check the output from each step of the

optimisation, so that manual intervention is possible at any point; intermediate values are printed out so that its performance can be observed and how the shape of the cost function is changing in the search space. This could provide valuable information for future work and a way to improve the optimiser.

4.4.2 Multiple-Layer Golden Section Search

The result of the PCA algorithm gives a list of modes of variation, the first mode being the principal mode of shape variation, the second mode being of less observed variation and so on. To minimise the RMS residual distance between the US-derived points and instantiated surface from the SSM, they were registered using ICP.

This optimisation method is designed as follows: In the *first* "layer", the weight for the first mode of variation, which describes the most significant mode of variation, is changed to minimised the RMS residual between the US-derived surface points and the instantiated surface. All the weights of other modes of variation are kept constant. Having optimised the weight for the first mode, this weight is kept constant along with the weights for the third, forth and fifth modes, while the weight for the second mode of variation is changed to minimise the RMS residual.

When the weight of the second mode has been optimised, the weight of the first mode may no longer be at the optimal value, therefore, in the *second* layer, the algorithm revises the weight of the first mode - the optimisation process starts at the weight of the first mode's previously optimised value in the first layer. Having optimised the weight of the first mode, the algorithm then goes on to optimise the weight of the second mode to produce the lowest RMS residual, and then optimising the weight of the third mode. During every optimisation step, only the weight of one mode is optimised while the weights of all other modes are kept constant. The algorithm finishes at the forth and last layer, when the weight of the fifth mode, of which describes the least mode of variation amongst the first five modes of variation, has been optimised to produce the lowest RMS residual.

The golden section search starts out with initially bracketing the minimum in an interval. In this strategy, the brackets are set to be the 3SD defined for each mode. The following describes how this method is used to sequentially find the best solution to the problem.

4.4.2.1 The Algorithm

In this scheme, the weight corresponding to each mode of variation was changed to produce an instance from the SSM, this is registered with the US-derived points using the ICP algorithm.

Working with the SSM's first five modes of variation, a four layer optimisation strategy was used. In each step of each layer, using golden section search (Press et al., 1992), the RMS residual distance between the US-derived points and the instance produced from the SSM is minimised for one mode by altering the weights of that mode, and keeping the weights of other modes of variation constant:

Layer 1: Modes 1 and 2

Layer 2: Modes 1, 2 and 3

Layer 3: Modes 1, 2, 3 and 4

Layer 4: Modes 1, 2, 3, 4 and 5

Here is the pseudo-code of this algorithm:

Given a bracketing triplet of fabscissas *x0, x1, x2* such that *x1* is between *x0* and *x2*.

CurrentBestWeight[1..5] = 0

For N=2 to -1 // Layers 1 to 4

For I=1 to (5-N-1) { // Steps: Defining the weight of which mode to optimise

Get Eigenvalue (I); // *I* is the current mode

CurrentSD = sqrt(Eigenvalue(I)) // Calculate standard deviation

// Golden section search

If this is the first iteration // Only required as the very first step

Set x0 = -3SD, x1 = 0, x2 = +3SD

Otherwise

x1 = CurrentBestWeight[I]

Golden_best = minimise (RMS point-to-surface distance between

US points and instantiated surface by changing CurrentBestWeight[I])

}

4.4.3 Results: Instantiation using Multiple-Layer Golden Section Search

This algorithm with the new optimisation scheme is tested using both the US only and US with centre of the femoral head as the centre of rotation. As with the previous 2 instantiations using PDS, 15 out of 20 starting positions converged to one minimum with the final RMS residual of 1.6mm (for US only) and 2.1mm (for US with centre of femoral head as pivot point). The results are shown in Figures 4.10 and 4.11 using the cross-sectional contours, and numerical results are shown in Tables 4.4 and 4.5. The RMS distance between all points on the instantiated surface and the phantom CT surface was 3.2mm and 3.0mm for US only and US with centre of femoral head

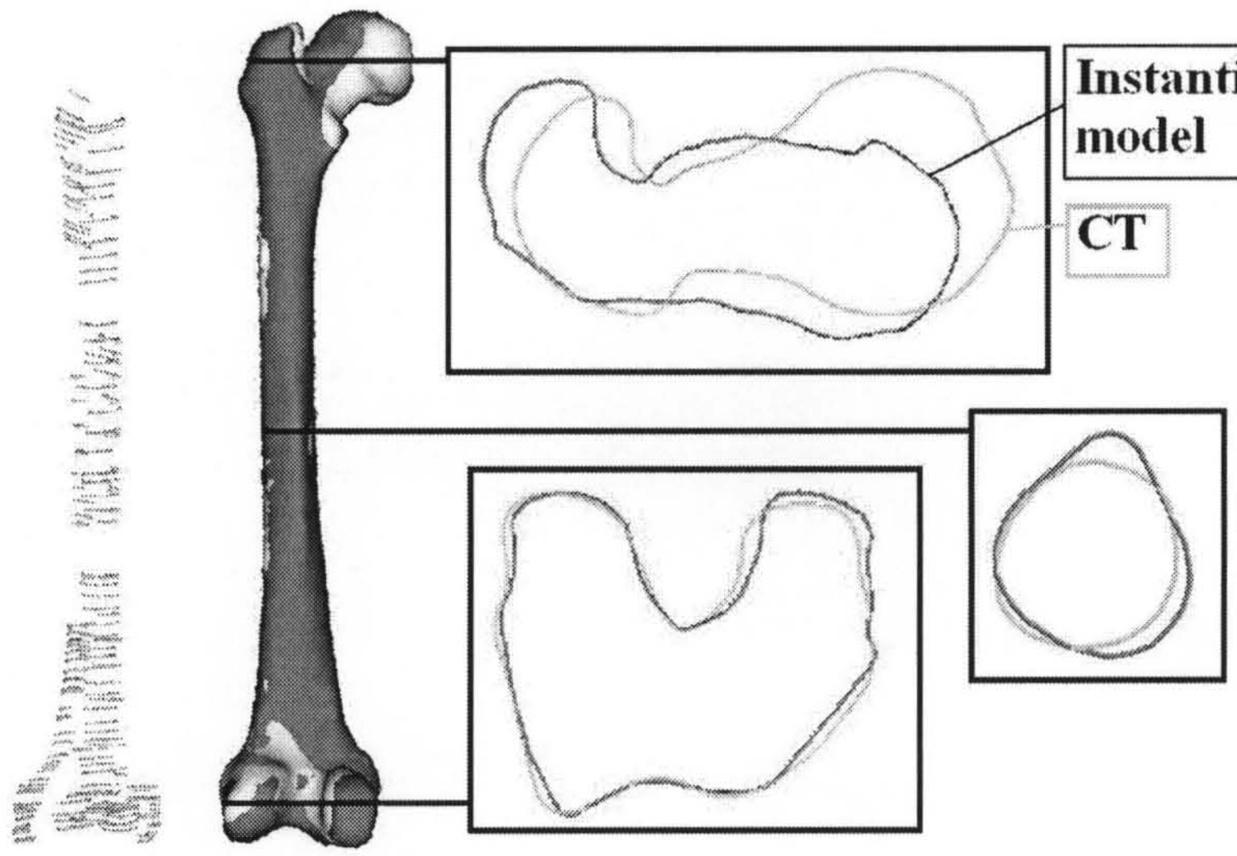

Figure 4.10: Visualisation of US only instantiation of the phantom femur using volume SSM (Multiple-layer golden section search): Parts of the US only instantiation (*black*) matched to the phantom CT (*grey*), showing the contours in the femoral head, shaft and near the condyles.

as pivot point respectively, when only the section near the femoral head is measured, the RMS distances were 4.2mm and 3.0mm respectively.

Table 4.6 shows how the weight of each mode was optimised while the RMS residual was minimised at each step of the layers and finally converged to a lowest RMS residual, for one of the starting positions.

4.5 Discussion

In this chapter, two optimisation methods were used to minimise the RMS residual distance between US surface points and SSM-instantiated surfaces. The method using PDS returned a RMS residual distance between the US-derived points and the final instantiated surface of 1.7mm and 1.8mm for US only and US with the centre of the femoral head as the pivoting point. Both of these instantiated surfaces, when matched to the nearest points on the CT-extracted surface using ICP, returned a RMS distance of 2.7mm; when errors were only calculated in a section near the femoral head was measured, both returned RMS distances of 3.3mm. However, when the gold standard registration was used, the instantiated surface using the centre of the femoral head as the pivoting point performed better, showing a better shape and final position compared with that using just US to instantiate.

A new optimisation strategy, the multiple-layer golden section search, was also used to in-

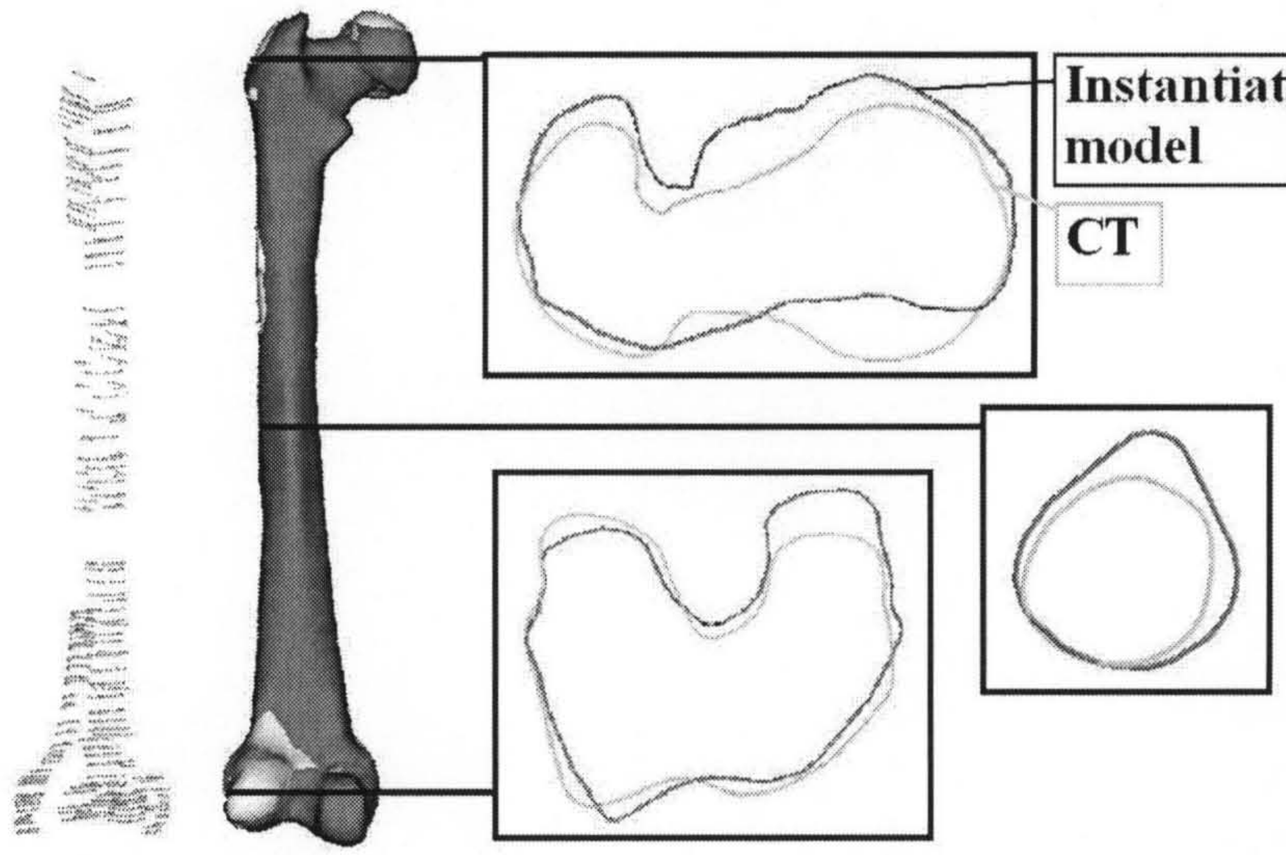

Figure 4.11: Visualisation of US with centre of rotation of femoral head instantiation of the phantom femur using volume SSM (Multiple-layer golden section search): Parts of the US only instantiation (*black*) matched to the phantom CT (*grey*), showing the contours in the femoral head, shaft and near the condyles.

stantiate the phantom femur in the water bath. The final RMS residual distance between the US-derived points and instantiated surface were 1.6mm and 2.1mm for US only and US with centre of the femoral head as the pivoting point. The RMS distance between the final instantiated surface and the gold standard CT-derived surface were 3.2mm and 3.0mm respectively; while that in the region of the femoral head were 4.2mm and 3.0mm respectively. Using the gold standard registration, the US only instantiation returned a lower RMS distance across the whole CT-derived surface, but using the femoral head as the pivoting point produced a better instantiation in the region of the femoral head.

This new optimisation strategy provided more user-level control than using the previous PDS implementation with the possibility of being terminated half-way. It also ran faster, looking at successful registrations, the time taken for the PDS method to converge was typically 5.5 hours and 5 hours for instantiations with US only and with the centre of rotation of the femoral head respectively; while that for the multiple layer golden section search, the time was reduced to typically under 4 hours for both types of instantiations.

It should be noted that this study was a suitability assessment of this optimisation method as a tailor-made minimisation for this application; the maximum difference in the RMS distances obtained between the two optimisation methods was on average $\pm$0.4mm, this shows that the multiple-layer golden section search method performs as well as PDS without loss of robustness.

Table 4.4: Errors for instantiated phantom femur surface using volume SSM - Multiple-layer golden section search (shape) (mm) - ICP

Phantom	Error statistic	US-Model*	CT-Model (global)**	CT-Model (regional)***
Ultrasound Only	RMS	1.6	3.2	4.2
	Median	1.0	2.4	3.1
	95% CL	3.2	6.1	7.9
Ultrasound with centre of rotation	RMS	2.1	3.0	3.0
	Median	1.4	2.5	2.1
	95% CL	4.0	5.4	5.7

95% CL = 95% Confidence Level

*Distance between US-derived bone surface points and the instantiated SSM surface.

**Distance between the vertices of the surface mesh, which describes the instantiated SSM surface, and the CT-derived bone surface calculated by aligning the datasets using the ICP algorithm.

***As for **, but with the measure restricted to regions of clinical interest.

It has also allowed me to understand how the optimisation process was working. It will be used in Chapter 6 where a cadaver study is carried out.

The results from the above experiments could be compared with those from the previous chapter, using a surface SSM to instantiate from the same phantom femur. For instantiations obtained using the surface SSM, the RMS distance between the final instantiated surface and the gold standard CT-derived surface were 4.5mm and 4.0mm for US only and US with the centre of the femoral head as the pivoting point respectively. The RMS distance for the region around the femoral head were 7.2mm and 4.7mm respectively. Instantiation results from using the volume SSMs building using B-spline node points have improved the accuracy of the SSM and the instantiation when compared with those instantiated using a surface SSM, especially in regions that are inaccessible to percutaneous ultrasound, mainly around the area of the femoral head.

Table 4.5: Errors for instantiated phantom femur surface using volume SSM - Multiple-Layer golden section search (shape and final position) (mm) - GS

Phantom	Error statistic	CT-Model (global)*	CT-Model(regional)**
Ultrasound	RMS	3.7	5.8
Only	Median	1.7	4.3
	95% CL	8.2	11.1
Ultrasound	RMS	3.9	4.2
with centre of	Median	2.4	2.7
rotation	95% CL	8.0	8.1

95% CL = 95% Confidence Level

*Distance between the vertices of the surface mesh, which describes the instantiated SSM surface, and the CT-derived bone surface calculated after transforming the CT surface to physical space using the gold standard, fiducial-based registration transformation.

**As for *, but with the measure restricted to regions of clinical interest.

4.5.1 Centre of the Femoral Head as Centre of Rotation

The centre of the femoral head has been added as an extra point into the template, to be used as the centre of rotation during ICP computation. It is noted that when combining this extra point with the volume SSM, the effect of using this point is reduced and the RMS errors, when using the femoral head pivot point, are much closer to the RMS error when this point is not used. It is thought that since the centre of the femoral head point was used as the pivoting point in ICP, the translational parameters are defined by this pivoting point and the algorithm would only be optimising on 3DOF - rotations. Although optimising on 3DOF is easier than 6DOF, unless other parameters, like the weights of the modes of variation, can compensate for this point, this point effectively restricts the "movement" of the instantiation. The instantiations produced from the surface SSM was not as good as those produced from the volume SSM. This might be the reason the surface SSM instantiations returned better results by incorporating the centre of the femoral head as the pivoting point. On the other hand, the volume SSM gave a more accurate representation of the modes of shape variations of the femur, therefore instantiations using US with the incorporation of this point were similar to using US-only.

It very much depends on how accurately this point was obtained by pivoting during surgery,

Table 4.6: How the weights of the modes of variation changed during the multiple-layer golden section search for the instantiation of the phantom femur.

Mode	1	2	3	4	5	RMS residual
Initial	0	0	0	0	0	5.707
Layer 1	1.62					1.694
		0.59				1.667
Layer 2	1.48					1.658
		0.88				1.657
			0.04			1.655
Layer 3	1.35					1.649
		1.27				1.646
			0.16			1.644
				0.99		1.644
Layer 4	1.27					1.641
		1.57				1.640
			0.32			1.638
				0.10		1.638
					1.30	1.595
Best mode combination:	1.27	1.57	0.32	0.10	1.30	1.595

These weights are presented as standard deviations, rounded off to 2 decimal places. The last column shows how the RMS residual was being minimised while the weights of each mode was optimised.

One row in each layer represents a step. Only the weight of one mode is optimised at any one time, therefore the weight of other modes were left blank to denote they were being kept constant at their previous (best) value.

in the case of this phantom experiment, this point was defined manually. It also depends on how accurately it was defined in the template originally. These procedures were described in Section 3.3.5 on Page 78. There are errors associated with the methods used to define this point.

Another potential problem with using this point is that the femoral head is not spherical. When using it as the centre of rotation, the femur is not rotating perfectly about this point, this will create complications when calculating the RMS error. There is no ground truth as to where this point should be defined. Also, the centre of the femoral head obtained by pivoting the leg and the centre of the femoral head defined in the template may not be at the same place. For the cadaver study in Chapter 6, real data is obtained for this point and RMS error values are calculated to estimate the error associated with it.

4.6 Chapter Summary

This chapter introduced a SSM produced based on the deformation fields of the B-spline node points from non-rigid registration to instantiate from US. The RMS distance between all points on the instantiated surface and the nearest points on the CT-extracted surface was 2.7mm; when compared with those instantiated using surface SSMs, the results were better including the regions inaccessible to percutaneous US *in vivo*, namely the femoral head region. The use of the model produced using the B-spline node points generated by non-rigid registration also provided much higher resolution and potentially allows more information to be included in the template surface, hence the model.

This experiment only included a femur immersed in a water bath which provides a homogeneous medium. In the clinical setting, the patient's bone will not be in a water bath and the US images obtained will contain soft tissue effects resulting in US passing through different structures. This will be addressed in Chapter 6 and it is likely that this will affect the experimental results when compared to the phantom experiment. At the end of the chapter the current optimisation method, parallel direct search (PDS), was reviewed and a new method with a multiple-layer approach utilising the golden section search algorithm was devised, this method was tested on the same data as the phantom experiments and shown to perform as good as the PDS method without loss of robustness. This method has been adopted and will be used to optimise the instantiation algorithm in Chapter 6 with a cadaver study with three cadavers.

Chapter 5

Volume Statistical Shape Model for the Pelvis

5.1 Introduction

Chapter 4 introduced the volume SSM of the femur and results from instantiation using the phantom femur in a box filled with water. It showed that the femur volume SSM instantiation results were better compared with the femur surface SSM when tested through the phantom femur experiment. In order for this instantiation algorithm to be applied to orthopaedic surgery, a pelvis model is also needed.

This chapter describes some steps in generating the SSM of the pelvis which was acquired according to the method described in the previous chapter. In this chapter, details were given regarding the materials used, addresses some of the problems encountered and presents the first two modes of shape variation of the model.

5.2 Construction of the Volume Statistical Shape Model for the Pelvis

As mentioned before, the SSM is being built on the B-spline node points from non-rigid registration plus 4 corners of the node points mesh for calcuating the scaling. A template surface is required for visualising the model and for instantiation purposes. The method used to produce this volume SSM for the pelvis is the same as that for the femur described in Section 4.2 (Page 89). The principle stays the same, but there are some issues related to the pelvis that are different and are being addressed here.

Figure 5.1: Pelvis template surface with 9183 points, shown on the left and the template mesh, shown on the right.

5.2.1 Surface Extraction

A template image was selected from the CT database as being visually close to the average pelvis. Just like the femur, because of high variability of soft tissues around bones, the template pelvis had to be segmented, using ANALYZE 6.0 (Robb et al., 1989, Mayo Foundation, Rochester, MN, USA). This pelvis template was again carefully delineated and the segmentation dilated by 5-8mm (please refer to Section 3.2.1 on Page 62 for details). The pelvis bone surface, after surface extraction to provide the template surface, contains 9183 points. This pelvis template surface and mesh (with vertices) are shown in Figure 5.1.

5.2.2 Non-Rigid Registration

This step was already described in Section 3.2.2 (Page 64), where the template image is aligned to the other images in the database using a non-rigid registration algorithm (Rueckert et al., 1999).

The issues with registration of the pelvis is different from that of the femur. Unlike the femur which has near cylindrical symmetry in the shaft area, the pelvis has a lot of structure in all 3 dimensions. The initial manual alignment was not easy because there are many features on the pelvis to match against.

The main precaution to take when registering was the femoral head deep inside the acetabulum. The femur is also a bony structure which would have similar intensity values as the pelvis. In addition to that, the acetabulum is not perfectly hemi-spherical; there is also a small depression (the acetabular fossa which normally contains a fat pad to act as shock absorber for the femoral head) which makes it slightly harder to match against. This could be overcome by matching the two acetabulae boundaries roughly when doing the initial alignment. The other place where mis-registration might occur were around the rim of the iliac crest, this is especially noticeable when

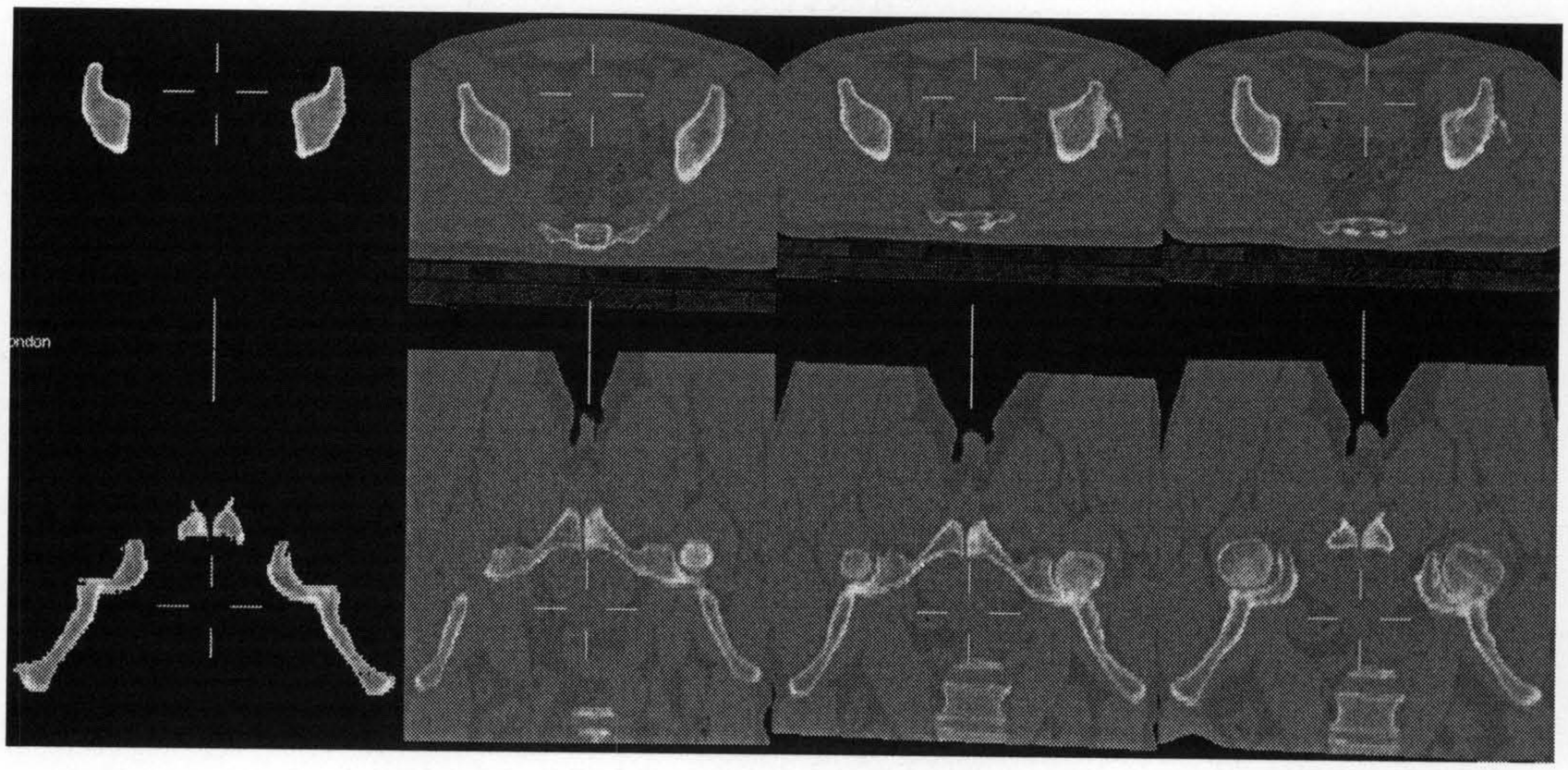

Figure 5.2: Example registration for the pelvis in transaxial (*top*) and coronal (*bottom*) views. From left to right: the target pelvis, the source pelvis, after rigid registration, after non-rigid registration.

the rim is rather thin on some patients.

The non-rigid registrations generally took slightly longer than the femurs because of more node points involved. This will be mentioned in the next section. Each registration took about between 2 to 10 hours on one processor of the Condor Cluster, with processor speeds of 1.4MHz and 1.8MHz and 1Gb memory. A node point spacing of 20mm was also used.

An example of the resulting alignment is shown in Figure 5.2 with transaxial and coronal views of the non-rigid registration results.

5.2.3 Building the Model

Just as in Chapter 4, using the results from the non-rigid registration described above, which registered training CT datasets to one template image, an SSM was built on the node points of the approximating B-splines used to define the free-form deformation, plus 4 corner points to calculate scaling. The output of the PCA was the mean deformation of the template, with the eigenmodes and eigenvalues representing the deformation fields. The number of node points used for this pelvis was 391, adding the 4 corner points, the pelvis volume SSM contains 395 points.

5.2.4 Results: The Pelvis Volume Model

The pelvis volume model was built on the B-spline node points that were used to define the FFD and scaling from non-rigid registration. As explained before, the model consists of how these

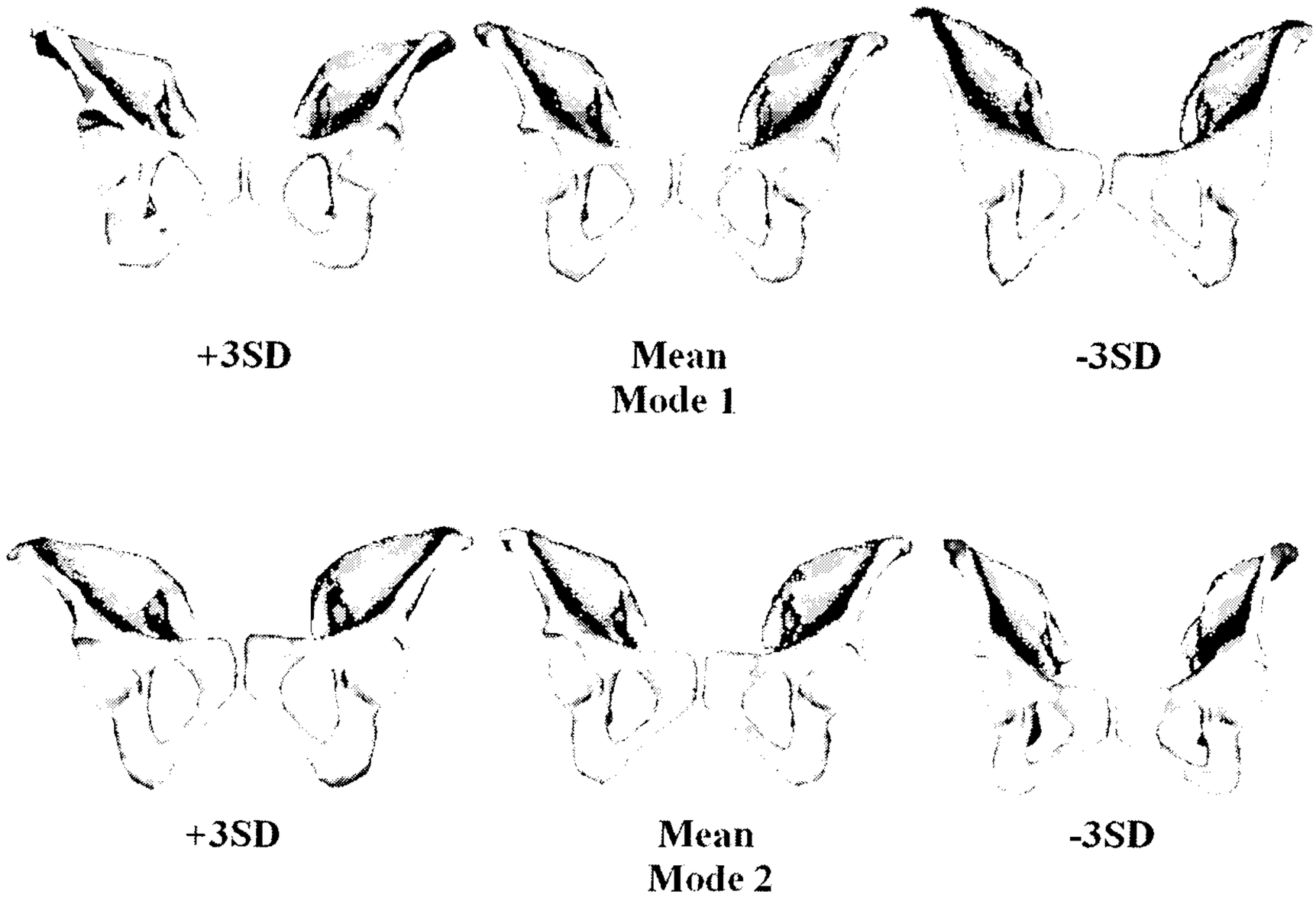

Figure 5.3: Representation of the female pelvis volume SSM. These were produced by deforming the template surface using the mean deformation and the principal and second modes of variation in the deformation fields, with three standard deviations.

node points deform the template. The model is represented visually in Figure 5.3 by transforming the template surface using the mean deformation and the principal modes of variations in the deformation fields. The figure shows the first and second modes for the pelvis when applying plus or minus three standard deviations to the mean deformation. This model was generated using 10 female pelvic CT scans. The first mode of variation of the female pelvis model corresponds largely to a change in the general size while the second mode include change in the size of the cavity being bound by the iliac crests.

Using 10 female pelves for the input to the SSM, the significant modes of variations for the female pelvis volume SSM are shown in Table 5.1. This information is plotted in Figures 5.4 and 5.5. The first 5 modes of variation explain at least 97% of the variance while the principal mode explains at least 85%.

Table 5.1: Eigenvalues λ_i of the covariance matrix derived from the deformation fields from non-rigid registration of female pelves

Eigenvalue $i = 1..9$	λ_i (to 1d.p.)	$\frac{\lambda_i}{\lambda_{TOTAL}}$ (to 3d.p.)	Cumulative (to 3d.p.)
λ_1	580355.0	0.851	0.851
λ_2	40257.4	0.059	0.910
λ_3	17671.5	0.026	0.936
λ_4	14125.5	0.021	0.957
λ_5	11245.2	0.017	0.973
λ_6	5827.7	0.009	0.982
λ_7	5635.3	0.008	0.990
λ_8	3983.9	0.006	0.996
λ_9	2826.4	0.004	1.000

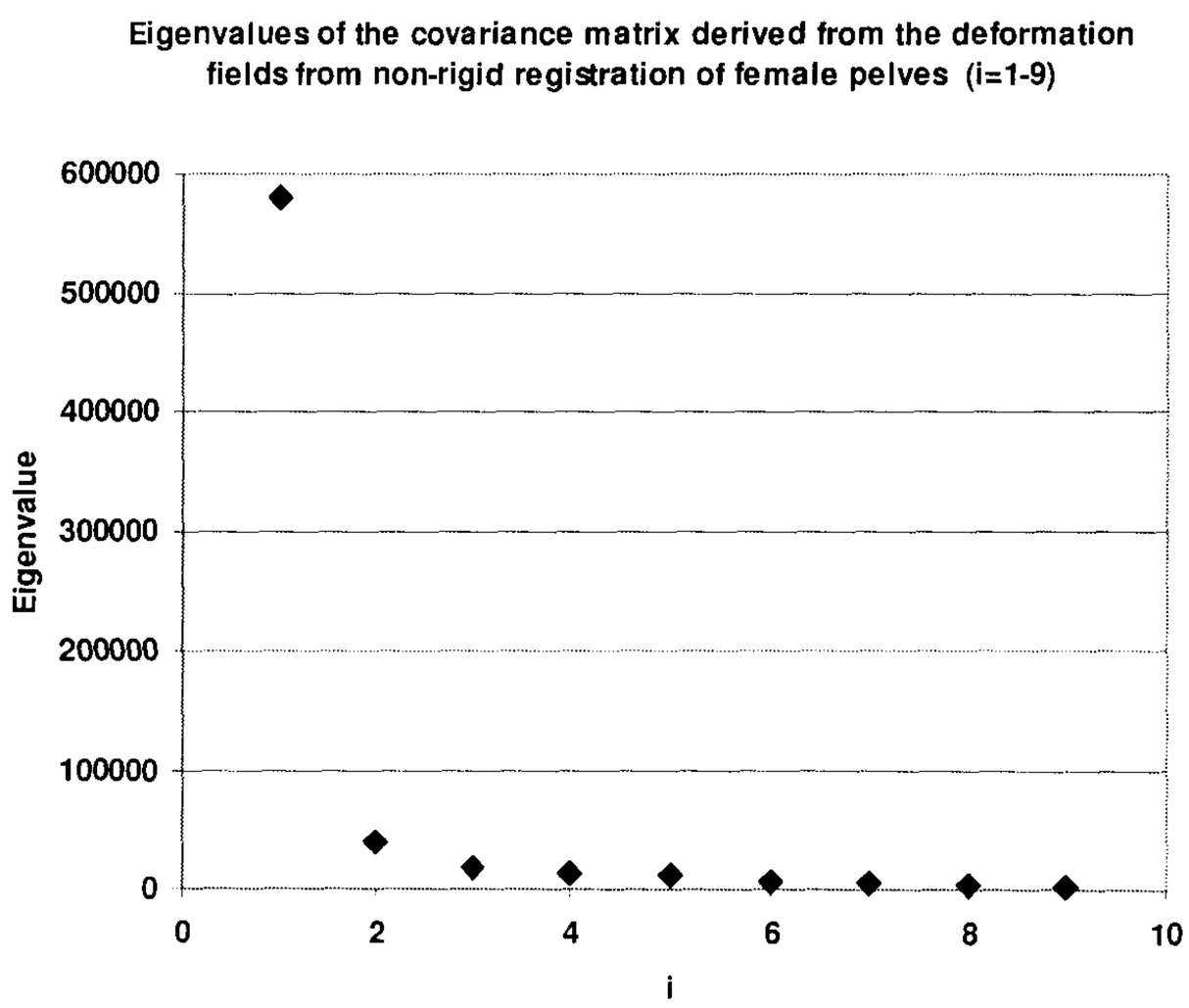

Figure 5.4: Eigenvalues λ_i of the covariance matrix derived from the deformation fields from non-rigid registration of female pelves (i=1-9)

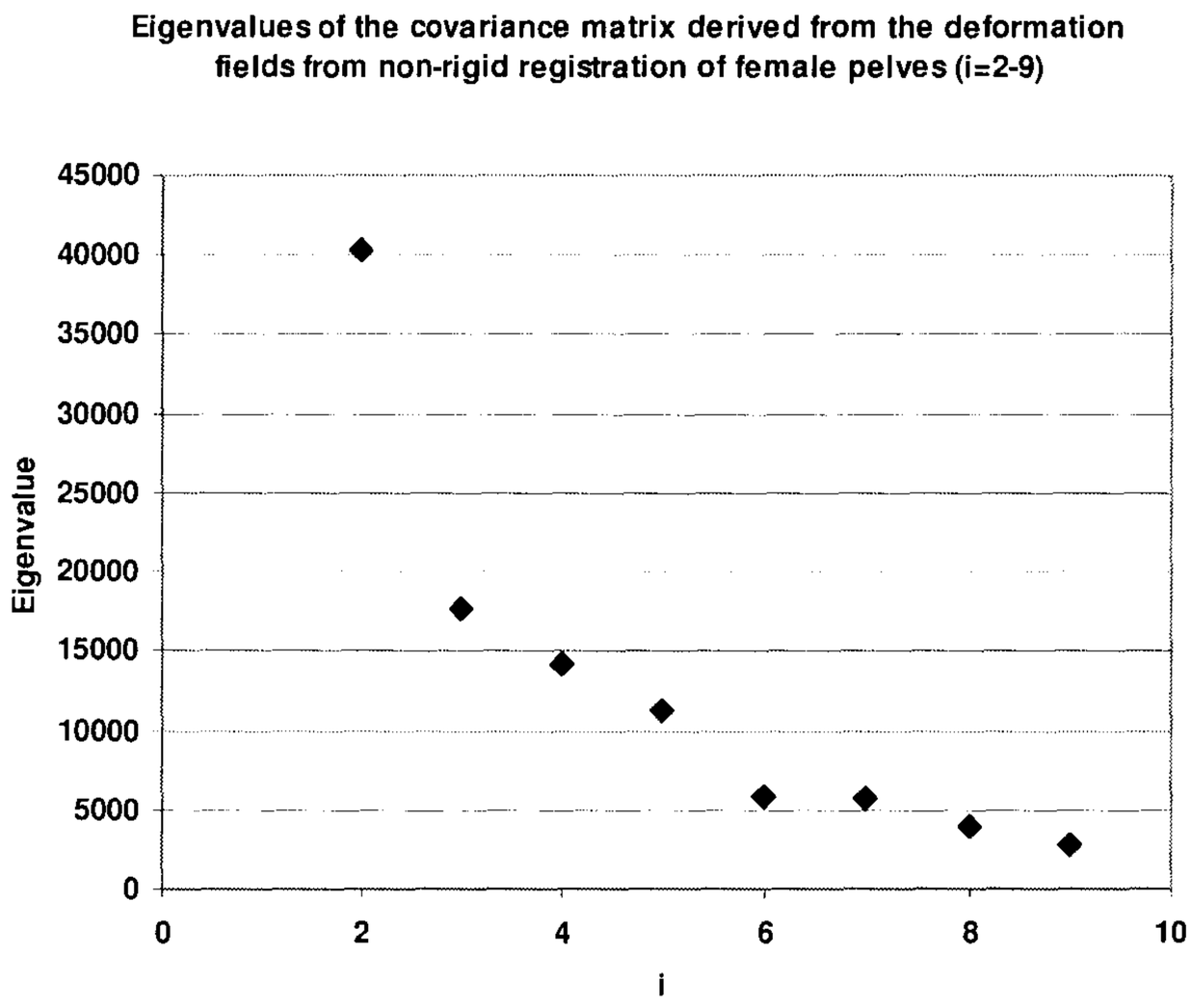

Figure 5.5: Eigenvalues λ_i of the covariance matrix derived from the deformation fields from non-rigid registration of female pelves (i=2-9)

5.3 Chapter Summary

This chapter presented the pelvis volume SSM and discussed some of the issues when producing the SSM. Having produced this SSM, there is now a complete set of models for both the femur and pelvis, which will pave the way for testing the instantiation algorithm against the cadaver datasets in the next chapter.

Chapter 6

Cadaver Validation

6.1 Introduction

The previous chapters have shown that instantiation is possible using US images of a phantom femur. However, there are a number of unrealistic aspects to that experiment. It could have been by chance that the phantom bone instantiations returned weights on each mode of variation that were not more than 1.6SD from the mean shape of the statistical shape model (SSM), where some weights were very close to the mean shape, hence an easy one for the SSM to instantiate from. The bone was immersed in water providing constant speed of sound and no tissue effects. When using ultrasound (US) in real tissue to image bone, the US images acquired could include multiple reflections, speckles, shadowing artefacts and variable contrast. Ultrasound on real bone and tissue is very different, the acquired images are much more difficult to interpret than a bone immersed in water.

Earlier only one bone was tested. This chapter addresses a number of the above issues and focuses on the test on real bone and tissue to obtain realistic images. In order to test the accuracy of the method, there needs to be a ground truth to compare the results with. To obtain high accuracy, an accurate gold standard image-to-physical registration transformation to a high resolution CT scan, based on bone-implanted fiducial markers, was calculated to provide validation. For ethical reasons, this could not be carried out in patients *in vivo*, and hence cadavers were chosen as the next best option, thought to be just as good. This cadaver study has therefore been carefully designed, unlike the water bath experiment, to obtain US image quality almost equivalent to that in the living human body. The cadavers were preserved in such a way that the muscles, soft tissue and bone interface were as realistic as an anaesthetised patient on an operating table and the images will have the same properties as real patients. This makes the experiment even closer to what would be

actually encountered in the operating room.

In Chapter 4, substantial changes were made to the node-points method to produce a volume SSM, so that the instantiated models resemble real bone instead of the blocky appearance of the surface SSM in chapter 3. The volume SSM also provided more accurate representation of the bone surface. The methods used for processing the template and building the models used in this chapter are the same as that in Chapter 4 on phantom experiments. Also following Chapter 4's investigation, the optimisation strategy has been changed to make the method more efficient.

The layout of this chapter is as follows: starting with describing the experimental procedure of the cadaver experiment, the method used to calculate the gold standard measures is given, moving on to give details of the instantiation process and finally to presenting the results. There are also sections devoted to analysing the starting positions to the instantiation process, and the effect of acquisition accuracy when obtaining the centre of the femoral head to be used as the centre of rotation by pivoting the leg around the hip joint.

6.2 Experimental Procedure

Experiments for this study made use of 3 complete female cadavers, provided by and carried out at the Institute of Anatomy, Ludwig-Maximilians University, Munich, Germany. A few days before the experiment, the US scanner, the optical tracking device with associated tools and computers were transported by van to Munich and set up. After the experiments, these equipment were driven back by van to London. The whole experiment including transportation took 9 days.

The following sections will describe how these cadavers were prepared and how the gold standard surface and registrations were obtained.

This is a high precision experiment which is often difficult *in vivo*, a lot of care and thought were given to make sure the experiments were performed accurately. It is necessary to be very accurate in each stage of the process and hence this experiment included the use of a high accuracy Optotrak. The experiment also utilised bone markers rather than markerless skin surface points and adopted an accurate US calibration technique.

6.2.1 Cadaver Preparation

The cadavers varied in size and fat compositions; they were stored at room temperature and prepared using the method of W. Thiel (2002), preserved in formalin and glycol to preserve flexibility, so that visually the US was equivalent in quality to the ones that could be obtained *in vivo*. With

the cadavers in the supine position, titanium bone screws with a 2mm diameter threaded tip (Part number 80-09051, Stryker-Leibinger UK Ltd., Newbury, Berkshire, UK) were implanted by an orthopaedic surgeon into the femur and pelvis of each cadaver. For the femur, four screws were inserted with one in the greater trochanter and the other three were distributed along the length of the femoral shaft on the anterior and lateral aspect; in the pelvis, five screws were inserted in each hemi-pelvis with one directly on the pubis bone and the other four distributed along the anterior iliac crest. Every care was taken to ensure that damage to the surrounding tissues were minimised so that US images, where accessible, could be obtained.

Two types of caps, or fiducial markers, could be attached to the end of the titanium screws for either imaging in the CT scanner or located by the optical tracker. These are discussed below.

6.2.2 Gold Standard Acquisition

To obtain the gold standard, the cadavers had to be CT-scanned with imaging caps and later replaced these caps with physical markers for localisation by the optical tracking device. The following sections describe the procedures.

6.2.2.1 CT Scan

Firstly, to register the cadavers in CT space, imaging caps - custom-made fiducial markers, filled with CT contrast agent (Urografin 370, Scherring Healthcare Ltd., West Sussex, UK), were attached to the end of each screw. The cadavers were taken to the radiology department to be scanned using a high-resolution spiral CT scanner (Siemens SOMATOM Plus 5 CT scanner, Siemens Medical Solutions, Erlangen, Germany). The whole of the pelvis and femurs were included in the field of view - the extent of the CT scan included the whole pelvis and leg down to below the knee, reconstructed with voxel dimensions $0.71 \times 0.71 \times 2\text{mm}^3$.

The CT scan was segmented by hand using ANALYZE 6.0 (Robb et al., 1989, Mayo Foundation, Rochester, MN, USA) to extract the bone surface as the gold standard surface. This process is the same as that described in Section 3.2.1 on Page 63. In short, the bone was carefully delineated using a semi-automatic method. To further improve on this method with full automation, an intensity-based method is being investigated which will hopefully remove further error introduced by manual segmentation, so that the gold standard obtained is almost equivalent to the actual bone surface. This is described more in Section 7.4.1.

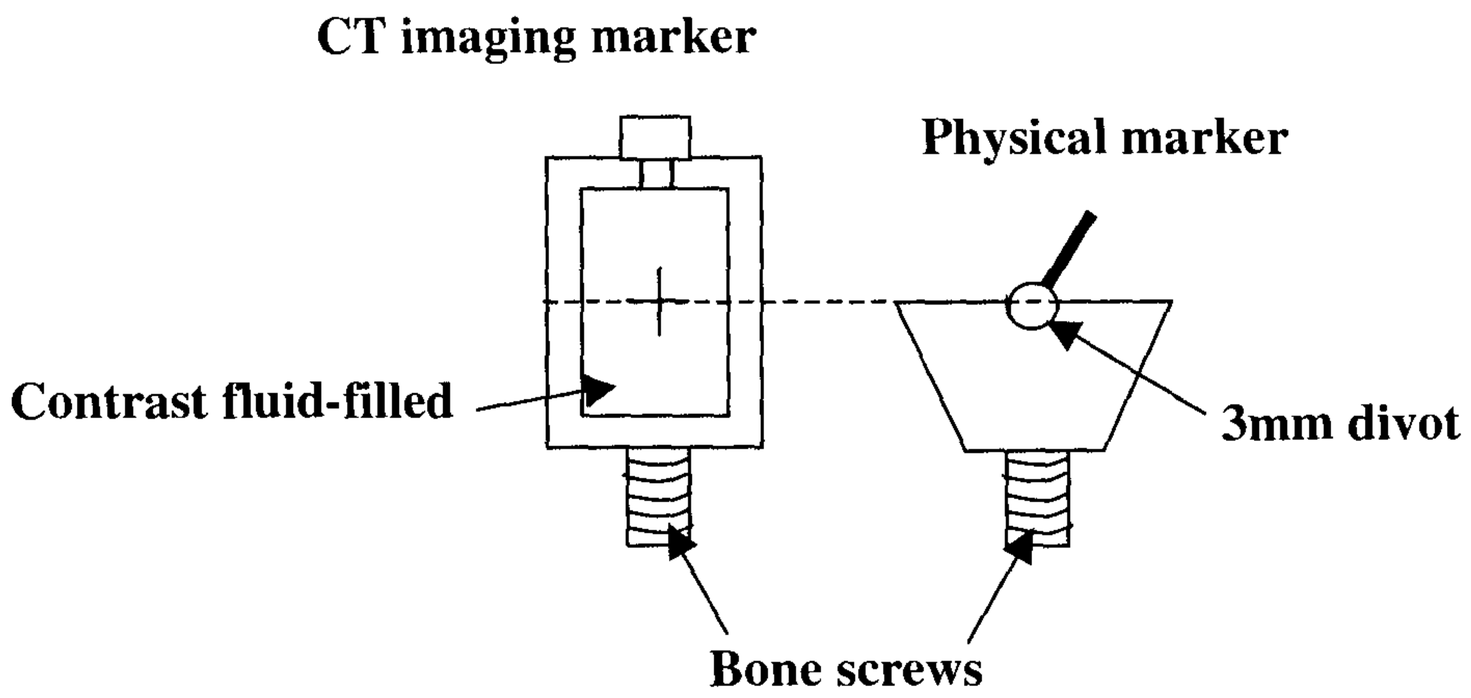

Figure 6.1: The centre of rotation of the divot (*right*) corresponded with the centre of gravity of the fluid in the imaging caps (*left*).

6.2.2.2 Localisation

Following the CT scan, each cadaver was returned to the laboratory and the contrast-filled fiducial markers were replaced with physical markers which had the 3mm re-locatable divot that docked accurately with a hand held tracker. These physical markers were designed so that the centre of rotation of the divot corresponded with the centre of gravity of the fluid in the imaging caps, see Figure 6.1. A tracked localiser was used to measure the 3D positions of the divot centres by inserting a 3mm ball-tip digitizer. The 3D coordinates of the tracker were measured with an Optotrak 3020 (Northern Digital Inc., Ontario, Canada). All measurements were recorded relative to the 3D co-ordinate system of a dynamic reference object (DRO) implanted into the femur or pelvis (see Figure 6.2). Six infra-red emitting diodes (IREDs) were fixed to the dynamic reference object on a T-shaped frame, the root mean square (RMS) error in localising individual IREDs is of the order of 0.2mm (Edwards et al., 2000) hence this should enable accurate determination of its 3D position. This enabled the CT scan to be accurately registered with physical space and with the DRO, the patient could be repositioned without re-registration during surgery. These trackers and the DRO are used in conventional image-guided orthopaedic surgery.

6.2.2.3 Calculation of the Gold Standard

The centre of each imaging marker from the CT scans were defined manually using in-house software. The position of the fiducial markers were registered from the CT to physical space and the gold standard registration was obtained. The gold standard physical-to-CT image was

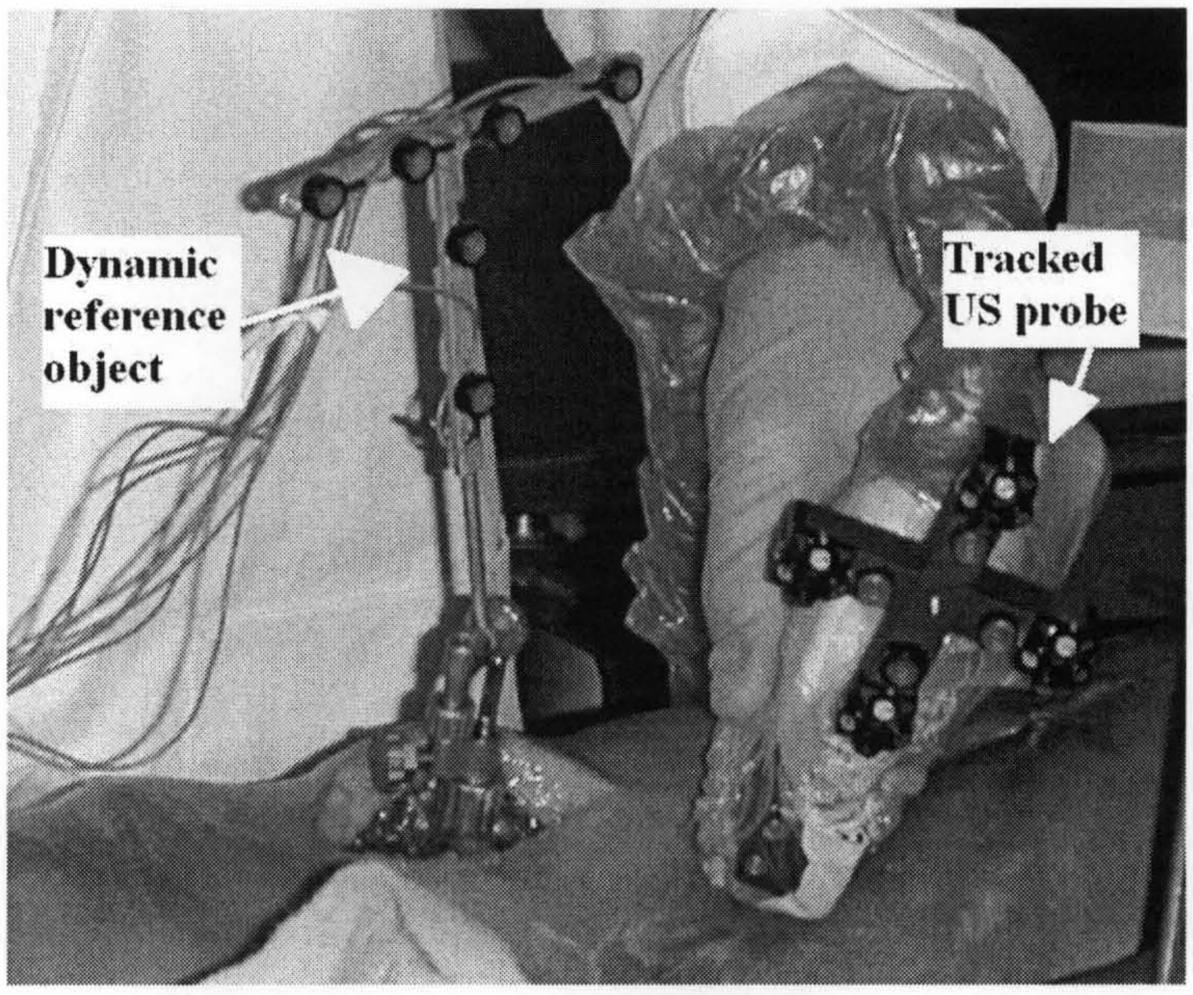

Figure 6.2: Tracked US probe scanning the cadaver femur with a dynamic reference object attached.

determined as the transformation which registered the contrast-filled fiducial marker centres. This transformation was computed using point-based registration (Fitzpatrick et al., 2000).

Fiducial registration error (FRE) is a basic measure of how well fiducials align after applying a registration transformation T. In the case where bone-implanted fiducial markers are used, the FRE is the RMS distance between fiducial points after applying T_{Gold}. This is illustrated in Figure 6.3. For N markers, the FRE could be calculated like this (Fitzpatrick et al., 1998):

$$FRE^2 \equiv \frac{1}{N}\sum_{i=1}^{N} |\mathbf{T_{Gold}} - y_i|^2$$

T_{Gold} could be defined as $T_{Gold} = \mathbf{R}x_i + t$ where x_i and y_i are corresponding set of points, i = 1, 2,..., N; $\mathbf{R}$ is the rotation and t is the translation between these sets of points.

The position of the fiducial markers were registered from the CT to physical space to obtain the gold standard registration. The FREs of these gold standard registrations were between 0.06 and 0.86mm as presented in Table 6.1. Using the equation of Fitzpatrick et al. (1998, 2000), the RMS target registration error (TRE) was estimated over the surface of the bone, for a target point on the bone surface:

$$TRE^2 \approx \frac{1}{N}(1 + \frac{1}{3}\sum_{k=1}^{3}\frac{d_k^2}{f_k^2})(FLE^2)$$

where N is the number of bone-implanted fiducials; d_k is the distance of the target point from the k^{th} principal axis of the fiducial; f_k is the RMS distance of the fiducial from the same axis.

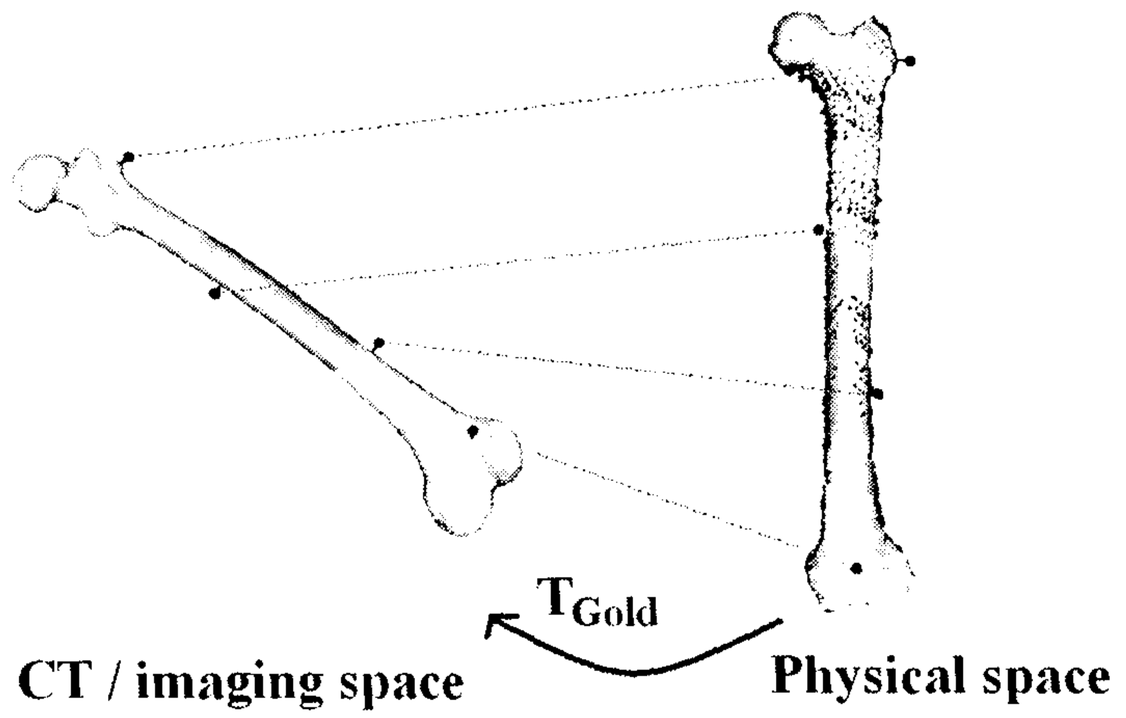

Figure 6.3: Calculating FRE using bone-implanted fiducials.

FLE^2 is an estimate of the fiducial localisation error (FLE) calculated by one of the two methods shown in the following, of which the results for all the cadavers are provided in Table 6.1.

In column "TRE 1", a different FLE was computed for each bone using the following equation:

$$FLE \approx \sqrt{\frac{FRE^2}{1-2/N}}$$

The column "TRE 2" is computed using an average FLE computed using

$$FLE \approx \sqrt{\frac{1}{M}\sum_{i=1}^{n}\frac{N_i.FRE_i^2}{N_i-2}}$$

where the number of bones, $M = 9$, N_i is the number of fiducials for the i^{th} bone and FRE_m is the RMS FRE calculated for the i^{th} bone. The estimated FLE was 0.81mm RMS.

6.2.3 Ultrasound Data Collection

The US images obtained cannot be used as-is, the bone surface needs to be delineated to obtain the bone contours before they could be registered with the SSM. The following sections describe the tracking and capture technology, calibration method, and how the images were acquired.

6.2.3.1 Ultrasound Image Tracking and Capture

In this study, a commercial US scanner (Philips-ATL HDI-5000, Philips Medical Systems, Bothell, WA, USA) and high-frequency scan-probe (L12-5, 5-12MHz broadband linear-array transducer) were used to acquire US images. Using an analogue-to-digital converter (Canopus ADVC-100, Canopus UK, Berkshire, UK) connected from the composite video output of the US scanner to the

Table 6.1: Predicted target registration errors for the gold standard registration based on bone implanted fiducials and the number of ultrasound images

Cadaver	Bone	FRE (mm RMS)	TRE 1 (mm RMS)	TRE 2 (mm RMS)	Number of US images used for registration (images acquired)
1	Left femur	0.06	0.13	1.09	211 (248)
	Right femur	0.15	0.36	1.11	124 (261)
	Pelvis	0.44	0.51	0.74	143 (282)
2	Left femur	0.47	0.74	0.90	149 (257)
	Right femur	0.63	1.43	1.30	342 (557)
	Pelvis	0.86	0.66	0.54	276 (482)
3	Left femur	0.39	0.50	0.74	375 (518)
	Right femur	0.73	0.97	0.77	510 (576)
	Pelvis	0.86	0.82	0.60	316 (342)

IEEE 1394 input of the laptop computer, the images were captured by means of custom-designed image acquisition software written in C++ using Visual Studio 6 (Microsoft Corp., USA). The digital images were stored in the Tagged Image File Format (TIFF) using the PACKBIT lossless compression scheme.

The Optotrak (optical tracker) was used to track a custom-built object on a $\times$-shaped frame (cross) with 20 IREDs, with each "arm" having four IREDs grouped near the tip and one nearer the centre, fixed to the US scan probe, as shown in Figure 6.2. This, in conjunction with the probe calibration, enabled the 3D position and orientation of each 2D US image to be calculated with respect to the dynamic reference coordinate system. The use of a tracked dynamic reference object enabled the position of the cadaver, in particular the position of the leg, to be changed during US acquisition. This allowed images to be obtained in regions, such as the posterior aspect, that would otherwise be inaccessible with the cadaver in the supine position.

6.2.3.2 Ultrasound Calibration

The US probe was calibrated using the method of Barratt et al. (2001) using a point-target phantom consisting of a pin head inside a box filled with water-glycerol solution (at room temperature). The calibration procedure involves scanning the pin head from many different views. In total 76

images were acquired and 71 of these were used to calculate the calibration transformation. The RMS residual error in locating the target of this transformation was 1.08mm, this provided an estimate of the 3D location of each pixel in the US image relative to the custom-built object. The estimated localisation accuracy has a median of 0.62mm by comparing, in the water bath, the 3D positions of the 1mm diameter ball-bearing centres, determined using the 3D US system, with those found using a 1mm ball-tip digitizer.

6.2.3.3 Ultrasound Image Acquisition

US images were collected using several approaches so that as many anatomical features as possible were scanned in order to ensure that the model instantiation was well constrained in regions such as the femoral neck and condyles. US images with poor tracking data were excluded. Poor tracking data is arbitrarily defined here as $\leq$10 IREDs visible on the tracked US probe - this is half the number of IREDs on the tracked probe, with a possible five IREDs visible on each arm of the custom-built object, if in the extreme case that only two arms were visible the calculated spatial information for this object would not be accurate, hence at least 11 IREDs need to be seen. For the DRO, all the IREDs must be visible due to the T-shape arrangement of the object, that is, if <6 IREDs were visible, this data would be rejected.

In this application, the structures to be imaged could be quite deep under the skin and muscles, and also include regions that are curved. To help with the image quality, the US scanner's 2D compounding function (SonoCT^{TM}) was switched on with a maximum penetration depth of 5cm and a single focal zone. Compound imaging combines multiple scanning angles, the scanner electronically steers the US beam and combines these images to produce a single compounded image, which in turn reduces speckle effects and also improve the echo intensity from curved surfaces not perpendicular to the axial direction of the compounded image.

The number of US image frames acquired was between 248 and 576 per bone, as shown in Table 6.1. The time used to acquire these images were between 7 and just over 30 minutes. These timings should be interpreted within the context of this experiment, where an optimal acquisition protocol was not available and there was little previous experience of intraoperative bone imaging using US. In these experiments large numbers of US images were carefully collected in order to test the feasibility of the US-based shape instantiation. These data can also be used to develop a clinical acquisition protocol, and this is the subject of future work and beyond the scope of this thesis. Nevertheless, from this experience, it is envisaged that in the clinical setting it would be possible for the surgeon with a relatively small amount of training and adopting a specific protocol

to acquire sufficient US images for registration and instantiation within 5 minutes.

The experiment started with cadaver 2's right femur and this accounted for the unusually high time required acquiring the images. The surgeon involved had to familiarise himself with the procedure and also with the images he is acquiring on the US scanner, hence taking more time. He then moved onto the pelvis and later the left femur. Next was cadaver 1, by this time the surgeon is more accustomed to the process and hence the time substantially reduced. For cadaver 3 the surgeon tried to acquire more frames hence the time increased.

6.2.4 Ultrasound Segmentation

The US images were segmented manually using a custom program in Matlab 7 (The Mathworks Inc, Natick, MA, USA) to extract points on the bone surface. Points were picked at the locus of maximum intensity which was assumed to be bone-soft-tissue interface. For features that are visible in the US images, sufficient points were picked to capture the bone curvature and an interpolating cubic spline was fitted to these points to approximate the surface within that frame.

The main difficulty is in distinguishing whether the image represents a bone contour, a soft tissue structure such as fat or muscle boundaries, or layers of muscle and fibres. If the US beam is at an oblique angle to the target structure, that is, not perpendicular to the layers of structure including soft tissue and bone could contribute to undesirable effects at the layers' interface. Materials have different refractive indices which means they can cause reflection as well as refraction, different beam thickness can also play a part.

The aim of this part is to generate a list of US points over the bone surface from freehand 3D US image. Figures 6.4 to 6.6 shows some of the US images acquired during the experiment. US points were extracted manually. Some of the femur bone surface can be easily seen in US images (Figure 6.4), some are not that well defined with possibly of ambiguity. A frame of US image could include bone as well as soft tissue, the more difficult frames included artefacts like noise and multiple reflections, Figure 6.5 (Femur US images) and Figure 6.6 (Pelvis US images) also show these examples. In some cases the frames were too noisy or difficult to distinguish whether bones were present, such that the frames were discarded.

Figures 6.7, 6.8 and 6.9 show all the US points extracted from femurs and pelves overlaid with their corresponding segmented CT surface using the gold standard registration. The CT surface and these US points were rendered using a script written in-house utilising the VTK libraries (Hartkens et al., 2002).

The femur US images concentrated mainly in the long shaft region where the femoral shaft

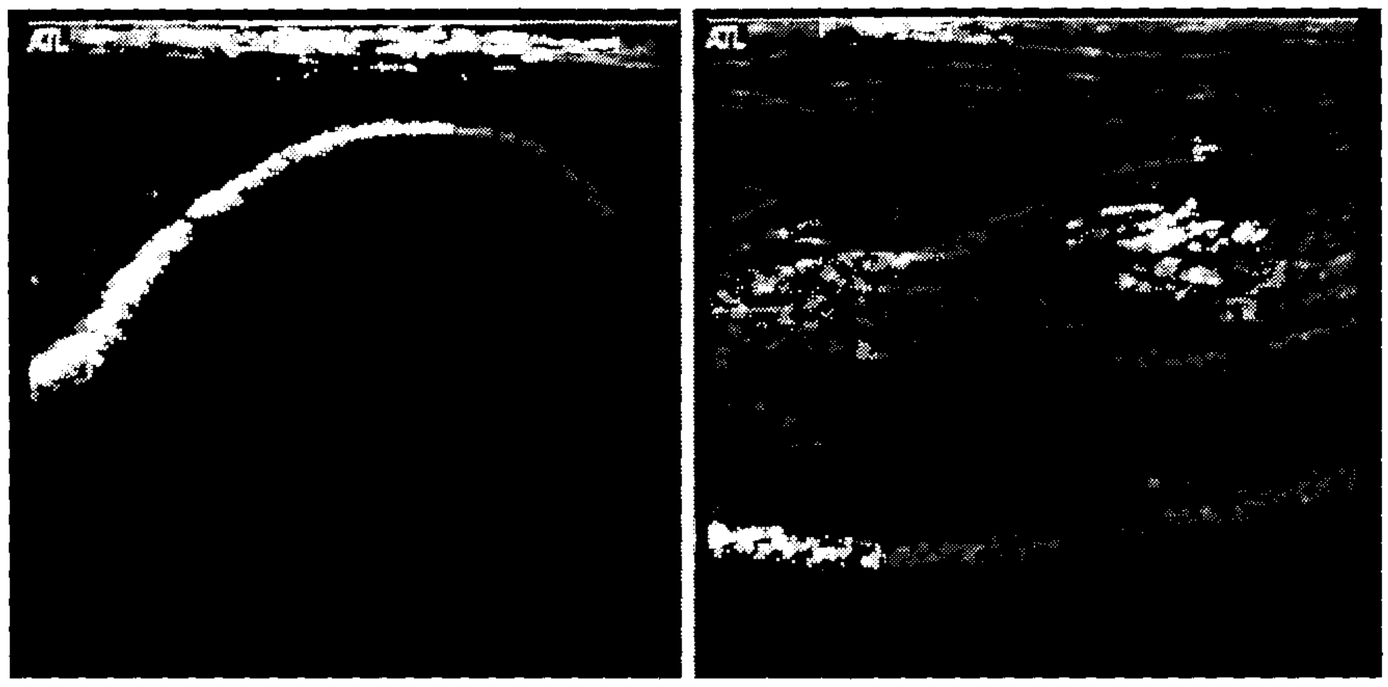

Figure 6.4: Examples of US images acquired from the femur during the experiment, showing images easily classified as brightly reflecting bone surfaces.

bone surface is clearly delineated with strong reflections, these can be unambiguously identified. This is the most accessible part of the femur and hence there are normally no complications associated with acquiring US images here. On the distal femur, images can usually be acquired on the condyles especially that behind the knee joint. On the proximal end of the femur, occasionally, images can be acquired near the greater trochanter. Unlike what was believed in the left femur phantom experiments in Chapters 3 and 4, here in a few cases, even some of the femoral neck and head can be imaged.

The pelvis US images, however, contain generally much more artefacts than the femur images. Unlike the femoral shaft, the pelvis does not have a long or flat region where clean images could be obtained, the whole pelvis is being surrounded by a big mass of thick muscle and layers of fat and soft tissues, so as to support the body and protect vital organs. This results in more multiple reflections than the femoral images, these appear as high intensity US reflections and it is therefore difficult to identify and delineate the bone-soft tissue interface. Some US images could be gathered on top of the pubic bones and around the iliac crests, but the bone around this rim is often quite thin cortical bone and hence not easy to be picked up as a bone surface during segmentation of the US images. There were also extracted points at a distance from the iliac crest which did not seem to be related. There are almost no points available for the ischium, except a few in cadaver 1. Also in cadaver 1, there were clearly some points coming away from the pubis, these probably arise from reflections from the implanted bone screws.

The time taken to segment these US images is rather dependent upon the number of images, but on average it takes around 30 seconds for each frame where points could be acquired.

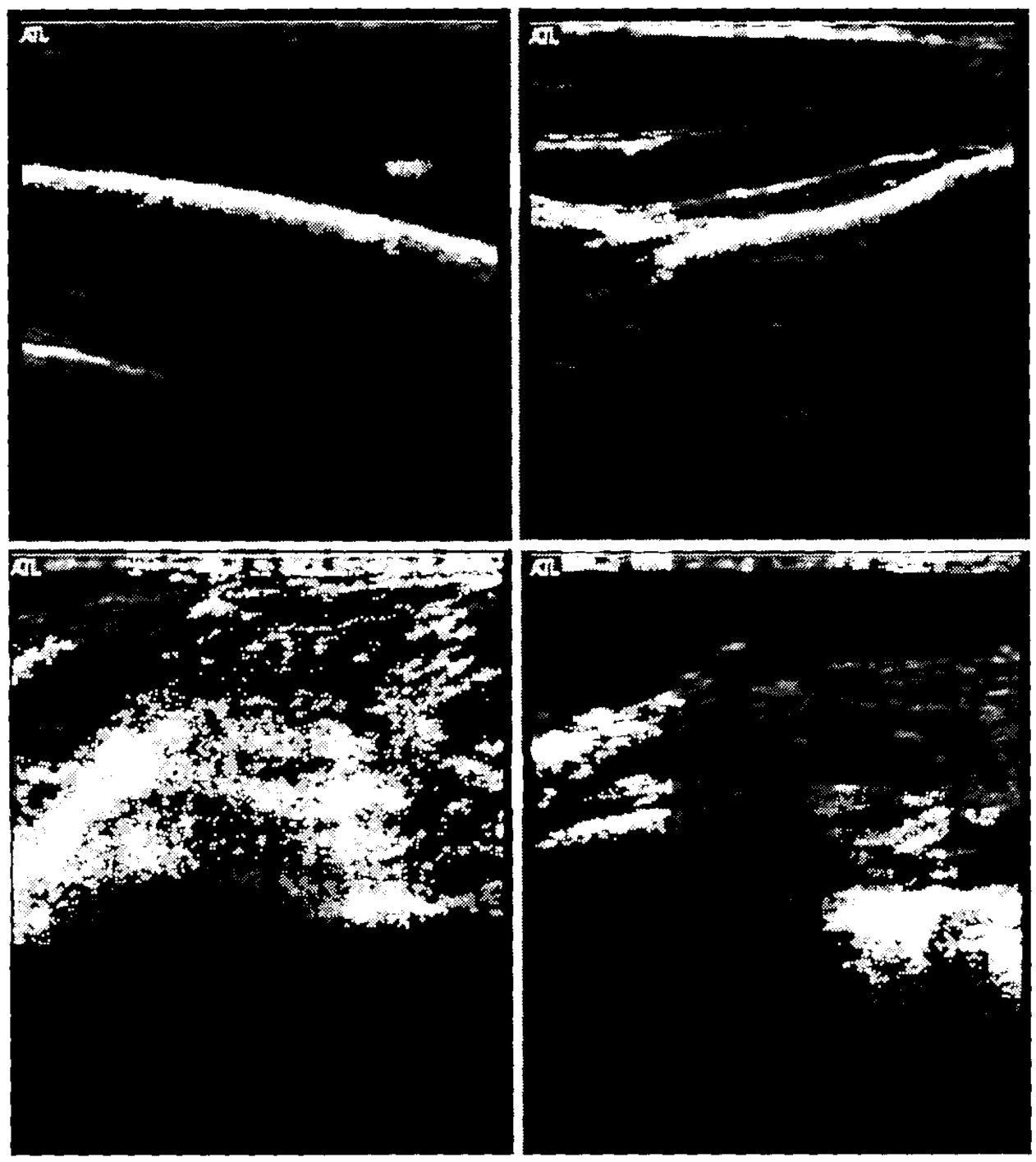

Figure 6.5: Examples of US images acquired from the femur during the experiment, showing different artefacts including multiple reflections (*top two*) and ambiguous images (*bottom two*).

6.2.5 Centre of Femoral Head

To calculate the centre of femoral head of the femur, the leg is moved continuously and slowly about the hip joint through around 45° flexion and 30° abduction/adduction for roughly one minute. As the leg is being moved, the dynamic reference object attached to the femur is being tracked, the centre of rotation is assumed to be unchanged during moving of the leg and this point is calculated by locating the invariant point relative to the reference coordinate system. Table 6.2 shows the localisation error for each femur's pivoting point.

6.3 Ultrasound Instantiation

The US instantiation procedure and ICP are the same as that described in chapters 3 and 4. The optimisation strategy adopted is the multiple-layer golden section search, described in Section 4.4.2.1 (page 100) and is quickly summarised in the next section.

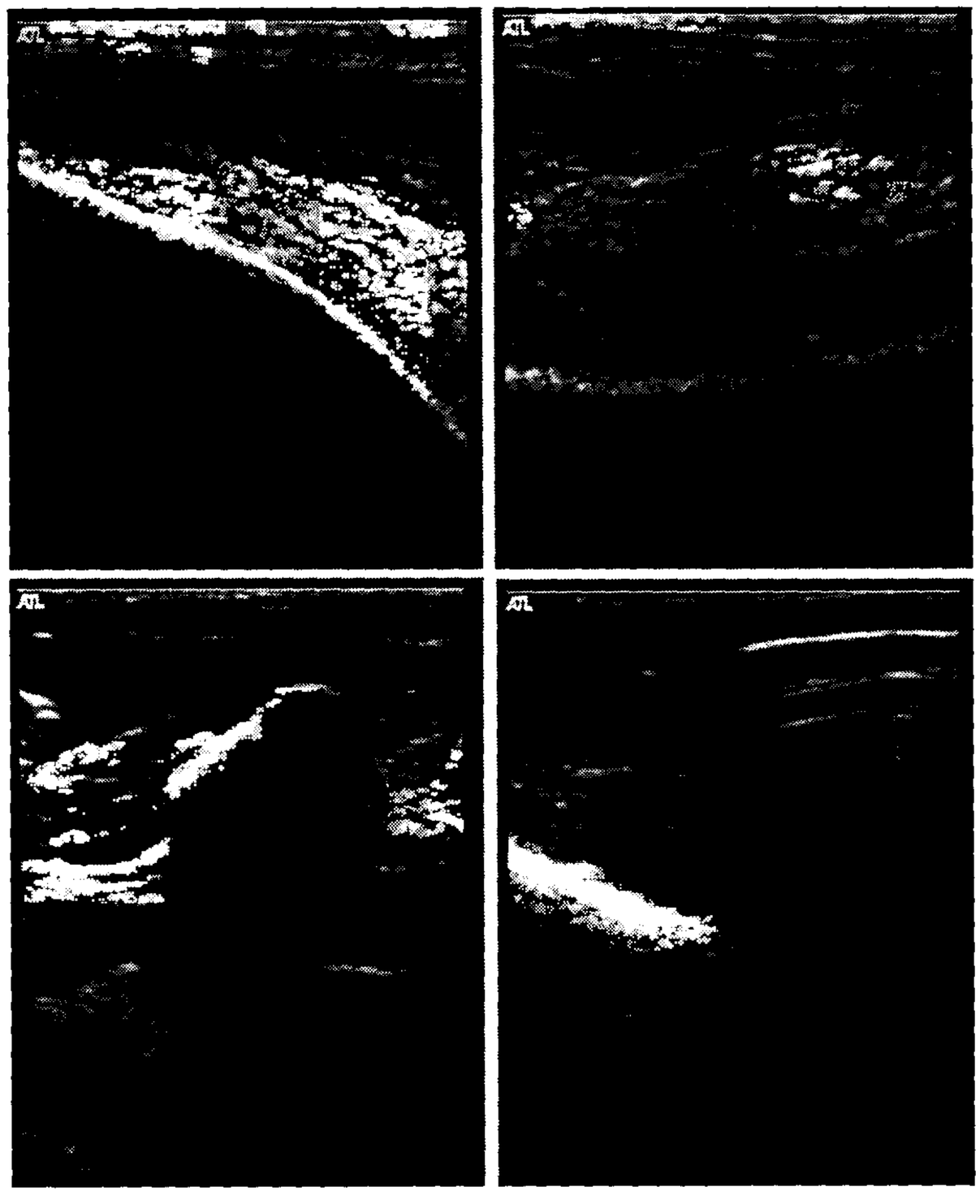

Figure 6.6: Examples of US images acquired from the pelvis during the experiment. These images show bones that could be easily classified as bright reflecting bone surfaces (*top two*) and ambiguous surfaces (*bottom two*).

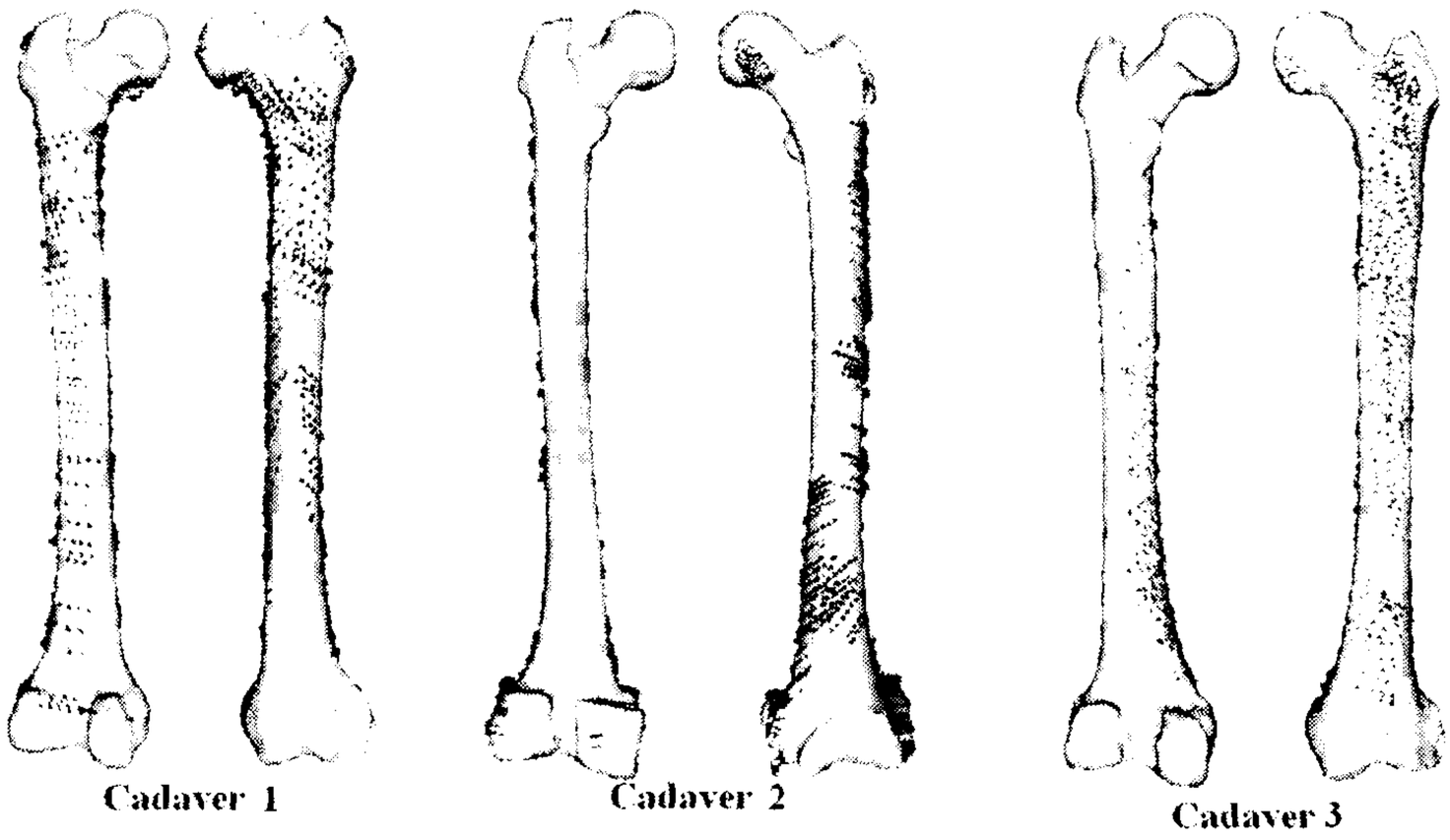

Figure 6.7: Posterior and anterior views of extracted US points of left femurs overlaid with their corresponding CT-derived surfaces.

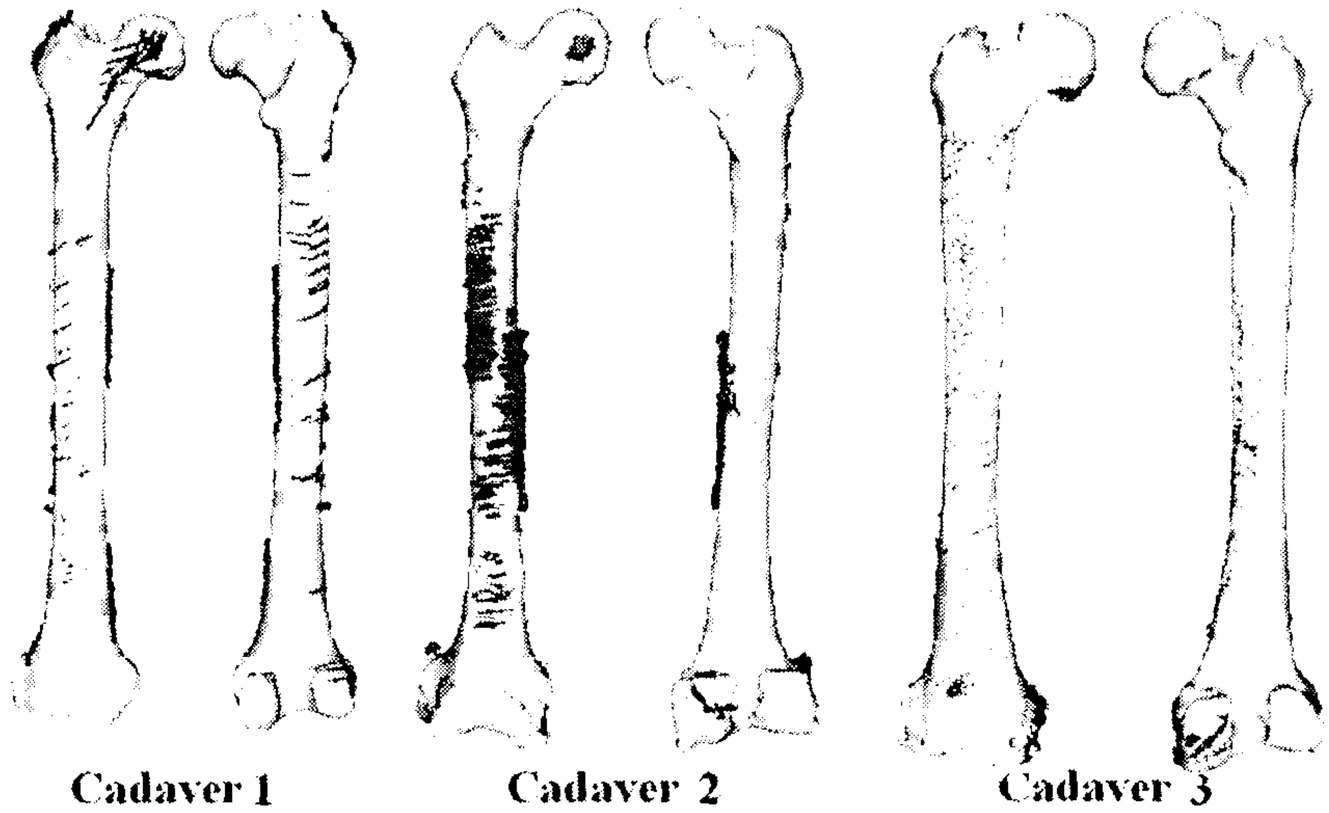

Figure 6.8: Posterior and anterior views of extracted US points of right femurs overlaid with their corresponding CT-derived surfaces.

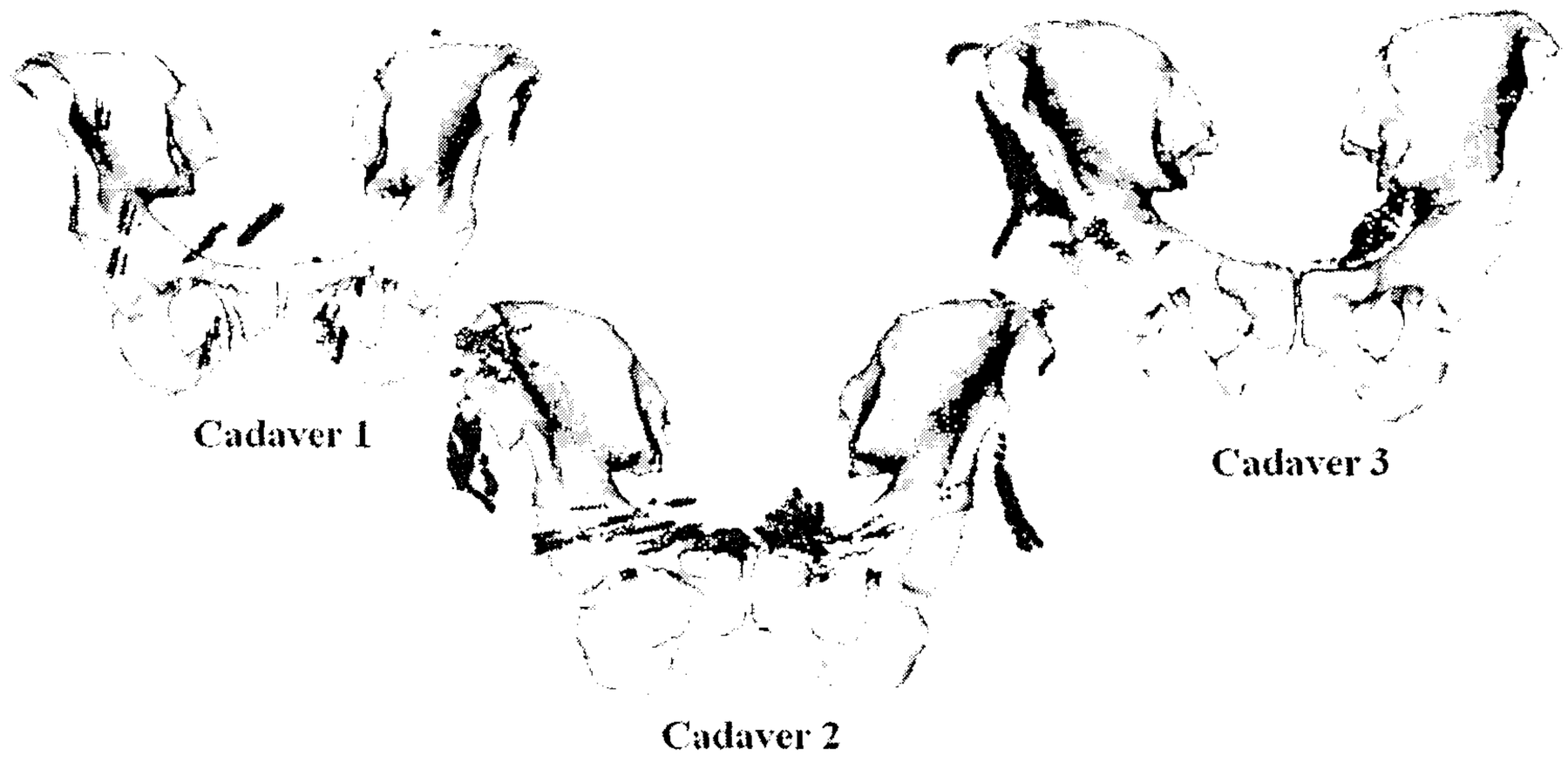

Figure 6.9: Extracted US points of pelves overlaid with their corresponding CT-derived surfaces.

Table 6.2: Centre of femoral head localisation error for each femur

Cadaver	Left Femur (mm)	Right Femur (mm)
1	0.49	0.46
2	0.64	0.70
3	0.98	0.58

6.3.1 Optimisation

Given the first 5 modes of variation, the root-mean-square (RMS) point-to-surface distance was minimised using a multiple layer optimisation strategy. In this scheme, the weight corresponding to each mode of variation of the SSM was varied and the US points registered to the resulting shape model using the ICP algorithm. This is a four layer optimisation strategy, where the weights of the first two modes were altered at layer 1 (modes 1 and 2) and this was increased to the weights of the first five modes by layer 4 (modes 1 to 5). On each iteration, a golden section search (Press et al., 1992; Thacker and Cootes, 1996) was used to optimise the shape within one mode alone, with the weight corresponding to all other modes held constant.

6.3.2 Removing Outliers

The total number of US-derived surface points used in each instantiation was between 992 and 3500. Using visual inspection, the femur images appear to have no outliers and therefore no points were removed before instantiation.

For the pelvis, Section 6.2.4 mentioned that the US points were segmented by hand and that some acquired images could be ambiguous to process. This means some images were wrongly classified as bone even though these brightly reflecting surface could be something else. This has especially prominent effects for the pelvic images because the pelvis is a complex structure and US points were generally harder to acquire. Incorrectly extracted US points also contribute towards outliers in the US point cloud generated which would confuse the optimisation algorithm causing inaccurate instantiations and registration.

The pelvic US points obtained from manual segmentation had clearly visible gross outliers. These were removed automatically using a method that involves aligning the US points with the mean shape, the 5% points with the largest RMS point-to-surface distance were excluded from the instantiation (referred to as "pruning 5%"). Table 6.3 shows the number of US points used in each cadaver's instantiation.

For comparison purposes, another method was employed to remove outliers. This method involves visual inspection by an expert with bone anatomy knowledge. The expert examines the 3D cloud of US points, with user control of view, which revealed a number of US points which were obvious outliers, these were removed manually. When viewing the US points of the pelvis, both cadavers 1 and 2 had obvious US surface points which were clearly not part of the pelvic bone. Some of these outliers appeared to be soft tissue, part of the femoral head or even the bone screws. In order not to remove genuine points, these points were carefully considered before

Table 6.3: Number of ultrasound points used for instantiation

Cadaver	Bone	Original Number of US surface points	Number of US points after pruning 5% outliers	Number of US points after manually removed outliers (number removed)
1	Left femur	1128	-	-
	Right femur	1477	-	-
	Pelvis	1500	1425	1384 (116)
2	Left femur	992	-	-
	Right femur	3071	-	-
	Pelvis	2889	2744	2040 (849)
3	Left femur	1129	-	-
	Right femur	3500	-	-
	Pelvis	2000	1900	2000 (0)

being removed. On the other hand, cadaver 3 looks very reasonable and no points were removed manually. The time taken for both processes were minimal and very quick. After the outliers were removed, the instantiation process starts.

6.3.3 Robustness Experiments

In order to test robustness of the instantiation, multiple starting positions for the rigid body registration parameters were used. In the phantom experiments in Chapters 3 and 4, different starting positions were generated randomly by adding random noise of standard deviation of 10° and 10mm to an initial position. To make this experiment similar to the clinical setting, four observers were invited to produce 3 starting positions where, for each attempt, the US surface point cloud had to be overlaid closest to the model mean shape, after each attempt this aligning program is restarted for the observer to produce another starting estimate. This process could potentially be automated, and is to be discussed in the next chapter.

This process gives 12 starting positions in total for each bone. Figure 6.10 shows the in-house program used, the bone surface shown is the mean shape overlaid with the US surface points. The user has full control over the view, moving both the mean shape surface or the US points, when the user is satisfied that both surface and points lie well in line with each other, the transformation

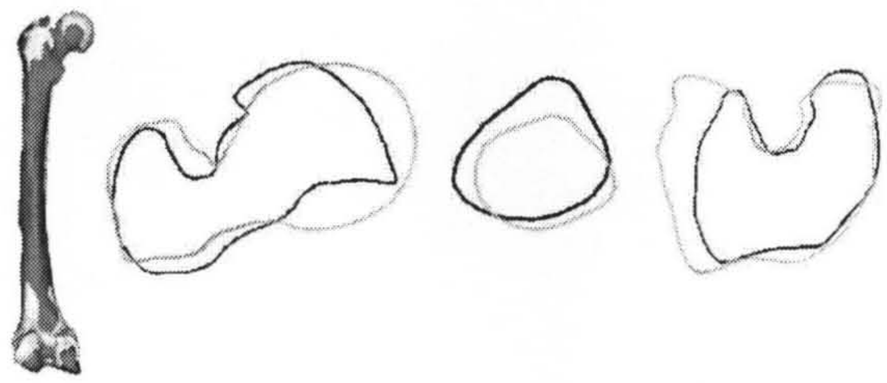

Figure 6.22: Visualisation of Cadaver 3 right femur instantiation results, US with centre of femoral head. These contours have shown large errors in the femoral head and condyles.

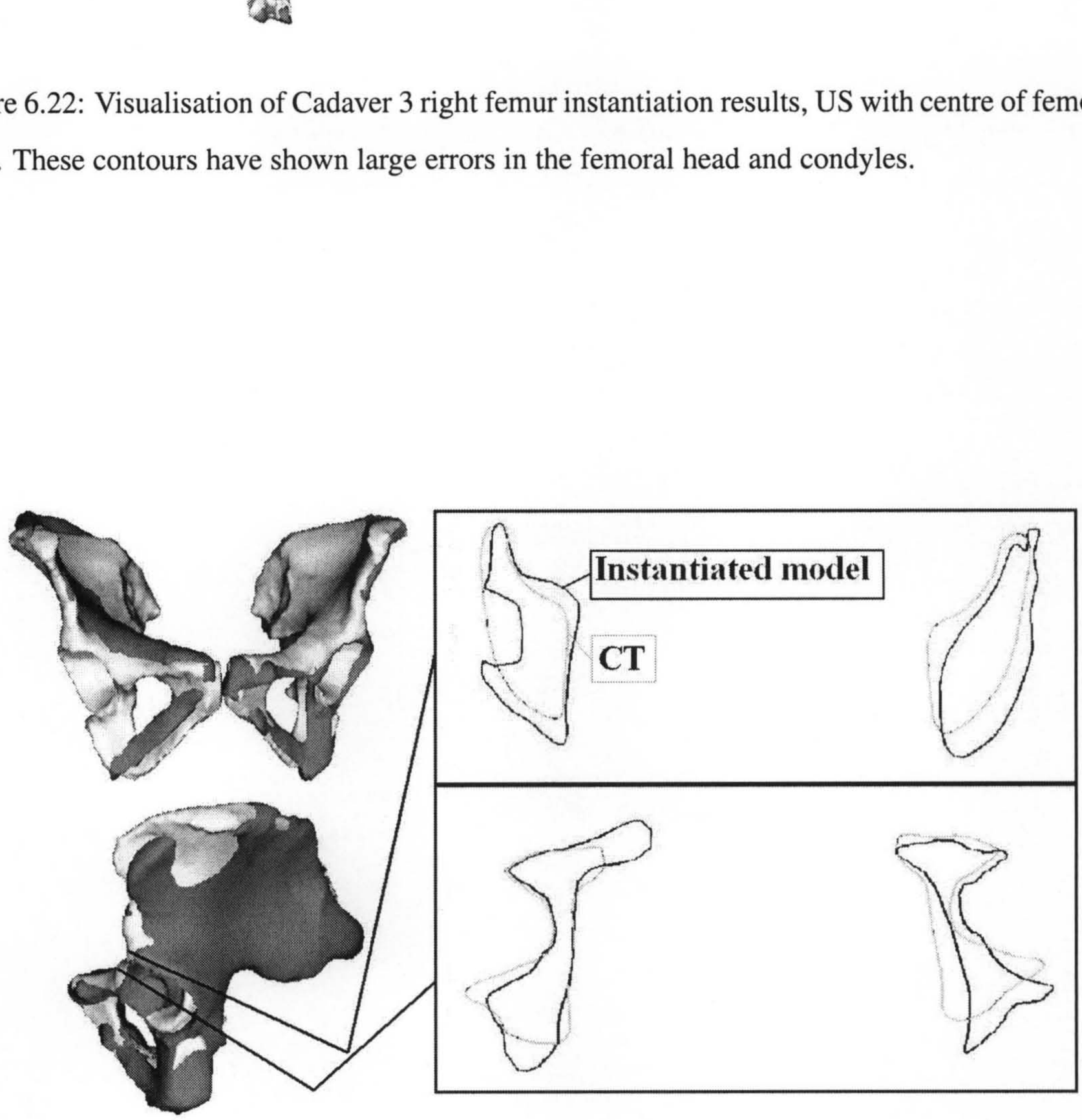

Figure 6.23: Visualisation of Cadaver 1 pelvis: The instantiated SSM (*frontal* and *lateral* views) overlaid on the CT-derived surface, shown in dark grey. Cross-sectional contours from the instantiated pelvis model (*black*) with corresponding contours from the CT-derived surface (*grey*). From top to bottom: near top of acetabulum and middle of acetabulum.

The rotation matrix $\mathbf{R}$ is a 3×3 matrix

$$\mathbf{R} = \begin{pmatrix} cos\beta cos\gamma & cos\alpha sin\gamma + sin\alpha sin\beta cos\gamma & sin\alpha sin\gamma - cos\alpha sin\beta cos\gamma \\ -cos\beta sin\gamma & cos\alpha cos\gamma - sin\alpha sin\beta sin\gamma & sin\alpha cos\gamma + cos\alpha sin\beta sin\gamma \\ sin\beta & -sin\alpha cos\beta & cos\alpha cos\beta \end{pmatrix}$$

While the translation $\mathbf{t}$ is a column vector with only 3 elements.

The rotation matrix and the translation components can be combined to form a rigid-body transformation, a 4×4 matrix using homogeneous coordinates:

$\mathbf{T_{rigid}(x)} =$

$$\begin{pmatrix} cos\beta cos\gamma & cos\alpha sin\gamma + sin\alpha sin\beta cos\gamma & sin\alpha sin\gamma - cos\alpha sin\beta cos\gamma & t_x \\ -cos\beta sin\gamma & cos\alpha cos\gamma - sin\alpha sin\beta sin\gamma & sin\alpha cos\gamma + cos\alpha sin\beta sin\gamma & t_y \\ sin\beta & -sin\alpha cos\beta & cos\alpha cos\beta & t_z \\ 0 & 0 & 0 & 1 \end{pmatrix} \begin{pmatrix} x \\ y \\ z \\ 1 \end{pmatrix} \tag{6.1}$$

In this experiment, 4 observers were invited to produce 3 starting positions each, giving a total of 12 starting positions for each femur or pelvis. For each femur the same starting positions were used for both US only and US with the centre of the femoral head as pivot point instantiations for comparison purposes.

There are 2 types of coordinate systems involved in the registration process: the world (US) coordinate system and the model (CT) coordinate system. The world coordinate system registers positions of the US scans, this coordinate system might somehow be registering the bone in a manner that is not easy to interpret because this follows an arbitrary orientation of the optical tracker. For the model coordinate system, since the bone was first CT scanned for producing the model, the bone is thought to be roughly aligning with the z-axis, meaning this is the axis along the shaft of the femur and the mid-line of the pelvis. The registration problem here involves determining the 4×4 homogeneous world-to-model transformation matrix.

This study finds out how similar were the starting estimates positioned in terms of standard deviations. The starting positions of the instantiations were stored as 4×4 transformation matrices. The translational components in the 4×4 transformation matrix could be used directly for the calculations because it is already in the model space. The rotations, however, required a few extra steps. In order to calculate the true rotational effects, the rotations should be calculated relative to the original axes they were rotated about in the world space, hence the rotations had to be transformed back to the world coordinates by inverting the transformation matrix, and then

Bone	Cadaver	Translation (mm) x	y	z	Rotation (degrees) x	y	z
Left	1	2.7	3.7	2.8	1.6	1.7	19.1
Femur	2	3.1	5.0	15.3	2.6	2.4	14.9
	3	5.1	4.7	7.3	4.8	1.1	25.6
Right	1	2.8	3.4	6.5	1.8	1.3	17.9
Femur	2	3.7	3.9	11.5	3.9	1.9	18.3
	3	7.4	9.6	6.5	3.2	1.7	19.9
Pelvis	1	5.1	10.8	5.7	10.1	8.4	12.4
	2	3.8	18.5	10.6	19.5	8.8	16.8
	3	4.0	10.9	9.6	12.9	6.1	23.4

Table 6.4: Starting positions analysis in terms of standard deviations

decomposed into their constituent parameters α, β and γ as described above in Equation 6.1. The results are shown in Table 6.4.

As mentioned earlier, in the model coordinate system, the bone was roughly aligned with the z-axis along the bone shaft. One of the main modes of shape variation of the femur was the length and other modes included twist of the bone. Since not all bones are of average length, it would be expected the translations and rotations of the z-axis would be the greatest for most femur starting positions. This is true for most cases except in the left femur of cadaver 1 and right femur of cadaver 3.

The pelves were generally harder to align because the points were mostly a band of points around the top rims and there were less prominent features to align with. The translations in the y-axis are relatively bigger than those in other axes. However, the y-axis rotations appear to be smaller compared with those in the x-axis and z-axis.

6.4 Results

The SSM models used in this experiment are the same as those described in Chapter 4 for the femur and Chapter 5 for the pelvis.

The results of the femur (without femoral head pivot point) and pelvis (using pruning of 5% points) instantiations from cadaver 1 are illustrated in Figures 6.11 and 6.24 respectively. In each figure, the bone surface segmented from the CT scan was used as the ground-truth shape model.

Results from other cadavers were similar and shown in subsequent pages.

6.4.1 Numerical Results

All the numerical results in this section were calculated using the method in Section 3.4.1 on page 81:

Tables 6.5 and 6.7 (femurs), 6.9, 6.10 and 6.12 (pelves) show residual distance between the instantiated SSM and the US-derived cadaver surface points registered using ICP, and RMS distance calculated between the instantiated SSM and the CT-derived surface registered using ICP. These tables show how consistent is the resulting bone shape with the original shape.

Tables 6.6 and 6.8 (femurs), 6.11 and 6.13 (pelves) show RMS distance calculated between the instantiated SSM and the CT-derived gold standard surface. This measure indicates the combined accuracy of the geometry of the instantiated model and its registration in physical space.

In the last two columns of each table, the column marked "CT-Model (global)" measures the RMS distance across the entire surface of the bone, while that marked "CT-Model (regional)" measures the RMS distance around the area of clinical relevance. For the purpose of hip replacement surgery, the area of interest would be around the femoral head and the trochanters for the femur and the acetabulum for the pelvis.

In all cases, all of the 12 starting positions converged to the same RMS distance within 0.1 mm.

6.4.2 Femur Results

Instantiation results for the femurs are shown graphically in Figures 6.11- 6.22 by aligning the instantiated surface with the corresponding CT-derived surface using ICP, and numerically in Tables 6.5 to 6.8. Results from cadaver 1's left femur, without the femoral head pivot point, are shown in Figure 6.12. Results from other femurs are also shown in subsequent figures.

The results show that the RMS residual error after registering the model and US points was between 1.1 and 2.0mm when using US only and between 2.3 and 3.5mm when the centre of the femoral head point was incorporated. When the RMS distance is calculated across the entire femur between the instantiated model and the CT-derived surface, registered using ICP, the results are between 1.9 and 4.1mm (US only) and 2.0 and 5.3mm (US with centre of femoral head as pivot point). This measure, shown in the tables marked "ICP", shows how consistent the instantiated bone shapes are with respect to the gold standard shape derived from the CT scan. When using the gold standard registration to transform the instantiated bone surfaces and comparing these surfaces

with their corresponding CT-derived surface, the results are between 2.7 and 5.0mm (US only) and 3.2 and 7.7mm (US with centre of femoral head as pivot point). These results, shown in the tables marked "GS", shows how well the instantiated shapes was registered in physical space as well as the accuracy of their geometry.

Since the application area of this study is hip replacement surgery, an RMS distance was also determined in the region of most clinical relevance: In the femur the RMS distance errors were recomputed in the region of the femoral head, femoral neck and the greater and lesser trochanters. In this region, the RMS distance after ICP (Tables marked "ICP") the range is 1.8 to 5.1mm (US only) and 2.6 to 6.4mm (US with centre of femoral head pivot point). When the gold standard registration was used (Tables marked "GS"), the RMS distance yielded were in the range 1.8 to 7.4mm (US only) and 3.2 to 8.6mm (US with centre of femoral head pivot point).

One of the femur RMS distances, the right femur of cadaver 3, is particularly high. Having checked through the data, this is thought to be due to poorly sampled US images in the region of the greater trochanter and femoral head. No data points were acquired near the proximal end of the trochanter region. This is shown in Figure 6.8's cadaver 3 (Page 126).

If this is excluded the range of RMS error, computed in the region of the femoral head and neck, reduces to between 1.8 and 4.4mm (without femoral head point) to the gold standard and 1.8 to 3.7mm (without femoral head point) after ICP.

6.4.3 Pelvis Results

Instantiation for pelves are shown graphically in Figures 6.23 to 6.29 by aligning the instantiated surface with the corresponding CT-derived surface using ICP, and numerically in Tables 6.9 to 6.13.

The pelvis is surrounded by layers of fat and soft tissues, and the US points acquired contained more artefacts than femurs. The errors from pelvis instantiations are therefore higher than those of the femurs.

Initially, instantiations were computed and the RMS distance error obtained were exceptionally high for cadaver 2; although the instantiated surface did have the shape of a pelvis, some of the instantiated modes were large numbers of standard deviations(SDs) and hence created a combination of distortions. Results from cadaver 1 are shown in Figure 6.23. The RMS error calculated between the instantiated SSM and the CT surface registered using ICP from all 3 cadavers are shown in Table 6.9.

Section 6.3.2 commented that cadavers 1 and 2 had visible gross outliers that were clearly

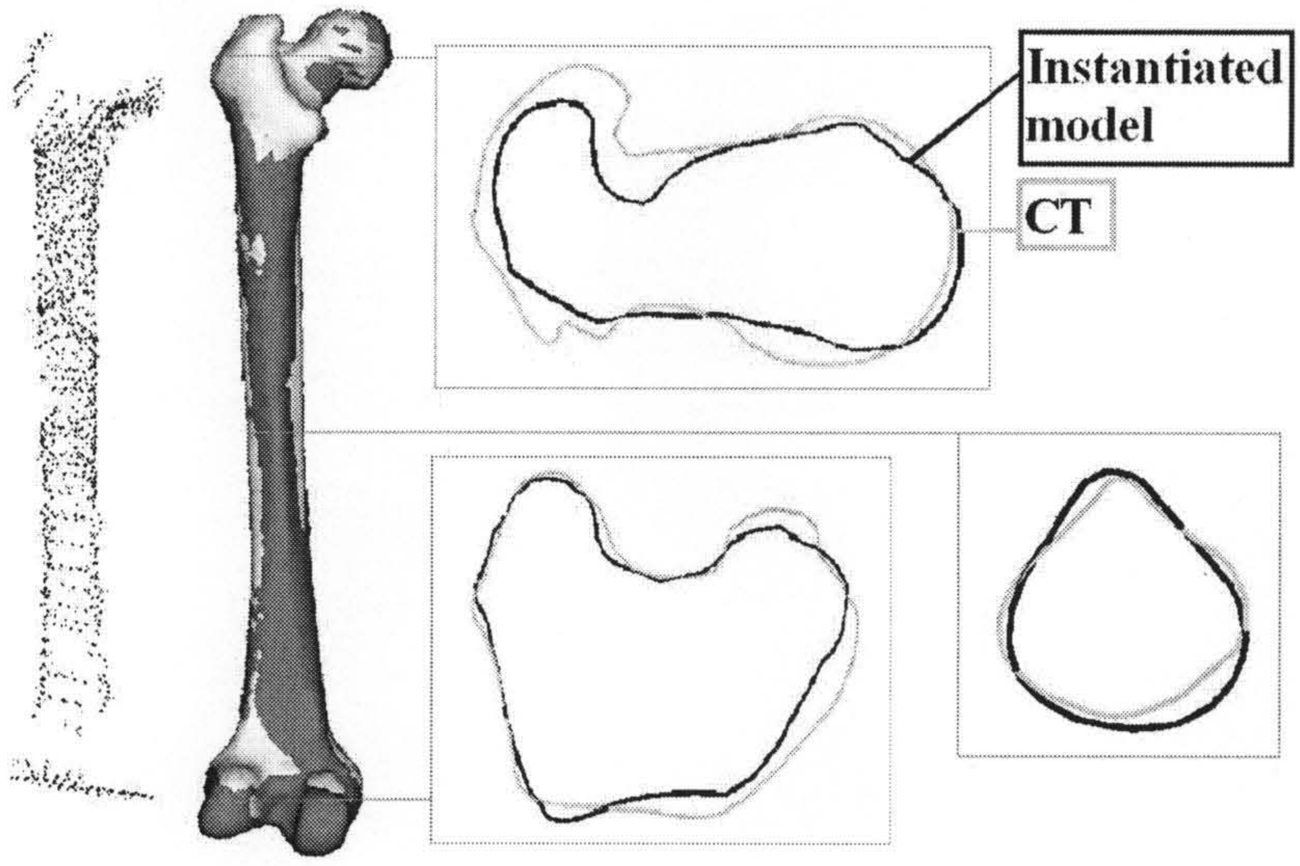

Figure 6.11: (Left to right) Visualisation of cadaver 1 left femur instantiation results, US only: Ultrasound-derived femur surface points (left) and the instantiated SSM overlaid on the CT-derived surface, shown in dark grey. Cross-sectional contours from the instantiated femur model (black) with corresponding contours from the CT-derived surface (grey). Anti-clockwise from top: the femoral head, condyles, and mid-shaft.

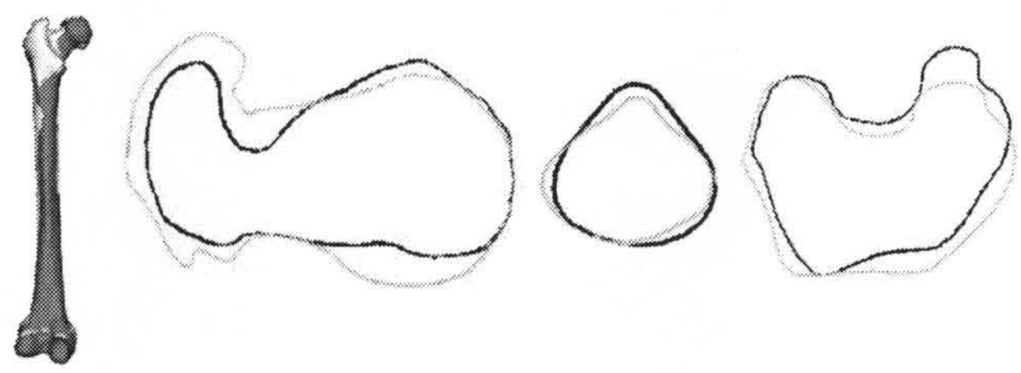

Figure 6.12: Visualisation of Cadaver 1 left femur instantiation results, US with centre of femoral head. Cross-sectional contours from the instantiated femur model (*black*) with corresponding contours from the CT-derived surface (*grey*). From left to right: the femoral head, mid-shaft, and condyle. This description holds for all the following figures.

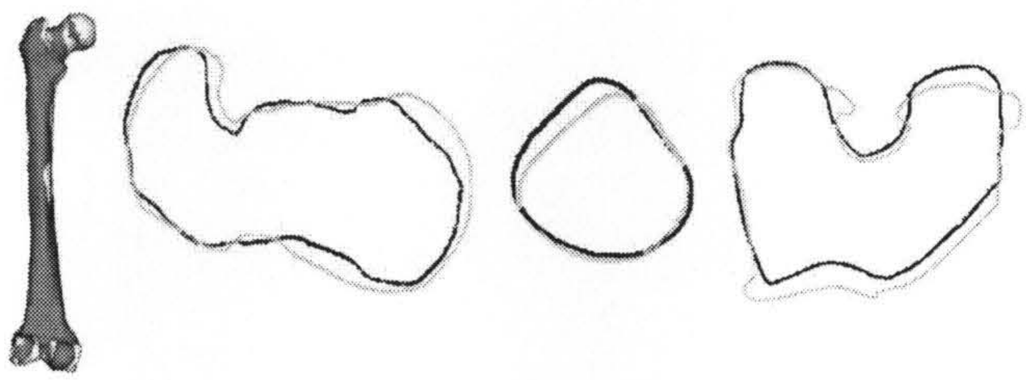

Figure 6.13: Visualisation of Cadaver 2 left femur instantiation results, US only.

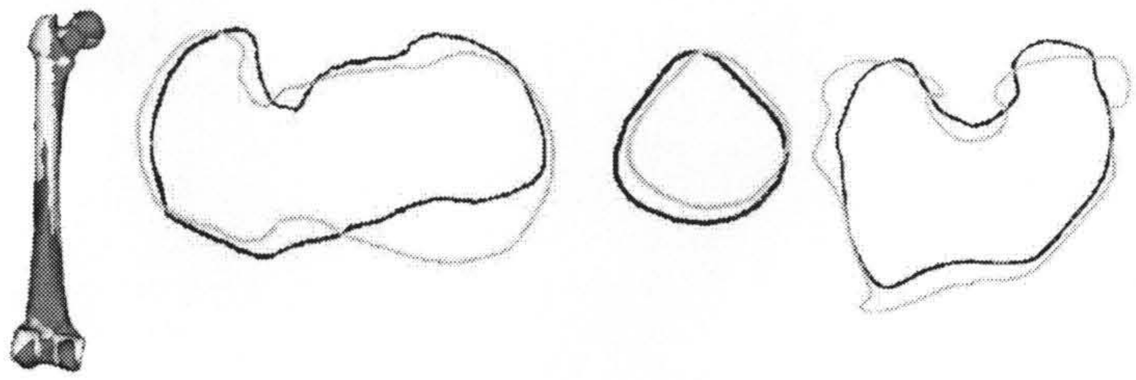

Figure 6.14: Visualisation of Cadaver 2 left femur instantiation results, US with centre of femoral head. Comparing with the same femur's instantiation using US only, the femoral head here is registered less accurately even with the centre of femoral head pivoting point. The shape of the condyles are also showing some errors.

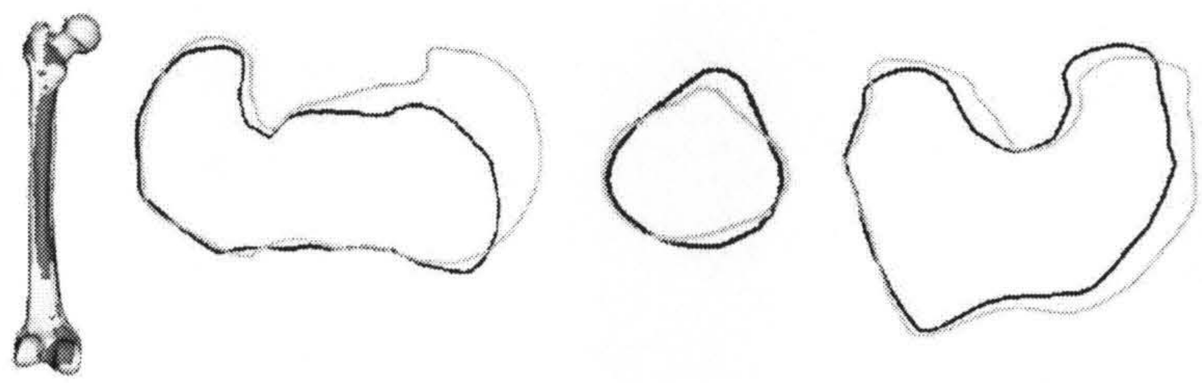

Figure 6.15: Visualisation of Cadaver 3 left femur instantiation results, US only. The part near the femoral head and condyles are both show some errors.

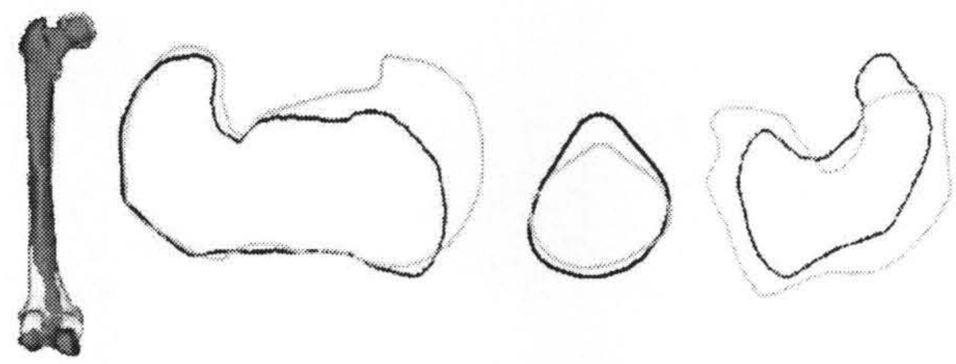

Figure 6.16: Visualisation of Cadaver 3 left femur instantiation results, US with centre of femoral head. The part near the femoral head and near the condyles show large errors. It can be seen in the overlay image on the very left that the instantiated surface is longer than the CT-derived surface.

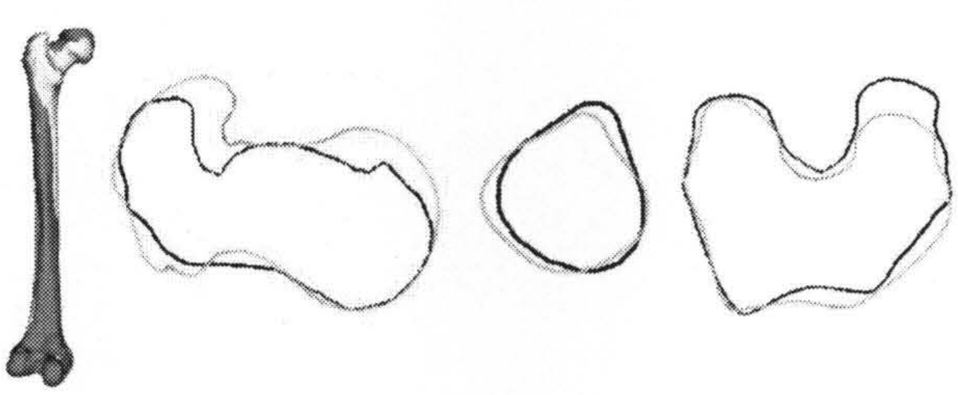

Figure 6.17: Visualisation of Cadaver 1 right femur instantiation results, US only. Small errors can be seen in the femoral head and condyles.

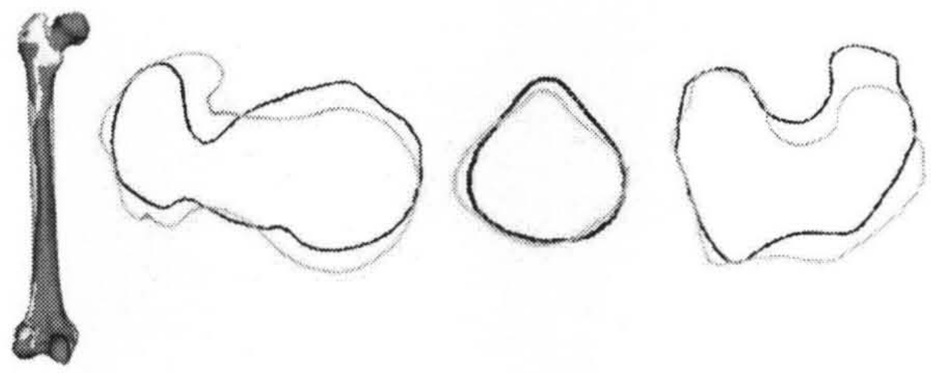

Figure 6.18: Visualisation of Cadaver 1 right femur instantiation results, US with centre of femoral head. While the part in the femoral head have shown some errors, there is clearly a rotational misalignment in the condyles.

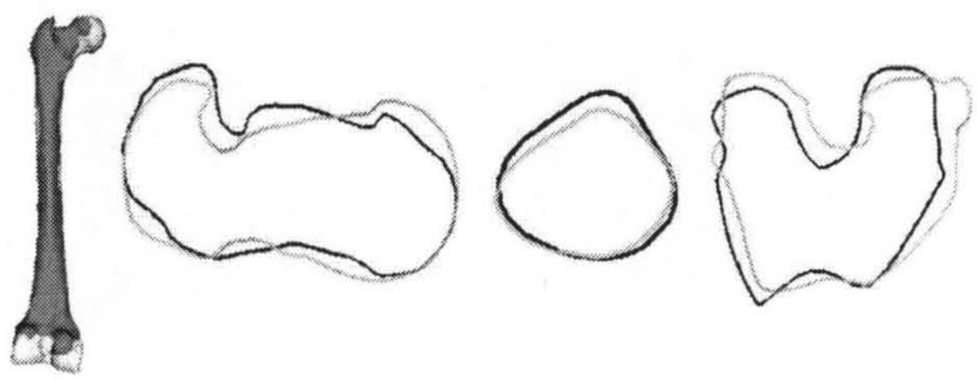

Figure 6.19: Visualisation of Cadaver 2 right femur instantiation results, US only. The part near the condyles shows some error. The overlay image on the left shows the instantiated surface is shorter than the CT-derived surface.

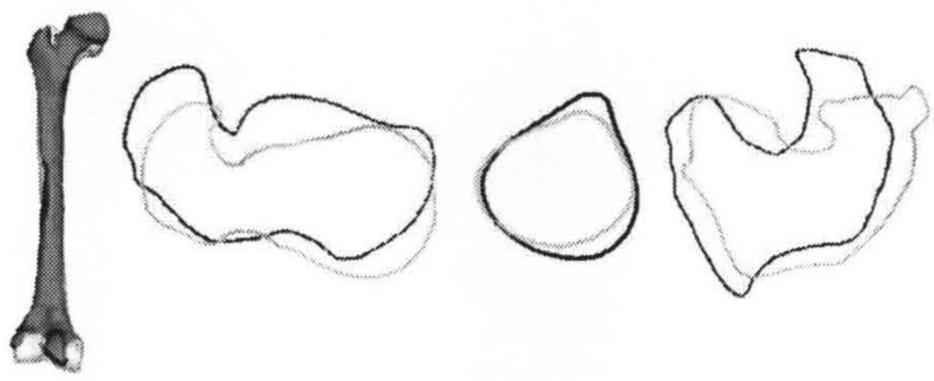

Figure 6.20: Visualisation of Cadaver 2 right femur instantiation results, US with centre of femoral head. Both the parts in the femoral head and condyles were not registered or instantiated accurately.

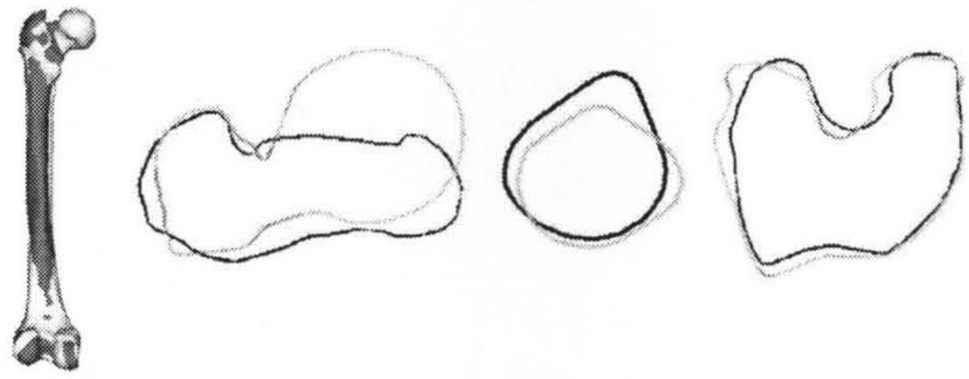

Figure 6.21: Visualisation of Cadaver 3 right femur instantiation results, US only. The femoral head shows large errors with a clearly rotational misalignment.

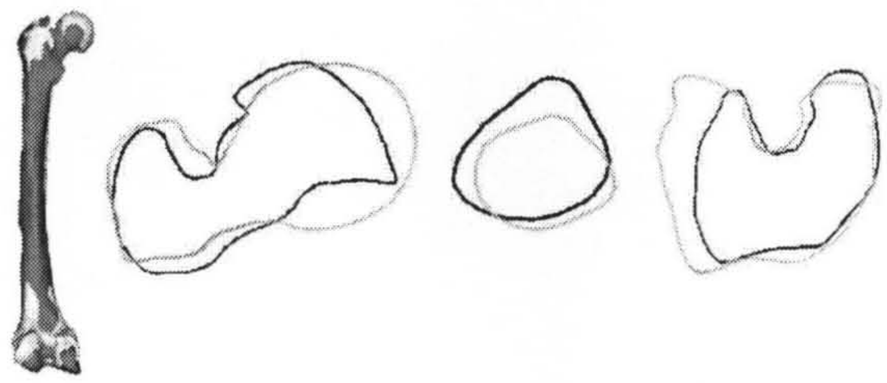

Figure 6.22: Visualisation of Cadaver 3 right femur instantiation results, US with centre of femoral head. These contours have shown large errors in the femoral head and condyles.

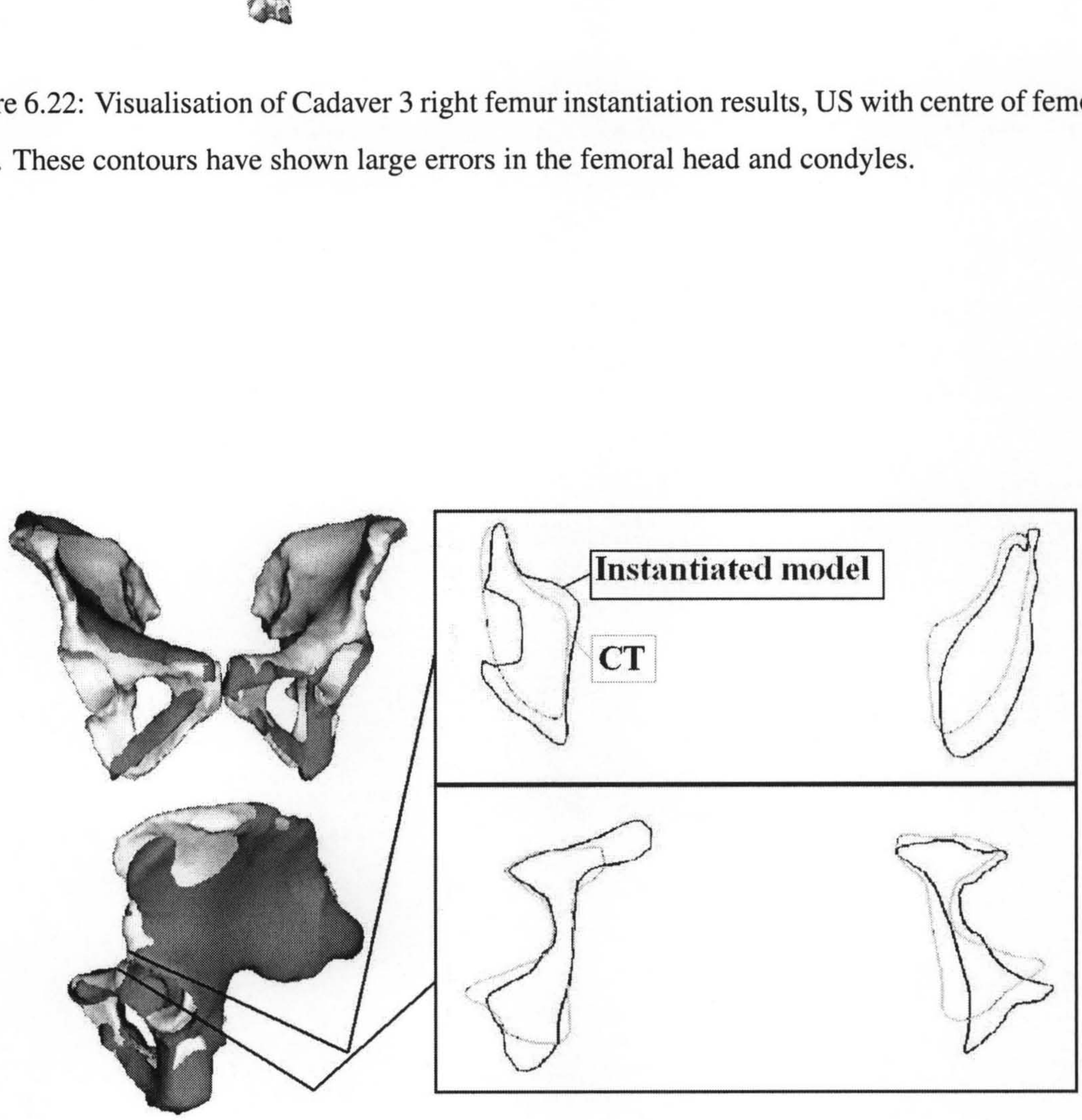

Figure 6.23: Visualisation of Cadaver 1 pelvis: The instantiated SSM (*frontal* and *lateral* views) overlaid on the CT-derived surface, shown in dark grey. Cross-sectional contours from the instantiated pelvis model (*black*) with corresponding contours from the CT-derived surface (*grey*). From top to bottom: near top of acetabulum and middle of acetabulum.

Table 6.5: Errors for instantiated cadaver femur surfaces, US only (shape) (mm) - ICP

Cadaver	Error statistic	US-Model*	CT-Model (global)**	CT-Model (regional)***
1	RMS	2.0	2.2	2.5
Left	Median	1.2	1.5	1.7
femur	95% CL	3.9	4.3	4.8
2	RMS	1.5	1.9	1.8
Left	Median	0.9	1.3	1.1
femur	95% CL	3.1	3.5	3.5
3	RMS	1.5	2.7	3.7
Left	Median	0.9	1.5	1.7
femur	95% CL	3.2	4.9	9.2
1	RMS	1.8	2.8	3.7
Right	Median	1.1	1.7	2.6
femur	95% CL	3.7	5.5	7.1
2	RMS	1.1	3.0	3.1
Right	Median	0.6	2.2	2.3
femur	95% CL	2.1	5.4	5.5
3	RMS	1.7	4.1	5.1
Right	Median	1.0	2.5	3.6
femur	95% CL	3.3	7.9	10.1

95% CL = 95% Confidence Level

*Distance between US-derived bone surface points and the instantiated SSM surface.

**Distance between the vertices of the surface mesh, which describes the instantiated SSM surface, and the CT-derived bone surface calculated by aligning the datasets using the ICP algorithm.

***As for **, but with the measure restricted to regions of clinical interest.

Table 6.6: Errors for instantiated cadaver femur surfaces, US only (shape and final position) (mm) - GS

Cadaver	Error statistic	CT-Model (global)*	CT-Model(regional)**
1	RMS	3.2	2.9
Left	Median	1.9	1.9
femur	95% CL	6.7	5.9
2	RMS	2.7	1.8
Left	Median	1.6	1.2
femur	95% CL	5.5	3.6
3	RMS	3.1	3.7
Left	Median	1.5	1.7
femur	95% CL	6.4	8.9
1	RMS	3.5	4.4
Right	Median	2.0	3.1
femur	95% CL	7.3	8.2
2	RMS	4.5	3.1
Right	Median	2.7	2.6
femur	95% CL	9.9	5.6
3	RMS	5.0	7.4
Right	Median	2.3	4.7
femur	95% CL	11.1	5.6

95% CL = 95% Confidence Level

*Distance between the vertices of the surface mesh, which describes the instantiated SSM surface, and the CT-derived bone surface calculated after transforming the CT surface to physical space using the Gold Standard, fiducial-based registration transformation.

**As for *, but with the measure restricted to regions of clinical interest.

Table 6.7: Errors for instantiated cadaver femur surfaces, US with centre of femoral head (shape) (mm) - ICP

Cadaver	Error statistic	US-Model	CT-Model (global)	CT-Model (regional)
1	RMS	2.3	2.0	2.6
Left	Median	1.3	1.5	1.8
femur	95% CL	5.0	3.6	5.0
2	RMS	3.5	3.2	3.0
Left	Median	1.8	2.1	2.0
femur	95% CL	8.8	6.3	5.7
3	RMS	2.6	5.3	6.4
Left	Median	1.6	3.5	4.0
femur	95% CL	5.0	11.3	12.8
1	RMS	3.0	2.5	3.3
Right	Median	1.6	1.7	2.5
femur	95% CL	5.0	4.9	5.8
2	RMS	2.7	4.3	5.4
Right	Median	1.4	2.8	3.9
femur	95% CL	6.2	8.7	10.1
3	RMS	2.3	4.4	5.6
Right	Median	1.4	2.8	3.7
femur	95% CL	4.7	8.8	10.8

Table 6.8: Errors for instantiated cadaver femur surfaces, US with centre of femoral head (shape and final position) (mm) - GS

Cadaver	Error statistic	CT-Model (global)	CT-Model(regional)
1	RMS	3.2	3.3
Left	Median	2.0	2.2
femur	95% CL	6.4	6.7
2	RMS	3.5	3.2
Left	Median	2.4	2.3
femur	95% CL	6.8	6.4
3	RMS	7.7	5.6
Left	Median	3.7	4.0
femur	95% CL	18.0	10.7
1	RMS	4.2	4.2
Right	Median	2.3	2.9
femur	95% CL	8.7	8.4
2	RMS	7.0	8.6
Right	Median	4.5	6.6
femur	95% CL	14.4	16.2
3	RMS	5.3	5.1
Right	Median	3.0	3.5
femur	95% CL	10.8	9.8

Table 6.9: Errors for instantiated pelvic surfaces (shape) (mm) - ICP

Cadaver	Error statistic	US-Model	CT-Model(global)	CT-Model(regional)
1	RMS	7.1	5.2	3.7
	Median	2.2	3.4	2.5
	95% CL	12.6	10.3	7.3
2	RMS	4.4	32.3	14.1
	Median	2.8	26.1	9.6
	95% CL	8.5	59.9	24.6
3	RMS	2.5	4.9	3.5
	Median	1.4	2.9	2.3
	95% CL	4.6	9.8	7.0

not part of the pelvic bone, these would have affected the instantiation results and therefore two methods were investigated to remove outliers in these pelvic datasets. For both methods, the RMS residual after registering the instantiated model and US points was between 2.3 and 4.2mm for the pelvis. An RMS distance error was also determined in the region of most clinical relevance - around the acetabulum, with a resulting RMS error in the ranges 3.3 to 6.5mm for GS and 2.1 to 3.5mm for ICP. The results when using the automatic (pruning 5%) and manual methods to remove outliers returned similar results.

The results from cadaver 1 are shown in Figure 6.24 and results from other cadavers are also shown in subsequent figures.

6.5 Model Specificity

This is the test of the instantiation results to check if the weights of the SSM lie within plausible limits and that these instantiations look like a femur or pelvis. Model specificity is about the ability of the model to represent only valid instances.

The test described here examines whether the surfaces instantiated using the SSMs within the region of shape space defined by the training datasets are plausible surfaces, that is, testing whether these surfaces were "false positives" (Hutton, 2004).

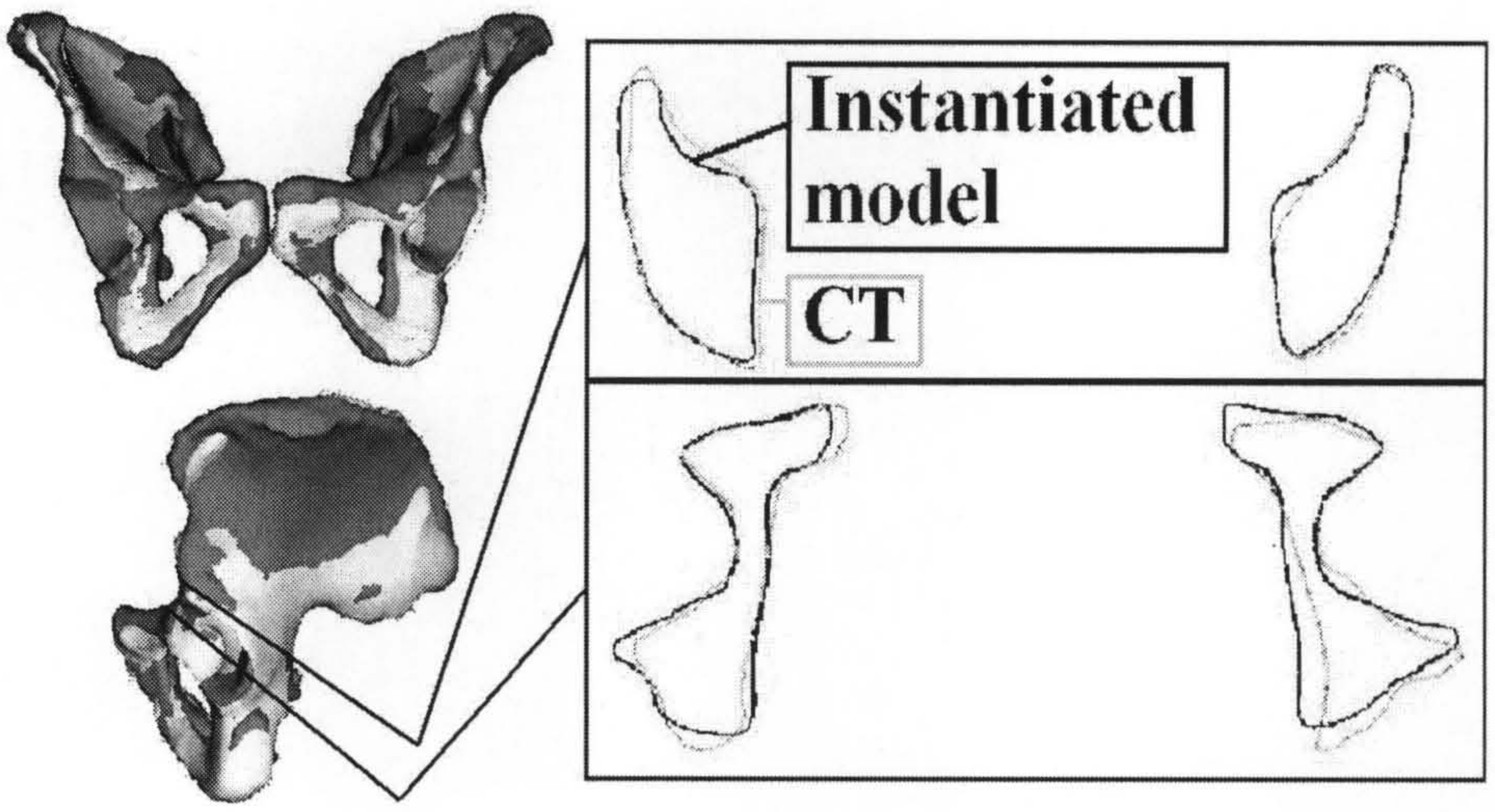

Figure 6.24: Visualisation of Cadaver 1 pelvis, pruning 5%: The instantiated SSM (*frontal* and *lateral* views) overlaid on the CT-derived surface, shown in dark grey. Cross-sectional contours from the instantiated pelvis model (*black*) with corresponding contours from the CT-derived surface (*grey*). From top to bottom: near top of acetabulum and middle of acetabulum. This description holds for all the following figures.

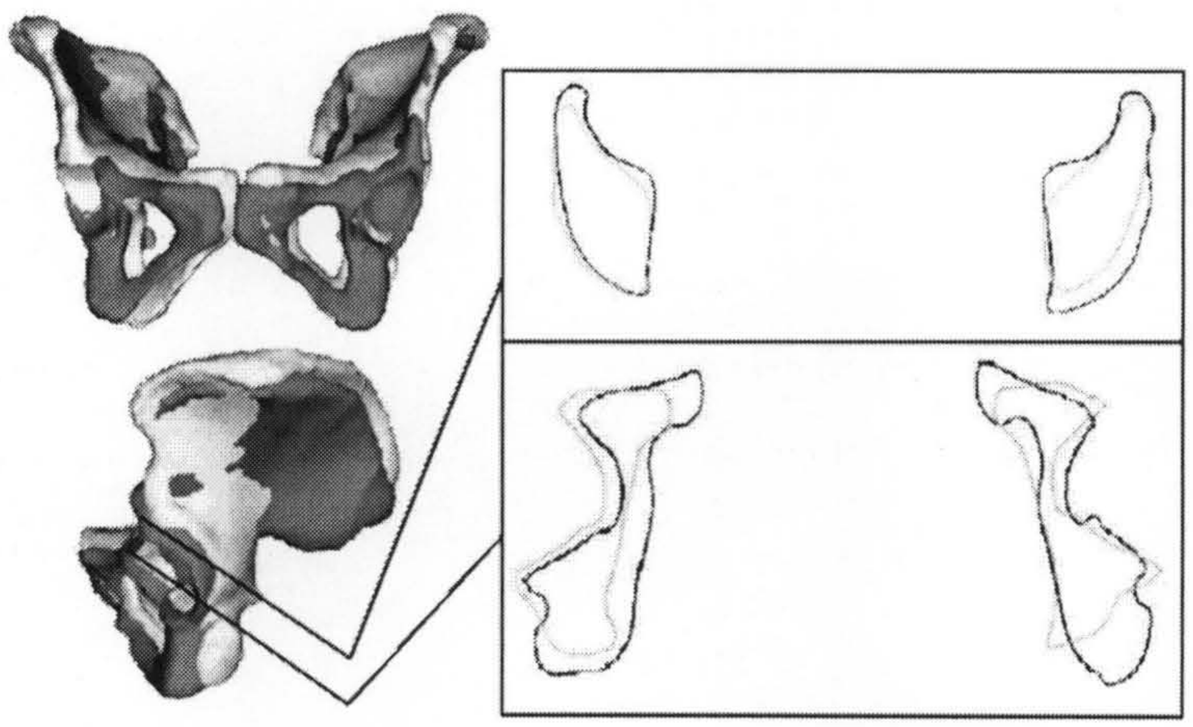

Figure 6.25: Visualisation of Cadaver 1 pelvis, manually removed outliers.

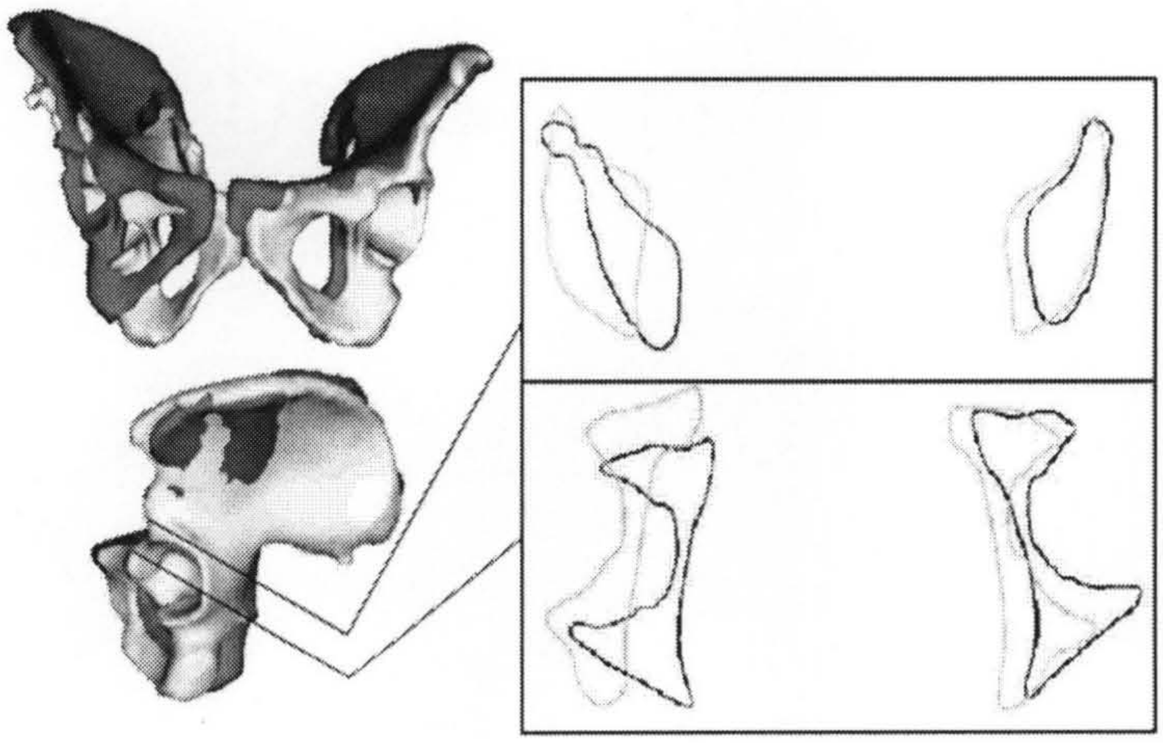

Figure 6.26: Visualisation of Cadaver 2 pelvis, pruning 5%. The contours from the top of the acetabulum have shown large errors. This might have been resulted from the outliers from that side of the iliac surface.

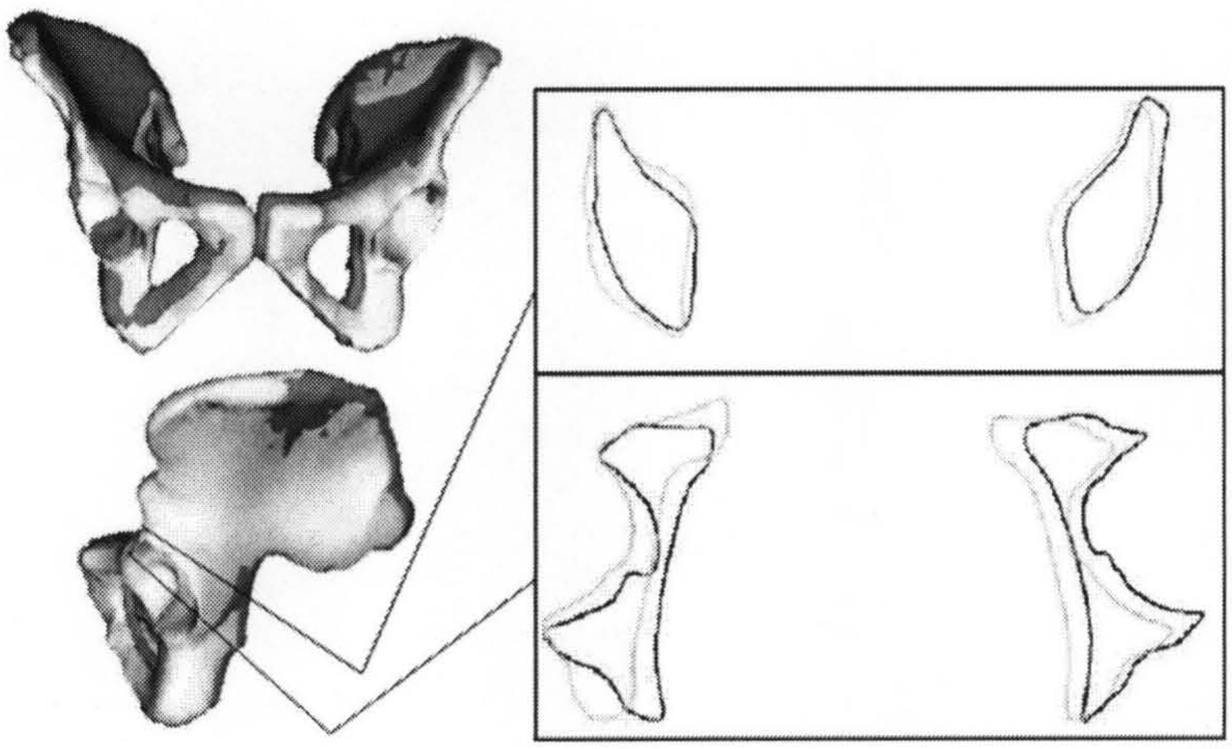

Figure 6.27: Visualisation of Cadaver 2 pelvis, manually removed outliers.

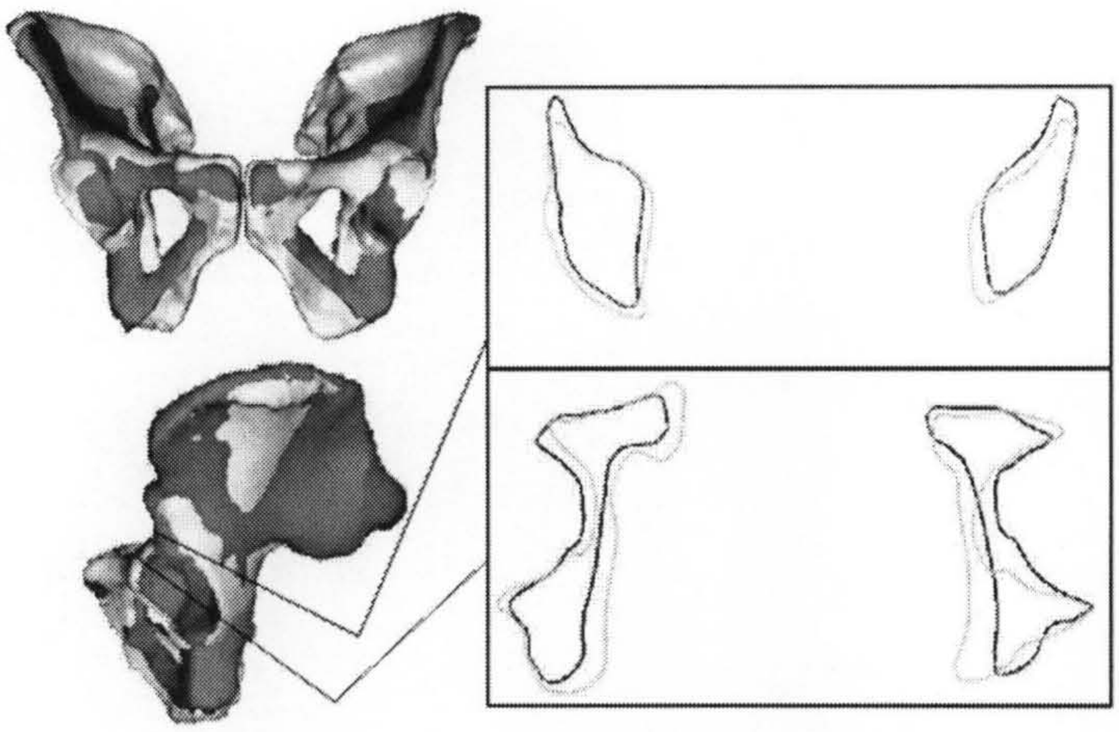

Figure 6.28: Visualisation of Cadaver 3 pelvis, pruning 5%.

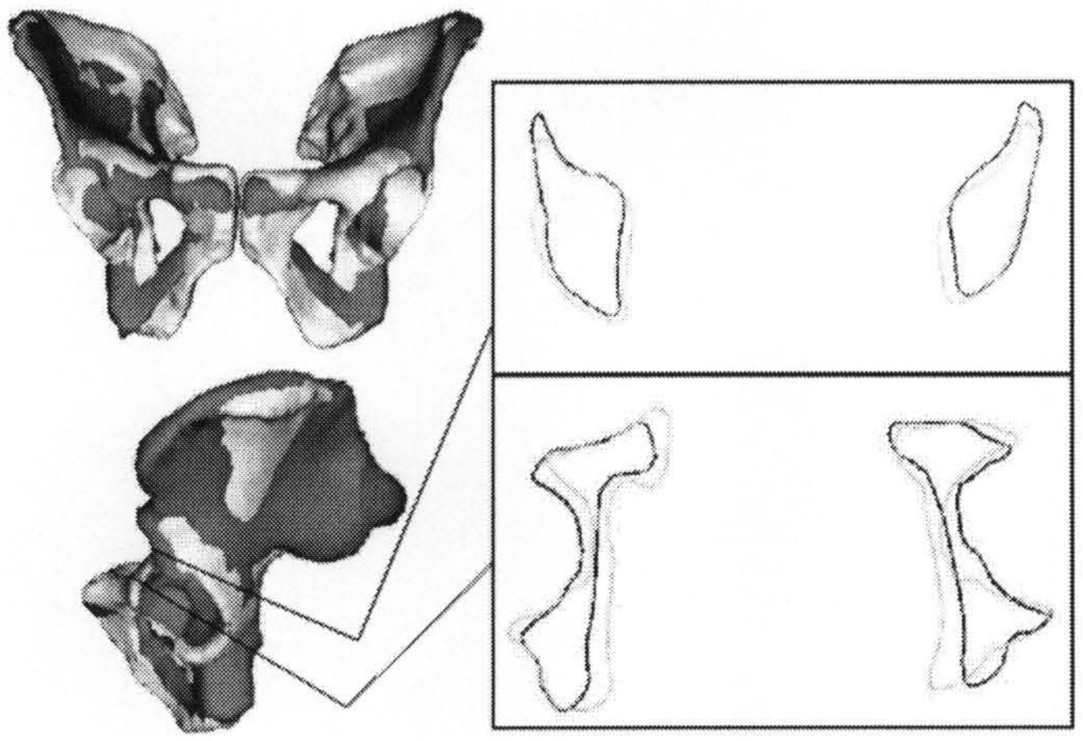

Figure 6.29: Visualisation of Cadaver 3 pelvis, manually removed outliers.

Table 6.10: Errors for instantiated pelvic surfaces (shape) by pruning 5% (mm) - ICP

Cadaver	Error statistic	US-Model	CT-Model(global)	CT-Model(regional)
1	RMS	4.2	2.9	2.4
	Median	1.9	1.9	1.6
	95% CL	10.3	5.8	4.5
2	RMS	3.1	3.9	3.4
	Median	1.6	2.7	2.6
	95% CL	5.9	7.3	6.1
3	RMS	2.3	4.8	3.3
	Median	1.4	2.8	2.2
	95% CL	4.3	9.5	6.6

Table 6.11: Errors for instantiated pelvic surfaces (shape and final position) by pruning 5% (mm) - GS

Cadaver	Error statistic	CT-Model(global)	CT-Model(regional)
1	RMS	4.9	3.6
	Median	2.9	2.1
	95% CL	10.1	7.5
2	RMS	10.7	6.5
	Median	6.2	4.1
	95% CL	23.6	13.3
3	RMS	5.2	3.3
	Median	3.0	2.3
	95% CL	10.6	6.2

Table 6.12: Errors for instantiated pelvic surfaces (shape) by manually removing outliers (mm) - ICP

Cadaver	Error statistic	US-Model	CT-Model(global)	CT-Model(regional)
1	RMS	3.7	3.0	2.1
	Median	1.7	2.1	1.4
	95% CL	9.3	5.9	4.2
2	RMS	3.3	3.3	2.8
	Median	1.5	2.2	2.0
	95% CL	6.9	6.1	5.4
3	RMS	2.5	4.9	3.5
	Median	1.4	2.9	2.3
	95% CL	4.6	9.8	7.0

Table 6.13: Errors for instantiated pelvic surfaces (shape and final position) by manually removing outliers (mm) - GS

Cadaver	Error statistic	CT-Model(global)	CT-Model(regional)
1	RMS	5.7	5.5
	Median	3.7	3.7
	95% CL	11.5	11.4
2	RMS	5.5	4.2
	Median	3.2	2.9
	95% CL	11.8	8.1
3	RMS	5.0	3.4
	Median	2.9	2.3
	95% CL	10.1	6.4

6.5.1 Femur

In Section 4.2.2 (Page 93) all the modes of variation were presented, please refer to Table 4.1 (Page 95) for the full table of figures in this calculation. To model 98% of shape variation for the population, 11 modes are required. In the 11-dimensional normal distribution, the χ^2 critical values give the size of the ellipsoid to include a given percentage of the cases.

For 98% of cases in 11 modes of variations (dimensions) with significance level 0.02, the χ^2 critical value is 22.6, hence the square root of this, 4.8 standard deviations is the limit to produce a plausible shape. Section 2.6.2 on page 48 stated that an SSM can be approximated by

$$\mathbf{x} = \bar{\mathbf{x}} + \sum_{i=1}^{m} \mu_i \phi_i$$

where $\mathbf{x}$ is the approximated instance, $\bar{\mathbf{x}}$ is the mean, μ_i are the weights for the first m eigenvectors to be used in this approximation and ϕ_i contains the eigenvectors of the SSM.

To calculate whether the instantiated shapes are plausible, let b be the list of the instantiated shape parameters and assume that they are independent and Gaussian. To calculate the total standard deviations which the instantiated surface covers (Cootes and Taylor, 2001):

$$SD_{TOTAL} = \sqrt{\sum_{i=1}^{m} \frac{b_i^2}{\lambda_i}}$$

Table 6.14 shows the detailed specificity calculation of cadaver 1's left femur instantiation

Table 6.14: Cadaver 1 left femur (US only) specificity calculations.

Mode	b	b^2	Corresponding Mode values, λ	$\frac{b^2}{\lambda_i}$
1	-10.0	100.6	119487.0	0.001
2	-67.8	4594.5	6308.4	0.728
3	37.4	1399.2	4197.2	0.333
4	90.4	8169.5	3936.9	2.075
5	-39.3	1544.0	2780.9	0.555
			Total:	3.692

results, showing that the instantiation lies within ($\sqrt{3.692}$ =) 1.9 standard deviations, which is well within the 4.8 standard deviations limit. This test is then extended to all other instantiation results to check if they all have plausible shapes. The results are shown in Table 6.15. All femur instantiations using US only are within plausible limits. However, when using the centre of the femoral head as pivoting point for cadaver 2's right femur and cadaver 3's left and right femurs instantiations, the results revealed that these are implausible shapes or "false positives", outside of the limit of 4.8 standard deviations. When the calculations were investigated further, it was found that for all of these implausible instantiations, the weight for the third mode of variation has either almost or completely reached the +3SD boundary set in the optimisation algorithm.

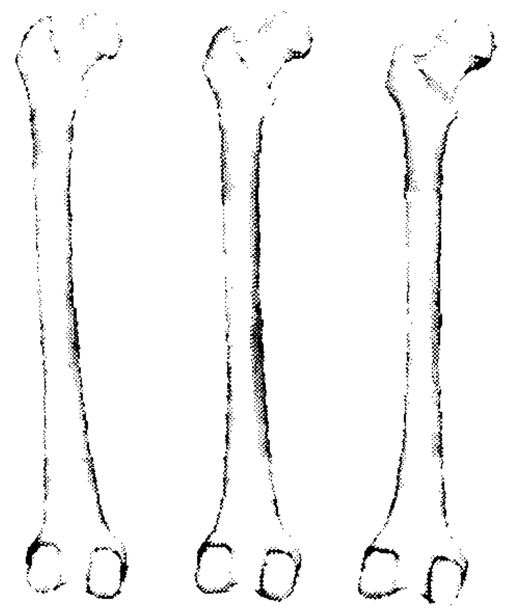

Figure 6.30: Representation of the left femur volume SSM showing the third mode of variation. This figure is produced by deforming the template surface using the mean deformation and the third mode of variation in the deformation fields, with three standard deviations.

Table 6.15: Specificity test results for cadaver femur instantiations

Cadaver	Bone	Instantiation	Standard deviation
1	Left Femur	US only	1.9
	Left Femur	US with centre of femoral head	1.1
	Right Femur	US only	3.0
	Right Femur	US with centre of femoral head	3.0
2	Left Femur	US only	2.7
	Left Femur	US with centre of femoral head	4.7
	Right Femur	US only	3.4
	Right Femur	US with centre of femoral head	6.6
3	Left Femur	US only	3.0
	Left Femur	US with centre of femoral head	6.6
	Right Femur	US only	4.2
	Right Femur	US with centre of femoral head	7.0

A representation of the left femur volume SSM, showing the third mode of variation can be seen in Figure 6.30. As the third mode of variation is varied from +3SD to -3SD, the femoral head gets progressively larger and the greater trochanter changes in shape, while the shaft down to the condyle bends from nearer to the midline to away from the midline.

By setting the centre of the femoral head as the centre of rotation in the instantiation algorithm, this has restrained the movement of the instantiation and the algorithm tried to alter the weights of this mode to match the femoral head as well as the pose of the condyles. Consequently, the weights of this mode has been set very high, and the weights of other modes of variation had to compensate for this change and to instantiate the resulting shape plausible limit was exceeded. The effect of the centre of the femoral head point will be discussed more in Section 6.6.1.1.

6.5.2 Pelvis

Again, in Section 5.2.4 (page 111) all the modes of variation were presented, please refer to Table 5.1 (Page 112) for the full table of figures in this calculation. To model 98% of shape variation for the population, 6 modes are required. In the 6-dimensional normal distribution, the χ^2 critical values give the size of the ellipsoid to include a given percentage of the cases.

For 98% of cases in 6 dimensions with significance level 0.02, the χ^2 critical value is 15.0,

Table 6.16: Specificity test results for cadaver pelvis instantiations

Cadaver	Outliers removal method	Standard deviation
1	Manual	2.1
	Pruning 5%	2.2
2	Manual	1.3
	Pruning 5%	1.5
3	Manual	3.4
	Pruning 5%	3.1

hence the square root of this, 3.9 standard deviations is the limit to produce a plausible shape. The results for the pelves are summarised in Table 6.16. All pelvis instantiations are within plausible limits.

This method to test for specificity of the models has its limitations but is sufficient for the context of this thesis.

6.6 Discussion

This cadaver study included a good range of sizes and varying bone shapes and soft tissue contents. The cadavers were preserved in such a way that the muscle flexibility could be maintained hence the US images collected appeared visually realistic, just as a patient that has been anaesthetised for surgery.

The RMS distance measured between the instantiated surface and CT-derived surface, registered using ICP, ranged from 1.8 to 5.1mm in the region of the femoral head, improving to between 1.8 mm and 3.7 mm when cadaver 3's right femur, the femur with poorly sampled US at the proximal end, is excluded and without using the femoral head point, and between 2.1 and 3.5mm in the region of the acetabulum.

Cadaver 1 is medium-built, of more or less average size. Collecting US images were not difficult and it took the least amount of time, yielding the least amount of points. Due to its average size, instantiation time is thought of as typical.

Cadaver 2, however, is above average weight. There was more fat involved that had to be insonated before the US beam could reach the bones, and the US images tended to be more noisy as a result. However, the surgeon still managed to get a reasonable number of US images.

Cadaver 3 is lower than average weight. A large number of US images were acquired in the shaft area but virtually no points were acquired in the right femoral head area which made the algorithm struggle to arrive at an instantiation which could potentially make the instantiation much more accurate.

The method for tracking the patient's leg might seem quite invasive due to the use of the dynamic reference marker fixed to the bone, however, this is standard practice, and can be performed with a relatively small incision. Minimally invasive implanted wireless trackers are being developed and these should be available commercially in due course.

The twelve manual starting positions were used to give an estimate of how the algorithm might converge but an automatic algorithm is in consideration to potentially increase the accuracy that could be attained.

6.6.1 Femur Instantiations

This study has shown that real femur US data could be used to instantiate an accurate 3D surface from a statistical shape model. It was also shown that a wide range of US-derived points leads to adequate instantiations. Notably, cadaver 2 left femur used the least number of US surface points (992 points) and returned one of the most accurate results for both instantiations with or without the femoral head point; conversely, cadaver 3's right femur had the most number of US surface points (3500 points)(however, it was undersampled in the greater trochanter and femoral head region), the instantiated surface gave the highest RMS distance when comparing with the gold standard CT-derived surface, by registering with ICP or the gold standard registration. The bone which had the second most US-derived surface points, cadaver 2 right femur (3071 points), returned RMS distances that were average among the 6 femurs. This implied it is where the points lie rather than the number of points that is the important consideration. The next step would be to investigate where these points should be populated to give the optimal instantiation results, which would be discussed in the next chapter under Future Work.

Some of the figures for visualisation of the instantiation results have shown large errors between the 2D contours of the instantiation surface and the gold standard CT-derived surface. In 3D, these surfaces curve around the 2D cross-sections, such that the 2D representations can make the errors look visually larger than they actually are. Therefore, these visualisations should be interpreted in conjunction with the numerical results.

6.6.1.1 Centre of the Femoral Head as Centre of Rotation

The effect of having an accurate centre of femoral head is very important. Table 6.17 compares various measures' RMS distance of instantiations using US only information or by incorporating this point. The localisation errors given in the last column have been presented in Section 6.2.5 on Page 124. The symbol "N" is given when the RMS residual distance of the instantiation result using US only is less than that from using the centre of the femoral head as the pivoting point. The symbol "**F**" is given when the RMS residual distance of the instantiation result using US with the centre of the femoral head as the pivoting point is equal or greater than that from using US only. Any of the above two symbols presented in italics form indicates a difference of no more than 0.1mm.

For these three cadavers, when the RMS localisation error of the centre of femoral head is below 0.49mm there is notable improvement in matching the CT ground-truth surface with the instantiated model mainly when registering using ICP. However, there are only 6 bones involved in this experiment, more tests need to be carried out to give a more quantitative analysis. It might also be impractical to obtain a low RMS localisation error for this point because the patient's hip joint might have degenerated too much, for example, the femoral head might have collapsed, hence leading to inaccurate information being collected. Note that the column where the comparison is made on measuring the RMS residual on the US-derived points with the instantiated surface ("US-model"), all RMS residuals using US only were less than that from US with the centre of femoral head as pivot point (hence this column were given all "N"s). This is not surprising because the method using US only information has 6 DOFs while when the centre of femoral head is added as the centre of rotation in the ICP algorithm, it was reduced to 3 DOFs. When more DOFs are added, the RMS residual error will tend to decrease.

In Section 6.5.1, 3 out of the 6 femurs (Cadaver 2's right femur and cadaver 3's left and right femurs) which used the centre of the femoral head as pivoting point returned instantiated shapes that exceeded the plausible limits. For these instantiations, it was discovered that the weights of the third mode of variation were very high. This mode of variation describes a change in the femoral head size, shape of greater trochanter and a bend along the shaft to the condyles. The centre of the femoral head must have been restrained in such a way that the algorithm struggled to find a match within plausible limits. It has already been mentioned that when collecting US images for cadaver 3's right femur, it was undersampled in the femoral head region. For cadaver 2's right femur and cadaver 3's left femur, referring to the last column in Table 6.17, the centre of femoral head point localisation errors were highest for these two femurs. The above factors coupled with the modes

of variation described by the SSM's mode 3 contributed to the implausible instantiations generated by the algorithm.

Also for reasons discussed at the end of chapter 4, the centre of the femoral head point is not recommended to be given a lot of weight in the instantiation process. An alternative is to incorporate this point as a normal point and give it the same weight as other points on the surface.

Table 6.17: Comparison of various measures for femur surface instantiations, US only and US with centre of femoral head

Cadaver femurs	US-model	CT-model (global)		CT-model (regional)		Centre of femoral head point localisation error
Left	ICP	GS	ICP	GS	ICP	RMS(mm)
1	N	**F**	**F**	N	*N*	0.49
2	N	N	N	N	N	0.64
3	N	N	N	N	N	0.98
Right						
1	N	N	**F**	**F**	**F**	0.46
2	N	N	N	N	N	0.70
3	N	N	N	**F**	N	0.58

N = RMS residual distance using US only $<$ RMS residual distance using femoral head pivot point.

F = RMS residual distance using femoral head pivot point $\leq$ RMS residual distance using US only.

Italics indicates a difference of no more than 0.1mm.

6.6.2 Pelvis Instantiations

Most of the pelvis instantiations produced higher RMS residual errors than femurs, especially when measuring errors between CT-derived surfaces and the model instantiations. This is mainly because the pelvis is being covered under thicker tissues, hence making collecting sufficient US images with brightly reflecting pelvic surfaces and instantiation a challenging task. Figure 6.9 on page 126 showed the US points being used in instantiation. Although some clearly showed points which were not part of the bone, when these images were cross-checked with the US im-

ages, brightly reflecting contours that looked like genuine bone were found and it is not currently possible to deduce what anatomical structures were causing these features in the US images.

The pelvis instantiations assumed that the whole pelvis could be treated as a single rigid body, that is the two coxal bones, the hemi-pelves, were rigidly fused at the symphysis pubis. This is considered sufficient for the purpose of this experiment.

In comparing the two methods to remove outliers, manually removing outliers appeared to be a better option. Extracting bone surface points from US images obtained from the pelvis is generally harder than for the femur. Using the "pruning" method, by registering the cloud of US surface points with the mean shape, and then removing the 5% points with the largest RMS point-to-surface distance to the mean, has the possibility that useful information is excluded from the instantiation process which is undesirable.

However even when an expert is involved in visual inspection and removing outliers from the cloud of US points, there will still be drawbacks. It is not easy to interpret the US point cloud with outliers and hence the expert can only use intuition and experience to decide, after careful consideration, whether certain points are obvious outliers or not. This remains an important field to be explored.

6.6.3 Breakdown of running times for each patient

Here is a breakdown of the running times at each stage of the instantiation algorithm, for each patient:

- US image acquisition: 7 to 30 minutes.
- US manual segmentation to obtain surface points: 1 to 2 hours.
- Instantiation algorithm using the US-derived surface points to reconstruct a complete 3D surface: 10 minutes to 4 hours.

Running time of the instantiation algorithm is further discussed in Section 7.4.7 on Page 163.

6.7 Chapter conclusion

This chapter presented a validation of using ultrasound to instantiate and register statistical shape models constructed using the B-spline node points from non-rigid registration of CT images to a single template CT image. Results were shown for the femurs and pelves of 3 intact cadavers. The

three cadavers in this study had a good coverage of the model's femur and pelvis sizes as well as varying amounts of fat and soft tissue, this contributed to the realism of this experiment.

The RMS residual distance between US surface points and instantiated surfaces were between 1.1 and 3.5mm for all femurs and 2.3 and 7.1mm for all pelves. With the exception of the right femur of cadaver 3, the RMS distance measured between the instantiated surfaces and their corresponding CT-derived surfaces for the femurs using ultrasound only information and all pelves converged to a low RMS distance, not more than 3.7mm in the regions of interest. When the centre of femoral head point was used as the centre of rotation in the algorithm, the maximum RMS distance between the instantiated femur surfaces and corresponding CT-derived surfaces were 6.4mm.

There are several reasons which affected the instantiation accuracy from the use of the centre of femoral head as the centre of rotation in the algorithm. These include the accuracy to which this point could be obtained, assigning the appropriate weighting for this point in the algorithm and the presence of sufficient US-derived points across the femur. In the phantom experiments in Chapters 3 and 4, it was thought that US images could only be obtained up to and around the anterior surface of the greater trochanter. In this cadaver study, it was possible to acquire US images in some regions of the femoral head. This information was better at constraining the model than using the centre of the femoral head pivot point. Before the above issues relating to the centre of the femoral head point were addressed, this point should be omitted from the instantiation algorithm.

This method has the potential to be used in the operating room where the surgeon could acquire some ultrasound images of the patient and the complete CT scan of the patient's bone could be reconstructed. This could remove the requirement for a preoperative CT scan and hence reduce radiation exposure to both the patient and operating room staff, this will also mean lower costs. This method could also avoid the need to insert CT- visible markers in the bone or expose bone for surface palpation.

Chapter 7

Conclusion and Future Work

7.1 Conclusion

This thesis presents the use of ultrasound (US) images to instantiate and register a statistical shape model constructed using either surface points or directly on the node points from the free-form deformation (FFD) fields produced using non-rigid registration. One advantage of models produced using FFD fields as opposed to surface points is that they provide a model of much higher resolution. The combination of a surface-based SSM and the incorporation of the rotation centre of the femoral head was found to improve the accuracy of the instantiation. The effects of using the rotation centre of the femoral head in the FFD-based SSM were found to be dependent on the acquisition accuracy of this point in the surgical environment. It was found that the region around where the US images were acquired also had an effect on the instantiation results. A figure illustrating the algorithm can be found in Figure 7.1.

The FFD instantiation process generates a high-resolution, 3D grey-level image, which is the spatial deformation of the template computed tomography (CT) image to the shape of the specific patient's bony anatomy. It has the appearance of a CT scan. In this application this allows propagation of a more densely sampled surface and incorporation of other features . On the other hand, when generating a SSM purely for surface data, there is the problem of finding point correspondence, which can only be achieved by interpolating within the surface, and may give rise to errors in surface shape and texture. The method proposed here provides an estimate of all correspondences within the volume of the bone fully automatically.

This thesis started with proof of principle through a study using a dry femur immersed in a water bath. US images were acquired from the femur around the condyles, femoral shaft and up to around the trochanter. US surface points were extracted from these images. These US points

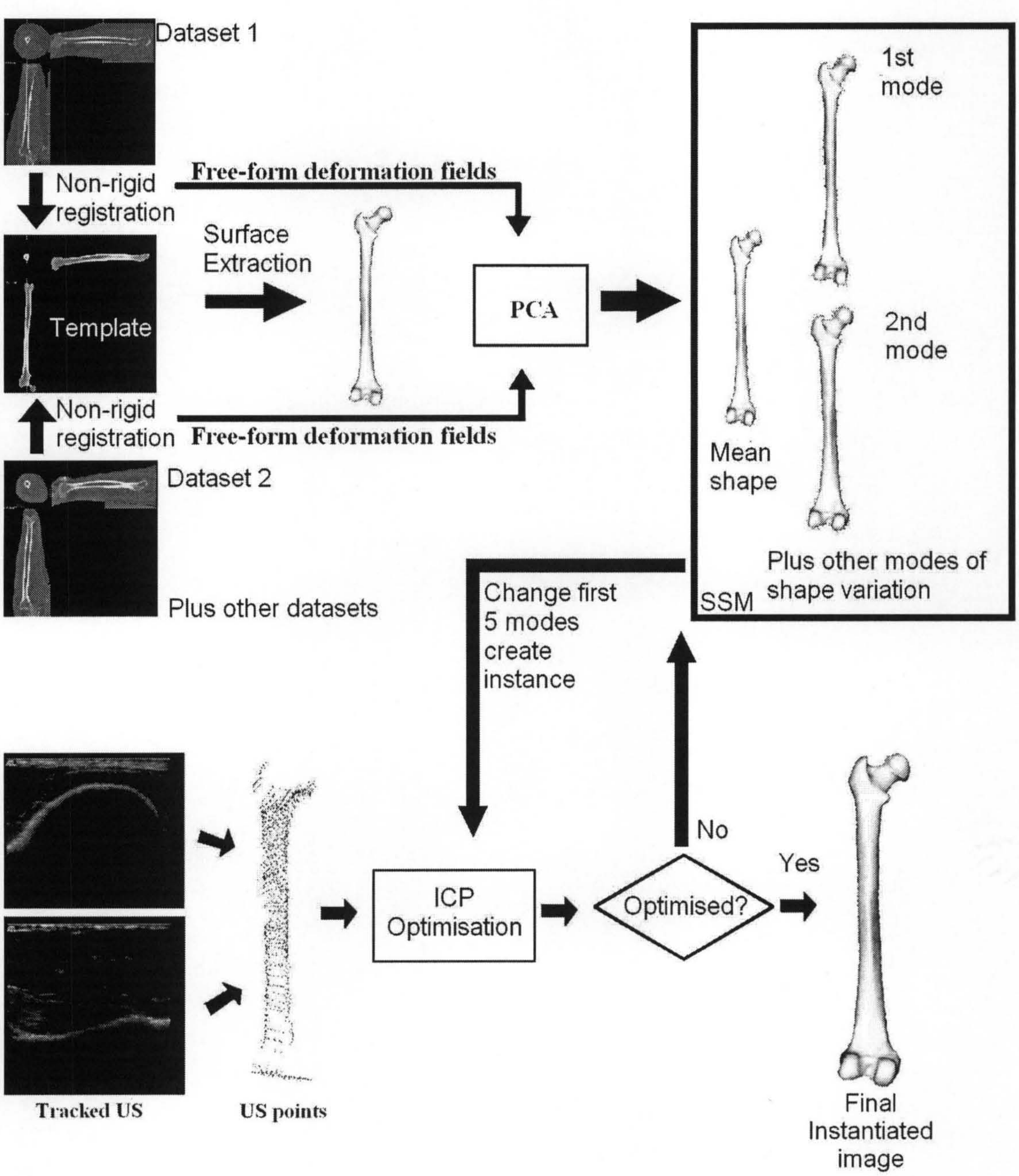

Figure 7.1: The SSM construction and instantiation algorithm.

were matched with instantiated surfaces from the SSM using ICP.

For the surface SSM experiments, 10 left femurs were used to build the model. Since no US information was available around the femoral neck and head regions, this might lead to inaccurate instantiation results, it was proposed to acquire an extra point at the centre of the femoral head. This could be done intraoperatively by pivoting the leg around the hip joint. Another model was produced which included this point and the algorithm used this as the centre of rotation. To test the robustness of the algorithm, 20 different starting positions were generated from 1 manual starting position by adding random noise of standard deviation of 10° and 10mm to this initial position. 14 of these starting positions converged to a final RMS residual distance between US-derived points and the instantiated SSM surface of under 2mm. The RMS distance between the instantiated surface and the gold standard CT-derived surface were 4.5 and 4.0mm when using US only or with the centre of the femoral head added as the pivoting point respectively. When only measuring the RMS in the region of the femoral head, the results were 7.2 and 4.7mm respectively. This experiment has shown that the extra point in the centre of the femoral head improved the accuracy of the instantiation, especially in the region that is inaccessible to percutaneous US.

Another model of the femur was produced based on the deformation fields of the B-spline node points from non-rigid registration to instantiate from US. In this volume SSM, 16 left femurs were used to build the femur model. 15 out of 20 of the starting positions converged to a final RMS residual of under 1.8mm. RMS distance between all points on the instantiated surface and the nearest points on the CT-extracted surface was 2.7mm while that around the femoral head was 3.3mm. When compared with those instantiated using surface SSMs, the results were better including the regions inaccessible to percutaneous US *in vivo*, namely the femoral head region. This has shown that the use of the model produced using the B-spline node points generated by non-rigid registration also provided much higher resolution and potentially allows more information to be included in the template surface, hence the model.

Later the method was validated with a carefully designed cadaver study to better test the validity and robustness of the method to varying thickness of soft tissue structures, using 3 complete cadavers where high-resolution CT scans and accurate image-physical registration transformations were available to provide gold standard measurements of shape and registration. In this cadaver study, the femur volume SSM consists of 16 male and female left femurs and the pelvis volume SSM contains 10 female pelves.

To test the robustness of the algorithm, 4 observers were invited to produce a total of 12 starting positions for each femur or pelvis. All femur and pelvis instantiations converged to one

RMS residual in the range of 1.1 to 2.0mm for the femurs and 2.3 to 4.2mm for the pelves between the US surface points and the instantiated model surface. When compared with the gold standard surface, RMS distance ranged between 1.9 to 3.0mm across the whole femur and 1.8 to 3.7mm in the region of the femoral head when the ultrasound images were sufficiently sampled. For the pelvis, the RMS distance ranged between 2.9 and 4.9mm across the whole pelvis and between 2.1 and 3.5mm in the region of the acetabulum.

7.2 Contribution to knowledge

This thesis has shown that tracked B-mode ultrasound can be used to instantiate femurs and pelves from SSMs to within a small error, especially in the area where it matters most to hip replacement surgery. In particular, the following were achieved:

- SSMs can be used to instantiate 3D models from ultrasound. This thesis introduced two methods, one based on the 3D surface points, and another based on the non-rigid registration deformation fields, to produce SSMs.

- Ultrasound can be used to reconstruct a complete 3D representation of the bony anatomy for image-guided surgery. Ultrasound data was obtained from a dry femur immersed in a water bath and from 3 complete cadavers (6 femurs and 3 pelves). Their corresponding complete 3D surfaces that were reconstructed were within plausible limits of the SSMs.

- The algorithm was validated using independent gold standards. In the cadaver study to test the validity (i.e. accuracy and robustness) of the method, 3 complete cadavers were used where high-resolution CT scans and accurate image-physical registration transformations were available to provide gold standard measurements of shape and registration.

- When incorporating the centre of the femoral head in the instantiation algorithm as the pivoting point, the cadaver study has shown that if the RMS localisation error of the centre of the femoral head is below 0.49mm there is notable improvement in matching the CT ground-truth surface with the instantiated surface.

- Ultrasound images were obtained in regions previously thought to be inaccessible to percutaneous ultrasound. These areas include the greater trochanter, femoral neck and parts of the femoral head. This has proved to provide more information for instantiation and registration.

7.3 Sources of Error

In bringing many parts together to form the algorithm, there are different sources of error:

- CT scan acquisition and manual segmentation: The error is expected to be of the order of 1 voxel.

- Tracking and localisation error of the optical devices: The RMS error in localising individual IREDs is of the order of 0.2mm.

- Ultrasound probe calibration error: In the cadaver experiment, the RMS residual error in locating the pin-head target was 1.08mm.

- Centre of the femoral head as pivoting point: When collecting clinical data, there would be errors incurred by locating this point due to various reasons discussed in Chapter 6. Since the femoral head is not perfectly spherical, this point is calculated by locating the invariant point relative to the reference coordinate system. In the cadaver experiment, the localisation error ranged between 0.46mm and 0.98mm.

7.4 Future Work

7.4.1 Automation

There are several parts in this work that currently require manual intervention.

In the clinical setting, it is not practical to segment US points manually, this is a problem being addressed and automatic methods are currently being tested. Several groups are investigating possible solutions to this problem including Amin et al. (2003) and Daanen et al. (2004).

Research is also underway to establish whether the volume SSMs produced in this project may then be used as input into an automated algorithm that registers directly using image intensities. A method has already been tested on tracked US images on an MR volume of a liver (Penney et al., 2004), and this method has also been shown to accurately align CT and US images of the femur and pelvis (Penney et al., 2005).

Also on the workplan is the further development of automatically aligning the US surface points from the segmentation process to the mean shape, as the starting position to the instantiation process. In the phantom experiments, these starting positions were generated by adding random noise to one manually produced position. It was shown that some starting positions were nearer to a local minimum than a global minimum, producing incorrect results. In the cadaver experiments,

the starting positions to the instantiation process were manually produced by 4 observers. For all cadavers, each set of starting positions converged to the cadaver's corresponding global minimum. Under clinical settings, the approximate orientation of the bone would be known. In the model coordinate system, the bone was roughly aligned with the z-axis along the bone shaft (see Section 6.3.4 on Page 130). This process of generating starting positions to the instantiation process could be automated and allow the surgeon to manually adjust any visual misalignment before the instantiation process begins.

7.4.2 Incorporating X-rays

X-rays taken during surgery have the limitation that the exact orientation of the radiograph is unknown. However, one or two X-rays could be included in the instantiation as additional input data. Algorithms were suggested by Fleute et al. (2002) to reconstruct bones by registering an SSM to some scattered 3D point data and segmented contours in an X-ray image, and Yao and Taylor (2002) to produce "virtual" CT scans of bones by registering statistical bone density atlas to a set of simulated X-rays. One strategy that could be explored is to instantiate the model from one or two X-rays and register using US, perhaps with some fine-tuning of the instantiation.

7.4.3 Atlas Generation and Mean CT Shape

Atlas generation using non-rigid registration is an area of active research and a more rigorous approach would be to register each example to the template and hence the generation of a mean shape and high contrast averaged CT scan. If the template was chosen arbitrarily from the database, the non-rigid registration could be biased towards the template. A mean CT should be generated and the non-rigid registrations repeated. Registration of this mean to each example shape should then produce a shape model largely free of bias to the arbitrarily chosen template. A similar approach has been proposed by Rueckert et al. (2001) where MR images of the brain were used to construct average models of the anatomy and their variability.

This mean CT scan could then be deformed to the shape of each individual patient to provide a "high contrast" CT scan corresponding to the particular patient. Bhatia et al. (2004) described a method for simultaneously registering a few subjects to a common average of the population, tested on 19 2D MR brain images with good results but there are limitations on CPU memory usage. Using this type of groupwise registration could help to reduce the bias to a minimum, but has yet to be applied to 3D images like CT scans of bones.

7.4.4 Linear Model

For this application, a linear model based on PCA has proved to be sufficient, although Independent Component Analysis (ICA) might have advantages, as reviewed in Section 2.6.5 on page 50. However, there is insufficient data to determine whether a linear model is sufficient to capture all variations across a population, and there is no evidence that this is the most compact model. Work has been reported on the derivation of optimal models from an information theoretic point of view like the work using a minimum description length approach to optimizing SSMs (Davies et al., 2002b) that produces the simplest model to explain the data.

7.4.5 Sufficiency of the Model

Section 6.5 on page 142 tested the cadaver instantiation results to check if the resulting weights of the SSM were plausible surfaces. In dealing with SSMs, there are also issues regarding the sufficiency of the shape models used. The SSMs constructed have only been generated from very limited data (16 mixed male and female femurs and 10 female pelves). Methods exist to estimate whether sufficient data has been acquired to form a complete sampling of the population shape variation of femurs and pelves and the shape of the probability density function of the weightings given to each mode, to within a certain tolerance. Examples include leave-one-out experiments which can be conducted in the following way: one scan can be left out in turn and a model constructed from the remaining set. The model is used to reconstruct a best representation of the bone in that scan by fitting the model to the scan and the residual error is recorded. This value for all datasets gives an estimate of the sufficiency of the model.

It is currently unclear whether a single femur model is sufficient for the whole population or whether different models for male and female, or different geo-genetic groups should be produced. These tests, using significantly more data than in this study, need to be done to answer these questions. In contrast, there is established evidence that shapes of female and male pelves are significantly different (see Section 2.2.1 on page 24), therefore separate models for each gender are necessary.

In general, discrete pathology such as fractures, dislocations and dysplasia are difficult to describe within a shape model built using PCA, as this presumes an underlying linear model with a normal distribution of variation within each mode. There is, however, an argument for using a model of normality in this work as that is what the surgeon is attempting to reconstruct during total hip replacement and other orthopaedic procedures.

7.4.6 System Integration

A substantial amount of further work is required to integrate the system into an image-guided surgery system. The system will only be practical when integrated with an algorithm to automatically align the model with the raw US data and that enables real-time tracking of the relative position of bony anatomy. With regard to the US image acquisition time, from the experience obtained from the cadaver experiments, it is envisaged that in the clinical setting it would be possible for the surgeon with a relatively small amount of training and adopting a specific protocol to acquire sufficient US images for registration and instantiation within 5 minutes.

7.4.7 Running Time of Instantiation Software

This instantiation process is currently an offline process, it is noted that the typical time for running the whole instantiation process is between 10 minutes and 4 hours. Although running time is not the main concern in this thesis, this procedure should be computationally efficient rather than taking up a lot of CPU time. Having changed the optimization strategy from the parallel direct search (PDS) methods to the multiple-layer golden section search, the instantiation time has reduced significantly from up to 5.5 hours using PDS to around 4 hours using multiple-layer golden section search. This is indeed not very practical and more work is required to make the algorithm run faster.

It was discovered that the ICP algorithm took up the most time. Due to the vast number of points involved, the time taken for ICP to compute each iteration is increased and convergence is generally slow.

7.4.8 Sufficient Ultrasound Points

It is thought that the quality of the US images, position, orientation and number of the US points acquired, can contribute to ensuring low RMS error.

In the cadaver experiments in Chapter 6, the right femur of cadaver 3 was undersampled in the greater and lesser trochanter and femoral head regions. As a result, for this particular bone, when the instantiation results were matched with the gold standard CT-derived bone surface, produced higher RMS distance compared with other bones, especially in the region of the femoral head. It is therefore thought that as much US data as possible should be acquired in the proximal end of the trochanter for effective instantiation.

A study could be carried out to find out if enough US points have been acquired. This could be done from simulated data or from all the US points acquired, along the accessible surface of

the femur or pelvis. For each iteration 10% of the points, selected randomly, could be removed, run the instantiation, and the RMS distance calculated. A graph can then be plotted to compare the effects of having less points.

Another experiment could be carried out to find out how the position and orientation of the bone can affect the instantiation results. This could be observed by removing points in specific areas of the bone, for example those in the condyles, to see if the instantiation can register and instantiate to a similar RMS error.

7.5 Summary Conclusion

This thesis proposed a method to instantiate bone from a model of bony anatomy using tracked US that is sufficiently accurate for image guided total hip replacement. The algorithm was validated on both a dry bone immersed in water and using data carefully collected on three cadavers. This thesis suggests that SSMs of the femur and pelvis can be simultaneously instantiated and registered to surgical space with a clinically useful accuracy using intraoperative US data, even in regions that are inaccessible to percutaneous US *in vivo*. The use of the models produced using B-spline node points from non-rigid registration also provided much higher resolution and potentially allows more information to be included in the model. This methodology will find application in other image guidance procedures where US provides sufficient data to instantiate an accurate model of surgical anatomy. It also provides the opportunity to develop less invasive procedures that reduce surgical exposure of bone and disruption of the joint capsule.

Appendix A

Software and Scripts Used

The following software and scripts (developed in-house) were used in this project, the authors and associated programming language are listed below:

Section 3.2.1 on Page 62: The dilation scripts (morphological operator) were written by Daniel Rueckert in C++.

Section 3.2.3 on Page 65: Bone surfaces were extracted using a script written by Matthew Clarkson in Tcl.

Section 3.3.3 on Page 74: The script to compute stochastICP was written by Graeme Penney in C++.

Section 3.3.5 on Page 78: The centre of femoral head point was defined using a script written by Philip Edwards in Tcl.

Section 3.3.6 on Page 80: The script for adding random noise to an initial starting position was written by Philip Edwards in C++.

Section 6.2.3.1 on Page 119: The US image acquisition program was written by Dean Barratt and Timothy Carter in C++.

Section 6.2.4 on Page 122: The US image segmentation program was written by Dean Barratt in Matlab 7.

Section 6.3.3 on Page 128 with the screenshot of Figure 6.10: The user interface was a script written by Philip Edwards in Tcl.

Bone surfaces, US-derived surface points and bone contours were displayed using a script written by Matthew Clarkson, Jane Blackall and Andy King in Tcl.

The surface SSMs were viewed using a script written by Jane Blackall and Matthew Clarkson in Tcl.

The volume SSMs were viewed using a script written by Carolyn Chan based on code by

Jane Blackall and Matthew Clarkson in Tcl.

Most of the codes in this project made extensive use of the Visualisation Toolkit (VTK) libraries:

http://www.vtk.org

The VTK CISG Registration toolkit was written by Thomas Hartkens based on code by Daniel Rueckert and Julia Schnabel.

The ICP, PBR, SSM generation, instantiation, golden section search routine and the multiple-layer golden section search optimisation implementations were written by Carolyn Chan in C++.

Bibliography

Amin, D., Kanade, T., DiGioia, A., Jaramaz, B., LaBarca, R., Nikou, C., 2001a. Non-invasive ultrasound registration of the pelvic bone surface for THR. In: 47th Annual Meeting of the Orthopaedic Research Society Poster session.

Amin, D., Kanade, T., DiGioia III, A. M., Jaramaz, B., January 2003. Biomedical paper - Ultrasound registration of the bone surface for surgical navigation. Computer Aided Surgery 8 (1), 1–16.

Amin, D. V., Kanade, T., DiGioia, A. M., Jaramaz, B., Nikou, C., LaBarca, R. S., 2001b. Ultrasound-based registration of the pelvic bone surface for surgical navigation. In: Proceedings of CAOS-International. Davos.

Amstutz, C., Caversaccio, M., Kowal, J., Bächler, R., Nolte, L.-P., Häusler, R., Styner, M., 2003. A-mode ultrasound-based registration in computer-aided surgery of the skull. Archives of Otolaryngology - Head & Neck Surgery 129, 1310–1316.

Arun, K. S., Huang, T. S., Blostein, S. D., 1987. Least-squares fitting of two 3-D point sets. IEEE Transactions on Pattern Analysis and Machine Intelligence 9 (5), 698–700.

Ault, T., Siegel, M. W., 1995. Frameless patient registration using ultrasonic imaging: a preliminary study. Journal of Image Guided Surgery 1, 94–102.

Bachler, R., Bunke, H., Nolte, L. P., 2001. Restricted surface matching-numerical optimization and technical evaluation. Computer Aided Surgery 6 (3), 143–152.

Bajcsy, R., Kovačič, S., 1989. Multiresolution elastic matching. Computer Vision, Graphics, and Image Processing 46 (1), 1–21.

Barbe, C., Troccaz, J., Mazier, B., Lavallée, S., 1993. Using 2.5D echography in computer assisted spine surgery. In: IEEE Engineering in Medicine and Biology Society Conference. pp. 160–161.

Barratt, D. C., Davies, A. H., Hughes, A. D., Thom, S. A., Humphries, K. N., 2001. Accuracy of an electromagnetic three-dimensional ultrasound system for carotid artery imaging. Ultrasound in Medicine and Biology 27, 1421–1425.

Bass, W. A., Galloway, R. L. J., Maurer, C. R., Maciunas, R. J., Aug. 2000. Patent: Apparatus and method for bone surface-based registration of physical space with tomographic images and for guiding an instrument relative to anatomical sites in the image. US Patent number: 6106464.

Bell, A. J., Sejnowski, T. J., 1997. The "independent components" of natural scenes are edge filters. Vision Research 37, 3327–3338.

Besl, P. J., McKay, N. D., 1992. A method for registration of 3-D shapes. IEEE Transactions on Pattern Analysis and Machine Intelligence 14 (2), 239–256.

Bhatia, K. K., Hajnal, J. V., Puri, B. K., Edwards, A. D., Rueckert, D., 2004. Consistent groupwise non-rigid registration for atlas construction. In: IEEE Internaional Symposium on Biomedical Imaging (ISBI). pp. 908–911.

Bookstein, F. L., 1989. Principal warps: Thin-plate splines and the decomposition of deformations. IEEE Transactions on Pattern Analysis and Machine Intelligence 11, 567–585.

Brendel, B., Winter, S., Rick, A., Stockheim, M., Ermert, H., 2002. Registration of 3D CT and ultrasound datasets of the spine using bone structures. Computer Aided Surgery 7, 146–155.

Brendel, B., Winter, S., Rick, A., Stockheim, M., H., E., 2003. Bone registration with 3D CT and ultrasound data sets. In: Proceedings of Computer Assisted Radiology and Surgery. Vol. 1256. pp. 426–432.

Bressan, M., Vitrià, J., 2001. Independent modes of variation in point distribution models. In: IWVF-4: Proceedings of the 4th International Workshop on Visual Form. Springer-Verlag, London, UK, pp. 123–134.

Carrat, L., Tonetti, J., Lavallée, S., Merloz, P., Pittet, L., Chirossel, J.-P., 1998. Treatment of pelvic ring fractures: Percutaneous computer assisted iliosacral screwing. In: Medical Imaging Computing and Computer-Assisted Intervention—MICCAI 1998, Lecture Notes in Computer Science. pp. 84–91.

Carrat, L., Tonetti, J., Merloz, P., Troccaz, J., 2000. Percutaneous computer assisted iliosacral screwing: Clinical validation. In: Medical Imaging Computing and Computer-Assisted Intervention—MICCAI 2000, Lecture Notes in Computer Science. pp. 1229–1237.

Chan, C. S. K., Barratt, D. C., Edwards, P. J., Penney, G. P., Slomczykowski, M., Carter, T. J., Hawkes, D. J., 2004a. Cadaver validation of the use of ultrasound for 3D model instantiation of bony anatomy in image guided orthopaedic surgery. In: Medical Imaging Computing and Computer-Assisted Intervention—MICCAI 2004, Lecture Notes in Computer Science. Vol. 3216. Springer-Verlag Heidelberg, pp. 397–404.

Chan, C. S. K., Edwards, P. J., Barratt, D. C., Slomczykowski, M., Hawkes, D. J., 2004b. Ultrasound-based reconstruction and registration of 3D bone anatomy using statistical shape models. In: Proceedings of CAOS-International. pp. 24–25.

Chan, C. S. K., Edwards, P. J., Hawkes, D. J., 2003. Integration of ultrasound based registration with statistical shape models for computer assisted orthopaedic surgery. In: SPIE Medical Imaging: Image Processing. Vol. 5032. pp. 414–424.

Christensen, G. E., Rabbit, R. D., Miller, M. I., 1996. Deformable templates using large deformation kinematics. IEEE Transactions on Image Processing 5 (10), 1435–1447.

Cinquin, P., Lavallée, S., Dubois, F., Brunie, L., Troccaz, J., Peria, O., Mazier, B., Sep. 1995. Patent: Method for determining the position of an organ. US Patent number: 5447154.

Cootes, T. F., Edwards, G., Taylor, C. J., 1999. Comparing active shape models with active appearance models. In: Proceedings of British Machine Vision Conference. Vol. 1. pp. 173–182.

Cootes, T. F., Edwards, G. J., Taylor, C. J., 1998. Active appearance models. In: European Conference on Computer Vision. Vol. 2. pp. 484–498.

Cootes, T. F., Taylor, C. J., 2001. Statistical models of appearance for medical image analysis and computer vision. In: SPIE Medical Imaging: Image Processing. pp. 236–248.

Cootes, T. F., Taylor, C. J., Cooper, D. H., Graham, J., 1992. Training models of shape from sets of examples. In: Proceedings of British Machine Vision Conference. pp. 9–18.

Cootes, T. F., Taylor, C. J., Cooper, D. H., Graham, J., 1995. Active shape models – their training and application. Computer Vision Image Understanding 61 (1), 38–59.

Daanen, V., Tonetti, J., Troccaz, J., 2004. A fully automated method for the delineation of osseous interface in ultrasound images. In: Medical Imaging Computing and Computer-Assisted Intervention—MICCAI 2004, Lecture Notes in Computer Science. Vol. 3216. Springer-Verlag Heidelberg, pp. 549–557.

Dance, D. R., 1988. Diagnostic radiology with X-rays. In: Webb, S. (Ed.), The Physics of Medical Imaging. IOP Publishing Ltd., Ch. 2, pp. 20–73.

Datamonitor, 2004. Commercial Perspectives: US Hip and Knee Replacement - Market surges in new millennium (Report highlights).
URL http://www.datamonitor.com/~5fb6d8491b45405a96f6db3e819a7-0f6~/industries/research/?pid=DMHC1940&type=Report

Davies, R. H., Cootes, T. F., Taylor, C. J., 2001a. A minimum description length approach to statistical shape modelling. In: Information Processing and Medical Images (IPMI). pp. 50–63.

Davies, R. H., Cootes, T. F., Taylor, C. J., 2001b. Optimising statistical shape models using a minimum description length approach. In: Medical Image Understanding and Analysis. pp. 77–80.

Davies, R. H., Twining, C. J., Cootes, T. F., Waterton, J. C., Taylor, C. J., 2002a. 3D statistical shape models using direct optimisation of description length. In: Proceedings for the 7th European Conference on Computer Vision (ECCV), Part III. pp. 3–20.

Davies, R. H., Twining, C. J., Cootes, T. F., Waterton, J. C., Taylor, C. J., 2002b. A minimum description length approach to statistical shape modelling. IEEE Transactions on Medical Imaging 21, 525–537.

Dennis, J. E. J., Torczon, V., 1991. Direct search methods on parallel machines. SIAM Journal on Optimization 1, 448–474.

DiGioia, A. M., Jaramaz, B., Blackwell, M., Simon, D. A., Morgan, F., Moody, J. E., Nikou, C., Colgan, B. D., Aston, C. A., Labarca, R. S., Kischell, E., Kanade, T., Oct. 1998a. Image guided navigation system to measure intraoperatively acetabular implant alignment. Clinical Orthopaedics and Related Research 355, 8–22.

DiGioia, A. M. I., Jaramaz, B., Colgan, B. D., 1998b. Computer assisted orthopaedic surgery. image guided and robotic assistive technologies. Clinical Orthopaedics and Related Research 354, 8–16.

Downey, D. B., Fenster, A., Williams, J. C., 2000. Clinical utility of three-dimensional US. Radiographics 20, 559–571.

Dryden, I. L., Mardia, K. V., 1998. Statistical Shape Analysis. Wiley.

Edwards, P. J., King, A. P., Maurer, C. R. de Cunha, D. A., Hawkes, D. J., Hill, D. L. G., Gaston, R. P., Fenlon, M. R., Jusczyzck, A., Strong, A. J., Chandler, C. L., Gleeson, M. J., 2000. Design and evaluation of a system for Microscope-Assisted Guided Interventions (MAGI). IEEE Transactions on Medical Imaging 19 (11), 1082–1093.

Eggli, S., Pisan, M., Muller, M., 1998. The value of preoperative planning for total hip arthroplasty. Journal of Bone and Joint Surgery - British volume 80, 382–390.

Fitzpatrick, J. M., Hill, D. L., Maurer, C. R. J., 2000. Image registration. In: Sonka, M., Fitzpatrick, J. M. (Eds.), Handbook of Medical Imaging Vol. II: Medical Image Processing and Analysis. SPIE-International Society for Optical Engineering, Belligham, WA, Ch. 8, pp. 447–513.

Fitzpatrick, J. M., West, J. B., Maurer, Jr., C. R., 1998. Predicting error in rigid-body point-based registration. IEEE Transactions on Medical Imaging 17 (5), 694–702.

Fleute, M., Lavallée, S., 1998. Building a complete surface model from sparse data using statistical shape models: application to computer assisted knee surgery. In: Medical Imaging Computing and Computer-Assisted Intervention—MICCAI 1998, Lecture Notes in Computer Science. Vol. 1496. Springer-Verlag GmbH, pp. 879–887.

Fleute, M., Lavallée, S., 1999. Nonrigid 3D/2D registration of images using statistical models. In: Medical Imaging Computing and Computer-Assisted Intervention—MICCAI 1999, Lecture Notes in Computer Science. Springer-Verlag GmbH, pp. 138–147.

Fleute, M., Lavallée, S., Desbat, L., 2002. Integrated approach for matching statistical shape models with intra-operative 2D and 3D data. In: Medical Imaging Computing and Computer-Assisted Intervention—MICCAI 2002, Lecture Notes in Computer Science. Vol. 2489. pp. 365–372.

Fleute, M., Lavallée, S., Julliard, R., 1999. Incorporating a statistically based shape model into a system for computer-assisted anterior cruciate ligament surgery. Medical Image Analysis 3, 209–222.

Frangi, A. F., Rueckert, D., Schnabel, J. A., 2001. Automatic 3D ASM construction via atlas-based landmarking and volumetric elastic registration. In: Information Processing in Medical Imaging. Vol. 2082. pp. 78–91.

Frangi, A. F., Rueckert, D., Schnabel, J. A., Niessen, W. J., 2002. Automatic construction of

multiple-object three dimensional statistical shape models: Application to cardiac modelling. IEEE Transactions on Medical Imaging 21 (9), 1151–66.

Golub, G., van Loan, C., 1996. Matrix computations, 3rd Edition. The John Hopkins University Press.

Gray, H., 1918. Osteology. In: Anatomy of the human body. Lea & Febiger.

Gregory, J. S., Testi, D., Stewart, A., Undrill, P. E., Reid, D. M., Aspden, R. M., 2004. A method for assessment of the shape of the proximal femur and its relationship to osteoporotic hip fracture. Osteoporosis International 15, 5–11.

Hartkens, T., Rueckert, D., Schnabel, J. A., Hawkes, D. J., Hill, A., 2002. VTK CISG registration toolkit: An open source software package for affine and non-rigid registration of single- and multimodal 3D images. In: Workshop on Bildverarbeitung für die Medizin, Informatik Aktuell. Springer-Verlag, pp. 409–412.

Hawkes, D. J., Barratt, D., Blackall, J. M., Chan, C., Edwards, P., Rhode, K., Penney, G., McClelland, J., Hill, D., 2005. Tissue deformation and shape models in image-guided interventions: a discussion paper. Medical Image Analysis 9, 163–175.

Hedrick, W. R., Hykes, D. L., Starchman, D. E., 1995. Ultrasound physics and instrumentation. Mosby, St. Louis.

Heger, S., Portheine, F., Ohnsorge, J. A. K., Radermacher, K., 2003. A new approach for user interactive A-mode ultrasound based registration. In: Proceedings of CAOS-International. pp. 136–137.

Herline, A. J., Herring, J. L., Stefansic, J. D., Chapman, W. C., Galloway Jr, R. L., Dawant, B. M., 2000. Surface registration for use in interactive, image guided liver sugery. Computer Aided Surgery 5 (1), 11–17.

Herring, J. L., Dawant, B. M., Maurer, C. R., Muratore, D. M., Galloway, R. L., Fitzpatrick, M., 1998. Surface-based registration of ct images to physical space for image-guided surgery of the spine: A sensitivity study. IEEE Transactions on Medical Imaging 17, 743–752.

Hill, D. L. G., Batchelor, P., 2001. Registration methodology: Concepts and algorithms. In: Hajnal, J. V., Hill, D. L. G., Hawkes, D. J. (Eds.), Medical Image Registration. CRC Press, Ch. 3, pp. 39–70.

Hufner, T., Oszwald, M., Kfuri Jr, M., Rosenthal, H., Citak, M., Krettek, C., 2003. A-mode ultrasound registration in computer assisted pelvic surgery. In: Proceedings of CAOS-International. pp. 148–149.

Hurri, J., Hyvärinen, A., Karhunen, J., Oja, E., 1996. Image feature extraction using independent component analysis. In: Proceedings of IEEE Nordic Signal Processing Symposium (NORSIG'96). Espoo, Finland.

Hutton, T., 2004. Dense surface models of the human face. Ph.D. thesis, University College London, UK.

Hyvärinen, A., 1999. Survey on independent component analysis. Neural Computing Surveys 2, 94–128.

Hyvärinen, A., Karhunen, J., Oja, E., 2001. Independent Component Analysis. John Wiley & Sons.

Hyvärinen, A., Oja, E., 2000. Independent component analysis: Algorithms and applications. Neural Networks 13 (4–5), 411–430.

Ionescu, G., Lavallée, S., Demongeot, J., 1999. Automated registration of ultrasound with CT images: Application to computer assisted prostate radiotherapy and orthopedics. In: Medical Imaging Computing and Computer-Assisted Intervention—MICCAI 1999, Lecture Notes in Computer Science. pp. 768–777.

Jaramaz, B., Nikou, C., Cavalier, B., Blendea, S., LaBarca, R., DiGioia, A. M., 2003. Experimetal validation of ultrasound registration of long bones. In: Proceedings of CAOS-International. pp. 160–161.

Kalender, W. A., 2000. Computed Tomography. Publicis MCD Verlag, Munich.

Kowal, J., Hamdam, R., Heini, P., Kothe, R., Nolte, L.and Styner, M., 2003. Ultrasound based registration for minimally invasive interventions. In: Proceedings of CAOS-International. pp. 196–197.

Lavallée, S., Merloz, P., Stindel, E., Kilian, P., Troccaz, J., Cinquin, P., Langlotz, F., Nolte, L. P., 2004. Echomorphing: introducing an intra-operative imaging modality to reconstruct 3D bone surfaces for minimally invasive surgery. In: Proceedings of CAOS-International. pp. 38–39.

Lavallée, S., Troccaz, J., Sautot, P., Mazier, B., Cinquin, P., Merloz, P., Chirossel, J., 1995. Computer-assisted spinal surgery using anatomy-based registration. In: Taylor, R. H., Lavallée, S., Burdea, G. C., Mosges, R. (Eds.), Computer-Integrated Surgery: Technology and Clinical Applications. Cambridge, MA : MIT Press, Ch. 32, pp. 425–449.

Lee, S., Wolberg, G., Shin, S. Y., 1997. Scattered data interpolation with multilevel B-splines. IEEE Transactions on Visualization and Computer Graphics 3, 228–244.

Lewis, J., Galloway, R. L. J., Schreiner, S., 1998. An ultrasonic approach to localization of fiducial markers for interactive, image-guided neurosurgery–part I: Principles. IEEE Transactions on Biomedical Engineering 45, 620–630.

Lorensen, W. E., Cline, H. E., 1987. Marching cubes: A high resolution 3-D surface reconstruction algorithm. Computer Graphics 21 (4), 163–169.

Maintz, J., Viergever, M., 1998. A survey of medical image registration. Medical Image Analysis 2 (1), 1–36.

Martini, F. H., Timmons, M. J., 1997. Human Anatomy. Prentice Hall.

Maurer, Jr., C., Fitzpatrick, J., 1993. Interactive Image-Guided Neurosurgery. American Association of Neurological Surgeons, Park Ridge, IL, Ch. A review of medical image registration, pp. 17–44.

Maurer, Jr., C. R., Gaston, R. P., Hill, D. L. G., Gleeson, M. J., Taylor, M. G., Fenlon, M. R., Edwards, P. J., Hawkes, D. J., 1999. Acoustick: A tracked A-mode ultrasonography system for registration in image guided surgery. In: Medical Imaging Computing and Computer-Assisted Intervention—MICCAI 1999, Lecture Notes in Computer Science. pp. 953–962.

Mehlman, C. T., DiPasquale, T. G., 1997. Radiation exposure to the orthopaedic surgical team during fluoroscopy: "how far away is far enough?". Journal of Orthopaedic Trauma 11, 392–398.

Meller, S., Kalender, W. A., 2004. Building a statistical shape model of the pelvis. In: Proceedings of Computer Assisted Radiology and Surgery. pp. 561–566.

Messmer, P., Long, G., Suhm, N., Regazzoni, P., Jacob, A. L., 2001. Volumetric model determination of the tibia based on 2D radiographs using a 2D/3D database. Computer Aided Surgery 6, 183–194.

Meza, J. C., Mar. 1994. Opt++: An object-oriented class library for nonlinear optimization. Tech. rep., Sandia Technical Report SAND94-8225, Sandia National Laboratories, Livermore, CA, USA.

Muratore, D. M., Russ, H. J., Dawant, B. M., Galloway, R. L., 2002. Three-dimensional image registration of phantom vertebrae for image-guided surgery: A preliminary study. Computer Aided Surgery 7, 342–352.

Nelson, T. R., Pretorius, D. H., 1998. Three-dimensional ultrasound imaging. Ultrasound in Medicine and Biology 24, 1243–1270.

Noble, P. C., Sugano, N., Johnston, J. D., Thompson, M. T., Conditt, M. A., Engh Sr, C. A., Mathis, K. B., 2003. Computer simulation: how can it help the surgeon optimize implant position? Clinical Orthopaedics and Related Research, 242–252.

Penney, G. P., Barratt, D. C., Chan, C. S. K., Slomczykowski, M., Carter, T. J., Edwards, P. J., Hawkes, D. J., 2005. Cadaver validation of intensity-based ultrasound to CT registration. In: Medical Imaging Computing and Computer-Assisted Intervention—MICCAI 2005, Lecture Notes in Computer Science. Vol. 3750. Springer-Verlag, pp. 1000–1007.

Penney, G. P., Blackall, J. M., Hamady, M. S., Sabharwal, T., Adam, A., Hawkes, D. J., 2004. Registration of freehand 3D ultrasound and magnetic resonance liver images. Medical Image Analysis 8, 81–91.

Penney, G. P., Edwards, P. J., King, A. P., Blackall, J. M., Batchelor, P. G., Hawkes, D. J., 2001. A stochastic iterative closest point algorithm (stochastICP). In: Medical Imaging Computing and Computer-Assisted Intervention—MICCAI 2001, Lecture Notes in Computer Science. Springer-Verlag, pp. 762–769.

Peters, T. M., 2000. Image-guided surgery: from X-rays to virtual reality. Computer Methods in Biomechanics and Biomedical Engineering 4, 27–57.

Prager, R., Rohling, R., Gee, A., Berman, L., 1998. Rapid Calibration for 3-D Freehand Ultrasound. Ultrasound in Medicine and Biology 24 (6), 855–869.

Press, W. H., Teukolsky, S. A., Vetterling, W. T., Flannery, B. P., 1992. Minimization or maximization of functions. In: Numerical Recipes in C. Cambridge University Press, Ch. 10, pp. 394–455.

Rajamani, K., Joshi, S., Styner, M., 2004a. Bone model morphing for enhanced surgical visualization. In: IEEE International Symposium on Biomedical Imaging (ISBI): Macro to Nano. pp. 1255–1258.

Rajamani, K., Nolte, L., Styner, M., 2004b. A novel approach to anatomical structure morphing for intraoperative visualization. In: Medical Imaging Computing and Computer-Assisted Intervention—MICCAI 2004, Lecture Notes in Computer Science. Springer-Verlag Heidelberg, pp. 478–485.

Rajamani, K. T., Hug, J., Nolte, L. P., Styner, M., 2004c. Bone morphing with statistical shape models for enhanced visualization. In: SPIE Medical Imaging: Visualization, Image-Guided Procedures, and Display. San Diego, CA, USA, pp. 122–130.

Robb, R. A., Hanson, D. P., Karwoski, R. A., Larson, A. G., Workman, E. L., Stacy, M. C., 1989. ANALYZE: A comprehensive, operator-interactive software package for multidimensional medical image display and analysis. Computerized Medical Imaging and Graphics 13, 433–454.

Rueckert, D., 2001. Nonrigid registration: Concepts, algorithms, and applications. In: Hajnal, J. V., Hill, D. L. G., Hawkes, D. J. (Eds.), Medical Image Registration. CRC Press, Ch. 13, pp. 281–301.

Rueckert, D., Frangi, A. F., Schnabel, J. A., 2001. Automatic construction of 3D statistical deformation models using non-rigid registration. In: Medical Imaging Computing and Computer-Assisted Intervention—MICCAI 2000, Lecture Notes in Computer Science. pp. 77–84.

Rueckert, D., Frangi, A. F., Schnabel, J. A., 2003. Automatic construction of 3-D statistical deformation models of the brain using nonrigid registration. IEEE Transactions on Medical Imaging 22 (8), 1014–1025.

Rueckert, D., Sonoda, L. I., Hayes, C., Hill, D. L. G., Leach, M. O., Hawkes, D. J., 1999. Nonrigid registration using free-form deformations: application to breast MR images. IEEE Transactions on Medical Imaging 18 (8), 712–721.

Schönemann, P. H., 1966. A generalized solution for the orthogonal procrustes problem. Psychometrika 31, 1–10.

Schreiner, S., Galloway, R. L. J., Lewis, J. T., Bass, W. A., Muratore, D. M., 1998. An ultrasonic

approach to localization of fiducial markers for interactive, image-guided neurosurgery–part II: Implementation and automation. IEEE Transactions on Biomedical Engineering 45, 631–641.

Schroeder, W., Martin, K., Lorensen, B., Avila, L., Avila, R., Law, C., 1997. The Visualization Toolkit: An Object-Oriented Approach to 3-D Graphics. Prentice-Hall.

Seeram, E., 1994. Computed Tomography: Physical Principles, Clinical Applications, and Quality Control. W. B. Saunders Company, Philadelphia.

Simon, D., O'Toole, R., Blackwell, M., Morgan, F., Di Gioia, III, M. A. M., Kanade, T., 1995. Accuracy validation in image-guided orthopaedic surgery. In: Proceedings of the Second International Symposium on Medical Robotics and Computer Assisted Surgery. pp. 185–192.

Stindel, E., Briard, J. L., Merloz, P., Plaweski, S., Dubrana, F., Lefevre, C., Troccaz, J., 2002. Bone morphing: 3D morphological data for total knee arthroplasty. Computer Aided Surgery 7, 156–168.

Studholme, C., Hill, D., Hawkes, D., 1999. An overlap invariant entropy measure of 3D medical image alignment. Pattern Recognition 32, 71–86.

Stulberg, S., Kienzle III, T., 1995. Computer- and robot- assisted orthopaedic surgery. In: Taylor, R. H., Lavallée, S., Burdea, G. C., Mosges, R. (Eds.), Computer-Integrated Surgery: Technology and Clincial Applications. Cambridge, MA : MIT Press, Ch. 27, pp. 373–378.

Sugano, N., Ohzono, K., Nishii, T., Haraguchi, K., Sakai, T., Ochi, T., 1998. Computed-tomography-based computer preoperative planning for total hip arthroplasty. Computer Aided Surgery 3, 320–324.

Suinesiaputra, A., Üzümcü, M., Frangi, A. F., Kaandorp, T. A. M., Reiber, J. H. C., Lelieveldt, B. P. F., 2004. Detecting regional abnormal cardiac contraction in short-axis MR images using independent component analysis. In: Medical Imaging Computing and Computer-Assisted Intervention—MICCAI 2004, Lecture Notes in Computer Science. Vol. 3216. pp. 737–744.

Thacker, N. A., Cootes, T. F., 1996. Vision through optimization. British Machine Vision Conference (BMVC) Tutorial notes.

The National Joint Registry (NJR) Centre, 2004. National Joint Registry for England and Wales: 1st Annual Report.

Thiel, W., 2002. Ergänzung für die konservierung ganzer leichen nach W. Thiel. Annals of Anatomy 184, 267–270.

Thomas, J. G., Peters, R. A., Jeanty, P., 1991. Automatic segmentation of ultrasound images using morphological operators. IEEE Transactions on Medical Imaging 10, 180–186.

Tonetti, J., Carrat, L., Blendea, S., Merloz, P., Troccaz, J., Lavallée, S., Chirossel, J. P., 2001a. Clinical results of percutaneous pelvic surgery. computer assisted surgery using ultrasound compared to standard fluoroscopy. Computer Aided Surgery 6, 204–211.

Tonetti, J., Carrat, L., Blendea, S., Troccaz, J., Merloz, P., Lavallée, S., Chirossel, J. P., 2001b. Clinical validation of computer assisted pelvic surgery using ultrasound. a percutaneous safe technique with low radiation exposure. Studies in Health Technology and Information 81, 515–520.

Tonetti, J., Carrat, L., Lavallée, S., Cinquin, P., Merloz, P., Pittet, L., 1997. Ultrasound-based registration for percutaneous computer assisted pelvis surgery: Application to iliosacral screwing of pelvis ring fractures. In: Proceedings of Computer Assisted Radiology and Surgery. pp. 961–966.

Tonetti, J., Carrat, L., Lavallée, S., Pittet, L., Merloz, P., Chirossel, J. P., 1998. Percutaneous iliosacral screw placement using image guided techniques. Clinical Orthopaedics and Related Research, 103–110.

Torczon, V., 1992. PDS: Direct search methods for unconstrained optimization on either sequential or parallel machines. Technical Report: CRPC-TR92206, Center for Research on Parallel Computing, Rice University.

Üzümcü, M., Frangi, A. F., Reiber, J. H. C., Lelieveldt, B. P. F., 2003. Independent component analysis in statistical shape models. In: SPIE Medical Imaging: Image Processing. Vol. 5032. pp. 375–383.

van Hellemondt, G., de Kleuver, M., Kerckhaert, A., Anderson, P., Langlotz, F., Nolte, L. P., Pavlov, P. W., 2002. Computer-assisted pelvic surgery: An in vitro study of two registration protocols. Clinical Orthopedics and Related Research 405, 287–293.

Viola, P., Wells III, W. M., 1997. Alignment by maximization of mutual information. International Journal of Computer Vision 24 (2), 137–154.

Wells, P. N. T., 1999. Ultrasonic imaging of the human body. Reports on Progress in Physics 62, 671–722.

Winter, S., Brendel, B., Rick, A., Stockheim, M., Schmieder, K., Ermert, H., 2002. Registration of bone surfaces, extracted from CT-datasets, with 3D ultrasound. Biomedizinische Technik 47 (1), 57–60.

Yagel, R., Alyassin, A. M., Blezek, D. J., Lorensen, W. E., Mar. 2002. Patent: Detect surface points of an ultrasound image. International Publication number: WO 02/24075 A1.

Yao, J., Taylor, R., 2001. A bone density atlas based on tetrahedral meshes. In: Proceedings of CAOS-Internationl. Pittsburgh, PA, USA.

Yao, J., Taylor, R., 2002. Deformable registration between a statistical bone density atlas and X-ray images. In: Proceedings of CAOS-Internationl. Santa Fe, pp. 168–169.

Yao, J., Taylor, R., 2003. A multiple-layer flexible mesh template matching method for nonrigid registration between a pelvis model and CT images. In: SPIE Medical Imaging: Image Processing. pp. 1117–1124.

Publications

Articles in conference proceedings

- Barratt, D.C., Penney, G.P., Chan, C.S.K., Slomczykowski, M., Carter, T.J., Edwards, P.J., Hawkes, D.J., 2005. Self-Calibrating Ultrasound-to-CT Bone Registration. In: Lecture Notes in Computer Science: Medical Image Computing and Computer-Assisted Intervention - MICCAI 2005. Vol. 3749. Springer-Verlag, pp. 605-612.

- Penney, G.P., Barratt, D.C., Chan, C.S.K., Slomczykowski, M., Carter, T.J., Edwards, P.J., Hawkes, D.J., 2005. Cadaver validation of intensity-based ultrasound to CT registration. In: Lecture Notes in Computer Science: Medical Image Computing and Computer-Assisted Intervention - MICCAI 2005. Vol. 3750. Springer-Verlag, pp. 1000-1007.

- Chan, C.S.K., Barratt, D.C., Edwards, P.J., Penney, G.P., Slomczykowski, M., Carter, T.J., Hawkes, D.J., 2004. Cadaver validation of the use of ultrasound for 3D model instantiation of bony anatomy in image guided orthopaedic surgery. In: Lecture Notes in Computer Science: Medical Image Computing and Computer-Assisted Intervention - MICCAI 2004. Vol. 3217. Springer-Verlag, pp. 397-404.

- Chan, C.S.K., Edwards, P.J., Barratt, D.C., Slomczykowski, M., Hawkes, D.J., 2004. Ultrasound-based reconstruction and registration of 3D bone anatomy using statistical shape models. In: Proceedings of CAOS International, pp. 24-25.

- Chan, C.S.K., Edwards, P.J., Hawkes, D.J., 2003. Integration of ultrasound based registration with statistical shape models for computer assisted orthopaedic surgery. In: Proceedings of SPIE Medical Imaging 2003: Image Processing. Vol. 5032. pp. 414-424.

Articles in journals

- Penney, G.P., Barratt, D.C., Chan, C.S.K., Slomczykowski, M., Carter, T.J., Edwards, P.J., Hawkes, D.J., 2006. Cadaver validation of intensity-based ultrasound to CT registration. Medical Image Analysis, accepted for publication.

- Barratt, D.C., Penney, G.P., Chan, C.S.K., Slomczykowski, M., Carter, T.J., Edwards, P.J., Hawkes, D.J., 2005. Self-calibrating 3D-Ultrasound-based Bone Registration for Minimally-invasive Orthopedic Surgery. IEEE Transactions in Medical Imaging, accepted for publication.

- Hawkes, D.J., Barratt, D., Blackall, J.M., Chan, C., Edwards, P.J., Rhode, K., Penney, G.P., McClelland, J., and Hill, D.L., 2005. Tissue deformation and shape models in image-guided interventions: a discussion paper, Medical Image Analysis 9, 163-175.

Index